



QUENCH - LOCA - REPORTS Nr. 2

**Results of the reference bundle test  
QUENCH-L1 with Zircaloy-4 claddings  
performed under LOCA conditions (SR-7651)**

J. Stuckert, M. Große, C. Rössger, M. Steinbrück, M. Walter



Karlsruher Institut für Technologie

in der Helmholtz-Gemeinschaft

Wissenschaftliche Berichte

## **QUENCH – LOCA – REPORTS Nr. 2**

# Results of the LOCA reference bundle test QUENCH-L1 with Zircaloy-4 claddings. (SR-7651)

J. Stuckert\*, M. Große\*, C. Rössger\*, M. Steinbrück\*, M. Walter\*\*

Institut für Angewandte Materialien:

\* Angewandte Werkstoffphysik (IAM-AWP)

\*\* Werkstoff- und Biomechanik (IAM-WBM)

Programm Nukleare Sicherheitsforschung

Karlsruher Institut für Technologie

March 2018

## Impressum

Karlsruher Institut für Technologie (KIT)

Institut für Angewandte Materialien

Angewandte Werkstoffphysik IAM-AWP-KOR

Nukleare Sicherheitsforschung

Hermann-von-Helmholtz-Platz 1

76344 Eggenstein-Leopoldshafen

[www.iam.kit.edu/awp/666.php](http://www.iam.kit.edu/awp/666.php)

DOI: 10.5445/IR/1000083067



# Zusammenfassung

## Ergebnisse des unter Bedingungen eines LOCA-Störfalls ausgeführten Referenzversuches QUENCH-LOCA-1

Der QUENCH-L1-Versuch wurde als Referenztest für die QUENCH-LOCA-Testserie konzipiert. Ziel der Bündel-Testserie ist die Prüfung von Brennstabhüllrohrmaterialien hinsichtlich Verformung, Bersten und Wasserstoffaufnahme bei der für deutsche Reaktoren repräsentativen LOCA-Auslegungsstörfallszenarien. Des Weiteren werden mittels detaillierter mechanischer Nachuntersuchungen anhand von Festigkeitseigenschaften Versprödungskriterien für Hüllrohre ermittelt. Das QUENCH-L1-Testbündel bestand aus 21 elektrisch beheizten Brennstabsimulatoren mit Hüllrohren aus Zircaloy-4 im Lieferzustand. Jeder Brennstabsimulator wurde separat mittels Krypton druckbeaufschlagt. Für alle Stäbe wurde ein Enddruck von 55 bar eingestellt. Während 90 s wurde die Temperatur in der transienten Phase von 570 auf 1100 °C erhöht. Die abnehmende Festigkeit und die zunehmende Duktilität des Hüllrohrmaterials mit zunehmender Temperatur führten zum lokalen Ausbeulen und anschließendem Bersten aller Brennstabsimulatoren in der transienten Phase. Das Experiment wurde durch Abschrecken des Bündels mit Wasser nach einer ca. 120 s dauernden Abkühlphase beendet. Nachuntersuchungen ergaben Werte für die Dehnung zwischen 25% und 45% im Bereich der Hüllrohre mit einem maximalen Oxidationsgrad von 2% ECR, der im Berstbereich gemessen wurde. Neutronen-radiographische Untersuchungen der Hüllrohre zeigten eine erhöhte Konzentration von absorbiertem Wasserstoff in den Hüllrohren in der Nähe der aufgeplatzten Beulen. Für die inneren Stäbe konnte nachgewiesen werden, dass der Wasserstoff in bandförmigen Bereichen an der Grenze zur inneren Oxidationszone absorbiert wurde. Zugversuche an den Hüllrohren mit erhöhtem Wasserstoffgehalt zeigten, dass alle Stäbe im Zentralbereich der Berstöffnungen versagten (Anmerkung - der Zentralstab konnte leider nicht getestet werden, da er bereits während der manuellen Entfernung der Heizer oberhalb und unterhalb der Berstöffnung im Bereich der Wasserstoffbänder zerbrach).



# Abstract

The QUENCH-L1 bundle experiment with Zircaloy-4 cladding tubes was defined as reference test for the QUENCH-LOCA test series. The overall objective of this bundle test series is the investigation of ballooning, burst and secondary hydrogen uptake of the cladding under representative design based accident conditions, as well as to check the embrittlement criteria by means of detailed mechanical post-test investigations. The QUENCH-L1 test bundle contained 21 electrically heated fuel rod simulators made of as-received Zircaloy-4 claddings. Each rod was separately pressurized with krypton gas using an initial pressure of 55 bar for all rods. The transient phase with heating up from 570 °C to 1100 °C lasted 90 s. The decreasing yield strength and increasing ductility of the heated claddings with increasing temperature resulted in a progressive ballooning and consequent burst of all rods during the transient. The duration of the slow cooling phase was about 120 s. The test was terminated by water quenching. Post-test investigations showed maximal strain values between 25 and 45% at cladding positions with oxidation degree corresponding to 2% ECR measured in the burst region. Neutron radiography investigations of inner cladding tubes showed elevated concentrations of absorbed hydrogen close to the burst positions in band shaped cladding regions formed at the boundary of inner oxidised zone (so called secondary hydriding). Tensile tests on the cladding tubes with higher hydrogen content showed, that all rods failed in the centre of the burst opening (remark – unfortunately, the centre cladding could not be tested since it already has broken during the manual withdrawal of heaters in the regions of the hydrogen bands above and below the burst opening).



# Contents

Zusammenfassung .....	i
Abstract.....	iii
Contents.....	v
List of Tables .....	vi
List of Figures .....	vii
Introduction .....	1
1 Description of the Test Facility.....	3
2 Test Bundle Instrumentation .....	5
2.1 Gas Measurement System .....	5
3 Data Acquisition and Process Control.....	6
4 Test Conduct and Results of Online Measurements.....	7
5 Posttest Examination .....	8
5.1 Visual observations .....	8
5.2 Profilometry of Claddings with Laser Scanner.....	8
5.2.1 Linear Laser Scanning .....	8
5.2.2 Main Characteristics of the Measuring Device and Procedures .....	9
5.2.3 Results of the Scans .....	9
5.3 Nondestructive Eddy Current Measurement .....	10
5.4 Optical Observation of Outer Cladding Surfaces .....	10
5.5 Metallographic Examination.....	11
5.6 Analysis of Absorbed Hydrogen by Means of Neutron Radiography and Tomography.....	11
5.6.1 Basic Principles .....	11
5.6.2 Technique .....	12
5.6.3 Results of Radiography .....	12
5.6.4 Results of Tomography.....	13
5.6.5 Conclusions of the Neutron Radiography and Tomography .....	13
5.7 X-Ray Diffractometry .....	13
5.8 Mechanical Tests .....	15
5.8.1 Tensile Test set-up.....	15
5.8.2 Results of the tensile tests.....	15
6 Summary and Conclusions .....	16
7 Acknowledgments .....	17
8 References.....	18
Tables and Figures .....	21

# List of Tables

<b>Table 1</b>	QUENCH Test Matrix 1997 – 2013 .....	22
<b>Table 2</b>	Design characteristics of the QUENCH-L1 test bundle .....	24
<b>Table 3</b>	Properties of Zircaloy-4 cladding tubes .....	25
<b>Table 4</b>	Main characteristics of the ZrO <sub>2</sub> pellet material, yttria-stabilized (type FZY) * .....	26
<b>Table 5</b>	QUENCH-L1; Electrical resistances of rods [mΩ] at 20°C.....	27
<b>Table 6</b>	Properties of zirconia fiber insulating boards* .....	28
<b>Table 7</b>	List of instrumentation for the QUENCH-L1 test .....	29
<b>Table 8</b>	QUENCH-L1; Rod thermocouple positions.....	36
<b>Table 9</b>	QUENCH-L1; Sequence of events.....	37
<b>Table 10</b>	QUENCH-L1; Burst parameters.....	38
<b>Table 11</b>	QUENCH-L1; Hydrogen absorbed by secondary hydrogenation (results of n <sup>0</sup> -radio- and tomography).....	39
<b>Table 12</b>	QUENCH-L1; Wetting of TFS thermocouples.....	39
<b>Table 13</b>	QUENCH-L1; Strain parameters at the middle of burst elevation .....	40
<b>Table 14</b>	QUENCH-L1; Results of tensile tests.....	41

# List of Figures

<b>Figure 1</b>	Flow diagram of the QUENCH test facility. ....	43
<b>Figure 2</b>	QUENCH Facility - Main components. ....	44
<b>Figure 3</b>	QUENCH Facility; Containment and test section. ....	45
<b>Figure 4</b>	QUENCH-L1; Test section with flow lines. ....	46
<b>Figure 5</b>	QUENCH-L1; Fuel rod simulator bundle (cross section, top view) including rod type indications corresponding to table “List of Instrumentation” ....	47
<b>Figure 6</b>	Heated fuel rod simulator. ....	48
<b>Figure 7</b>	QUENCH-L1; Rod pressure control and measurement panel. ....	49
<b>Figure 8</b>	QUENCH-L1; Rod pressurization. ....	50
<b>Figure 9</b>	QUENCH-L1; Rod pressurization process at $T_{pct}=550^{\circ}\text{C}$ . ....	51
<b>Figure 10</b>	QUENCH-L1; Concept for TC fastening at the test rod. ....	52
<b>Figure 11</b>	Axial temperature measurement locations in the QUENCH-L1 test section. ....	53
<b>Figure 12</b>	QUENCH-L1; Test bundle; TC instrumentation and rod designation (top view). ....	54
<b>Figure 13</b>	QUENCH-L1; Arrangement of the thermocouples inside the corner rods. ....	54
<b>Figure 14</b>	QUENCH Facility; H <sub>2</sub> measurement with the GAM 300 mass spectrometer. ....	55
<b>Figure 15</b>	Mass spectrometer sampling position at the off-gas pipe of the QUENCH test facility. ....	55
<b>Figure 16</b>	QUENCH-L1; Test scenario. ....	56
<b>Figure 17</b>	QUENCH-L1; Current and voltage of DC generators GS1 and GS2. ....	56
<b>Figure 18</b>	QUENCH-L1; System pressure measured at test section inlet P 511, at outlet P 512, and in the off-gas pipe P 601. ....	57
<b>Figure 19</b>	QUENCH-L1; Argon pressure between shroud and cooling jacket P 406 demonstrates tightness of the shroud. ....	57
<b>Figure 20</b>	QUENCH-L1; Quench measurement of collapsed water level (L 501), top, water mass flow rate (Fm 104), center, condensed water (L 701), bottom. ....	58
<b>Figure 21</b>	QUENCH-L1; Steam rate, top, Hydrogen, center, Krypton, bottom, measured by mass spectrometry (MS). ....	59
<b>Figure 22</b>	QUENCH-L1; Temperatures measured by rod cladding (TFS 7/1) thermocouple at -250 mm elevation. ....	60
<b>Figure 23</b>	QUENCH-L1; Temperatures measured by rod cladding (TFS 7/2) thermocouple at -150 mm elevation. ....	60
<b>Figure 24</b>	QUENCH-L1; Temperatures measured by rod cladding (TFS 7/3) and shroud (TSH 3/0) thermocouples at -50 mm elevation. ....	61
<b>Figure 25</b>	QUENCH-L1; Temperatures measured by rod cladding (TFS 7/4) and shroud (TSH 4/90) thermocouples at 50 mm elevation. ....	61
<b>Figure 26</b>	QUENCH-L1; Temperatures measured by rod cladding (TFS 7/5) and shroud (TSH 5/180) thermocouples at 150 mm elevation. ....	62
<b>Figure 27</b>	QUENCH-L1; Temperatures measured by rod cladding (TFS) and shroud (TSH 6/270) thermocouples at 250 mm elevation. ....	62
<b>Figure 28</b>	QUENCH-L1; Temperatures measured by rod cladding (TFS) and shroud (TSH 7/0) thermocouples at 350 mm elevation. ....	63

<b>Figure 29</b>	QUENCH-L1; Temperatures measured by rod cladding (TFS) and shroud (TSH 8/90) thermocouples at 450 mm elevation.....	63
<b>Figure 30</b>	QUENCH-L1; Temperatures measured by rod cladding (TFS) and shroud (TSH 9/180) thermocouples at 550 mm elevation.....	64
<b>Figure 31</b>	QUENCH-L1; Temperatures measured by rod cladding (TFS) and shroud (TSH 10/270) thermocouples at 650 mm elevation.....	64
<b>Figure 32</b>	QUENCH-L1; Temperatures measured by rod cladding (TFS) and shroud (TSH 11/0), and corner rod internal (TIT D/11) thermocouples at 750 mm elevation. ....	65
<b>Figure 33</b>	QUENCH-L1; Temperatures measured by rod cladding (TFS) and shroud (TSH 12/90), and corner rod internal (TIT C/12) thermocouples at 850 mm elevation. ....	65
<b>Figure 34</b>	QUENCH-L1; Temperatures measured by rod cladding (TFS) and shroud (TSH 13/90), and corner rod internal (TIT A/13) thermocouples at 950 mm elevation. ....	66
<b>Figure 35</b>	QUENCH-L1; Temperatures measured by rod cladding (TFS) and shroud (TSH 14/270) thermocouples at 1050 mm elevation.....	66
<b>Figure 36</b>	QUENCH-L1; Temperatures measured by rod cladding (TFS) and shroud (TSH 15/0) thermocouples at 1150 mm elevation.....	67
<b>Figure 37</b>	QUENCH-L1; Temperatures measured by rod cladding (TFS) thermocouples at 1250 mm elevation.....	67
<b>Figure 38</b>	QUENCH-L1; Temperatures measured by rod cladding (TFS 7/17) thermocouple at 1350 mm elevation. ....	68
<b>Figure 39</b>	QUENCH-L1; Overview of the TCI (inner cooling jacket). ....	68
<b>Figure 40</b>	QUENCH-L1; Axial and radial temperature distribution on time of the first burst case for selected rods. ....	69
<b>Figure 41</b>	QUENCH-L1; Axial temperature profile TFS internal and external rod group together with TSH, left, and axial temperature profile of all TFS, right, at 55.2 s (first cladding burst).....	70
<b>Figure 42</b>	QUENCH-L1; Axial temperature profile TFS internal and external rod group together with TSH, left, and axial temperature profile of all TFS, right, at 87.6 (last cladding burst).....	71
<b>Figure 43</b>	Comparison of maximal cladding temperatures at different elevations for QUENCH-L0 and -L1.....	72
<b>Figure 44</b>	QUENCH-L1; Sequence of thermocouple wetting of rod #7 by 2-phase fluid formed above collapsed water front. ....	73
<b>Figure 45</b>	QUENCH-L1; Sequence of thermocouple wetting of rods #4 and #11 by 2-phase fluid formed above collapsed water front. ....	74
<b>Figure 46</b>	QUENCH-L1; Pressure changing during heating phase; ballooning and burst. ....	75
<b>Figure 47</b>	QUENCH-L1; Mass spectrometer measurements: integral hydrogen release and krypton as burst indicator. ....	76
<b>Figure 47 b</b>	QUENCH-L1; Mass spectrometer measurements: steam release during reflood. ....	76
<b>Figure 48</b>	QUENCH-L1; Post-test bundle view between GS3 and GS4: buckled rods.....	77
<b>Figure 49</b>	QUENCH-L1; Bending of central rods with indication of maximal bending for each rod. ....	78
<b>Figure 50</b>	QUENCH-L1; Bending of periphery rods with indication of maximal bending values. ....	79
<b>Figure 51</b>	QUENCH-L1; Estimation of rod positions near to middle elevation between two spacer grids.....	80
<b>Figure 52</b>	QUENCH-L1; Axial and circumferential burst positions. ....	81
<b>Figure 53</b>	QUENCH-L0 and -L1; Comparison of circumferential positions of bursts. ....	82



<b>Figure 54</b>	QUENCH-L1; Axial burst positions.....	83
<b>Figure 55</b>	QUENCH-L1; Tube scanner laser profilometry.....	84
<b>Figure 56</b>	QUENCH-L1, Rod #2; longitudinal circumferential strain changing (top); azimuthal diameter changing downwards from burst (bottom).....	85
<b>Figure 57</b>	QUENCH-L1, Rod #3; longitudinal circumferential strain changing (top); azimuthal diameter changing downwards from burst (bottom).....	86
<b>Figure 58</b>	QUENCH-L1, Rod #4; longitudinal circumferential strain changing (top); azimuthal diameter changing downwards from burst (bottom).....	87
<b>Figure 59</b>	QUENCH-L1, Rod #5; longitudinal circumferential strain changing (top); azimuthal diameter changing downwards from burst (bottom).....	88
<b>Figure 60</b>	QUENCH-L1, Rod #6; longitudinal circumferential strain changing (top); azimuthal diameter changing downwards from burst (bottom).....	89
<b>Figure 61</b>	QUENCH-L1, Rod #7; longitudinal circumferential strain changing (top); azimuthal diameter changing downwards from burst (bottom).....	90
<b>Figure 62</b>	QUENCH-L1, Rod #8; longitudinal circumferential strain changing (top); azimuthal diameter changing downwards from burst (bottom).....	91
<b>Figure 63</b>	QUENCH-L1, Rod #9; longitudinal circumferential strain changing (top); azimuthal diameter changing downwards from burst (bottom).....	92
<b>Figure 64</b>	QUENCH-L1, Rod #10; longitudinal circumferential strain changing (top); azimuthal diameter changing downwards from burst (bottom).....	93
<b>Figure 65</b>	QUENCH-L1, Rod #12; longitudinal circumferential strain changing (top); azimuthal diameter changing downwards from burst (bottom).....	94
<b>Figure 66</b>	QUENCH-L1, Rod #13; longitudinal circumferential strain changing (top); azimuthal diameter changing downwards from burst (bottom).....	95
<b>Figure 67</b>	QUENCH-L1, Rod #14; longitudinal circumferential strain changing (top); azimuthal diameter changing downwards from burst (bottom).....	96
<b>Figure 68</b>	QUENCH-L1, Rod #15; longitudinal circumferential strain changing (top); azimuthal diameter changing downwards from burst (bottom).....	97
<b>Figure 69</b>	QUENCH-L2, Rod #16; longitudinal circumferential strain changing (top); azimuthal diameter changing downwards from burst (bottom).....	98
<b>Figure 70</b>	QUENCH-L1, Rod #17; longitudinal circumferential strain changing (top); azimuthal diameter changing downwards from burst (bottom).....	99
<b>Figure 71</b>	QUENCH-L1, Rod #18; longitudinal circumferential strain changing (top); azimuthal diameter changing downwards from burst (bottom).....	100
<b>Figure 72</b>	QUENCH-L1, Rod #19; longitudinal circumferential strain changing (top); azimuthal diameter changing downwards from burst (bottom).....	101
<b>Figure 73</b>	QUENCH-L1, Rod #20; longitudinal circumferential strain changing (top); azimuthal diameter changing downwards from burst (bottom).....	102
<b>Figure 74</b>	QUENCH-L1, Rod #21; longitudinal circumferential strain changing (top); azimuthal diameter changing downwards from burst (bottom).....	103
<b>Figure 75</b>	Blockage of coolant channel for QUENCH-L0 and -L1 bundles.....	104
<b>Figure 76</b>	QUENCH-L1; Results of eddy-current measurements of axial layer thickness distribution for inner rods. ....	105

<b>Figure 77</b>	QUENCH-L1; Results of eddy-current measurements of axial layer thickness distribution for outer rods. ....	105
<b>Figure 78</b>	QUENCH-L1; Results of eddy-current measurements of axial layer thickness distribution for two opposite sides of rods #4 and #8. ....	106
<b>Figure 79</b>	Comparison of eddy-current measurements of axial layer thickness distribution for bundles QUENCH-L1 and QUENCH-L0. ....	106
<b>Figure 80</b>	QUENCH-L1; Post-test bundle investigation by videoscope at positions of three withdrawn corner rods. ....	107
<b>Figure 81</b>	QUENCH-L1; Overview of burst structures of rods #2 - #5. ....	108
<b>Figure 82</b>	QUENCH-L1; Overview of burst structures of rods #6 - #9. ....	109
<b>Figure 83</b>	QUENCH-L1; Overview of burst structures of rods #10 - #13. ....	110
<b>Figure 84</b>	QUENCH-L1; Overview of burst structures of rods #14 - #17. ....	111
<b>Figure 85</b>	QUENCH-L1; Overview of burst structures of rods #18 - #21. ....	112
<b>Figure 86</b>	QUENCH-L1; Structure of cladding layers for rod #1 at cladding side opposite to burst opening. ....	113
<b>Figure 87</b>	QUENCH-L1; Outer and inner cladding oxidation at elevation 900 mm for rod #1. ....	114
<b>Figure 88</b>	QUENCH-L1; Outer and inner cladding oxidation at elevation 920 mm for rod #1. ....	115
<b>Figure 89</b>	QUENCH-L1; Axial distribution of inner oxidation in region of hydrogen band below burst opening for rod #1 at azimuth 315°. ....	116
<b>Figure 90</b>	QUENCH-L1; Axial distribution of inner oxidation in region of secondary hydrogenation for rod #6 at azimuth 25°. ....	117
<b>Figure 91</b>	QUENCH-L1; Hydrogen bands on neutron radiographs of inner rods and maximum hydrogen content. ....	118
<b>Figure 92</b>	QUENCH-L1; Absence of hydrogen bands on neutron radiographs of outer rods. ....	119
<b>Figure 93</b>	QUENCH-L1; Tomography projection of the reconstructed hydrogen distribution in rod #2. ....	120
<b>Figure 94</b>	QUENCH-L1; correspondance between reconstruction of tomography image and plots of mean and maximal hydrogen concentration in rod #2. ....	121
<b>Figure 95</b>	QUENCH-L1; Results of XRD analyses for hydrogen bands of rod #3 (max hydrogen content 1115 wppm). Comparison with as received cladding (a) and with hydrides (b). ....	122
<b>Figure 96</b>	QUENCH-L1; Results of XRD analyses for hydrogen bands of rod #4 (max hydrogen content 730 wppm). Comparison with as received cladding (a) and with hydrides (b). ....	123
<b>Figure 97</b>	QUENCH-L1; Results of XRD analyses for hydrogen bands of rod #5 (max hydrogen content 755 wppm). Comparison with as received cladding (a) and with hydrides (b). ....	124
<b>Figure 98</b>	Fig QUENCH-L1; Results of XRD analyses for hydrogen bands of rod #9 (max hydrogen content 1270 wppm). Comparison with as received cladding (a) and with hydrides (b). ....	125
<b>Figure 99</b>	QUENCH-L0 and QUENCH-L1; Fracture modes, occurred in tensile tests. ....	126
<b>Figure 100</b>	QUENCH-L1; Central rod #1: brittle rupture during handling. ....	127
<b>Figure 101</b>	QUENCH-L1; Results of tensile tests for inner rods. ....	128
<b>Figure 102</b>	QUENCH-L1; Results of tensile tests for outer rods. ....	129
<b>Figure 103</b>	Results of tensile tests on as-received and annealed Zircaloy-4 claddings, failure by necking. ....	130
<b>Figure 104</b>	QUENCH-L1; Optical recognition of segment strains during tensile test with rod #16. Failure due to pre-crack inside burst. ....	131

# Introduction

Under the licensing procedures for pressurized water reactors (PWR) evidence must be given that the impacts of all pipe ruptures hypothetically occurring in the primary loop and implying a loss of coolant can be controlled. The double-ended break of the main coolant line between the main coolant pump and the reactor pressure vessel is considered to constitute the design basis for the emergency core cooling system (ECCS) in a loss-of-coolant accident (LOCA). The break of a main coolant line leads to the loss of coolant in the primary circuit of a PWR and the decrease in system pressure from 15.5 MPa to eventually around 0.32 MPa (boiling point, corresponding to 135 °C). Consequently, the remaining coolant in the core as well as the emergency cooling water fed into the reactor core evaporate, the temperature of the fuel elements rises and the fuel rods start to balloon since they contain pressurized filling gas and fission gas products. At temperatures above 700°C, the load within the metallic wall reaches a critical value and the most ballooned section finally bursts.

Upon rupture of the reactor coolant line the reactor is shut down. However, as the production of decay heat will be continued, reliable sustainment of the reactor core rod geometry and long-term emergency cooling of the core are required. To retain the core rod geometry it should be established the acceptable limit of cladding embrittlement, which is increased during oxidation in steam. The current LOCA criteria and their safety goals are applied worldwide with minor modifications since the NRC release in 1973 [1, 2]. The criteria are given as limits on peak cladding temperature ( $T_{PCT} \leq 1200$  °C) and on oxidation level ECR (equivalent cladding reacted) calculated as a percentage of cladding oxidized ( $ECR \leq 17\%$  using the Baker-Just oxidation correlation). These two rules constitute the criterion of cladding embrittlement due to oxygen uptake and, according to the RSK (Reactor Safety Commission) Guidelines, are included in the current German LOCA criteria, too [3].

The results elaborated worldwide in the 1980's on the Zircaloy-4 (Zry-4) cladding tubes behavior (oxidation, deformation and bundle coolability) under LOCA conditions constitute a reliable data base and an important input for the safety assessment of LWRs. With respect to the LOCA conditions for German LWRs, different off-pile [4, 5, 6], the FR2 in-pile [7] single rod as well as the REBEKA bundle tests [8, 9] were performed. It was concluded that the ECC-criteria established by licensing authorities are conservative and that the coolability of an LWR and the public safety can be maintained in a LOCA [10]. In-pile test data (with burn-up up to 35 MWd/kgU) were consistent with the out-of-pile data and did not indicate an influence of the nuclear environment on cladding deformation.

Due to major advantages in fuel-cycle costs, optimised reactor operation, and waste management, the current trend in the nuclear industry is to increase fuel burn-up. At high burn-up, fuel rods fabricated from conventional Zry-4 often exhibit significant oxidation, hydriding, and oxide spallation. Thus, fuel vendors have developed and proposed the use of new cladding alloys, such as Duplex DX-D4, M5<sup>®</sup>, ZIRLO™ and other. Therefore, it is important to verify the safety margins for high burn-up fuel and fuel claddings with advanced alloys. In recognition of this, LOCA-related behaviour of new types of cladding is being actively investigated in several countries [11, 12]. Due to long cladding hydriding period for the high fuel burn-up, post-quench ductility is not only influenced by oxidation, it is also significantly depending on the hydrogen concentration. Consequently, the 17% ECR limit is inadequate to ensure post-quench ductility at hydrogen concentrations higher than  $\approx 500$  wppm [13]. Due to so-called secondary hydriding (during oxidation of inner cladding surface after burst), which was firstly observed in JAERI [14], the hydrogen content can reach 4000 wppm in Zircaloy cladding regions around burst [15].

Particularly to investigate the influence of the secondary hydriding phenomena on the applicability of the embrittlement criteria for the German nuclear reactors, it was decided to perform the QUENCH-LOCA bundle test series in the QUENCH facility of KIT, supported by the association of the German utilities (VGB) [16]. Additionally, the QUENCH-LOCA bundle tests could support experiments performed in-pile and in-cell, respectively, e.g. single-rod tests as those planned in the OECD SCIP-2 project [17]. Compared to single-rod experiments, bundle tests have the advantage to study the mutual interference of rod ballooning among fuel rod simulators as well as to take into account the local coolant channel blockages in this more realistic arrangement.

The first test QUENCH-L0 was performed with Zry-4 cladding tubes not pre-oxidised on 22.07.2010 as commissioning test and terminated with reflood immediately after the transient phase [18, 19]. The QUENCH-L1 test was performed on 02.02.2012 as reference test, using a similar bundle compared to the QUENCH-L0 test but including a cool-down phase between transient and reflood.

# 1 Description of the Test Facility

The QUENCH facility was constructed 1997 at KIT for investigation of the so-called hydrogen source term during reflood, i.e. of the measurement of hydrogen release during the reflood of an overheated reactor core. Since then 17 bundle tests were successfully performed under severe accident conditions ([Table 1](#)). The main components of the QUENCH test facility are presented in [Fig. 1](#). The test section is enclosed by a safety containment with a wall thickness of 5.6 mm and an inner diameter of 801.8 mm. The facility can be operated in two modes: a forced-convection mode depicted in the flow diagram of [Fig. 2](#) and a boil-off mode. In the forced-convection mode (relevant for QUENCH-LOCA-1) superheated steam from the steam generator and superheater together with argon as a carrier gas enter the test bundle at the bottom ([Figs. 3 and 4](#)). The system pressure in the test section for the QUENCH-LOCA test is about 0.3 MPa. The argon, steam and hydrogen produced in the zirconium-steam reaction flow upward inside the bundle and from the outlet at the top through a water-cooled off-gas pipe to the condenser where the remaining steam is separated from the non-condensable gases argon and hydrogen. The water cooling circuits for bundle head and off-gas pipe are temperature-controlled to guarantee that the steam/gas temperature is high enough so that condensation at the test section outlet and inside the off-gas pipe can be avoided. The temperature at the bundle head is kept at 348 K, and the flow rate of the cooling water is  $\approx 250$  g/s. The off-gas pipe consists of a water-cooled inner pipe with a countercurrent flow and a flow rate of  $\approx 370$  g/s. The water inlet temperature is controlled at 393 K. Between the off-gas pipe and inner cooling jacket there is stagnant off-gas. The main dimensions of the tubes that make up the off-gas pipe are:

Inner pipe:	outer diameter 139.7 mm, wall thickness 4.5 mm total length 3256 mm, material: stainless steel
Inner cooling jacket:	outer diameter 154 mm, wall thickness 2 mm, material: stainless steel
Outer cooling jacket:	outer diameter 168.3 mm, wall thickness 5 mm, material: stainless steel

The quenching water is injected into the bundle through a separate line marked "bottom quenching" in [Fig. 4](#). The design characteristics of the test bundle are given in [Table 2](#). The test bundle is made up of 21 fuel rod simulators, each with a length of approximately 2.5 m, and of four corner rods (see cross section in [Fig. 5](#)). The bundle is surrounded by a shroud, which has two functions: 1) The shroud acts as steam and gas guide tube; 2) It simulates an adiabatic surrounding of the reactor core. The consideration of heated rod claddings, corner rods and shroud, manufactured from similar zirconium alloys, results in the surface of 30,6 effective rod simulators.

The fuel rod simulators ([Fig. 6](#)) are held in their positions by five grid spacers, four of Zry-4, and one of Inconel 718 in the lower bundle zone. This bundle design is applied with a pitch of 14.3 mm. All test rods are heated electrically over a length of 1900 mm (thereof 1024 mm Ta heater and the residual length - Mo heaters). The Zry-4 cladding of the fuel rod simulator has an outside diameter of 10.75 mm and a wall thickness of 0.725 mm (see also [Table 2](#)). The cladding properties are listed in [Table 3](#).

Tantalum heating elements of 6 mm diameter are installed in the center of rods. Ta heaters were used for the first time in the QUENCH-L1 experiment. Their higher electrical resistance in comparison to tungsten results in higher maximum heating rates, especially during the first transient phase and hence to a more prototypical test conduct. These heaters are surrounded by annular yttria-stabilized ZrO<sub>2</sub> pellets. The physical properties of

the ZrO<sub>2</sub> pellets are described in [Table 4](#). The tantalum heaters (chemically clean tantalum) are connected to molybdenum heater (chemically clean molybdenum) and copper electrode (material 2.1293 with Cr 0.8, Zr 0.08 and balance Cu) at each end of the heater. The molybdenum and copper parts are joined by high-frequency/high-temperature brazing under vacuum ( $2 \times 10^{-3}$  mbar) using an AuNi 18 powder (particle size <105 μm). The electrical resistance of the internal rod heating system, combined of Ta and Mo heaters as well Cu alloy electrodes, was measured before (at the end of bundle assembling) and after the test ([Table 5](#)). For electrical insulation the surfaces of Mo and Cu parts are plasma-coated with 0.2 mm ZrO<sub>2</sub>. To protect the copper electrodes and the O-ring-sealed wall penetrations against excessive heat they are water-cooled (lower and upper cooling chambers filled with demineralized water). The copper electrodes are connected to the DC electric power supply by means of special sliding contacts at the top and bottom. The total heating power is limited by a maximal current of 7200 A and voltage of 9 V. Two DC-generators were used for two groups of rods connected in parallel: 1) 10 internal rods: #1 - #9 and rod #15; 2) 11 external rods: #10 - #14 and #16 - #21. The measured electric resistance of a single heater (Ta+Mo+Cu sections) is about 3.3 mΩ at room temperature. This value increases significantly with temperature. The additional resistance of the external electric circuit between the axial end of the single heater and the connection to the generator (sliding contacts, cables, and bolts) is 3.75 mΩ for the inner rod group and 4.05 mΩ for the outer rod group. These values can be taken as constant because the external electric circuit remains at ambient temperature throughout the experiment.

The lower boundary for the lower cooling chamber is a sealing plate made of stainless steel with plastic inlays for electrical insulation, sealed toward the system by O-shaped rings. The upper boundary of the lower cooling chamber is a sealing plate of stainless steel. An insulation plate made of plastic (PEEK) forms the top of the upper cooling chamber, and a sealing plate of Al<sub>2</sub>O<sub>3</sub>, functioning as a heat-protection shield, is the lower boundary of the upper cooling chamber (see [Fig. 6](#)).

In the region below the upper Al<sub>2</sub>O<sub>3</sub> plate the copper electrode is connected firmly to the cladding. This is done by rotary swaging the cladding onto the electrode. In the swaging region a sleeve of boron nitride is put between electrode and cladding for electrical insulation. The axial position of the fuel rod simulator in the test bundle is fixed by a groove and a locking ring in the top Cu electrodes. Referred to the test bundle the fixing point of the fuel rod simulators is located directly above the upper edge of the upper insulation plate. So, during operation the fuel rod simulators are allowed to expand downwards. Clearance for expansion of the test rods is provided in the region of the lower sealing plate. Also in this region, relative movement between cladding and internal heater/electrode can take place.

The test bundle is surrounded by a 3.17 mm thick shroud (79.66 mm ID) made of Zr 702 with a 36 mm thick ZrO<sub>2</sub> fiber insulation (physical properties are given in [Table 6](#)) and an annular cooling jacket made of Inconel 600 (inner tube) and stainless steel (outer tube; see [Fig. 5](#)). The annulus between shroud and cooling jacket was filled (after several cycles of degasing) with stagnant argon of about 0.3 MPa ([Fig. 19](#)) and was connected to a flow-controlled argon feeding system in order to prevent steam access to the annulus after possible shroud failure. The 6.7 mm annulus of the cooling jacket is cooled by an argon flow. Above the tantalum heaters, i.e. above the 1024 mm elevation there is no ZrO<sub>2</sub> fiber insulation to allow for higher radial heat losses. This region of the cooling jacket is cooled by a water flow ([Figs. 3 and 4](#)). Both the lack of ZrO<sub>2</sub> insulation above 1024 mm and the water cooling force the axial temperature maximum downward.

Insertion of four corner rods avoids an atypically large flow cross section at the outer positions and hence helps to obtain a rather uniform radial temperature profile.

According to LOCA scenarios the fuel rod simulators were separately pressurized. The gas supply system (Fig. 7) for individual pressurization of rods consists of pressure controller, 21 valves, 21 pressure transducers, and 21 justified compensation volumes for setting of original volume value of 31.5 cm<sup>3</sup> (the compensation is needed because of the absence of empty plenums inside the rod simulators). The gas supply is connected with capillary tubes (with inner diameter 1 mm, length ca. 1.2 m) to each rod at its lower end with drilled copper electrode (Fig. 8). The gas gap under the cladding is: 0.15 mm in the region of Cu-electrodes/Mo-heaters and 0.075 mm in the region of Ta-heater/ZrO<sub>2</sub>-pellets. Before gas filling the rods and gas supply system were evacuated.

At the beginning of experiment, the fuel rod simulators were backfilled with Kr gas to 20 bar. Then, before the transient, they were separately pressurized to the target pressure of 55 bar as shown in Fig. 9.

## 2 Test Bundle Instrumentation

The test bundle was instrumented with sheathed thermocouples (TC) attached to the rod claddings (Fig. 10) at 17 different elevations between -250 mm and 1350 mm and at different orientations according to Figs. 11 and 12. The NiCr/Ni thermocouples (1 mm diameter, stainless steel sheath 1.4541 (X6CrNiTi18-10), MgO insulation) are used for temperature measurement of rod cladding and shroud outer surfaces. The TC tip is held in place by a Zr ferrule welded to the surface. The cables of the thermocouples from the -250 mm to the 850 mm level leave the test section at the bottom of the test section whereas those of the TCs above 850 mm are routed out on the top of the test section to prevent TC cables to pass the hot zone. The thermocouples attached to the outer surface of the rod claddings are designated "TFS" for all heated rods. The shroud thermocouples (designation "TSH") are mounted at the outer surface between -250 mm and 1250 mm. The thermocouples that are installed inside the Zry-4 instrumentation rods at the three corner positions of the bundle (positions A, C and D) are designated "TIT" (see Fig. 13). The thermocouples of the cooling jacket are installed inside the wall of the inner cooling tube (from -250 mm to 1150 mm, designation "TCI") and at the outer surface of the outer cooling tube (from -250 mm to 950 mm, designation "TCO").

A list of all instruments for experiment QUENCH-L1 installed in the test section and at the test loop is given in Table 7. The distribution of the thermocouples along the bundle is shown in Table 8. No failed thermocouples were detected during the test.

The flow rates of noble gases (Ar, Kr) are regulated with the BRONKHORST flow controllers. Steam and water flows are controlled with the SIEMENS flow controllers. Numerous pressure transmitters from WIKA measure absolute and differential pressures along the gas supply system, at inlet and outlet of the test section.

### 2.1 Gas Measurement System

The outlet gases are analyzed by a Balzers mass spectrometer (MS) "GAM 300" (Fig. 14). Due to its location at the off-gas pipe in the facility the mass spectrometer responds almost immediately (less than 10 s). The "BALZERS GAM 300" is a completely computer-controlled quadrupole MS with an 8 mm rod system which allows reliable quantitative measurement of gas concentrations down to about 10 ppm. For the MS measurement a sampling tube is inserted in the off-gas pipe located approx. 2.7 m downstream from the test section outlet (see Fig. 2 and 4). It has several holes at different elevations to guarantee that the sampling of the gas to be analyzed is representative (see Fig. 15). To avoid steam condensation in the gas pipes between

the sampling position and the MS the temperature of the gas at the MS inlet is controlled by heating tapes to about 150 °C (the upper operating temperature of the MS inlet valves). This allows the MS to analyze the steam production rate. Besides, the concentrations of the following species were continuously measured by the mass spectrometer during all test phases: argon, hydrogen, steam, nitrogen, oxygen, and krypton. The fuel rod simulators are filled with krypton which can be used as an indicator for a cladding failure. Additionally, the MS is used to control the atmosphere in the facility, e.g., to monitor the gas composition at the beginning of the test.

The temperature and pressure of the analyzed gas are measured near the inlet valve of the MS. The MS is calibrated for hydrogen with well-defined argon/gas mixtures and for steam with mixtures of argon and steam supplied by a BRONKHORST controlled evaporator mixing (CEM) device. The MS off-gas is released into the atmosphere because the amount of sampling gas taken out of the system is negligible. A heated measuring gas pump was used to ensure a continuous flow of the steam-gas mixture from the off-gas pipe to the mass spectrometer.

For the MS the hydrogen mass flow rate is calculated by referring the measured H<sub>2</sub> concentration to the known argon mass flow rate according to equation (1):

$$\dot{m}_{H_2} = \frac{M_{H_2}}{M_{Ar}} \cdot \frac{C_{H_2}}{C_{Ar}} \cdot \dot{m}_{Ar} \quad (1)$$

with M representing the molecular masses, C the concentrations in vol% and  $\dot{m}$  the mass flow rates of the corresponding gases.

### 3 Data Acquisition and Process Control

A LabView-based control and data acquisition system is used in the QUENCH facility. Data acquisition, data storage, online visualization as well as process control, control engineering and system protection are accomplished by three computer systems that are linked in a network.

The data acquisition system allows recording of about 200 measurement channels at a maximum frequency of 25 Hz per channel. The experimental data and the date and time of the data acquisition are stored as raw data in binary format. After the experiment the raw data are converted into SI units and stored as ASCII data.

For process control, a system flow chart with the most important actual measurement values is displayed on the computer screen. Furthermore, the operating mode of the active components (pumps, steam generator, superheater, DC power system, valves) is indicated. Blocking systems and limit switches ensure safe plant operation. Operating test phases, e.g. heating or quenching phases, are pre-programmed and can be started on demand during the experiment. The parameter settings of the control circuits and devices can be modified online.

Online visualization allows to observe and to document the current values of selected measurement positions in the form of tables or plots. Eight diagrams with six curves each can be displayed as graphs. This means that altogether 48 measurement channels can be selected and displayed online during the course of the experiment.



The data of the main data acquisition system and of the mass spectrometers are stored on different computers. Both computers are synchronized. The data of the main acquisition system are stored at a frequency of 5 Hz. The mass spectrometer data are recorded at a frequency of approx. 1 Hz during the entire test.

## 4 Test Conduct and Results of Online Measurements

The test procedure was based on pre-test calculations performed by the Paul Scherrer Institute (PSI, Villigen) using the SCDAP/RELAP5 and IBRAE (Moscow) using the SOCRAT code systems. According to the planned LOCA scenario, the transient phase should be performed with 8 K/s followed by slow cool-down phase and quenching.

The sequence of the test events is represented in [Table 9](#). The experiment started ([Fig. 16](#)) by stabilizing the bundle conditions with an application of electrical bundle power of 3.5 kW (corresponding to a linear heat rate of  $\approx 1$  W/cm) in argon - superheated steam mixture (with rates of 6 g/s argon and 2 g/s steam, or specific rates 0.2 g/s/(effective rod) and 0.07 g/s/(effective rod) correspondingly) resulting in maximum bundle temperatures of 800 K.

Oscillation of gas pressures during the test are presented in [Figs. 18, 19](#). [Fig. 20](#) shows water flow characteristics. Mass spectrometer data on steam registration (during steam supply and evaporation phases), hydrogen production (due to oxidation of bundle and shroud) and krypton release (due to failure of claddings) are presented in [Fig. 21](#). The development of integral hydrogen production is illustrated in [Fig. 47a](#). The dependence of evaporation rate of the quench water on the position of collapsed water front is depicted in [Fig. 47b](#).

The transient was initiated by rapidly increasing the electrical power to 43 kW (linear heat rate  $\sim 9$  W/cm) followed by steady increase to 59 kW (linear heat rate  $\sim 13$  W/cm) within 63 s and stayed at that level for the rest of the transient (until 87 s). During this period the temperatures increased from their initial values to a maximum in excess of 1300 K, as planned. Due to limitation of the maximal electrical current of the DC generators ([Fig. 17](#)) the average heating rate of 5.7 K/s was realised. [Fig. 43](#) shows the development of maximum temperature at each elevation. The readings of thermocouples at each bundle elevation are shown in [Figs. 22 - 38](#). The temperatures of cooling jacket were practically not changed during the whole test ([Fig. 39](#)).

The axial temperature profile in the bundle has a pronounced maximum between 850 and 1050 mm ([Figs. 40 - 42](#)). There is also a radial temperature gradient due to two reasons: 1) radial heat flux to the shroud, 2) electrical power supplied to internal rod group was higher than the power for external group because both DC generators reached current limit ( $\approx 3600$  A) but electrical resistance of 11 external rods connected in parallel is lower than for 10 internal rods.

According to the later measurements during the tests QUENCH-L2...-L5, the tangential temperature gradient across a rod was between 30 and 70 K on the burst onset [20]. As a consequence, according to the REBEKA criterion [8], a smaller ballooning strain could be expected for claddings with larger temperature gradient. Significant radial temperature difference can be developed during the transient not only due to global radial temperature gradient across the bundle (heat loss through the shroud), but due to non-coaxial positioning of pellets and cladding. For each rod, the highest cladding temperature is achieved at the contact between pellet and cladding (absence of gas gap with relatively low heat conductivity). The temperature difference between

this contact position and opposite cladding side increased during the 3D ballooning process, due to the increase of the gas gap at the cold side whereas no gas gap formed at the hot side.

The experiment continued with power decrease to 3.5 kW at 87 s to simulate decay heat and injection of steam at a nominal of 20 g/s. There was an initial minor temporary increase in temperatures at some locations, but this phase was mostly steady cooling to about 900 K.

The cooling phase was followed by 100 g/s water injection at 207 s. There was a period of about 40 s while the lower volume was being filled during which time the temperatures increased somewhat in the absence of significant flow. The first quench occurred at the bottom of the bundle at 246 s. Quenching progressed readily toward the top (indicated by wetting of thermocouples at different elevations, [Figs. 44, 45, Table 12](#)), and the first quench in the ballooned region occurred at 266 s. Complete quench was achieved at 293 s.

The decreased yield strength and increased ductility of claddings during the transient phase resulted in a progressive ballooning and consequent burst of all of the pressurized rods ([Table 10](#)). The first burst occurred 55 s after initiation of the transient phase at about 1154 K at rod 4. All 21 pressurized rods failed within 32 s ([Fig. 46](#)). The individual rod failures were indicated by internal pressure readings and precisely correlated with krypton peaks measured in the off-gas pipe by mass spectrometer. The Kr release indicates failure of inner and outer rod groups ([Fig. 47a](#)). The first failed rod was the central rod #4, the last one was the peripheral rod #10 ([Table 10](#)). The temperature range for bursts is estimated from thermocouple readings to be between 1074 and 1169 K. Significant rod bending was observed ([Fig. 48 - 50](#)). Due to this bending there are mechanical contacts between some rods at hottest elevations ([Fig. 51](#)) observed by means of the videoscope (also [Fig. 80](#)).

## 5 Posttest Examination

### 5.1 Visual observations

After the test, the bundle was dismounted and all rods were inspected separately. The radial burst positions of all rods, except the central one, correspond to the hottest rod region and are directed mostly to the bundle centre ([Figs. 52, 53](#)). Several burst openings were directed not to the bundle centre due to rod internal temperature gradient. All bursts are axially located between 800 and 980 mm ([Fig. 54](#)). The measured burst lengths are between 8 (rod #4) and 33 mm (rod #12). The average linear burst opening parameters ([Table 6](#)): width  $4.2 \pm 2.6$  mm, length:  $15 \pm 6$  mm. No global blockage was formed due to the variation of the ballooning positions.

### 5.2 Profilometry of Claddings with Laser Scanner

#### 5.2.1 Linear Laser Scanning

The profilometry of rods was performed with a Linear Laser Scanner ([Fig. 55](#)). It was custom built by ANT Antriebstechnik GmbH for quantifying the deformations produced on the rods as a result of the QUENCH LOCA experiments. The ballooned parts of the bundle rods submitted to LOCA scenarios acquire a variety of shapes and sizes due to different temperature conditions. Therefore a precise method to detect the local variations in diameter along the rod was required.

### 5.2.2 Main Characteristics of the Measuring Device and Procedures

The measuring mechanism is based upon photocells which compare the amount of laser light blocked by the rod in relation to the portion of light that reaches the sensors. The equipment is mounted vertically and supported on a wall of the experimental hall in order to minimize the effects of shocks and vibrations propagated by the floor. The rod to be measured is placed vertically and linked to a stepper motor which is responsible for the precise turning of the rod according to a given number of measurements that should be made each 360°. A resolution of 0.25° is provided. The laser scanner itself moves a predetermined length up or down the driving rails in order to cover a specific section of the examined rod. The smallest vertical step is 100 µm and the maximum length which the scanner can handle is 2000 mm.

Automatic settings allow the scanner to work for many hours without the need of supervision. On the other hand, for safety reasons and because of mechanical limitations, the data gathering is quite slow. A total of approximately 5700 points are measured each hour. This means that a scanning of a 1500 mm rod section takes roughly 4 days considering a measurement every 1 mm and 1°.

All data generated can be processed in various ways in order to determine different information. For instance, it allows the exact location and orientation of each burst, determination of circumferential cladding strain, calculation of increase of the cladding cross-section area and thus blockage. Also, a digital 3D rendered image is generated as a record and for further analysis, since every rod is sooner or later damaged by mechanical testing or cut for metallographic examination.

### 5.2.3 Results of the Scans

The evaluation of the scans can be divided into azimuthal and longitudinal analysis.

The azimuthal plots ([Figs. 56 - 74, bottom](#)) clearly show the orientation of the bursts and also give an idea of the shape. It was revealed that the bursts were oriented mainly to the center of the bundle, because of the radial thermal gradient which was established in the test section. The maximal cladding diameter was observed in the burst plane, the minimal diameter – in the perpendicular plane. It is interesting to mention, that immediately below and above the burst opening the maximal diameter was measured in the plane perpendicular to the burst plane. Fig. 60 (bottom) illustrates this fact for the rod #6 (rod with prototypical small bending): the neighboring elevations lower the burst evident the maximal diameter in the plane perpendicular to the burst. I.e. during ballooning, the cladding extends here more in the directions perpendicular to the burst plane.

The shape of the bursts vary widely, neither size nor symmetry have any apparent correlation to burst temperature.

Also based on these scans, the circumferential strains can be calculated ([Table 13](#)), which are depicted on [Figs. 56-74, top](#). Inside the burst axial region, the strain includes here the burst opening width at each measured elevation. To obtain the maximum strain before burst, the opening width in its middle should be subtracted from the measured cladding perimeter at this elevation.

There is a clear correlation of the burst mean location and the temperature distribution on the longitudinal axis. Maximum strain of 62% was observed on the inner rod #5, minimum strain of 20% was observed on the outer rod #17.

For all rods the deformation starts at elevations about 250 mm and ends at 1250 mm. The portions of the rods which suffered more than 5% strain are usually smaller than 185 mm. These high strain sections are not symmetrically distributed around the burst and are located with 75% on the lower levels of the burst.

For each bundle elevation, the blockage is the quotient of total increase of the rod cross-sections divided by initial empty area inside the inner surface of the shroud. Percentaged, the blockage shows the reduction of the bundle fluid channel. Since the burst locations are scattered between elevations 800 and 980 mm, the blockage wasn't too significant. As shown in [Fig. 75](#), the maximum blockage occurs at 950 mm and reaches 24% of area reduction. If, hypothetically, all burst were located at the same level, the blockage would be 46%.

### 5.3 Nondestructive Eddy Current Measurement

Before cutting of cladding tubes for further investigations, the oxidation degree of each cladding was measured with the eddy current measurement device ISOSCOPE FMP30 from Helmut Fischer GmbH. The device was calibrated with two plastic foils of 24.3 and 99.3  $\mu\text{m}$  thicknesses, which were disposed to the surface of as-received Zry-4 tube. At least 20 circumferential measurements at each axial position were used to achieve the averaged result. The axial step was 20 mm. The measurement results for seven inner rods and nine outer rods are depicted in [Figs. 76 - 77](#). The device shows distance between the gauge and internal metallic layer; i.e. the measured value corresponds to the sum of the thicknesses of  $\text{ZrO}_2$  and  $\alpha\text{-Zr(O)}$  layers. The comparison of eddy current results with metallographic results confirms this fact.

The diagrams illustrate clearly the existence of radial temperature gradient: the inner rod group is more oxidized than the outer group of rods. This radial temperature gradient causes also azimuthal difference in oxidation of each rod: the side of cladding oriented to the central (hottest) rod is more oxidized than the cladding side oriented to shroud ([Fig. 78](#)). Irregular thickness changings were observed inside of the axial zone with the pronounced ballooning of gas loaded tubes due to deviation of cladding thickness from this parameter for the original calibration sample. The most oxidized region is between 750 and 950 mm, what corresponded to the axial temperature profile. [Fig. 79](#) illustrates the similar oxidation degree of bundles QUENCH-L0 and -L1.

### 5.4 Optical Observation of Outer Cladding Surfaces

First observations of burst positions were performed immediately after the test by means of the OLYMPUS videoscope. The camera of videoscope (diameter 6 mm, total cable length 9 m) was introduced through the bundle bottom at positions of withdrawn corner rods ([Fig. 80](#)).

Observations of cladding surface were performed with a Keyence digital microscope equipped with a macroscopic objective. The form of burst openings and the structure of oxidized cladding surface near to openings are shown in [Figs. 81 - 85](#). It can be seen that the cladding surface is covered with a network of crossed longitudinal cracks developed during the ballooning process. Large scale cells of crack network are located near to the burst opening, whereas small scale cells are typical for the cladding side opposite to burst. The cell size changed not only circumferentially, but also longitudinally: cell size decreased with increase of the distance to the burst location. The cracks are disappeared practically at distances between 50 and 60 mm from the burst position – accordingly to the sharp strain decrease in upper diagrams of [Figs. 56-74](#). The cell size strongly depends on strain: the higher the strain the larger are the cells.

## 5.5 Metallographic Examination

The metallographic investigation of the cross section of rod #1 at the elevation of the burst middle evidences oxide layer growth at the outer cladding surface as well as oxidation of the inner surface (Fig. 86). The averaged maximal outer oxide thickness of 15  $\mu\text{m}$  and corresponding  $\alpha\text{-Zr(O)}$  thickness of 16  $\mu\text{m}$  was reached at elevation of 900 mm (oxide thickness at some azimuth positions reached 20  $\mu\text{m}$ ). The thickness of the inner oxide layer decreases axially, and at the elevation of 920 mm (i.e. 20 mm above the burst opening edge) only very thin oxide layer was observed at the azimuth of the burst line (Figs. 87, 88).

Axial profiles of inner oxide layer in vicinity of burst openings of rods #1 and #6 are shown in Fig. 89 and Fig. 90, respectively. If around the burst opening the oxide layer thickness reaches 12...25  $\mu\text{m}$ , only very thin oxide layer (less 3  $\mu\text{m}$ ) were found at distances 30...50 mm from the burst middle. According to the radiography observations, the hydrogen bands were formed at these positions with very thin oxide layers.

The internal cladding oxidation is caused by steam penetration through the burst opening. It can be assumed that the hydrogen, released during the oxidation of the inner cladding surface, propagated in the gap between cladding and pellet up to boundary of the inner oxidised region. Outside of this region there is no more barrier for the absorption of hydrogen by the metal, and this internally oxidised region should be surrounded by hydrided zones. This assumption was confirmed by neutron radiography. Even inside the hydride zones no zirconium hydrides were detected by optical microscopy.

## 5.6 Analysis of Absorbed Hydrogen by Means of Neutron Radiography and Tomography

### 5.6.1 Basic Principles

Neutron radiography is a powerful tool for the determination of hydrogen concentration and distribution in zirconium alloys [21-24]. Hydrogen can be quantitatively and non-destructively determined with a spatial resolution of about 25  $\mu\text{m}$ . The method was applied for the post-test hydrogen analysis of selected QUENCH-L1 cladding tubes.

Firstly, a short introduction into neutron radiography will be given. The sample is positioned into a parallel neutron beam. The intensity distribution behind the sample is measured for each pixel. From the intensity the transmission  $T$  can be calculated:

$$T(x, y) = \frac{I(x, y) - I_B(x, y)}{I_0(x, y) - I_B(x, y)} \quad (2)$$

where  $x$  and  $y$  are the coordinates of the pixel position.  $I$ ,  $I_0$  and  $I_B$  are the intensities behind and before the sample and the background intensity, respectively. From the neutron transmission the total macroscopic neutron cross section  $\Sigma_{\text{total}}$  can be calculated:

$$\Sigma_{\text{total}}(x, y) = \frac{-\ln(T(x, y))}{s(x, y)} \quad (3)$$

where  $s$  is the neutron path length through the material. The total macroscopic neutron cross section is the sum of the total microscopic cross section  $\sigma$  of the isotopes  $i$  multiplied with their number density  $N$ :

$$\Sigma_{total}(x, y) = \sum_i \sigma_i \cdot N_i = \underbrace{N_{Zry}(x, y) \overline{\sigma_{Zry}}}_{\Sigma_{samples\ received}} + N_O(x, y) \sigma_O + N_H(x, y) \sigma_H \quad (4)$$

In the case of steam oxidation of cladding materials it can be assumed that only the amount of oxygen and hydrogen is changed whereas the amount of zirconium and the alloying elements is not influenced significantly.

In order to reconstruct the specimen three-dimensionally, radiography projections have to be taken from different orientations. According to the sampling theorem, the number  $n$  of projections is connected with the resolution  $d$  and the radius  $R$  of the object circle that fully encompasses the object formed by the rotating of the sample:

$$n = \sqrt{2\pi} \frac{R}{d} \quad (5)$$

### 5.6.2 Technique

The neutron radiography measurements were performed in two beam times at the ICON facility at the Swiss neutron source SINQ at Paul Scherrer Institute Villigen. The investigations were performed applying the so called micro-tomography setup providing the highest resolution (pixel distance 13  $\mu\text{m}$ ). The field of view is 28 mm x 28 mm. The samples were scanned through the field of view with a step width of 20 mm. Exposure times of 300 s were applied. The specimens were measured horizontally.

The neutron tomography experiments were performed at the ConRad facility at the Berlin Neutron Scattering Centre (BENSC) of the Helmholtz Zentrum Berlin. 601 projections were measured with a pixel size of 44  $\mu\text{m}$  and an illumination time of 60 s. In order to fit the detector resolution to the sampling theorem and save measurement time, the number of image pixels was reduced. 2 x 2 pixels were transformed into one. The specimens were investigated vertical oriented.

### 5.6.3 Results of Radiography

The radiography measurements were performed from September 16 – 21, 2012. The investigations comprise measurements of all rods of the QUENCH-L1 test. Firstly, the calibration of the correlation between hydrogen concentration and total macroscopic neutron cross section was performed for the experimental setup applied. Calibration specimens were produced by annealing of Zry-4 cladding tube segments in argon/hydrogen atmosphere with different hydrogen partial pressures at various temperatures. The hydrogen uptake of calibration samples was determined by measurement of the weight gain. From the slope of the curve the calibration was determined:

$$\frac{H}{Zr} = \frac{\Sigma_{total} - 0.21 \text{ cm}^{-1}}{1.9541 \text{ cm}^{-1}} \quad (6)$$

Fig. 91 shows the radiographs taken from internal rods, whereas Fig. 92 depicted results for outer rods. For the inner rods, not only the bended hydrogen enriched bands known from the QUENCH-L0 test were found but

also hydrogen enrichments directly at the burst opening. The hydrogen enrichments are more blurred and show less contrast to the neighboring regions, compared to the bands found in rods of the QUENCH-L0 test. [Table 11](#) gives the local (spot of several voxels) maximal hydrogen concentrations estimated for each cladding on the basis of radiography data.

#### 5.6.4 Results of Tomography

The tomography measurements were performed from June 18 – 22, 2013. For the experimental setup applied the following correlation was determined:

$$\frac{H}{Zr} = \frac{\Sigma_{total} - 0.2375 \text{ cm}^{-1}}{2.4914 \text{ cm}^{-1}} \quad (7)$$

The reasons for the difference between equations (6) and (7) are different neutron spectra of the SINQ and the Berlin research reactor and different wavelength efficiencies of the two detector systems applied at PSI and BENSC, respectively.

Due to different difficulties, only one rod was investigated by tomography: a projection of the 3D-reconstruction of the hydrogen enrichment of rod #2 is given in [Fig. 93](#). The plots of the axial distributions of maximal and average hydrogen concentrations determined for each cladding tomography slice with the width of one pixel are given in [Fig. 94](#). At such location the cracks can be induced under mechanical loading. For the comparison with frequently used hot extraction methodic, the average hydrogen concentration values, determined for axial zone, corresponding to hot extraction sample, should be used.

In contrast to the neutron imaging results obtained for the QUENCH-L0 test, no clear dependence of the hydrogen concentration and the burst time can be found. The reasons can be 1) the shorter time interval in which the burst of the inner rods of the QUENCH-L1 test occurred and 2) and different temperature histories during the cool-down phase. However, a comparison between inner and peripheral rods of both tests gives a hint that hydrogen enrichments are formed if the temperature exceeds 1273 K.

#### 5.6.5 Conclusions of the Neutron Radiography and Tomography

Neutron radiography and tomography give new information about the secondary hydrogen uptake during LOCA scenarios, not yet obtained by other methods. Spatial resolutions of about 25 and about 50  $\mu\text{m}$  were achieved in the radiography and the tomography investigations, respectively.

Hydrogen is distributed in sloped and bended bands in regions close to the burst position and directly at the burst opening. According to metallographic investigations, positions of hydrogen containing bands correspond to boundaries of inner oxide regions observed by the metallographic investigations. For the formation of significant hydrogen enrichments temperatures above 1273 K seem to be needed. This means that the enrichments are only formed if the tetragonal phase of the zirconium oxide is stable. According to the neutron tomography results, the maximum hydrogen concentration of about 1690 wppm was reached.

### 5.7 X-Ray Diffractometry

X-ray diffractometry (XRD) analysis was applied to investigate the phases existing in the tested rods including possibly precipitated hydrides. A Seifert C3000 equipped with a Meteor 1D linear detector and a MZ4

goniometer was used. As commonly applied in this technique, a monochromatic radiation corresponding to the copper  $\text{CuK}\alpha$  emission line was used ( $E = 8047 \text{ eV}$ ,  $\lambda = 0.154 \text{ nm}$ ). The objective of crystallographic diffraction was to identify crystalline components in a sample by a search/match method [25]. Since the X-ray diffraction pattern of a pure substance is very characteristic, the powder diffraction method can be used for identification and quantification of polycrystalline phases. Additionally, the areas under the peak are related to the amount of each phase present in the sample. However, the method can fail if, for instance, one of the crystalline phases is strongly texturized, the grain size of a phase is less than a few microns or if the lattice is strongly disturbed. The CIF files (Crystallographic Information File) for inorganic compounds ("Inorganic Crystal Structure Database") can be consulted at the "Fachinformationszentrum Karlsruhe" (FIZ) and also at the JCPDS files.

Each of the four samples investigated were arranged as short longitudinal sections that were axially cut out from rods #3, #4, #5 and #9 (at the hydrogen enriched zones). The X-rays reach a maximum depth of about  $15 \mu\text{m}$ , so that the most important factor is a sufficient probe area which should also be flat [26].

In all of the obtained diffraction patterns solely metallic zirconium was detected (Figs. 95 - 98). The agreement with the JCPDS card 05-0665, corresponding to pure metallic zirconium, revealed to fit almost perfectly, despite the presence of 1.5 wt% tin and the intrinsic crystallographic texture of the samples extracted from the rods. Only small and wide peak at  $2\theta = 55.2^\circ$  could indicate small content of  $\epsilon$ -hydrides.

The following line shifts between the pattern obtained from the as-received specimen and the specimen from the hydrogen enriched zone were observed:  $0.08^\circ$  (rod #3 with 1115 wppm hydrogen),  $0^\circ$  (rod #4 with 730 wppm),  $0.02^\circ$  (rod #5 with 755 wppm) and  $0.06^\circ$  (rod #9 with 1270 wppm hydrogen). This indicates that hydrogen is at least partially dissolved in the  $\alpha$ -Zr lattice. A raw estimation gives less of 300 wppm dissolved hydrogen for rod #3.

The turquoise and red bars shown in Figs. 95 - 98 represent the diffraction peaks of  $\gamma$ - and  $\delta$ -Zr hydrides, respectively, accordingly to JCPDS card numbers 5-665 and 36-1340. The detection limit of the applied laboratory diffractometer is about 2 vol%. A raw estimation shows that this detection limit corresponds to a hydrogen concentration less than 370 wppm for hydrogen bonded in zirconium hydrides. This is a factor of about 4 lower than the results obtained by neutron radiography. The discrepancy can be explained by 1) partial solution of hydrogen in the lattice, and/or 2) a low grain size and/or a strong lattice distortion of the hydrides.

Whereas the integral intensity of Bragg lines depends on the chemical position, the crystalline structure, the volume fraction and the texture of the phase, the width of the reflection is determined by the crystallite size and lattice distortion. According to Scherrer's formula, the line broadening due to low grain size  $\Delta B \sim \lambda/L$  becomes noticeable for grain sizes less than  $L \sim 100 \text{ nm}$ . From the metallography investigations it is known that no hydrides are visible by optical microscope (visibility limit  $\sim 1 \mu\text{m}$ ). Therefore, the results of both methods, XRD and metallography are consistent and give hints that the size of the hydrides - if existent - is very small. However, both methods are not appropriate in this case to deliver information on the existence, size and structure of zirconium hydrides. Therefore it is intended to apply other methods like neutron small-angle scattering of specimens loaded with deuterium and transmission electron microscopy (TEM) to get more information on the status of hydrogen in zirconium additionally to solid solution indicated with XRD.



## 5.8 Mechanical Tests

To determine the residual strength and ductility of QUENCH-LOCA tested claddings, particularly to identify the embrittlement in dependence of the different quench test conditions, tensile tests on relevant cladding sections were performed at room temperature. Previously, the mechanical properties of the axially homogeneous hydrogenated Zircaloy-4 claddings were investigated in 2010 during the single rod test series [27].

### 5.8.1 Tensile Test set-up

The tensile tests were carried out using an universal testing machine from INSTRON (type 4505, 50 kN load cell), equipped with specially developed grip holders. The experiments were performed displacement-controlled with a displacement rate of 4 mm/min at room temperature (RT). To clamp the tubes without deforming their end sections, exact fitting end plugs were mounted. Since a quench tested cladding usually shows an inhomogeneous  $ZrO_2/\alpha-Zr(O)$  layer thickness along the main tube axis, the specimens were optically subdivided with paint markers to determine both the global and the local axial elongation during a test by using a CCD-camera measurement system. The initial gauge length  $l_0$  of a specimen in general was 1000 mm and a sample was prepared in that way, that the ballooning section was positioned in the axial center. To increase the resolution of the optical measurement device, two cameras were used for the tests. However, with respect to a central position of the ballooning section, particularly the specimens which revealed a strongly warped shape after the QUENCH test, had to be cut to a measuring length of 250 mm (# 4, #6, #7, #17, #18, #20) in order to replace the heating rod as well as all ceramic pellets. For these samples, only one camera was used during an experiment. The strain was calculated from the captured pictures by using the Digital Image Correlation and Tracing program provided by MATLAB [28, 29] and the stress was calculated by using average values of the measured initial inner and outer diameters from the ends of a tube.

### 5.8.2 Results of the tensile tests

The experiments showed that in contrast to QUENCH-L0 all tensile tested claddings failed in the centre of the burst opening by brittle fracture (compare [Fig. 99](#)). This failure behavior is caused by stress concentrations, based on discontinuities like buckles or small cross cracks at the crack edges of the burst openings. The failure due to hydrogen embrittlement was observed only for the rod #1, which was ruptured along two hydrogen bands during handling ([Fig. 100](#)).

Compared to the QUENCH-LOCA-0 test it is as well remarkable, that almost every cladding had to be straightened at the beginning of the tensile test, since nearly all samples revealed a more or less pronounced warped initial shape. One can observe that the most warped samples exhibit both lower strength and lower ductility at fracture (see [Fig. 101](#) and [Fig. 102](#)). This behavior might be explained by higher superimposed tensile stresses in the region of the burst opening, resulting from the bending moment, necessary to straighten the samples (compare [Fig. 91](#) and [Fig. 92](#) – to straighten a sample, the bending moment leads to both superimposed tension on the side of the burst opening and compression on the opposite side). In general, the strength at fracture of the QUENCH tested cladding varies between ca 310 – ca 530 MPa, and the elongation at fracture varies between ca 0.3 – 8.3% ([Table 14](#)). The annealing influence on decrease of the yield and ultimate strengths is illustrated in [Fig. 103](#). [Fig. 104](#) shows comparison of local mechanical properties obtained with cameras for rod #16.

## 6 Summary and Conclusions

Test QUENCH-LOCA-1 (QUENCH-L1) with electrically heated bundle (center Ta heaters inside each of 21 rods) was performed according to a temperature/time-scenario typical for a LBLOCA in a German PWR with maximal heat-up rate of 7 K/s, the cooling phase lasted 120 s and terminated with 3.3 g/s/(effective rod) water flooding. The maximal temperature of 1373 K was reached at the end of the heat-up phase at elevation 850 mm (for reference test QUENCH-L0 with lower heat up rate - at 950 mm).

The cladding burst occurred at temperatures between 1074 and 1169 K with average value of  $1130 \pm 30$  K (for QUENCH L0 - between 1123 K and 1223 K). The inner rod pressures relief to the system pressure during less of 40 s (similar to QUENCH-L0). The average linear burst opening parameters are: width  $4.2 \pm 2.6$  mm, length:  $15 \pm 6$  mm. The opening sizes are quite small for release of usual pellet fragments.

Strong rod bending up to 23 mm was observed for several rods (the reason was the limited axial expansion of heaters). Without take into account strong bended rods, the average cladding strain at the burst opening was about  $30 \pm 6\%$  including burst opening width.

The maximum blockage ratio of cooling channel (24%) was observed at elevation 950 mm (similar blockage of QUENCH-L0 was observed at 990 mm). If, hypothetically, all burst would located at the same level, the blockage would be 46% - still enough for bundle coolability (which should be up to 90% blockage achievable according to the REBEKA tests).

Similar to QUENCH-L0, the oxide layer thickness on the inner cladding surface was measured up to 25  $\mu\text{m}$  at burst elevations and less 2  $\mu\text{m}$  at hydrogenated bands.

No hydrogen bands around the burst openings were observed by means of neutron radiography for outer rods. Maximum hydrogen content inside hydrogen bands of inner rods varied between 700 and 1800 wppm. No linear zirconium hydrides were detected, instead the hydride domains with sizes less of 30  $\mu\text{m}$  were observed. Concentration of hydrogen dissolved in matrix estimated as  $< 300$  wppm.

During quenching, following the high-temperature phase, no fragmentation of claddings was observed (residual strengths or ductility is sufficient).

During tensile tests at room temperature, all from thirteen tested claddings were fractured due to stress concentration at the burst position - similar to rods of the QUENCH-L0 bundle with hydrogen concentration  $< 1500$  wppm. The central rod (rod #1) was destroyed brittle at the hydrogen bands during pulling out of its heater with hand.

## 7 Acknowledgments

The QUENCH-LOCA experiments are supported and partly sponsored by the association of the German utilities (VGB).

The broad support needed for preparation, execution, and evaluation of the QUENCH-L1 experiment is gratefully acknowledged. In particular, the authors would like to thank Mr. J. Moch for the assembly including instrumentation as well as disassembly of the test bundle, Dr. H. Leiste for the X-ray diffractometry measurements, Mrs. U. Peters for the metallographic examinations and the photographic documentation, Mrs. J. Laier for data processing and editing of manuscript.

The determination of the test protocol was based on numerous calculations with SCDAP/RELAP5 and SCDAPSIM performed by Dr. J. Birchley and Dr. L. Fernandez-Moguel, Paul Scherrer Institute (PSI), Switzerland.

## 8 References

- [1] Atomic Energy Commission Rule-Making Hearing, Opinion of the Commission, Docket RM-50-1, 28 December, 1973.
- [2] G. Hache and H. M. Chung, "The History of LOCA Embrittlement Criteria," NUREG/CP-0172, May 2001, pp. 205-237, <https://www.nrc.gov/reading-rm/doc-collections/nuregs/conference/cp0172/>
- [3] RSK-Leitlinien für Druckwasserreaktoren. Ursprungsfassung (3. Ausgabe vom 14. Oktober 1981) mit Änderungen vom 15.11.1996. <http://www.rskonline.de/sites/default/files/reports/rsklldwr1996.pdf>
- [4] P. Hofmann, S. Raff. Verformungsverhalten von Zircaloy-4-Hüllrohren unter Schutzgas im Temperaturbereich zwischen 600 und 1200°C. Wissenschaftliche Berichte, KFK 3168, Karlsruhe, 1981. <https://publikationen.bibliothek.kit.edu/270016057/3812276>
- [5] L. Schmidt, H. Lehning, D. Piel. Berstversuche an Zircaloy-Huellrohren unter kombinierter mechanisch-chemischer Beanspruchung (FABIOLA). In: Projekt Nukleare Sicherheit. Jahresbericht 1982. KfK-3350 (Juli 1983), S. 4200/69-4200/70. <https://publikationen.bibliothek.kit.edu/270019106/3812628>
- [6] M. E. Markiewicz, F. J. Erbacher. Experiments on Ballooning in Pressurized and Transiently Heated Zircaloy-4 Tubes. Wissenschaftliche Berichte, KFK-4343, Karlsruhe, 1988. <https://publikationen.bibliothek.kit.edu/270025905/3813281>
- [7] E. H. Karb, M. Prüßmann, L. Sepold, P. Hofmann, G. Schanz. LWR Fuel Rod Behavior in the FR2 In-pile Tests Simulating the Heatup Phase of a LOCA. Final Report. Wissenschaftliche Berichte, KFK-3346, Karlsruhe, 1983. <https://publikationen.bibliothek.kit.edu/270018525/3812543>
- [8] K. Wiehr. REBEKA-Bündelversuche Untersuchungen zur Wechselwirkung zwischen aufblähenden Zircaloyhüllen und einsetzender Kernnotkühlung. Abschlußbericht. Wissenschaftliche Berichte, KFK-4407, Karlsruhe, 1988. <https://publikationen.bibliothek.kit.edu/270026029/3813291>
- [9] F. J. Erbacher, H. J. Neitzel, K. Wiehr. Cladding Deformation and Emergency Core Cooling of a Pressurized Water Reactor in a LOCA. Summary Description of the REBEKA Program. Wissenschaftliche Berichte, KFK-4781, Karlsruhe, 1990. <https://publikationen.bibliothek.kit.edu/270029557/3813416>
- [10] F. J. Erbacher, S. Leistikow. A Review of Zircaloy Fuel Cladding Behavior in a Loss-of-Coolant Accident. Wissenschaftliche Berichte, KFK-3973, Karlsruhe, 1985. <https://publikationen.bibliothek.kit.edu/270021792/3812948>
- [11] J.-C. Brachet, V. Vandenberghe-Maillot, L. Portier, D. Gilbon, A. Lesbros, N. Waeckel, and J.-P. Mardon, Hydrogen Content, Preoxidation, and Cooling Scenario Effects on Post-Quench Microstructure and Mechanical Properties of Zircaloy-4 and M5<sup>®</sup> Alloys in LOCA Conditions. J. ASTM Intl., Vol. 5, No. 5 (2008). Available online as JAI101116 at [www.astm.org](http://www.astm.org)
- [12] T. Chuto, F. Nagase and T. Fuketa. High Temperature Oxidation of Nb-containing Zr Alloy Cladding in LOCA Conditions. Nuclear Engineering and Technology, Vol.41, No.2, March 2009.
- [13] Hee M. Chung. Fuel Behavior under Loss-of-Coolant Accident Situations. Nuclear Engineering and Technology, Vol.37 No.4, August 2005.
- [14] H. Uetsuka, T. Furuta and S. Kawasaki. Zircaloy-4 Cladding Embrittlement due to Inner Surface Oxidation under Simulated Loss-of-Coolant Condition. Journal of Nuclear Science and Technology, 18[9], pp. 705-717 (September 1981).
- [15] M. Billone, Y. Yan, T. Burtseva, R. Daum, H. Scott. Cladding Embrittlement During Postulated Loss-of-Coolant Accidents, NUREG/CR-6967, July 2008. <https://www.nrc.gov/docs/ML0821/ML082130389.pdf>

- [16] J. Stuckert, M. Große, C. Rössger, M. Klimenkov, M. Steinbrück, M. Walter. QUENCH-LOCA program at KIT on secondary hydriding and results of the commissioning bundle test QUENCH-L0. *Nuclear Engineering and Design*, 255(2013), pp. 185-201. DOI:10.1016/j.nucengdes.2012.10.024.
- [17] OECD SCIP-2 Project: <http://www.oecd-nea.org/jointproj/scip-2.html>
- [18] J. Stuckert, M. Große, C. Rössger, M. Steinbrück, M. Walter. Results of the commissioning bundle test QUENCH-L0 performed under LOCA conditions. *KIT Scientific Reports*, KIT-SR 7571 (March 2013).
- [19] M. Grosse, J. Stuckert, M. Steinbrück, A. Kaestner. Secondary hydriding during LOCA – Results from the QUENCH-L0 test, *Journal of Nuclear Materials* 420 (2012) 575–582. doi:10.1016/j.jnucmat.2011.11.045.
- [20] J. Stuckert, M. Große, C. Rössger, M. Steinbrück, M. Walter. The QUENCH-LOCA Experimental Program. Final report. *KIT Scientific Reports*, KIT SR 7740 (2017).
- [21] M. Große, G. Kühne, M. Steinbrück, E. Lehmann, P. Vontobel, J. Stuckert. Determination of the hydrogen uptake of steam-oxidised zirconium alloys by means of quantitative analysis of neutron radiographs. *J. Phys.: Condens. Matter* 20 (2008), 104263.
- [22] M. Grosse, E. Lehmann, M. Steinbrueck, G. Kühne, J. Stuckert. Influence of oxide layer morphology on hydrogen concentration in tin and niobium containing zirconium alloys after high temperature steam oxidation. *J. Nucl. Mater.* 385 (2009), 339.
- [23] J. Stuckert, J. Birchley, M. Grosse, B. Jaeckel, M. Steinbrück. Experimental and calculation results of the integral reflood test QUENCH-14 with M5 cladding tubes. *Annals of Nuclear Energy*, 37(2010) S.1036-47, DOI:10.1016/j.anucene.2010.04.015.
- [24] M. Grosse, M. Van den Berg, C. Goulet E. Lehmann, B. Schillinger. In-situ neutron radiography investigations of hydrogen diffusion and absorption in zirconium alloys. *Nuclear Instruments and Methods in Physics Research Section A: Accelerators, Spectrometers, Detectors and Associated Equipment*, Volume 651, Issue 1, 21 September 2011, Pages 253–257.
- [25] M.R. Warren, D.K. Bhattacharya.  $\gamma$  Zr-Hydride precipitate in irradiated massive  $\delta$  Zr Hydride. *Journal of Nuclear Materials* 56 (1975), pp. 121-123.
- [26] Yang-Soon Park, Yeong-Keong Ha, Sun-Ho Han, Kwang-Yong Jee, Won-Ho Kim. Changes in chemical structure of oxidation reaction layers of Zircaloy-4 and Ti by micro X-ray diffractometry. *Journal of Nuclear Materials* 372 (2008) 59–65.
- [27] J. Stuckert, M. Große, M. Walter. Mechanical properties of pre-hydrogenated (600 – 5000 wppm) cladding segments. 16th International QUENCH-Workshop, Karlsruhe, November 2010, ISBN 978-3-923704-74-3.
- [28] C. Eberl, D.S. Gianola, K. J. Hemker. Mechanical Characterization of Coatings Using Microbeam Bending and Digital Image Correlation Techniques. *Experimental Mechanics*, January 2010, Volume 50, Issue 1, pp 85-97.
- [29] C. Eberl, D.S. Gianola, K.J. Hemker. Mechanical Characterization of Coatings Using Microbeam Bending and Digital Image Correlation Techniques. *Experimental Mechanics*, January 2010, Volume 50, Issue 1, pp 85-97.



## Tables and Figures

**Table 1** QUENCH Test Matrix 1997 – 2013

Test	Quench medium and injection rate	Temp. at onset of flooding <sup>1)</sup>	Max. ZrO <sub>2</sub> before transient <sup>2)</sup>	Max. ZrO <sub>2</sub> (X s) before flooding <sup>2)</sup>	Posttest average ZrO <sub>2</sub> thickness <sup>3)</sup>	H <sub>2</sub> production before / during cooldown, g	Remarks, objectives
<b>QUENCH-00</b> Oct. 9 - 16, 97	Water 80 g/s	≈ 1800 K			completely oxidized		Commissioning tests.
<b>QUENCH-01</b> Febr 26, 98	Water 52 g/s	≈ 1830 K	312 μm		500 μm at 913 mm	36 / 3	COBE Project; partial fragmentation of pre-oxidized cladding.
<b>QUENCH-02</b> July 7, 98	Water 47 g/s	≈ 2400 K			completely oxidized	20 / 140	COBE Project; no additional pre-oxidation; quenching from high temperatures.
<b>QUENCH-03</b> January 20, 99	Water 40 g/s	≈ 2350 K			completely oxidized	18 / 120	No additional pre-oxidation, quenching from high temperatures.
<b>QUENCH-04</b> June 30, 99	Steam 50 g/s	≈ 2160 K	82 μm		280 μm	10 / 2	Cool-down behavior of slightly pre-oxidized cladding by cold steam injection.
<b>QUENCH-05</b> March 29, 2000	Steam 48 g/s	≈ 2020 K	160 μm		420 μm	25 / 2	Cool-down behavior of pre-oxidized cladding by cold steam injection.
<b>QUENCH-06</b> Dec 13 2000	Water 42 g/s	≈ 2060 K	207 μm <sup>5)</sup>	300 μm, (60 s), SVECHA modeling	670 μm <sup>4)</sup> (60% metal converted to outer ZrO <sub>2</sub> )	32 / 4	OECD-ISP 45; prediction of H <sub>2</sub> source term by different code systems.
<b>QUENCH-07</b> July 25, 2001	Steam 15 g/s	≈ 2100 K	230 μm		completely oxidized	66 / 120	COLOSS Project; impact of B <sub>4</sub> C absorber rod failure on H <sub>2</sub> , CO, CO <sub>2</sub> , and CH <sub>4</sub> generation.
<b>QUENCH-09</b> July 3, 2002	Steam 49 g/s	≈ 2100 K			completely oxidized	60 / 400	As QUENCH-07, steam-starved conditions prior to cooldown.
<b>QUENCH-08</b> July 24, 2003	Steam 15 g/s	≈ 2090 K	274 μm		completely oxidized	46 / 38	As QUENCH-07, no absorber rod



Test	Quench medium and injection rate	Temp. at onset of flooding <sup>1)</sup>	Max. ZrO <sub>2</sub> before transient <sup>2)</sup>	Max. ZrO <sub>2</sub> (X s) before flooding <sup>2)</sup>	Posttest average ZrO <sub>2</sub> thickness <sup>3)</sup>	H <sub>2</sub> production before / during cooldown, g	Remarks, objectives
<b>QUENCH-10</b> July 21, 2004	Water 50 g/s	≈ 2200 K	514 μm	613 μm (at 850 mm)	completely oxidized	48 / 5	LACOMERA Project; Air ingress.
<b>QUENCH-11</b> Dec 08, 2005	Water 18 g/s	≈ 2040 K		170 μm	completely oxidized	9 / 132	LACOMERA Project; Boil-off.
<b>QUENCH-12</b> Sept 27, 2006	Water 48 g/s	≈ 2100 K	160 μm, breakaway	300 μm, (110 s), breakaway	completely oxidized	34 / 24	ISTC Project No. 1648.2; VVER bundle with E110 claddings
<b>QUENCH-13</b> Nov 7, 2007	Water 52 g/s	≈ 1820 K		400 μm, after AgInCd rod failure	750 μm	42 / 1	SARNET; impact of AgInCd absorber rod failure on aerosol generation.
<b>QUENCH-14</b> July 2, 2008	Water 41 g/s	≈ 2100 K	170 μm <sup>6)</sup>	470 μm <sup>6)</sup> , (30 s)	840 μm <sup>4)</sup> (74% metal converted to outer ZrO <sub>2</sub> )	34 / 6	ACM series: M5 <sup>®</sup> cladding
<b>QUENCH-15</b> May 27, 2009	Water 48 g/s	≈ 2100 K	145 μm <sup>6)</sup>	380 μm <sup>6)</sup> , (30 s)	630 μm <sup>4)</sup> (70% metal converted to outer ZrO <sub>2</sub> )	41 / 7	ACM series: ZIRLO <sup>™</sup> cladding
<b>QUENCH-L0</b> July 22, 2010	Water, 100 g/s	1330 K	1 μm	≈ 18 μm	≈ 20 μm (central rod)	0.748/0.3	VGB Project; Commissioning test
<b>QUENCH-16</b> July 27, 2011	Water 53 g/s	≈ 1870 K	135 μm	130 μm at 450-950 mm, breakaway	1075 μm at 550-650 mm	16 / 128	LACOMEKO Project; Air ingress.
<b>QUENCH-L1</b> Feb. 02, 2012	Water, 100 g/s	1373 K	1 μm	≈ 19 μm	≈ 22 μm (central rod)	0.718/0.01	VGB Project; Reference test
<b>QUENCH-17</b> Jan 31, 2013	Water 10 g/s	≈ 1800 K		completely oxidized	completely oxidized	110 / 1	SARNET-2; Debris formation and coolability.

<sup>1)</sup> Maximum measured bundle temperature at 950 mm elevation. <sup>2)</sup> Measured at the withdrawn corner rod at 950 mm elevation.

<sup>3)</sup> Measured posttest at the bundle elevation of maximum temperature, i.e. 950 mm

<sup>4)</sup> Some claddings were completely oxidized at 950 mm elevation. <sup>5)</sup> Oxide thickness during transient phase. <sup>6)</sup> Zircaloy-4 corner rods.

**Table 2** Design characteristics of the QUENCH-L1 test bundle

Bundle type		PWR
Bundle size		21 heated rods
Effective number of rods	(considering surface of heated rods, shroud and corner rods)	30.6 rods (21 + 7.4 from shroud + 2.2 from corner rods)
Pitch		14.3 mm
Coolant channel area		29.65 cm <sup>2</sup>
Hydraulic diameter		11.5 mm
Rod outside diameter		10.75 mm
Cladding material		Zircaloy-4
Cladding thickness		0.725 mm
Rod length	(elevations)	2480 mm (-690 to 1790 mm)
Internal rod pressure	(gas)	5.5 MPa abs.; rod#10: 4.6 MPa due to leakage before heating; (Kr)
Material of middle heater	surface roughness	Tantalum (Ta) Ra=1.6 μm
Ta heater length		1024 mm
Ta heater diameter		6 mm
Annular pellet	material dimensions surface roughness	ZrO <sub>2</sub> ;Y <sub>2</sub> O <sub>3</sub> -stabilized Ø 9.15/6.15 mm; L=11 mm Ra=0.3 μm
Pellet stack		0 mm to ~1020 mm
Corner rod (4)	material instrumented (A, C, D)  not instrumented (B)	Zircaloy-4 tube Ø 6x0.9 (bottom: -1140 mm) rod Ø 6 mm (top: +1300 mm) rod Ø 6 mm (-1350 to +1155 mm)
Grid spacer	material length sheet thickness elevation of lower edge	Zircaloy-4, Inconel 718 Zircaloy: 42 mm, Inconel: 38 mm 0.5 mm Inc: -100 mm; Zry: 150, 550, 1050, 1410 mm
Shroud	material wall thickness outside diameter length (extension)	Zirconium 702 (flange: Zry-4) 3.17 mm 86.0 mm 1600 mm (-300 mm to 1300 mm)
Shroud insulation	material insulation thickness elevation	ZrO <sub>2</sub> fiber ~ 36 mm -300 to ~1000 mm
Molybdenum heaters and copper electrodes	length of upper part length of lower part outer diameter: prior to coating after coating with ZrO <sub>2</sub> coat. surface roughness borehole of Cu-electrodes	766 mm (576 Mo, 190 mm Cu) 690 mm (300 Mo, 390 mm Cu)  8.6 mm 9.0 mm Ra=6-12 μm diameter 2 mm, length 96 mm
Cooling jacket	Material: inner/outer tube inner tube outer tube	Inconel 600 (2.4816) / SS (1.4571) Ø 158.3 / 168.3 mm Ø 181.7 / 193.7 mm

**Table 3** Properties of Zircaloy-4 cladding tubes

Table 3.1. Chemical composition of Zircaloy-4 in Weight-%

Element	Symbol	Specified Value
Tin	Sn	1.20-1.40
Iron	Fe	0.21-0.24
Chromium	Cr	0.07-0.13
Oxygen	O	0.10-0.15
Silicon	Si	0.005-0.012

Table 3.2. Mechanical properties at 400 C ± 3 C in tension

Element	Specified Value
0.2 Yield strength Rp 0.2	200-300 N/mm <sup>2</sup>
Tensile strength Rm	≥ 270 N/mm <sup>2</sup>
Breaking elongation A <sub>50</sub> mm	≥ 10 %

Table 3.3. Microstructure

<b>Grain size: 6.7 μm</b>	according to ASTM-E 112-96: <b>Nr. 11.5</b> (for final size tubing; samples are recrystallized; magnification x500)
<b>Surface Conditions:</b> Roughness (inside): <b>Ra ≤ 1.0 μm</b> Roughness (outside): <b>Ra ≤ 0.7 μm</b>	

**Table 4** Main characteristics of the ZrO<sub>2</sub> pellet material, yttria-stabilized (type FZY) \*

Property		Data
Density		5.5-5.8 g/cm <sup>3</sup>
Open porosity		0
Mean grain size		50 μm
Hardness (Knoop, 100 g)		17000 N/mm <sup>2</sup>
Yield strength under compression		2000 N/mm <sup>2</sup>
Bending strength		350 N/mm <sup>2</sup>
Elastic modulus		165 GPa
Specific heat at 20 °C		400 J/kg K
Thermal conductivity at 100 °C		2.5 W/m K
Linear expansion, 20-1000 °C		10.5 x 10 <sup>-6</sup> /K
Specific electric resistance	at 20 °C	10 <sup>10</sup> Ω cm
	at 500 °C	5000 Ω cm
	at 1000 °C	50 Ω cm

\*According to FRIATEC, Mannheim

**Table 5** QUENCH-L1; Electrical resistances of rods [mΩ] at 20°C

Table 5.1. Internal circuit with 9+1 rods

rod	1	2	3	4	5	6	7	8	9	16	Ave- rage	10 rods parallel
pre- test	6.5	6.5	6.4	6.4	6.5	6.6	6.4	6.4	6.4	6.2	6.4	0.64
post- test	6.4	6.9	6.8	6.7	5.7	6.4	6.7	6.5	6.7	7.7	6.7	0.66

Note: Measured values include the resistance of slide contacts  $R_s=0.75$  mΩ

Table 5.2. External circuit with 11 rods

rod	10	11	12	13	14	15	17	18	19	20	21	Ave- rage	11 rods parallel
pre- test	6.3	6.4	6.2	6.2	6.2	6.3	6.2	6.2	6.5	6.2	6.3	6.3	0.57
post- test	7.8	6.8	7.1	6.5	6.8	7.7	6.7	7.4	6.8	6.5	6.7	7.0	0.63

Note: Measured values include the resistance of slide contacts  $R_s=0.75$  mΩ

Each circuit connected to the DC generator with 4 parallel bonded cables. The resistance of each cable is  $R_c=1.2$  mΩ. Therefore, the external (outside) resistance corresponding to each heated rod (indicated by SCDAP/RELAP as **fxwid**) is  $R_{ie}=R_s+10*R_c/4=3.75$  mΩ for the inner rod group and  $R_{oe}=R_s+11*R_c/4=4.05$  mΩ for the outer rod group.

**Table 6** Properties of zirconia fiber insulating boards\*

Table 6.1. Chemical composition

Oxide	ZrO <sub>2</sub>	Y <sub>2</sub> O <sub>3</sub>	HfO <sub>2</sub>	TiO <sub>2</sub>	SiO <sub>2</sub>	CaO	MgO	Fe <sub>2</sub> O <sub>3</sub>	Al <sub>2</sub> O <sub>3</sub>	Na <sub>2</sub> O
typical wt%	88	10	2	0.14	0.12	0.09	0.03	0.04	0.01	0.01

Table 6.2. Physical properties

bulk density	porosity	shrinkage		thermal expansion coefficient @298-1453 K	melting point	max. service temperature	flexural strength	compressive strength @10% compression
		(1 hour @1925 K)	(24 hours @1925 K)					
g/cm <sup>3</sup>	%	%		1/K	K	K	MPa	MPa
0.48	92	1.2	2.8	10.7*10 <sup>-6</sup>	2866	2500	0.59	0.29

Table 6.3. Thermal conductivity

temperature, K	673	1073	1373	1673	1923
conductivity, W/(m*K)	0.08	0.11	0.14	0.19	0.24

Table 6.4. Specific heat capacity

temperature, K	366	2644
specific heat capacity, J/(kg*K)	544	754

\*According to specifications of manufacturer ZIRCAR PRODUCTS on the ZYFB3 material

**Table 7** List of instrumentation for the QUENCH-L1 test

Chan	Designation	Instrument, location	Unit
0	P rod 13	Internal pressure of rod #13	bar
1	P rod 14	Internal pressure of rod #14	bar
2	P rod 15	Internal pressure of rod #15	bar
3	P rod 12	Internal pressure of rod #12	bar
4	P rod 03	Internal pressure of rod #03	bar
5	P rod 04	Internal pressure of rod #04	bar
6	P rod 05	Internal pressure of rod #05	bar
7	P rod 16	Internal pressure of rod #16	bar
8	P rod 11	Internal pressure of rod #11	bar
9	P rod 02	Internal pressure of rod #02	bar
10	P rod 01	Internal pressure of rod #01	bar
11	P rod 06	Internal pressure of rod #06	bar
12	P rod 17	Internal pressure of rod #17	bar
13	P rod 10	Internal pressure of rod #10	bar
14	P rod 09	Internal pressure of rod #09	bar
15	P rod 08	Internal pressure of rod #08	bar
16	P rod 07	Internal pressure of rod #07	bar
17	P rod 18	Internal pressure of rod #18	bar
18	P rod 21	Internal pressure of rod #21	bar
19	P rod 19	Internal pressure of rod #19	bar
20	P rod 20	Internal pressure of rod #20	bar
21..23		20 mA, Reserve	
24	P 511 top	Absolute pressure at bottom of L 501 long leg	bar
25	Fm 401	Argon gas mass flow rate, (20 mA)	g/s
26..31		20 mA, Reserve	
<b>32..34</b>		TC (W/Re), Reserve	
35	TSH 15/0	TC (NiCr/Ni), shroud outer surface, 1150 mm, 21°	K

Chan	Designation	Instrument, location	Unit
36	TSH 14/270	TC (NiCr/Ni), shroud outer surface, 1050 mm, 289°, behind shroud isolation	K
<b>37</b>		TC (W/Re)	K
38	TFS 15/13	TC (NiCr/Ni), surface of fuel rod simulator 15, group 5, 950 mm	K
39	TFS 19/12	TC (NiCr/Ni), surface of fuel rod simulator 19, group 5, 850 mm	K
<b>40</b>		TC (W/Re)	
<b>41</b>		TC (W/Re)	K
42	TFS 7/12	TC (NiCr/Ni), surface of fuel rod simulator 7, group 3, 850 mm	K
43	TFS 15/12	TC (NiCr/Ni), surface of fuel rod simulator 15, group 5, 850 mm	K
44	TFS 2/12	TC (NiCr/Ni), surface of fuel rod simulator 2, group 2, 850 mm	K
45	TFS 4/12	TC (NiCr/Ni), surface of fuel rod simulator 4, group 2, 850 mm	K
46	TFS 19/13	TC (NiCr/Ni), surface of fuel rod simulator 19, group 5, 950 mm	K
<b>47..57</b>		TC (W/Re)	K
58	TFS 7/10	TC (NiCr/Ni), surface of fuel rod simulator 7, group 3, 650 mm	K
<b>59</b>		TC (W/Re)	K
<b>60</b>		TC (W/Re)	K
61	TFS 11/12	TC (NiCr/Ni), surface of fuel rod simulator 11, group 4, 850 mm	K
62		Reserve	
63		Reserve	
64	T 402 b	TC (NiCr/Ni), Ar super heater	K
<b>65..67</b>		TC (W/Re)	K
68	T 512	TC (NiCr/Ni), gas temperature bundle outlet	K
<b>69</b>		TC (W/Re)	K
<b>70</b>		TC (W/Re)	K
71	<i>Ref. T01</i>	<i>Temperature of measuring crate 1 (reference temperature)</i>	K
72	TFS 11/13	TC (NiCr/Ni) surface of fuel rod simulator 11, group 4, 950 mm	K
73	TFS 7/13	TC (NiCr/Ni), surface of fuel rod simulator 7, group 3, 950 mm	K
74	TFS 2/13	TC (NiCr/Ni), surface of fuel rod simulator 2, group 2, 950 mm	K
75	TFS 4/13	TC (NiCr/Ni), surface of fuel rod simulator 4, group 2, 950 mm	K



Chan	Designation	Instrument, location	Unit
76	TFS 15/11	TC (NiCr/Ni), surface of fuel rod simulator 15, group 5, 750 mm	K
77	TFS 19/11	TC (NiCr/Ni), surface of fuel rod simulator 19, group 5, 750 mm	K
78	TFS 11/11	TC (NiCr/Ni) surface of fuel rod simulator 11, group 4, 750 mm	K
79	TFS 7/11	TC (NiCr/Ni), surface of fuel rod simulator 7, group 3, 750 mm	K
80	TFS 2/11	TC (NiCr/Ni) surface of fuel rod simulator 2 group 2, 750 mm	K
81	TSH 12/90	TC (NiCr/Ni), shroud outer surface, 850 mm, 109°	K
82	TFS 2/10	TC (NiCr/Ni); surface of fuel rod simulator 2, group 2, 650 mm	K
83	TSH 10/270	TC (NiCr/Ni), shroud outer surface, 650 mm, 289°	K
84	TSH 9/180	TC (NiCr/Ni), shroud outer surface, 550 mm, 191°	K
85	TSH 8/90	TC (NiCr/Ni), shroud outer surface, 450 mm, 109°	K
86	TSH 7/0	TC (NiCr/Ni), shroud outer surface, 350 mm, 11°	K
87	TSH 6/270	TC (NiCr/Ni) shroud outer surface, 250 mm, 281°	K
88	TSH 5/180	TC (NiCr/Ni), shroud outer surface, 150 mm, 191°	K
89	TSH 4/90	TC (NiCr/Ni), shroud outer surface, 50 mm, 109°	K
90	TSH 11/0	TC (NiCr/Ni), shroud outer surface, 750 mm, 11°,	K
91	TCI 9/270	TC (NiCr/Ni), cooling jacket inner tube wall, 550 mm, 270°	K
92	TCI 10/270	TC (NiCr/Ni), cooling jacket inner tube wall, 650 mm, 270°	K
93	TCI 11/270	TC (NiCr/Ni), cooling jacket inner tube wall, 750 mm, 270°	K
94	TCI 13/270	TC (NiCr/Ni), cooling jacket inner tube wall, 950 mm, 270°	K
95	TFS 4/11	TC (NiCr/Ni), surface of fuel rod simulator 4, group 2, 750 mm	K
96	TFS 15/10	TC (NiCr/Ni), surface of fuel rod simulator 15, group 5, 650 mm	K
97	TFS 19/10	TC (NiCr/Ni), surface of fuel rod simulator 19, group 5, 650 mm	K
98	TFS 11/10	TC (NiCr/Ni), surface of fuel rod simulator 11, group 4, 650 mm	K
99	TSH 13/180	TC (NiCr/Ni), shroud outer surface, 950 mm, 191°	K
100	TSH 3/0	TC (NiCr/Ni), shroud outer surface, -50 mm, 11°	K
101	TFS 4/10	TC (NiCr/Ni), surface of fuel rod simulator 4, group 2, 650 mm	K
102	TFS 15/14	TC (NiCr/Ni), surface of fuel rod simulator 15, group 5, 1050 mm	K

Chan	Designation	Instrument, location	Unit
103	TFS 19/14	TC (NiCr/Ni), surface of fuel rod simulator 19, group 5, 1050 mm	K
104	TFS 11/14	TC (NiCr/Ni), surface of fuel rod simulator 11, group 4, 1050 mm	K
105	TFS 7/14	TC (NiCr/Ni), surface of fuel rod simulator 7, group 3, 1050 mm	K
106	TFS 2/14	TC (NiCr/Ni), surface of fuel rod simulator 2, group 2, 1050 mm	K
107	TFS 4/14	TC (NiCr/Ni), surface of fuel rod simulator 4, group 2, 1050 mm	K
108	TFS 15/9	TC (NiCr/Ni), surface of fuel rod simulator 15, group 5, 550 mm	K
109	TFS 11/9	TC (NiCr/Ni), surface of fuel rod simulator 11, group 4, 550 mm	K
110	TFS 7/9	TC (NiCr/Ni), surface of fuel rod simulator 7, group 3, 550 mm	K
111	TFS 4/9	TC (NiCr/Ni), surface of fuel rod simulator 4, group 2, 550 mm	K
112	TFS 15/15	TC (NiCr/Ni), surface of fuel rod simulator 15, group 5, 1150 mm	K
113	TFS 19/15	TC (NiCr/Ni), surface of fuel rod simulator 19, group 5, 1150 mm	K
114	TFS 11/15	TC (NiCr/Ni), surface of fuel rod simulator 11, group 4, 1150 mm	K
115	TFS 7/15	TC (NiCr/Ni), surface of fuel rod simulator 7, group 3, 1150 mm	K
116	TFS 2/15	TC (NiCr/Ni), surface of fuel rod simulator 2, group 2, 1150 mm	K
117	TFS 4/15	TC (NiCr/Ni), surface of fuel rod simulator 4, group 2, 1150 mm	K
118	TFS 11/8	TC (NiCr/Ni), surface of fuel rod simulator 11, group 4, 450 mm	K
119	TFS 7/8	TC (NiCr/Ni), surface of fuel rod simulator 7, group 3, 450 mm	K
120	TFS 4/8	TC (NiCr/Ni), surface of fuel rod simulator 4 group 2, 450 mm	K
121	TFS 11/16	TC (NiCr/Ni), surface of fuel rod simulator 11, group 4, 1250 mm	K
122	TFS 7/16	TC (NiCr/Ni), surface of fuel rod simulator 7, group 3, 1250 mm	K
123	T 601	Temperature off-gas, 2660 mm from test section outlet (flange)	K
124	TFS 11/7	TC (NiCr/Ni), surface of fuel rod simulator 11, group 4, 350 mm	K
125	T 514	Temperature bundle head, cooling water inlet	K
126	TFS 7/7	TC (NiCr/Ni), surface of fuel rod simulator 7, group 3, 350 mm	K
127	TFS 4/7	TC (NiCr/Ni), surface of fuel rod simulator 4, group 2, 350 mm	K
128	T 104	Temperature quench water	K
129	T 201	Temperature steam generator heating pipe	K
130	TIT C/12	TC (NiCr/Ni), center line of corner rod C, 850 mm	K

Chan	Designation	Instrument, location	Unit
131	T 205	Temperature upstream steam flow instrument location 10 g/s	K
132	T 301A	Temperature downstream superheater	K
133	T 302	Temperature superheater heating pipe	K
134	T 303	Temperature upstream total flow instrument location	K
135	T 401	Temperature upstream Ar flow instrument (orifice) location	K
136	T 403	Temperature of Ar at inlet cooling jacket	K
137	T 404	Temperature of Ar at outlet cooling jacket	K
138	T 501	Temperature in containment (near from bundle head)	K
139	TFS 7/6	TC (NiCr/Ni), surface of fuel rod simulator 7, group 3, 250 mm	K
140	TFS 4/6	TC (NiCr/Ni), surface of fuel rod simulator 4, group 2, 250 mm	K
141	TFS 7/17	TC (NiCr/Ni), surface of fuel rod simulator 7, group 3, 1350 mm	K
142	TFS 7/5	TC (NiCr/Ni), surface of fuel rod simulator 7, group 3, 150 mm	K
143	TFS 7/4	TC (NiCr/Ni), surface of fuel rod simulator 7, group 3, 50 mm	K
144	TFS 7/3	TC (NiCr/Ni), surface of fuel rod simulator 7, group 3, -50 mm	K
145	TFS 7/2	TC (NiCr/Ni), surface of fuel rod simulator 7, group 3, -150 mm	K
146	TFS 7/1	TC (NiCr/Ni), surface of fuel rod simulator 7, group 3, -250 mm	K
147	T 510	Temperature at outer surface of containment, 270°, 4.4 m	K
148	T 511	Gas temperature at bundle inlet	K
149	TIT D/11	TC (NiCr/Ni), center line of corner rod D, 750 mm	K
150	TIT A/13	TC (NiCr/Ni), center line of corner rod A, 950 mm	K
151	<i>Ref. T02</i>	<i>Temperature of measuring crate 2 (reference temperature)</i>	K
152	P 201	Pressure steam generator	bar
153	P 204	Pressure at steam flow instrument location 50 g/s	bar
154	P 205	Pressure at steam flow instrument location 10 g/s	bar
155	P 303	Pressure upstream total flow instrument (orifice) location	bar
156	P 401	Pressure upstream gas flow instrument location	bar
157	P 511	Pressure at bundle inlet	bar
158	P 512	Pressure at bundle outlet	bar

Chan	Designation	Instrument, location	Unit
159	P 601	Pressure upstream off-gas flow instrument (orifice) F 601	bar
160	P 901	Pressure He supply for unheated rods	bar
161	L 201	Liquid level steam generator	mm
162	L 501	Liquid level quench water	mm
163	L 701	Liquid level condensation vessel	mm
164	<b>Fm 401B</b>	Argon flow rate (Bronkhorst device)	g/s
165	P 411	Pressure Kr supply for heated rods, Reserve	bar
166	P 403	Pressure Ar cooling of cooling jacket	bar
167	P 406	Pressure insulation shroud/cooling jacket	bar
168	Fm 104	Flow rate quench water	g/s
169	Fm 204	Flow rate steam 50 g/s	g/s
170	Fm 205	Flow rate steam 10 g/s	g/s
171	F 303	Flow rate at bundle inlet (steam + argon), orifice	mbar
172	F 401	Reserve	
173	Fm403	Flow rate cooling gas (Ar)	g/s
174	F 601	Flow rate off-gas (orifice), 2000 mm from test section outlet (flange)	mbar
175	Fm 406	Flow rate argon into room between shroud and cooling jacket	g/s
176	E 201	Electric current steam generator	A
177	E 301	Electric current superheater	A
178	E 501	Electric current of left group of fuel rod simulators	A
179	E 502	Electric current of right group of fuel rod simulators	A
180	E 503	Electric voltage of left group of fuel rod simulators	V
181	E 504	Electric voltage of right group of fuel rod simulators	V
182	Hub_V302	Gas supply valve lift	%
183	<i>Ref. T03</i>	<i>Temperature of buffer amplifier (reference temperature)</i>	K
184.....1 99		Binary inputs	
200.....2 15		Analog outputs	

Chan	Designation	Instrument, location	Unit
250	E 505	Electric power inner ring of fuel rod simulators	W
251	E 506	Electric power outer ring of fuel rod simulators	W
252	EP	Gross electrical power	kW

**Indications:**

TFS - TC at the rod surface;

TIT - TC inside corner rods;

TSH - TC at outer surface of shroud;

- gauge outside of containment.

**Groups of the rods for modeling:**

*central groups*

group 1: rod 1;

group 2: rods 2, 4, 6, 8;

group 3: rods 3, 5, 7, 9;

*peripheral groups*

group 4: rods 11, 14, 17, 20;

group 5: rods 10, 12, 13, 15, 16, 18, 19, 21.

**Table 8** QUENCH-L1; Rod thermocouple positions

Elevation, mm	-250	-150	-50	50	150	250	350	450	550	650	750	850	950	1050	1150	1250	1350
Rod/Elevation	1	2	3	4	5	6	7	8	9	10	11	12	13	14	15	16	17
1																	
2										X	X	X	X	X	X		
3																	
4						X	X	X	X	X	X	X	X	X	X		
5																	
6																	
7	X	X	X	X	X	X	X	X	X	X	X	X	X	X	X	X	X
8																	
9																	
10																	
11							X	X	X	X	X	X	X	X	X	X	
12																	
13																	
14																	
15									X	X	X	X	X	X	X		
16																	
17																	
18																	
19										X	X	X	X	X	X		
20																	
21																	

Number per elevation      1      1      1      1      1      2      3      3      4      6      6      6      6      6      6      6      2      1

<b>TFS (rod surface), indicated in table above</b>	<b>56</b>
<b>TIT (inside corner rods)</b>	<b>3</b>
<b>TSH (outer shroud surface)</b>	<b>13</b>
<b>Total quantity of bundle and shroud NiCr/Ni thermocouples</b>	<b>72</b>

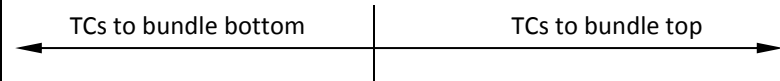


**Table 9** QUENCH-L1; Sequence of events

Time [s]	Event
-3248 (11:00:00; 02.02.2012)	Start data recording, $T_{max} = TFS\ 4/13 = 839\ K$ , el. power at 3.49 kW. L701 = 1438 mm. L 501 = -405 mm. System pressure 3 bar. Ar 6 g/s, superheated steam 2 g/s.
-2260... -2170	Pressurization of rods from 15 to 55 bar.
0	Start of transient with max electrical power increase rate.
2; 4	Electrical power 32; 43 kW.
<b>36...58</b>	<b>Sequential onset of ballooning for rods pressurized to 55 bar.</b>
<b>55...87</b>	<b>Sequential onset of burst for rods from inner rod #4 to peripheral rod #10.</b> See burst table (Table 10).
87	Switch of the electrical power from max 58.65 kW to decay heat of 3.5 kW. Initiation of rapid steam supply line (20 g/s) additionally to carrier argon (6 g/s). Switch-off of slow steam supply (2 g/s). $T_{max} = TFS\ 4/12 = 1345\ K$ .
91	Cladding surface temperature maximum reached. Maximal hydrogen production rate. <b><math>T_{max} = TFS\ 4/12 = 1373\ K</math>.</b>
91...209	Cool-down of bundle in steam. Decrease of TFS 4/12 reading from 1373 K to 1023 K.
212	Initiation of quench water supply. Switch-off of steam supply. Switch of argon to bundle top supply.
212...221	Increase of bundle temperatures to $\sim 1073\ K$ due to switch-off of the steam cooling.
237	Maximal quench rate (about 100 g/s) reached.
247...293	Wetting of cladding surface thermocouples (TFS) at elevations between -250 and 1350 mm at temperatures between 484 (TFS 7/1) and 858 K (TFS 7/12) (Table 12).
270...305	Maximal water evaporation rate (about 25 g/s).
351	Bundle completely filled with water (L 501 = 1307 mm)
417	Electrical power switched off. $T_{max} = TFS\ 15/15 = 333\ K$
1688 (12:22:20)	End of data recording. L 501 = 1289 mm

**Table 10** QUENCH-L1; Burst parameters

rod	burst time, s	interpolated burst T, K	burst azimuthal position, °	burst middle elevation, mm	burst width, mm	burst length, mm	burst area, mm <sup>2</sup>
1	55.6	1169	45	900		13	
2	57.2	1132	45	907	2.4	17	29.5
3	59	1118	190	968	3.0	13	25
4	55.2	1154	210	982	2.5	8	13.5
5	57.2	1104	270	966	12.8	24	198
6	55.2	1110	315	952	4.3	12	30
7	59.8	1074	350	953	2.8	12	19.5
8	58.6	1132	350	908	1.5	13	11
9	62.6	1162	45	909	7.8	20	110
10	87.6	1143	64	943	3.0	12	24
11*	67.6	1056	250	1034	0.3	1	0.35
12	76.8	1092	130	807	5.6	33	126
13	73.6	1147	135	946	4.8	15	40
14	68.6	1154	156	947	3.4	11	24
15	64.4	1159	190	945	4.3	14	35
16	68.8	1156	225	946	5.0	17	42
17	67.6	1104	270	848	2.3	10	18
18	72.6	1081	316	967	2.9	11	17
19	83.6	1163	354	941	4.3	13	22
20	76	1105	20	886	4.3	25	92
21	80.6	1140	15	900	2.0	10	17
average		1130 ± 30		931 ± 48	4.2 ± 2.6	15 ± 6	47 ± 49

\* rod #11 was burst at the welding point of the fastening of the TFS 11/14 thermocouple.



**Table 11** QUENCH-L1; Hydrogen absorbed by secondary hydrogenation (results of n<sup>0</sup>-radio- and tomography)

rod #	radiography: absolute local maximum, wppm	tomography: averaged for one cladding cross section (cross section thickness: 1 pixel), wppm
2	1800	980
3	1115	
4	730	
5	755	
6	795	
7	695	
8	1435	
9	1270	

**Table 12** QUENCH-L1; Wetting of TFS thermocouples

Bundle elevation, mm	Wetting time, s	Collapsed water front, mm
-250	247	-270
-150	251	-145
-50	253	-100
50	256	4
150	259	79
250	261	144
350	262..263	168..212
450	263..264	212..239
550	264..268	239..330
650	265..269	267..355
750	263..273	212..427
850	273..286	427..680
950	264..286	239..680
1050	265..288	267..709
1150	266..293	287..828
1250	267..284	309..638
1350	264	239

**Table 13** QUENCH-L1; Strain parameters at the middle of burst elevation

rod group	rod #	elevation of burst <i>middle, mm</i>	max D mm	<i>at</i> <i>azimuth</i> <sup>o</sup>	min D mm	<i>at</i> <i>azimuth</i> <sup>o</sup>	Strain* %
central group	1	900	-	-	-	-	-
	2	907	15.2	63	11.6	146	<b>23.7</b>
	3	968	16.1	154	13.8	256	<b>36.3</b>
	4	982	15	31	13	124	<b>28.9</b>
	5	966	18.6	226	16	348	<b>61</b>
	6	952	15.8	295	13.3	208	<b>33.9</b>
	7	953	14.7	143	12.5	234	<b>24.8</b>
	8	908	14.5	206	12.2	270	<b>21.3</b>
	9	909	16.7	257	13.2	158	<b>40.6</b>
peripheral group	10	943	14.7	77	12.4	157	26.1
	11	1034	-	-	-	-	-
	12	807	15.3	82	11.6	142	27.5
	13	946	15.4	125	12.9	51	34.1
	14	947	16.4	141	13.8	245	39.3
	15	945	15.7	205	13.2	100	34.5
	16	946	15.6	243	13.1	317	34.1
	17	848	13.5	257	12.4	180	20.1
	18	967	15	306	12.8	226	28.8
	19	941	15.3	340	13.2	258	31.5
	20	886	16.9	249	14.6	307	44.9
	21	900	15.2	247	12.5	187	26.7
average			<b>15.56 ± 1.09</b>		<b>13.06 ± 1.02</b>		<b>32.5 ± 9.6</b>

\*including the burst opening width

**Table 14** QUENCH-L1; Results of tensile tests

rod l <sub>0</sub> =1000 mm *l <sub>0</sub> = 250 mm	ultimate tensile strength [MPa]	fracture stress [MPa]	elongation at fracture (graded) [%]	rupture based on:
04*	416	414	0.75 (0.68)	stress concentration
06*	499	481	1.70 (1.68)	stress concentration
07*	436	425	1.03 (0.81)	stress concentration
09	307	307	0.59 (0.09)	stress concentration
12	464	464	5.50 (5.27)	stress concentration
13	518	515	5.13 (5.03)	stress concentration
14	472	472	3.96 (3.80)	stress concentration
15	473	471	4.57 (4.35)	stress concentration
16	462	456	4.31 (4.10)	stress concentration
17*	333	327	0.33 (0.33)	stress concentration
18*	270	263	0.19 (0.19)	stress concentration
19	530	528	8.30 (8.20)	stress concentration
20*	367	356	1.13 (1.06)	stress concentration



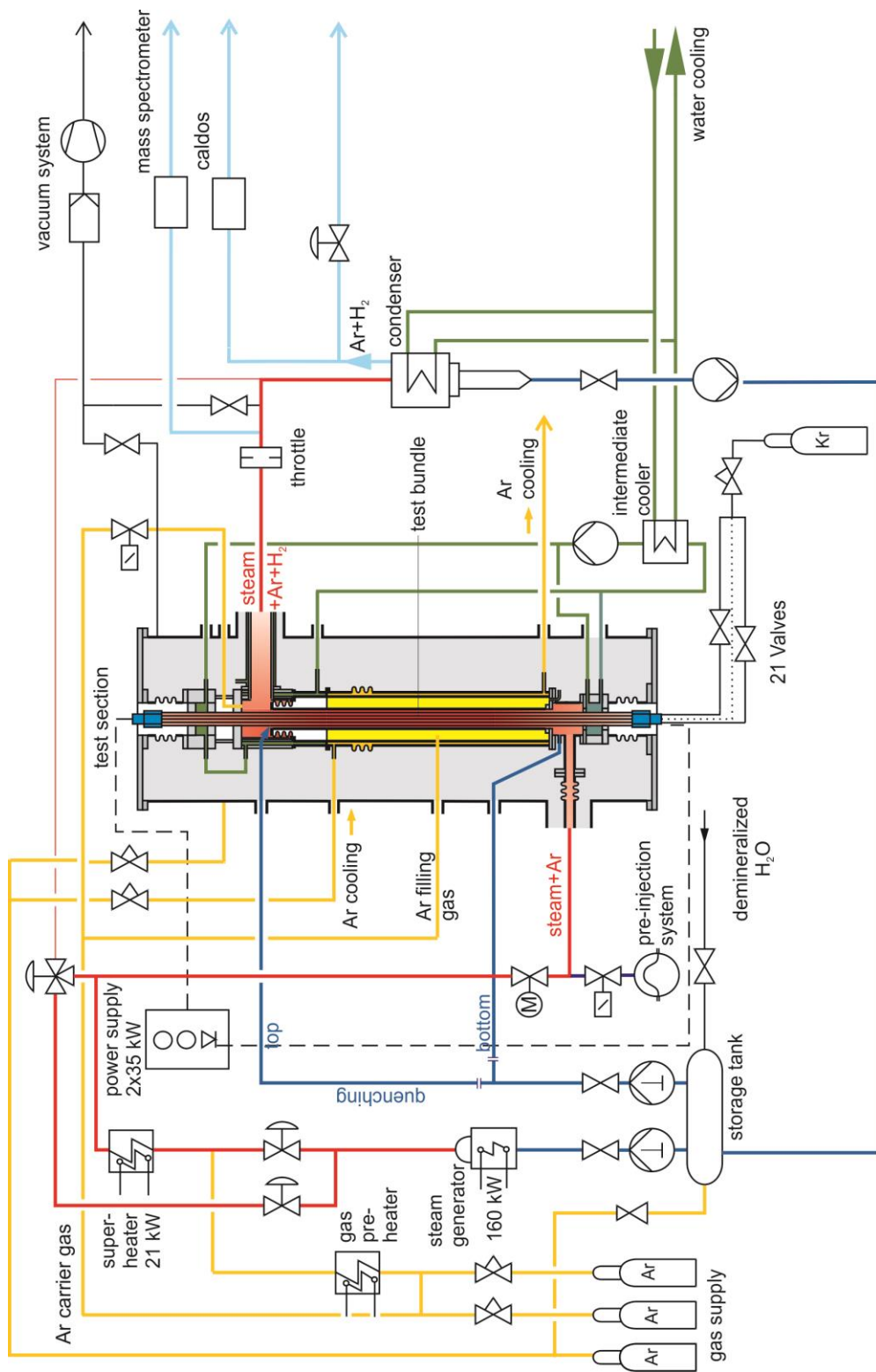


**Figure 1** Flow diagram of the QUENCH test facility.

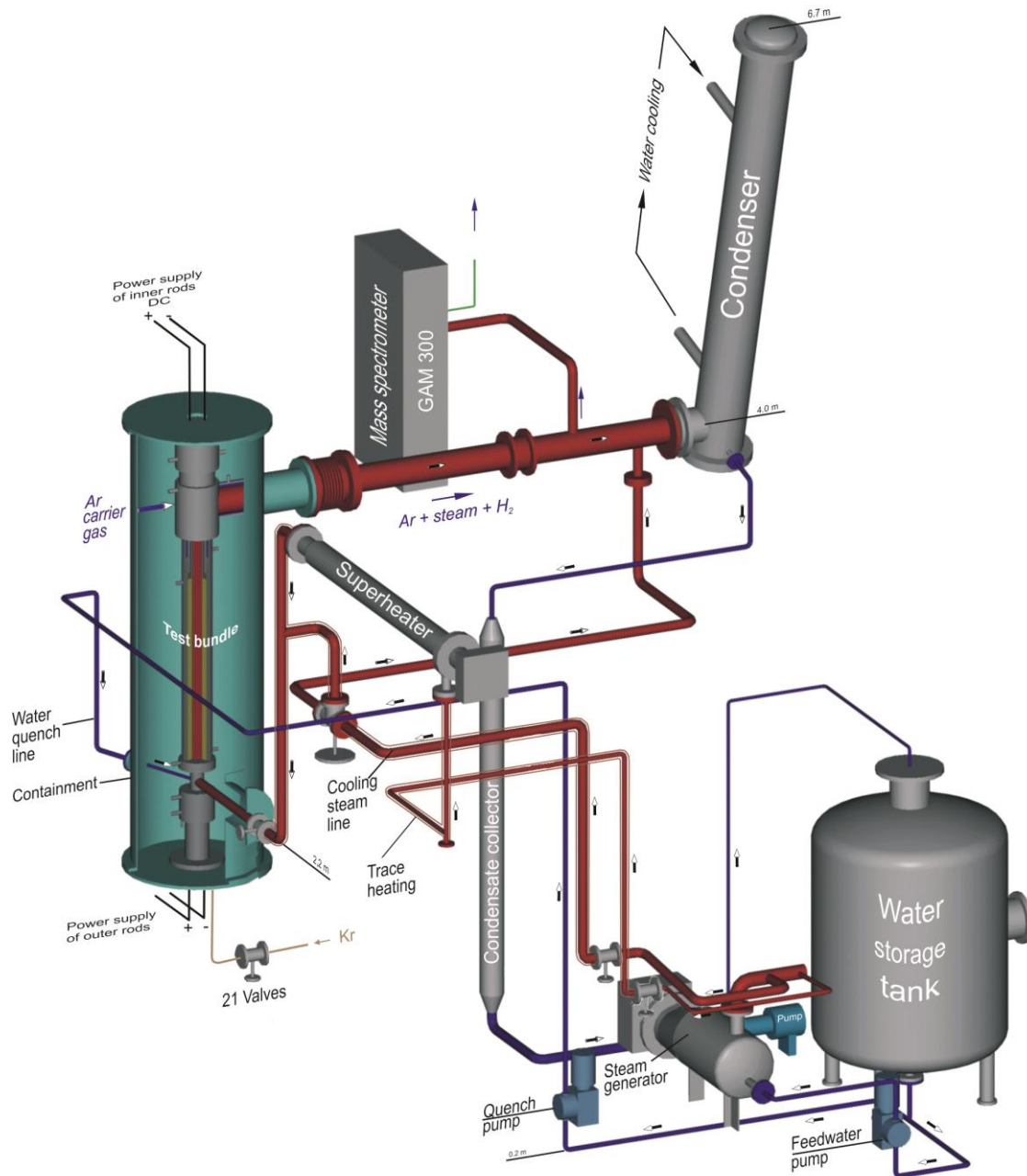
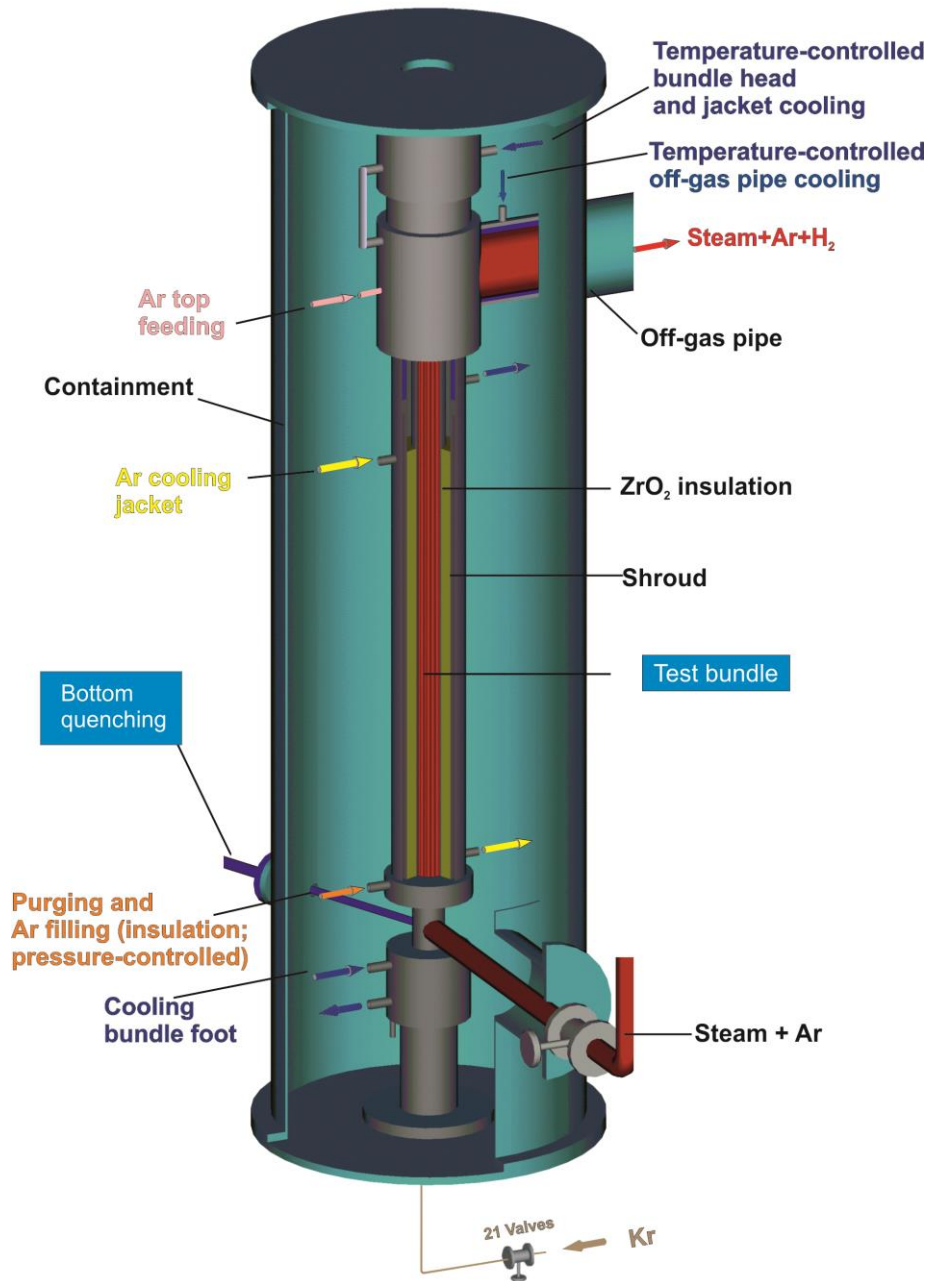
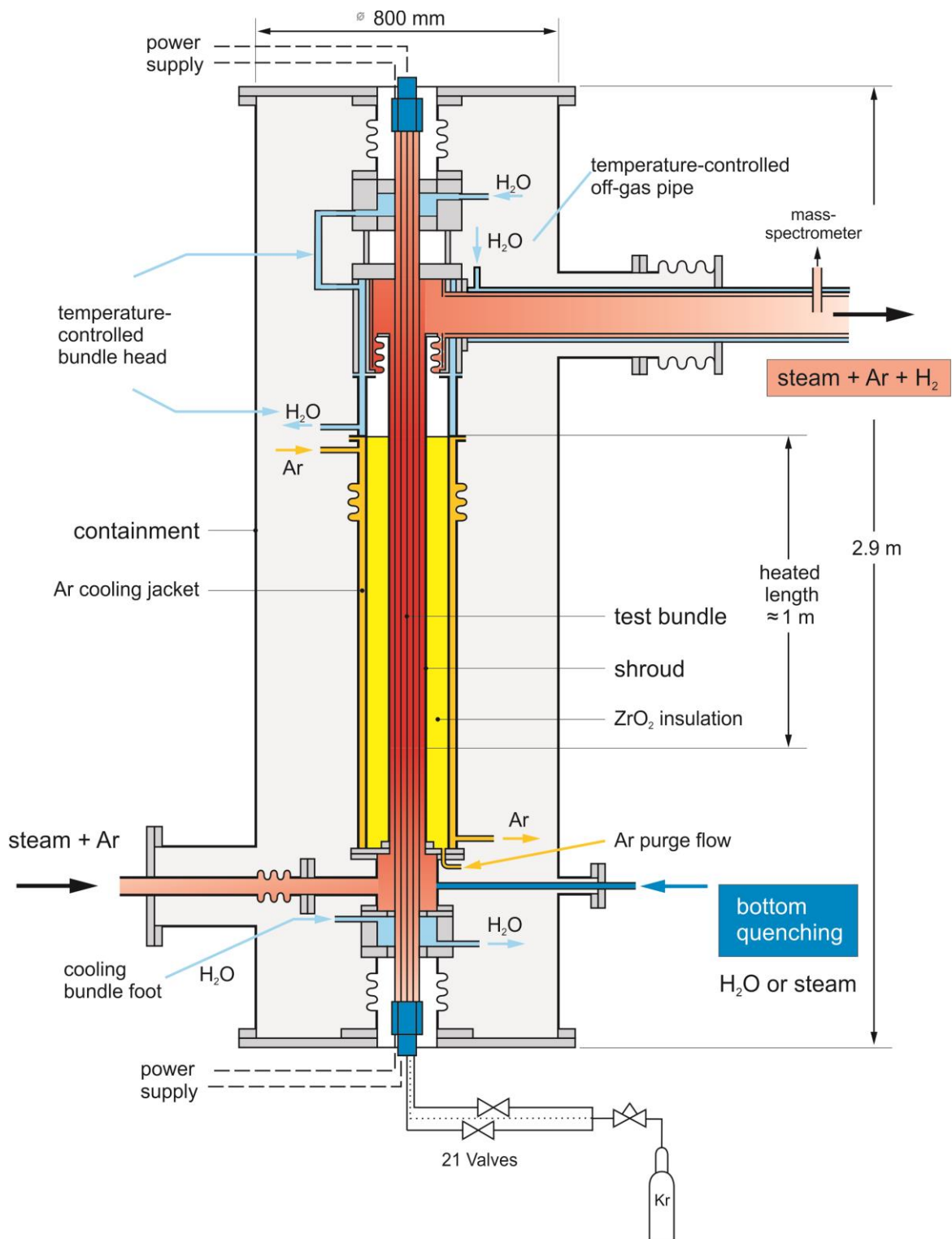


Fig.2-QUE-L1-Gesamtanlage.cdr  
21.09.10 - IMF

**Figure 2** QUENCH Facility - Main components.



**Figure 3** QUENCH Facility; Containment and test section.



**Figure 4** QUENCH-L1; Test section with flow lines.



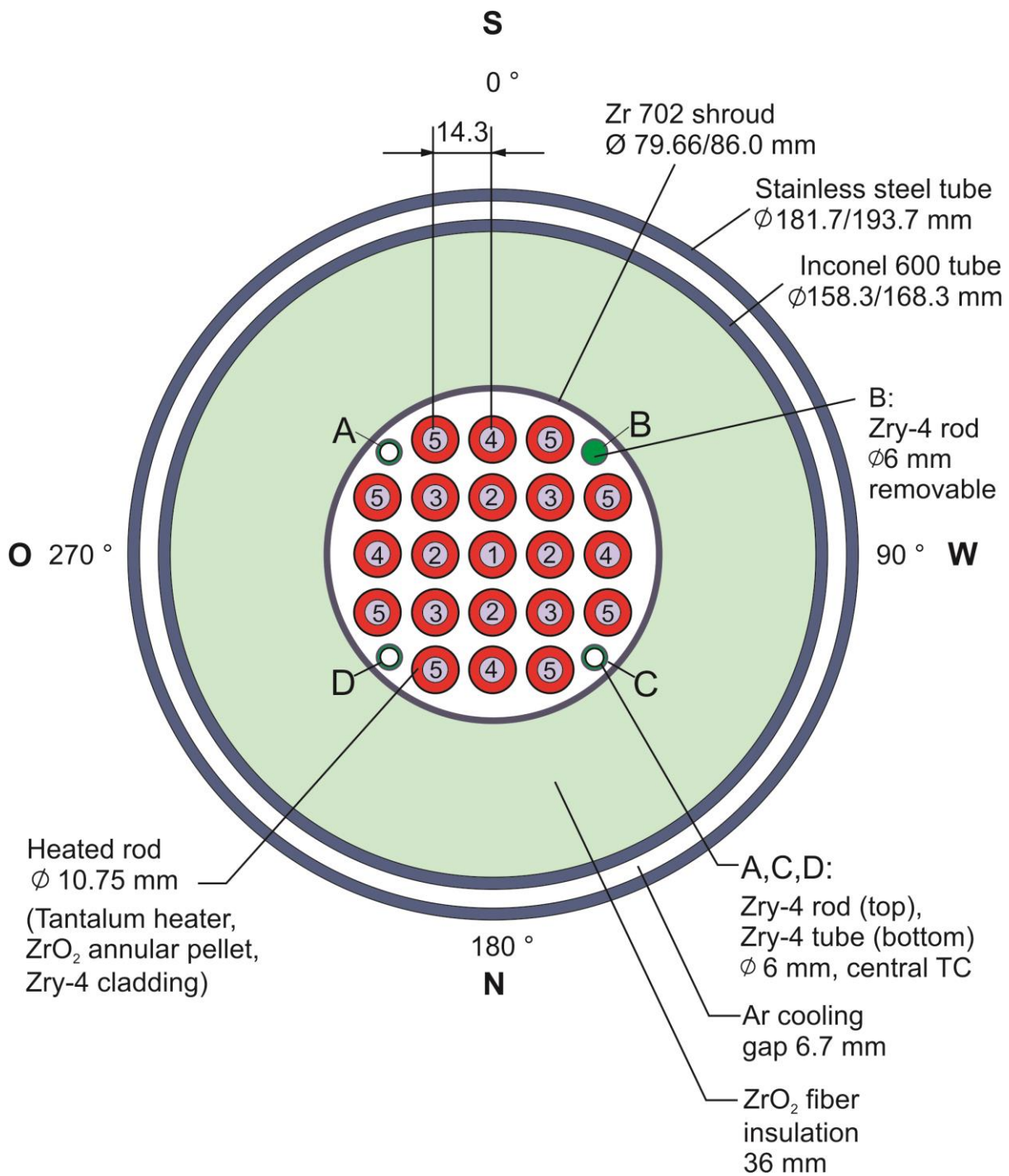


**Figure 5** QUENCH-L1; Fuel rod simulator bundle (cross section, top view) including rod type indications corresponding to table “List of Instrumentation”.

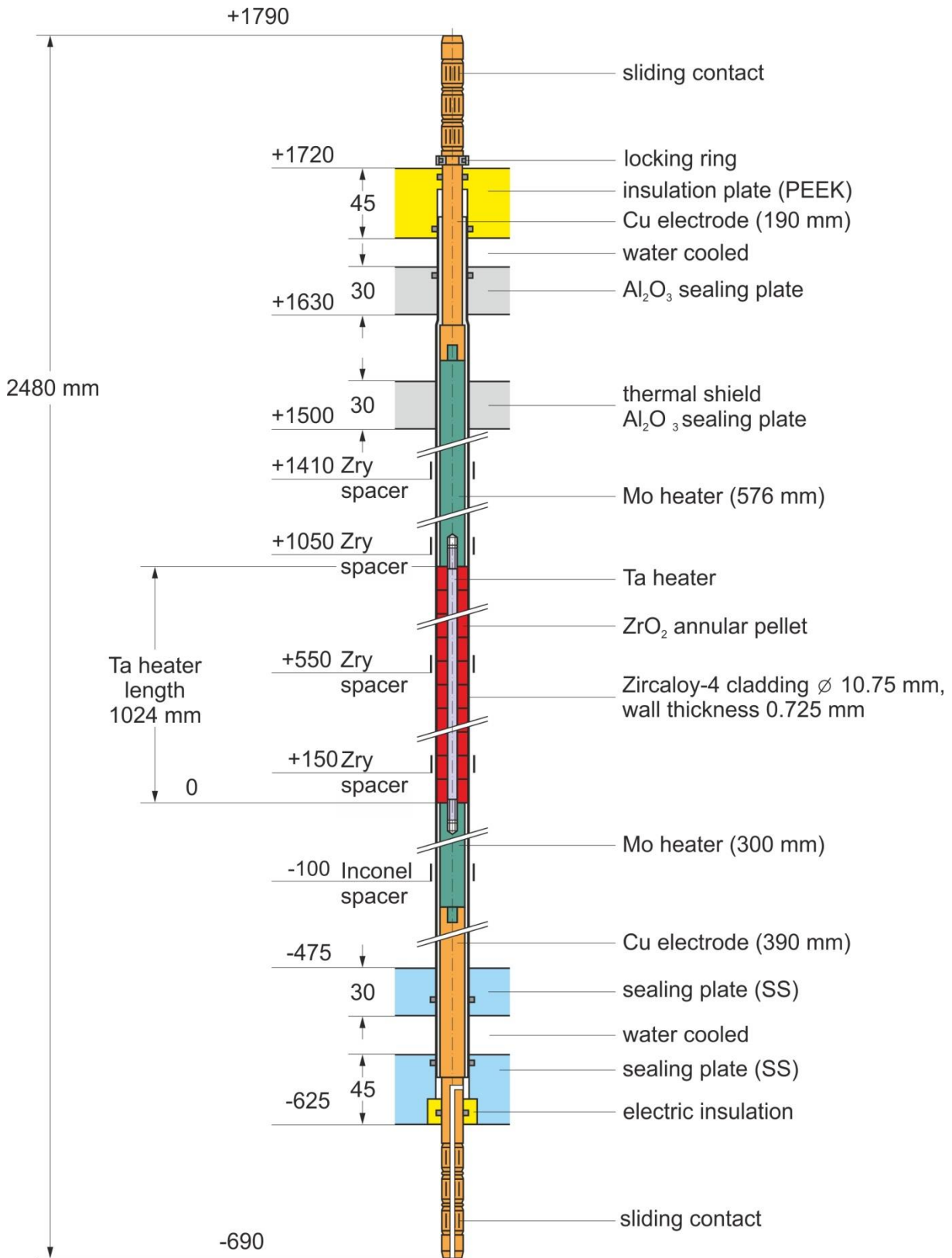
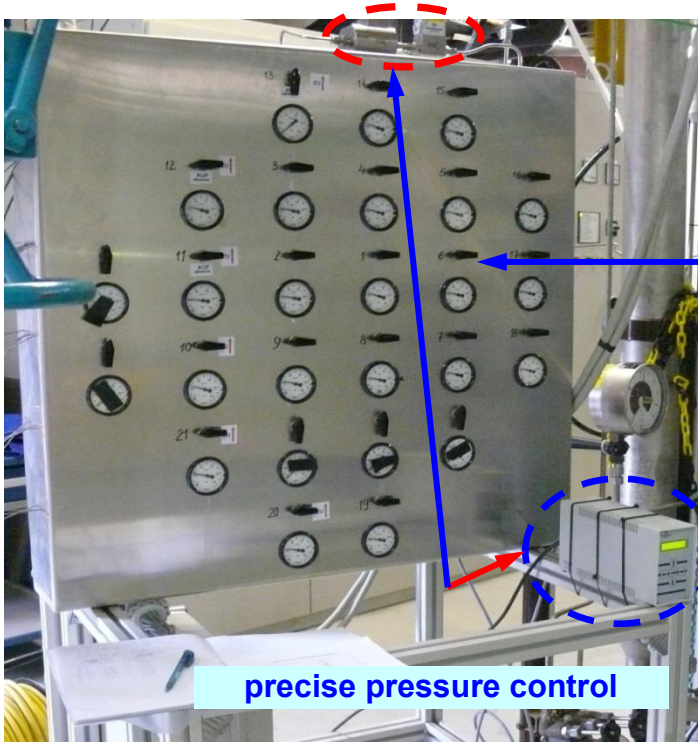
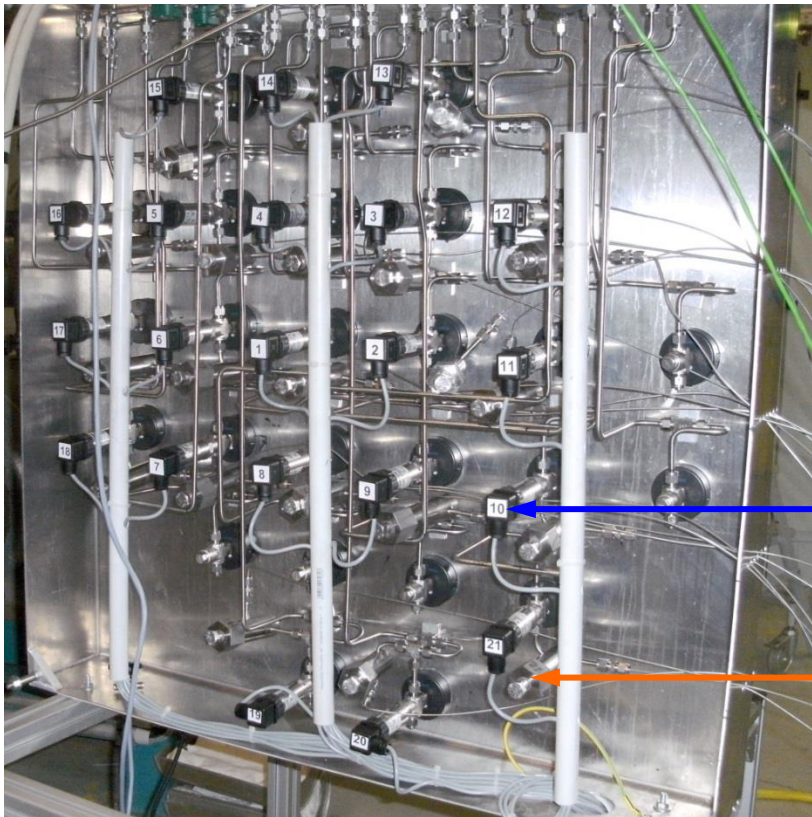


**Figure 6** Heated fuel rod simulator.



Front side with:  
21 pressure valves

precise pressure control



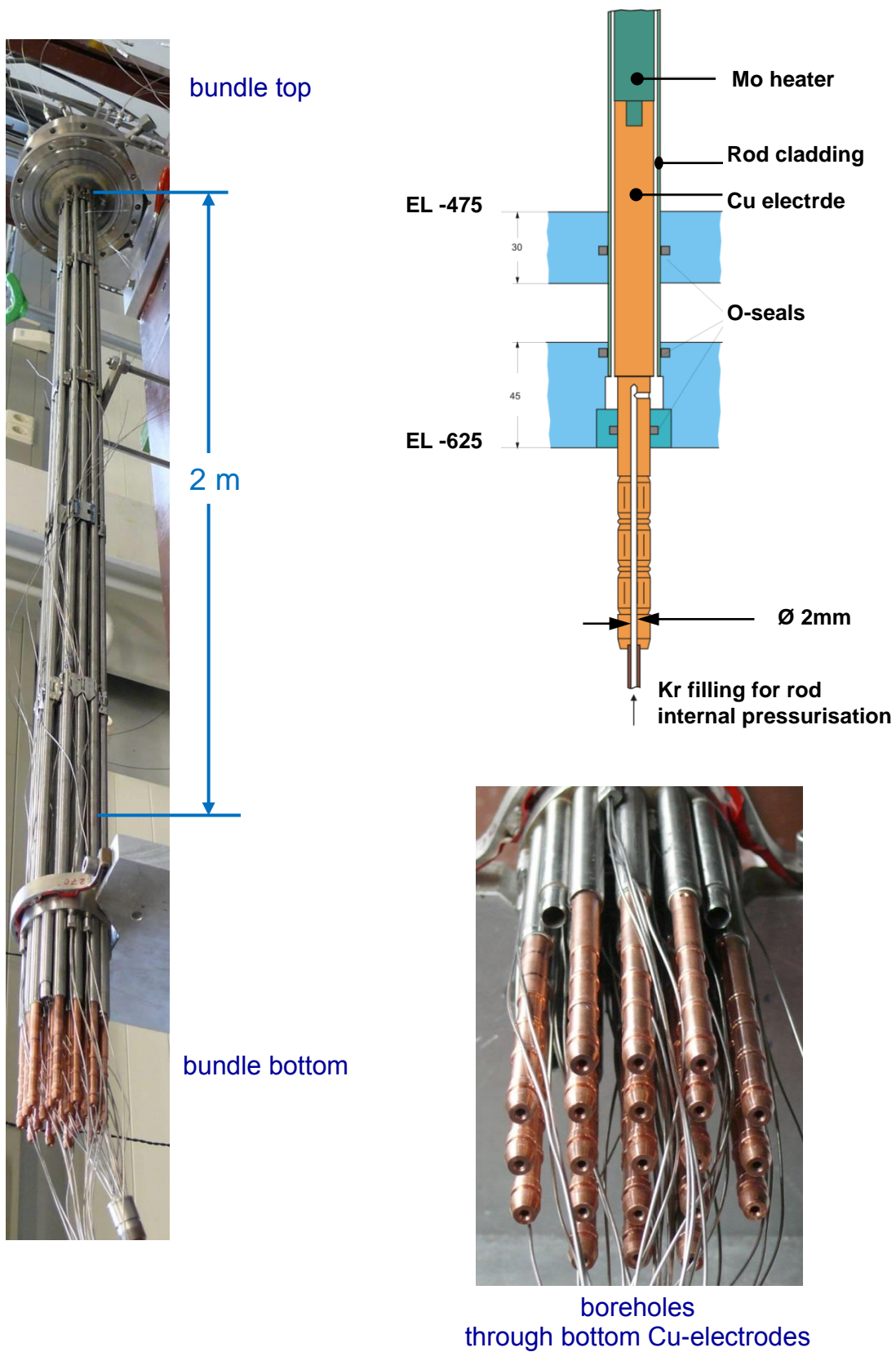
Rear side with :

21 capillary tubes  
to test bundle

21 pressure  
transducers

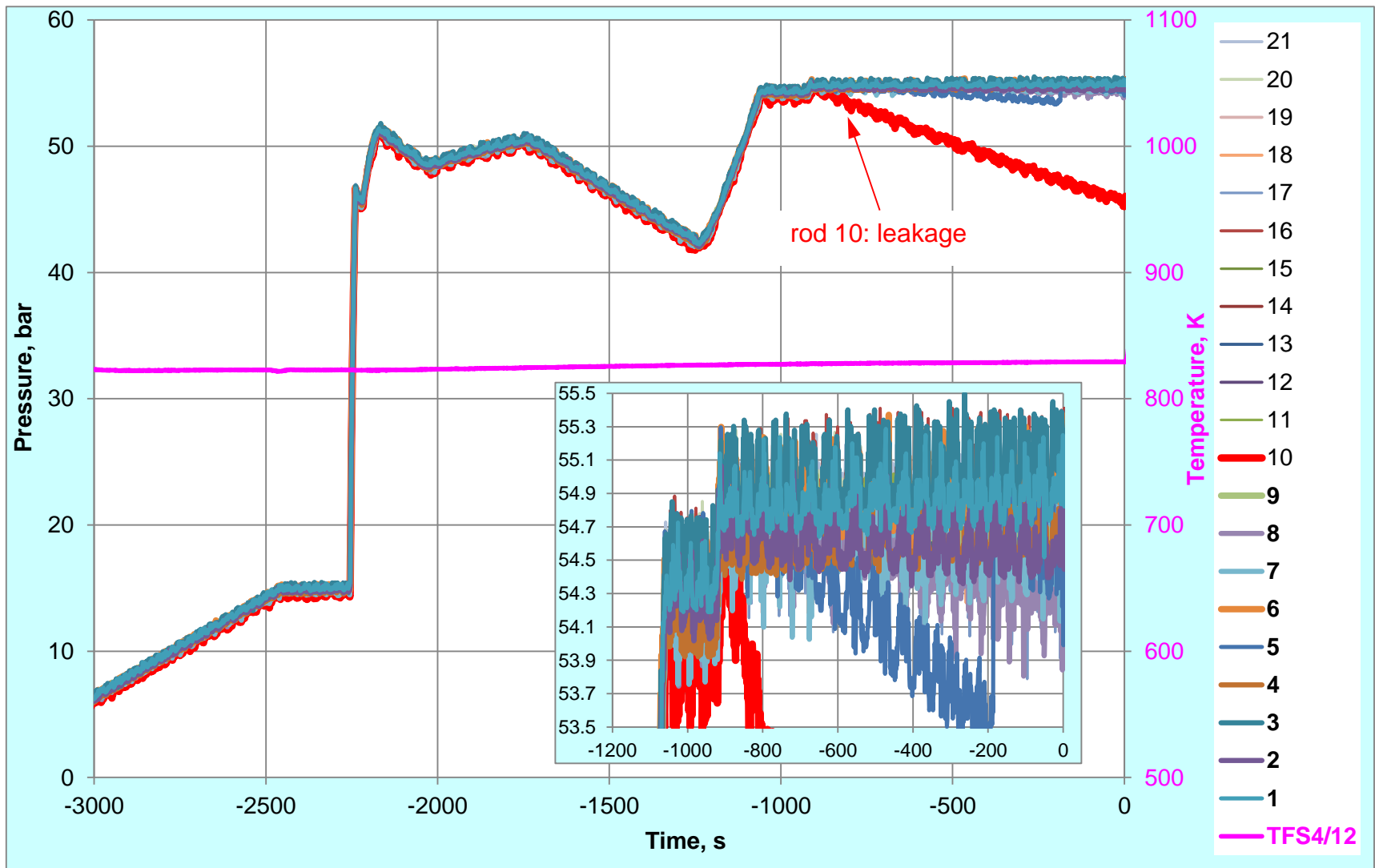
21 adjustable  
compensation volumes  
to setting of original  
volume value  
of  $31.5 \text{ cm}^3$

Figure 7 QUENCH-L1; Rod pressure control and measurement panel.



**Figure 8** QUENCH-L1; Rod pressurization.





**Figure 9** QUENCH-L1; Rod pressurization process at  $T_{pct}=550^{\circ}\text{C}$ .

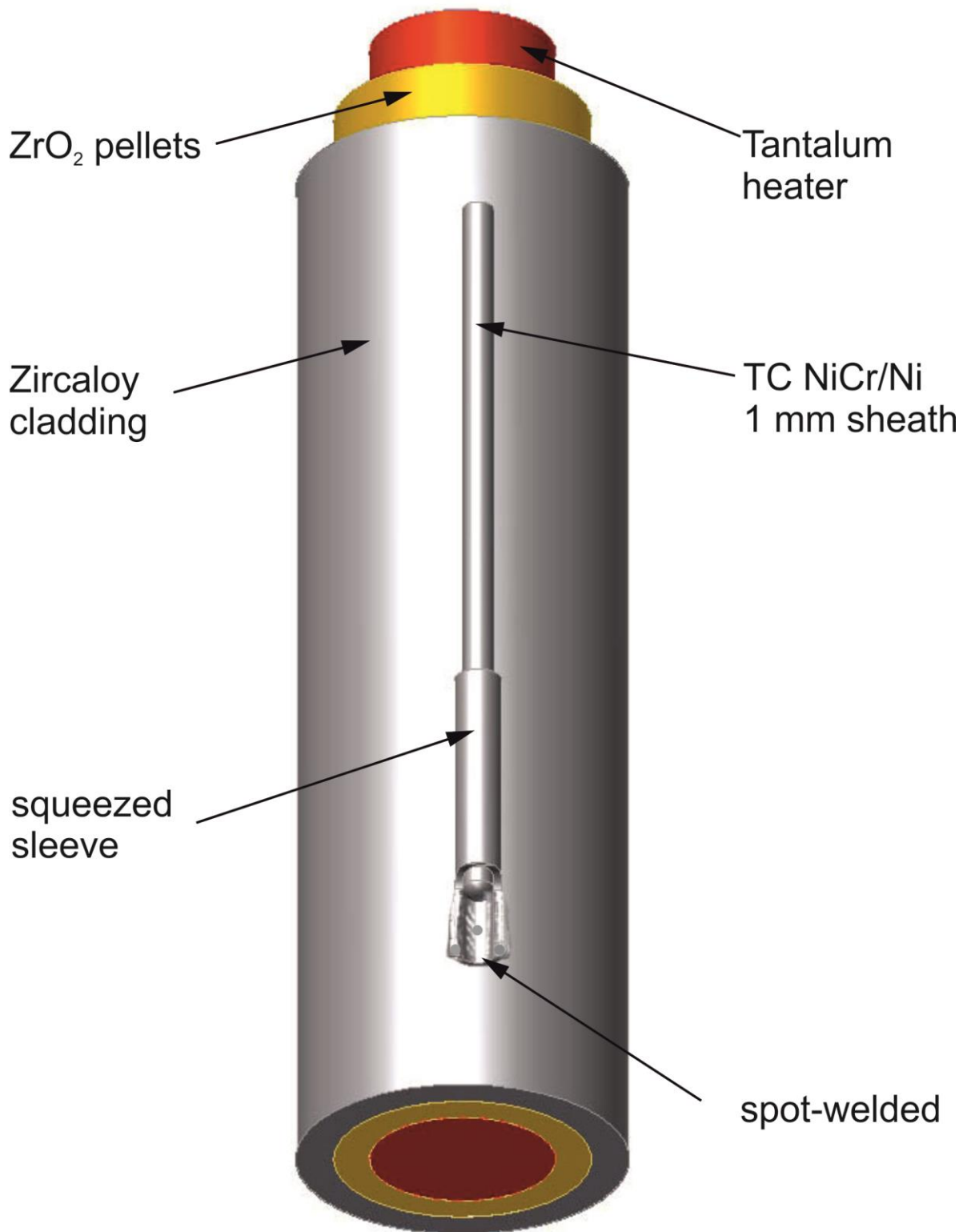


**Figure 10** QUENCH-L1; Concept for TC fastening at the test rod.

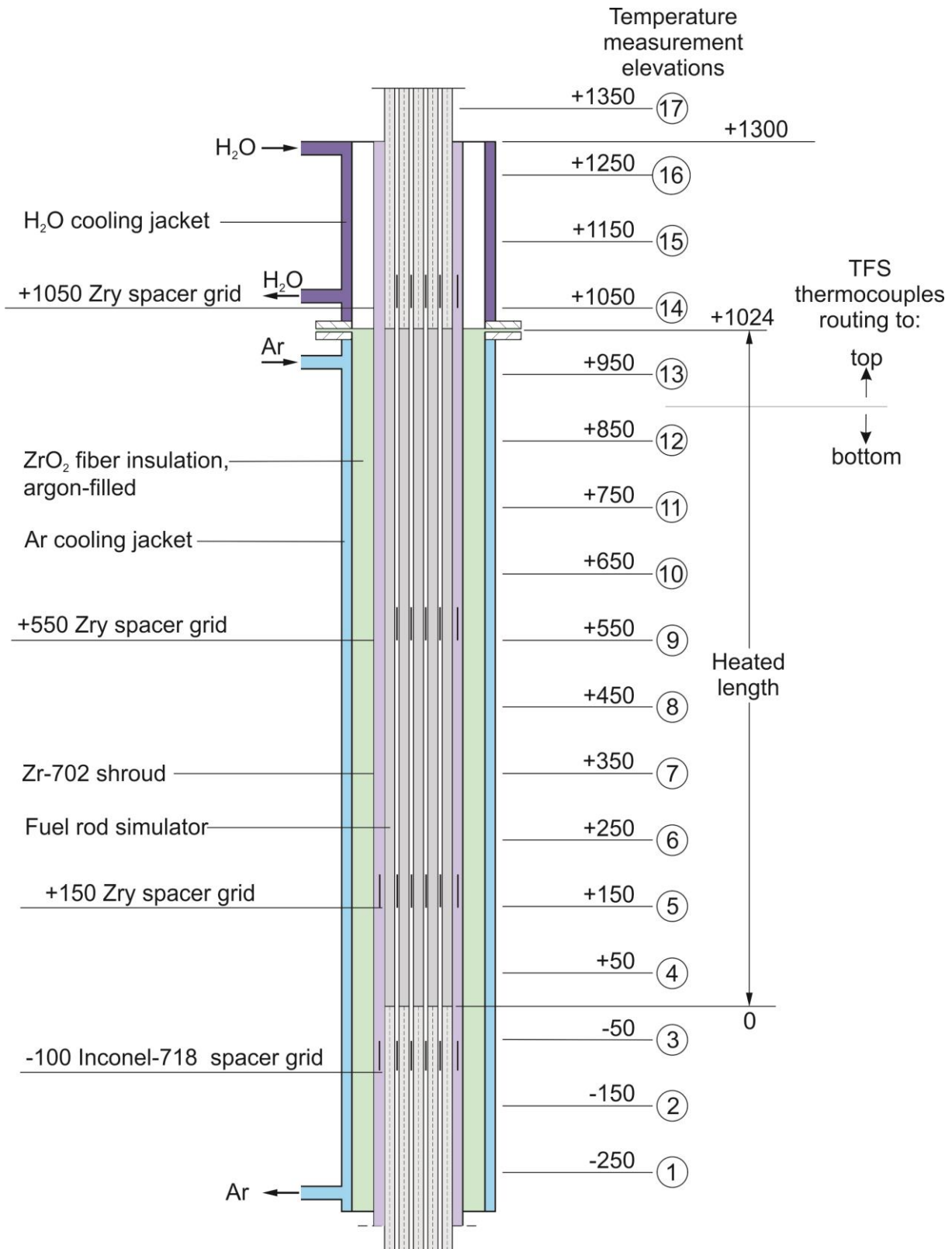


**Figure 11** Axial temperature measurement locations in the QUENCH-L1 test section.

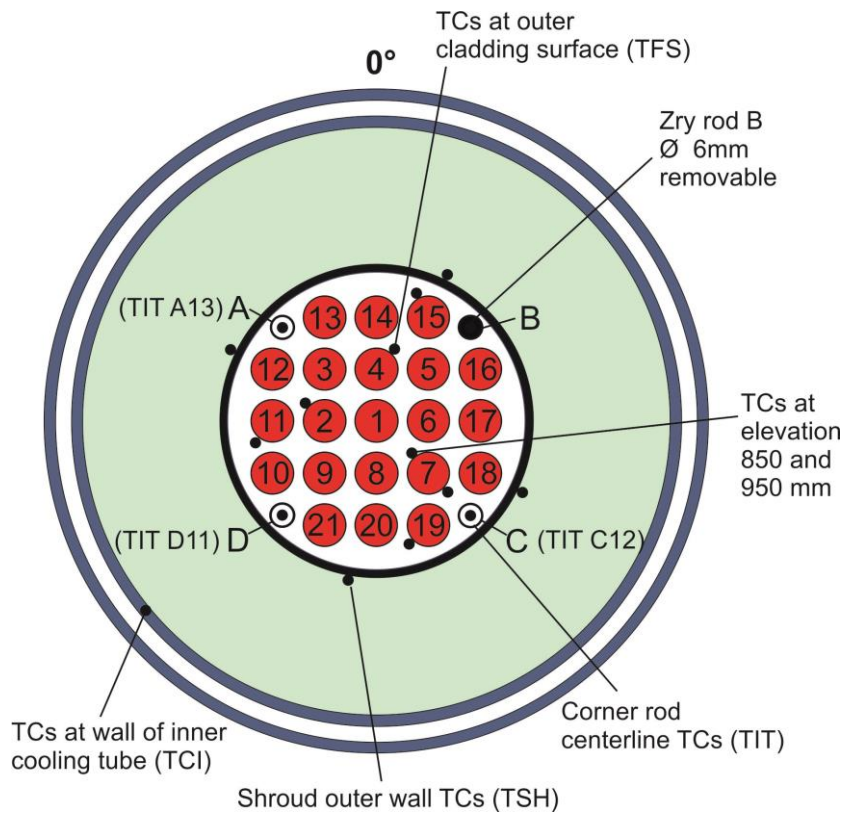
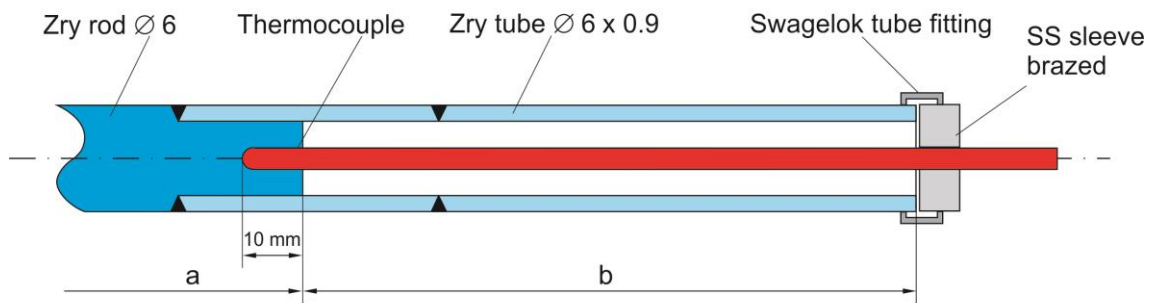


**Figure 12** QUENCH-L1; Test bundle; TC instrumentation and rod designation (top view).

(TIT A13, TIT C12, TIT D11)



Rod A: TIT A13 (950 mm), a = 360 mm, b = 2080 mm

Rod C: TIT C12 (850 mm), a = 460 mm, b = 1980 mm

Rod D: TIT D11 (750 mm), a = 560 mm, b = 1880 mm

(Rod B: Zry-4 rod, Ø 6 mm, removable)

**Figure 13** QUENCH-L1; Arrangement of the thermocouples inside the corner rods.



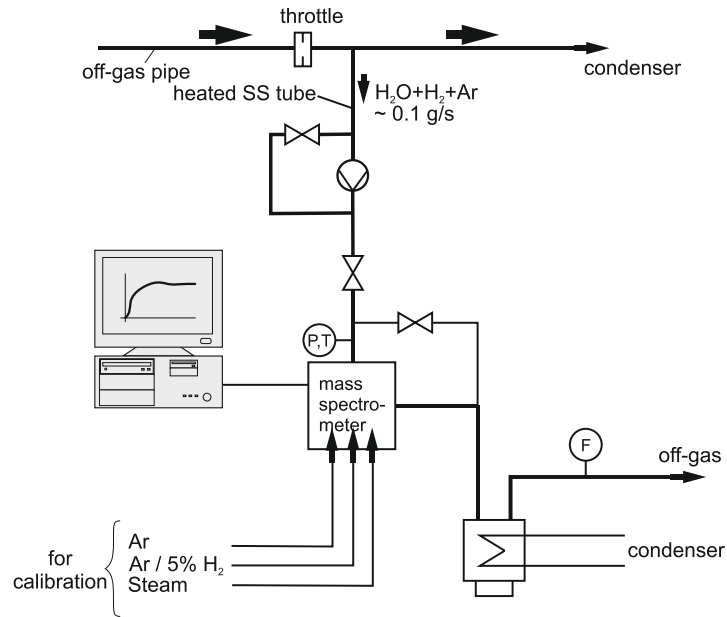


**Figure 14** QUENCH Facility; H<sub>2</sub> measurement with the GAM 300 mass spectrometer.

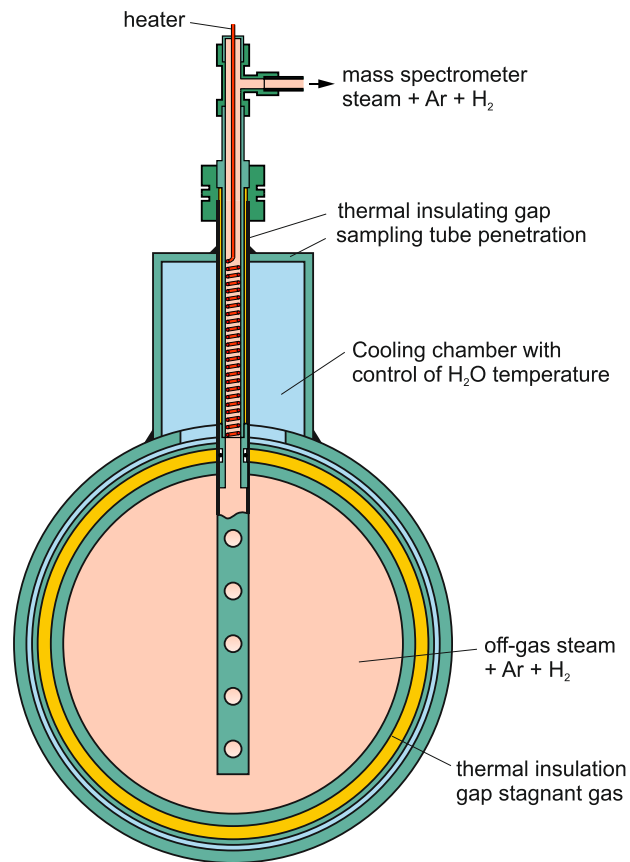


**Figure 15** Mass spectrometer sampling position at the off-gas pipe of the QUENCH test facility.

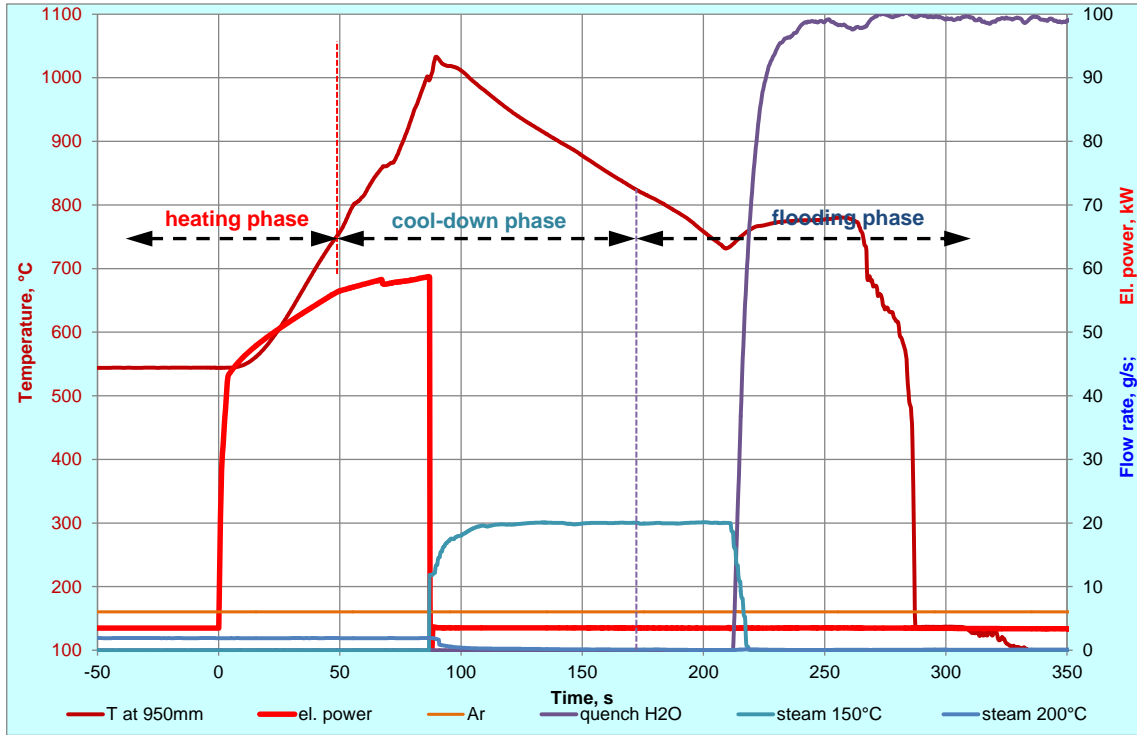


Figure 16 QUENCH-L1; Test scenario

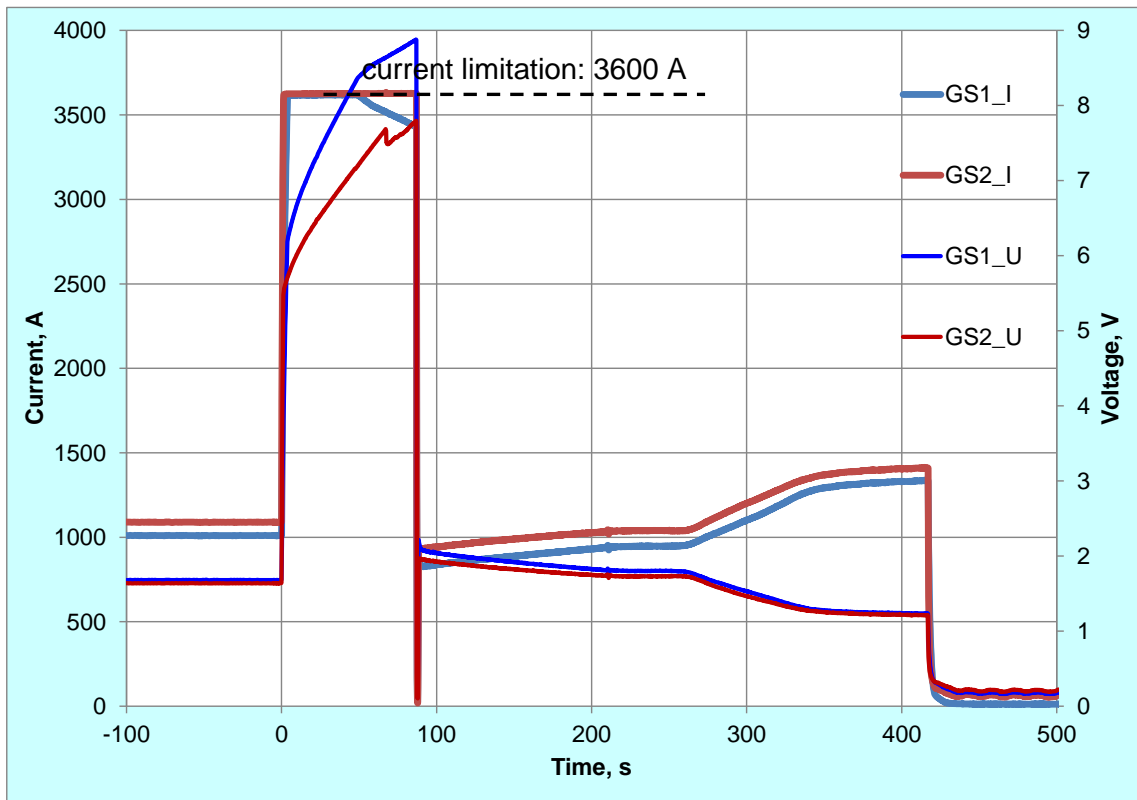
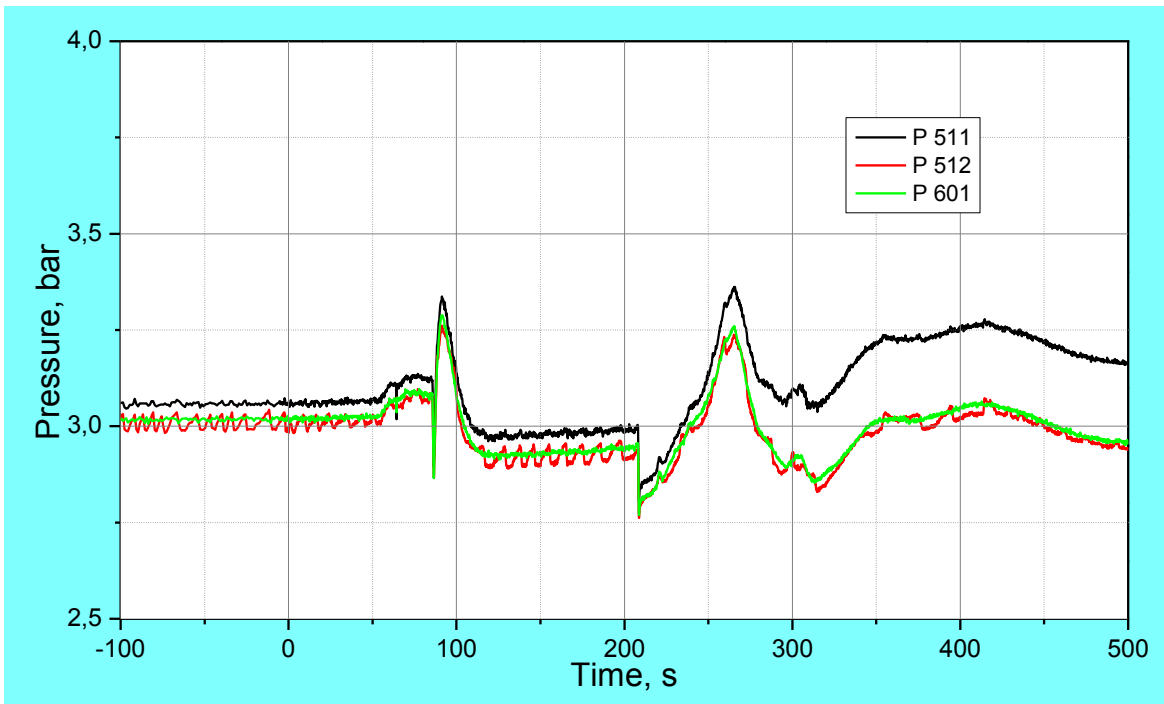
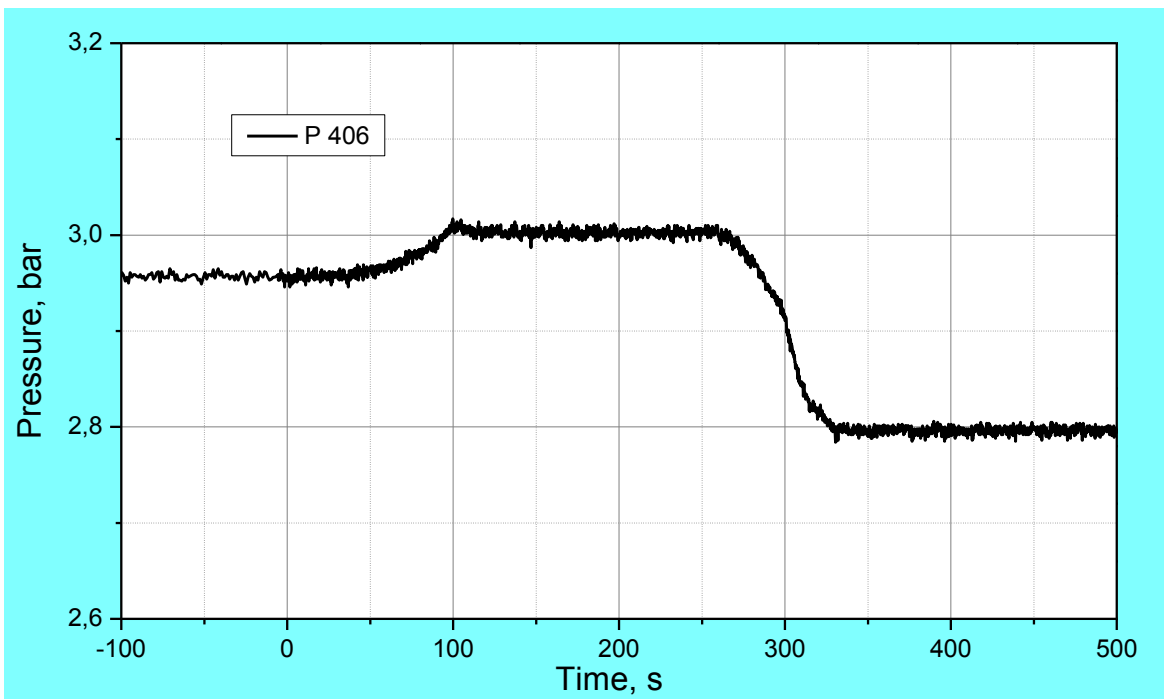


Figure 17 QUENCH-L1; Current and voltage of DC generators GS1 and GS2.



**Figure 18** QUENCH-L1; System pressure measured at test section inlet P 511, at outlet P 512, and in the off-gas pipe P 601.



**Figure 19** QUENCH-L1; Argon pressure between shroud and cooling jacket P 406 demonstrates tightness of the shroud.

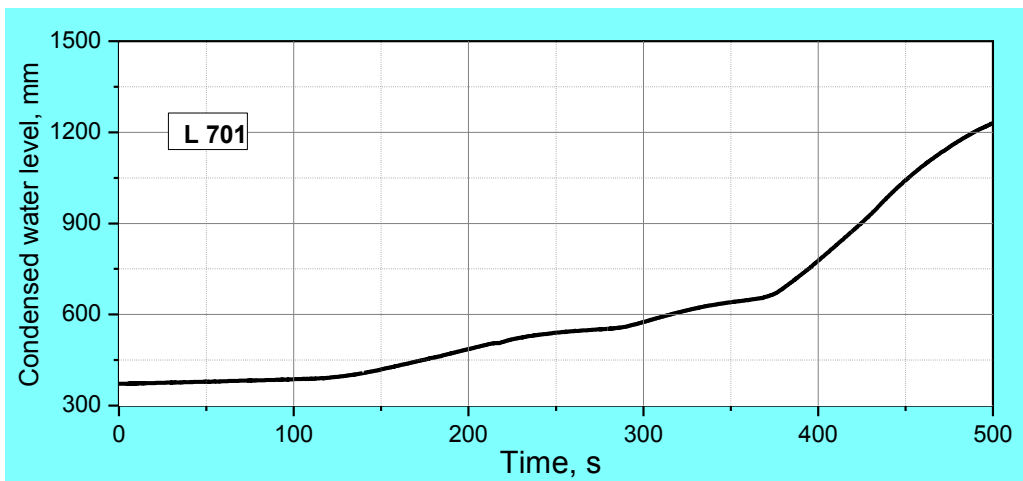
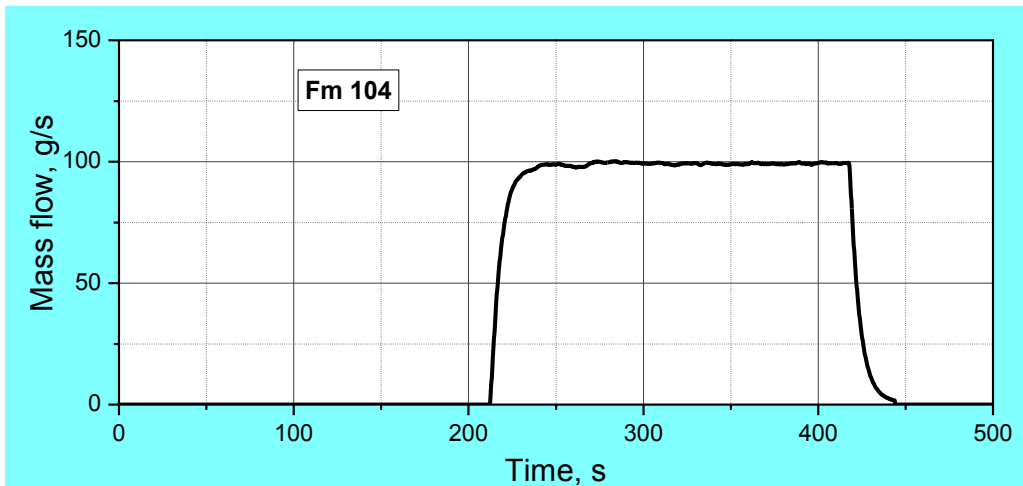
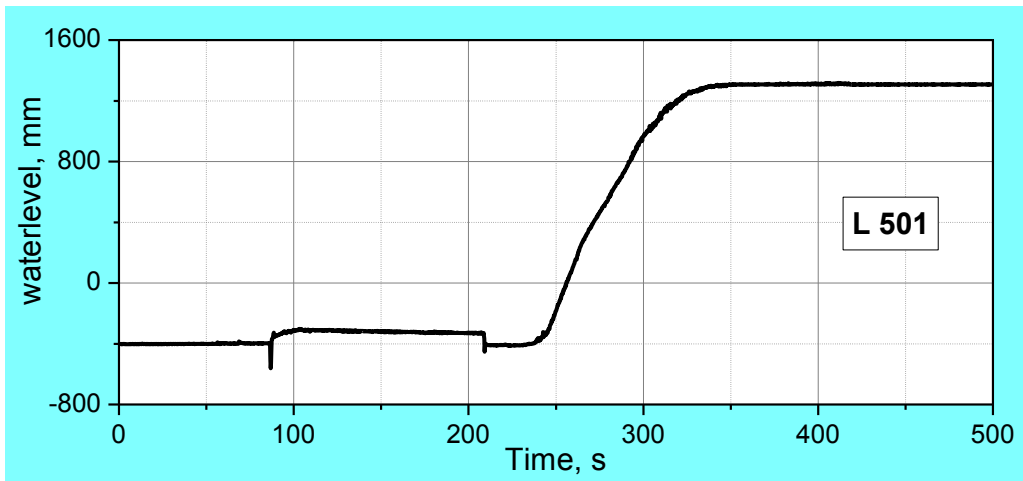


**Figure 20** QUENCH-L1; Quench measurement of collapsed water level (L 501), top, water mass flow rate (Fm 104), center, condensed water (L 701), bottom.

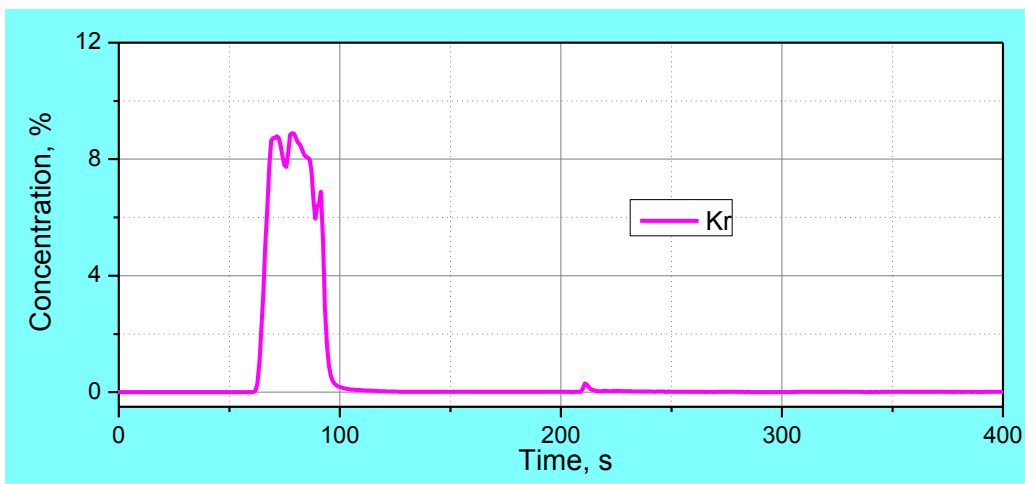
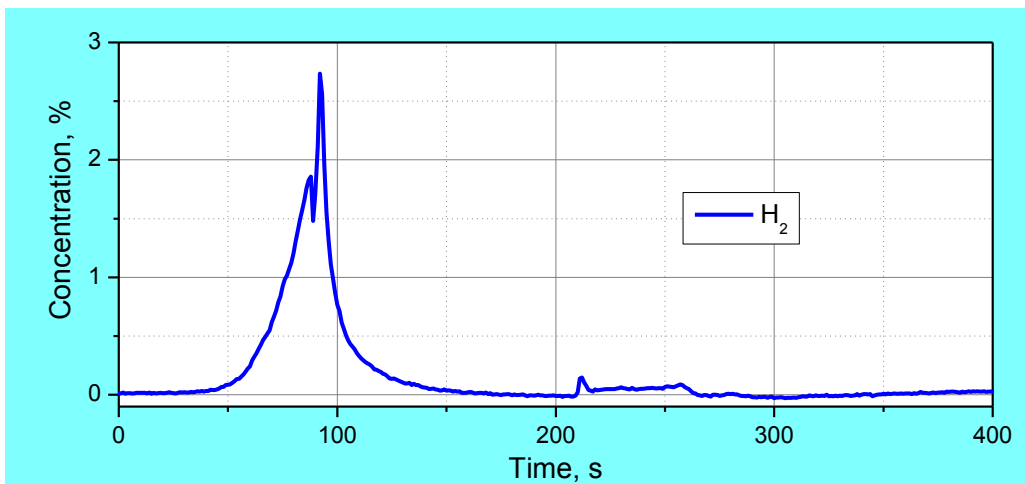
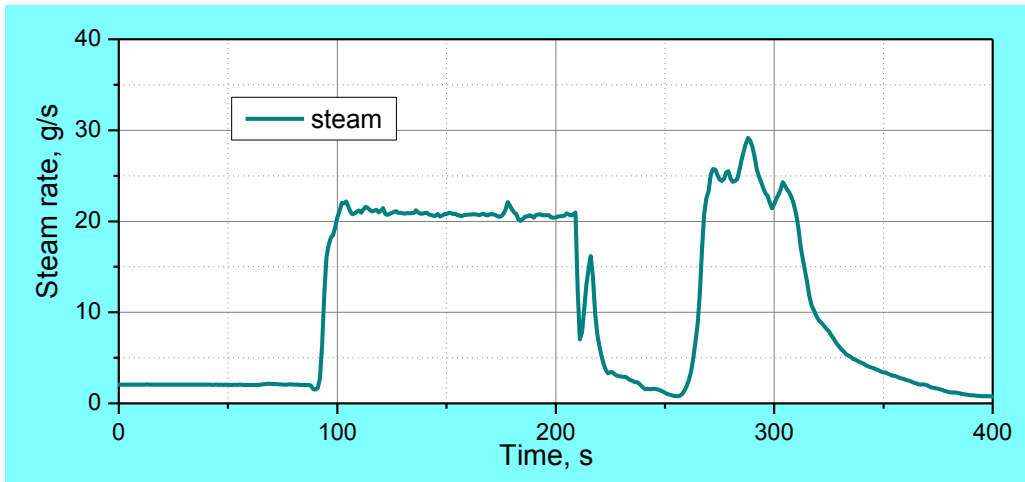


**Figure 21** QUENCH-L1; Steam rate, top, Hydrogen, center, Krypton, bottom, measured by mass spectrometry (MS).

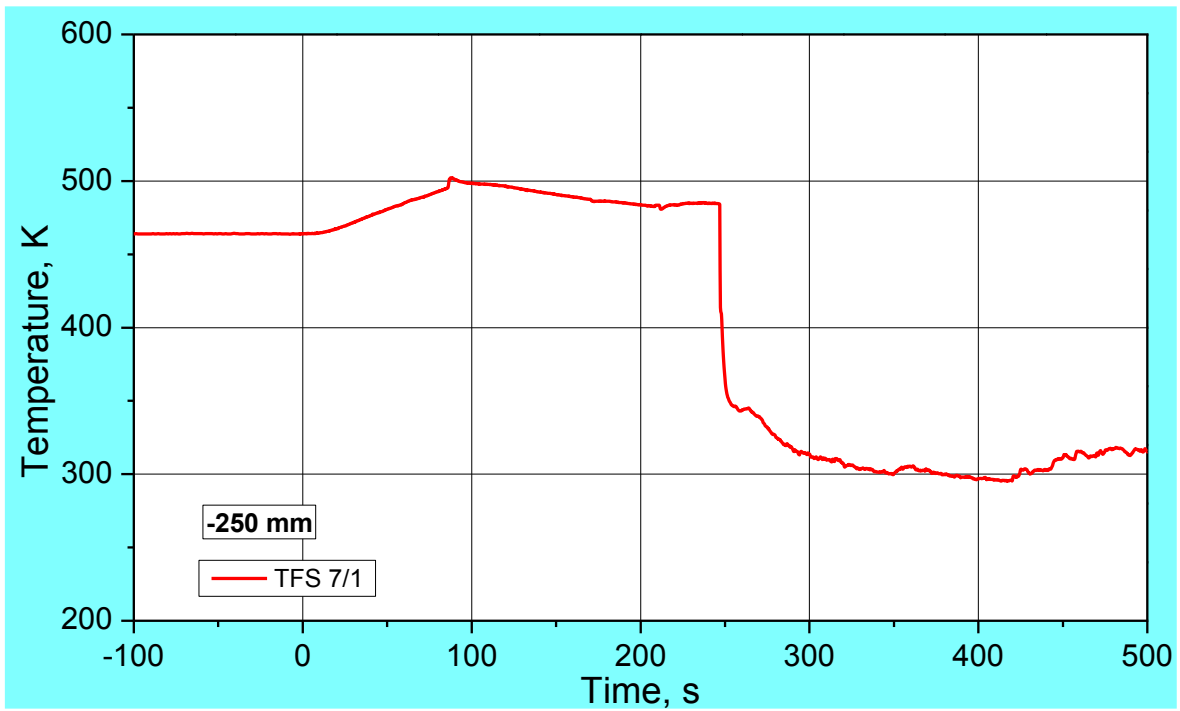


**Figure 22** QUENCH-L1; Temperatures measured by rod cladding (TFS 7/1) thermocouple at -250 mm elevation.

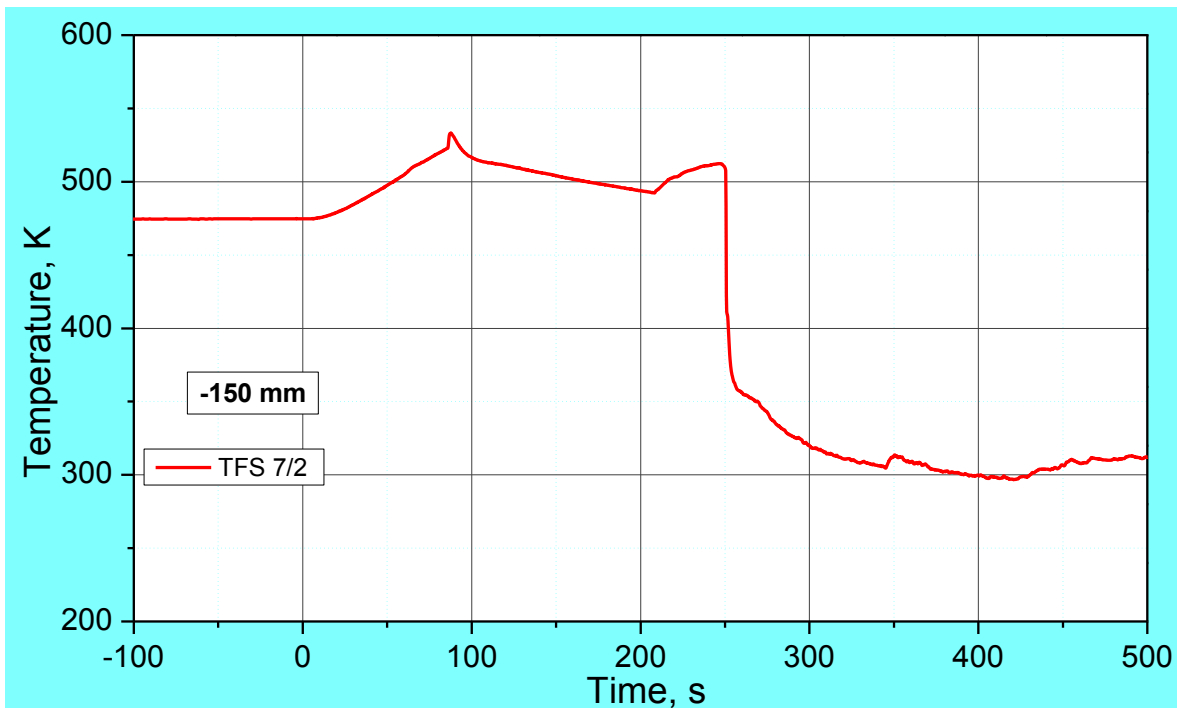


**Figure 23** QUENCH-L1; Temperatures measured by rod cladding (TFS 7/2) thermocouple at -150 mm elevation.

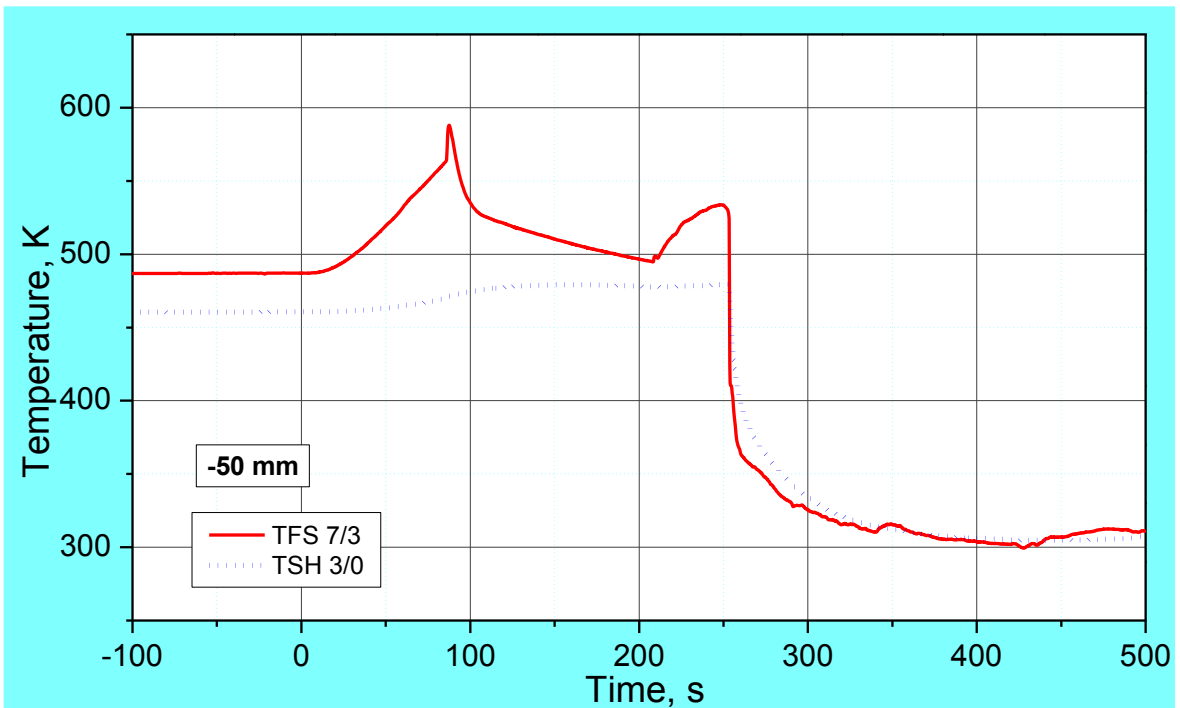


**Figure 24** QUENCH-L1; Temperatures measured by rod cladding (TFS 7/3) and shroud (TSH 3/0) thermocouples at -50 mm elevation.

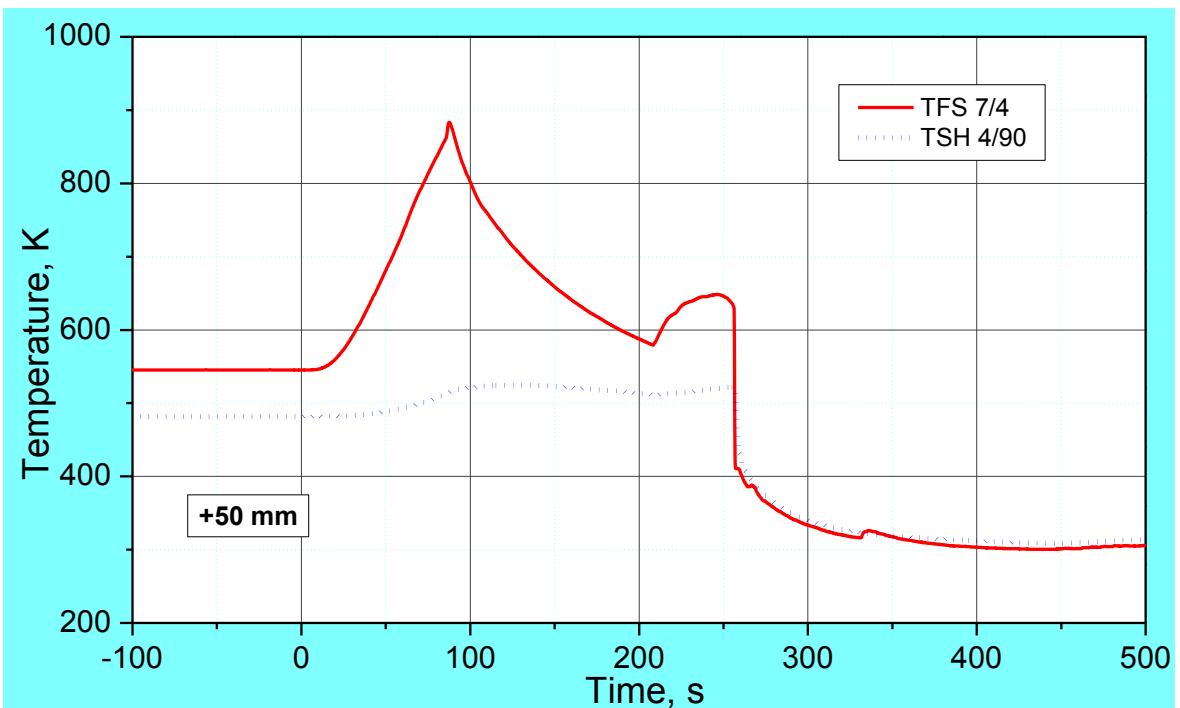


**Figure 25** QUENCH-L1; Temperatures measured by rod cladding (TFS 7/4) and shroud (TSH 4/90) thermocouples at 50 mm elevation.

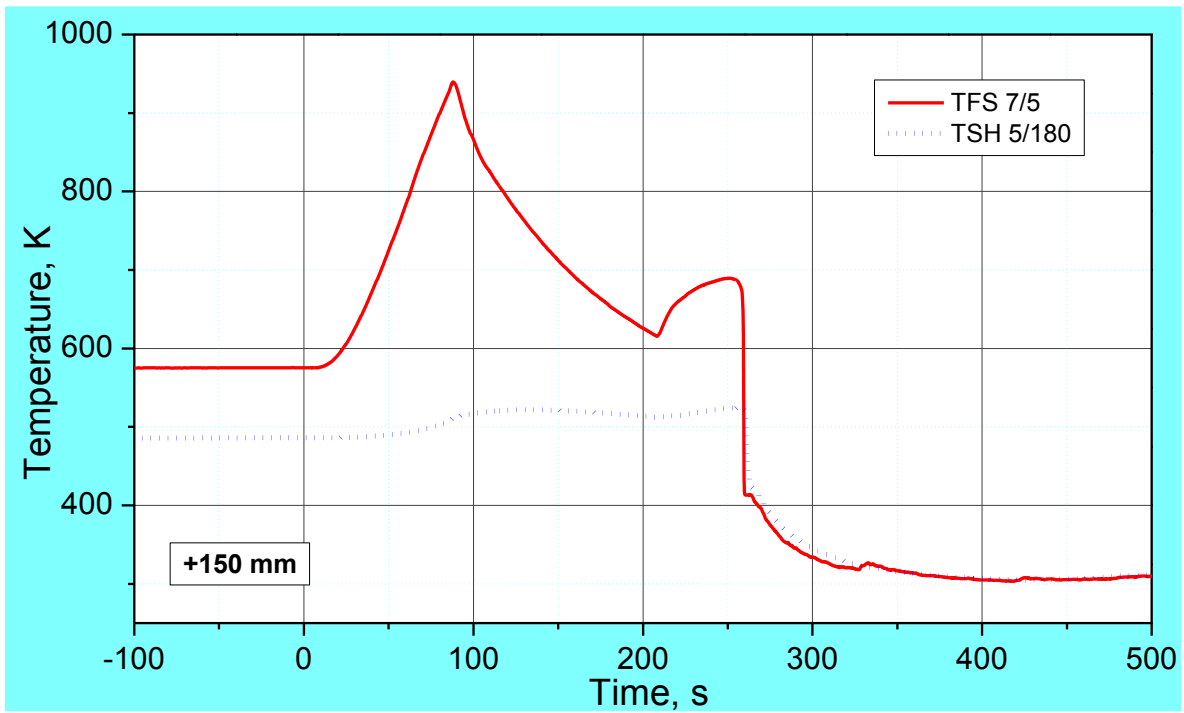


**Figure 26** QUENCH-L1; Temperatures measured by rod cladding (TFS 7/5) and shroud (TSH 5/180) thermocouples at 150 mm elevation.

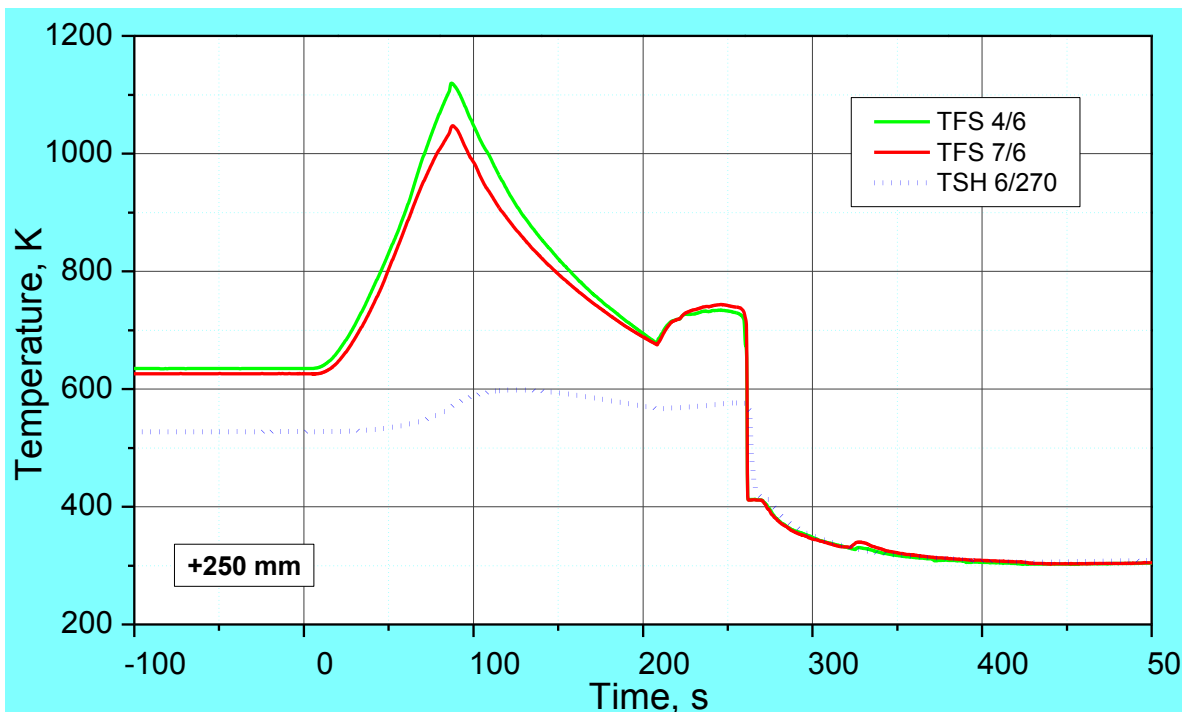


**Figure 27** QUENCH-L1; Temperatures measured by rod cladding (TFS) and shroud (TSH 6/270) thermocouples at 250 mm elevation.



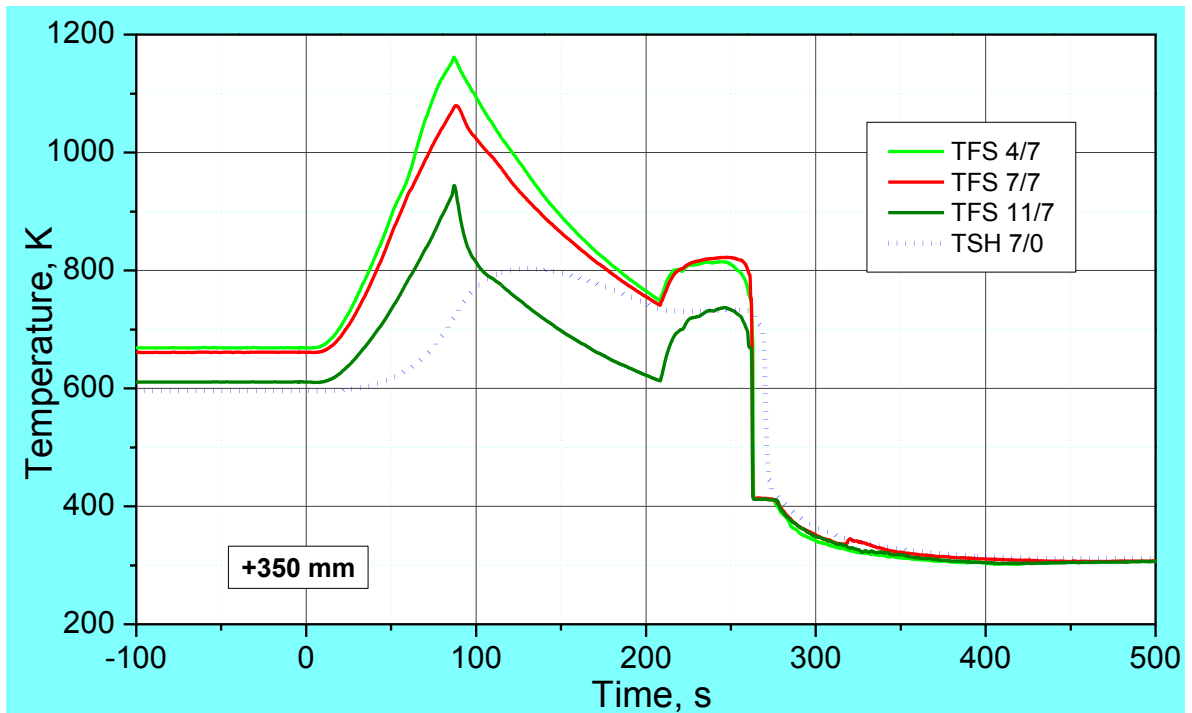


**Figure 28** QUENCH-L1; Temperatures measured by rod cladding (TFS) and shroud (TSH 7/0) thermocouples at 350 mm elevation.

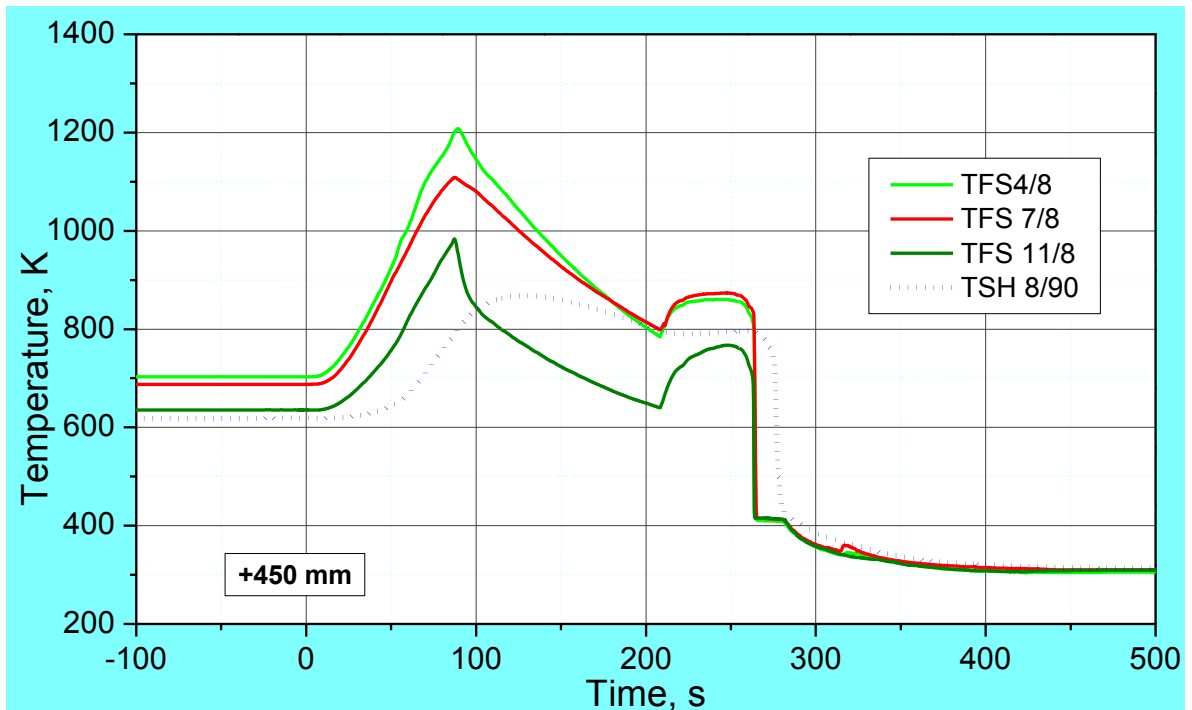


**Figure 29** QUENCH-L1; Temperatures measured by rod cladding (TFS) and shroud (TSH 8/90) thermocouples at 450 mm elevation.

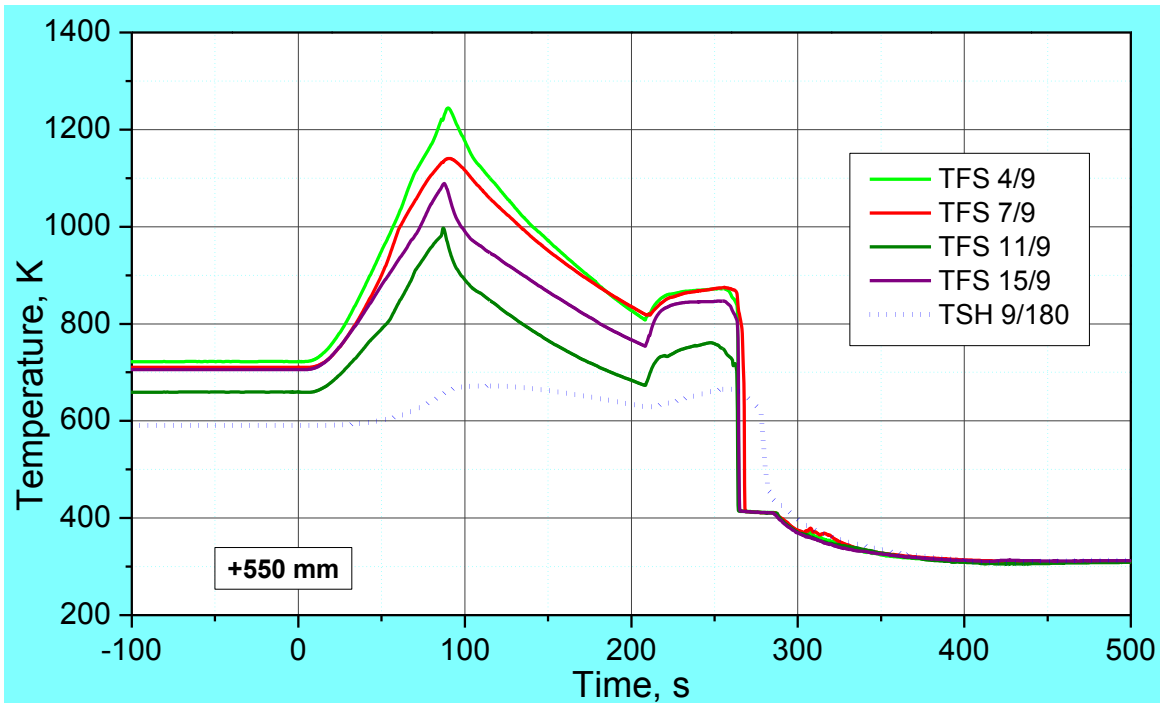


**Figure 30** QUENCH-L1; Temperatures measured by rod cladding (TFS) and shroud (TSH 9/180) thermocouples at 550 mm elevation.

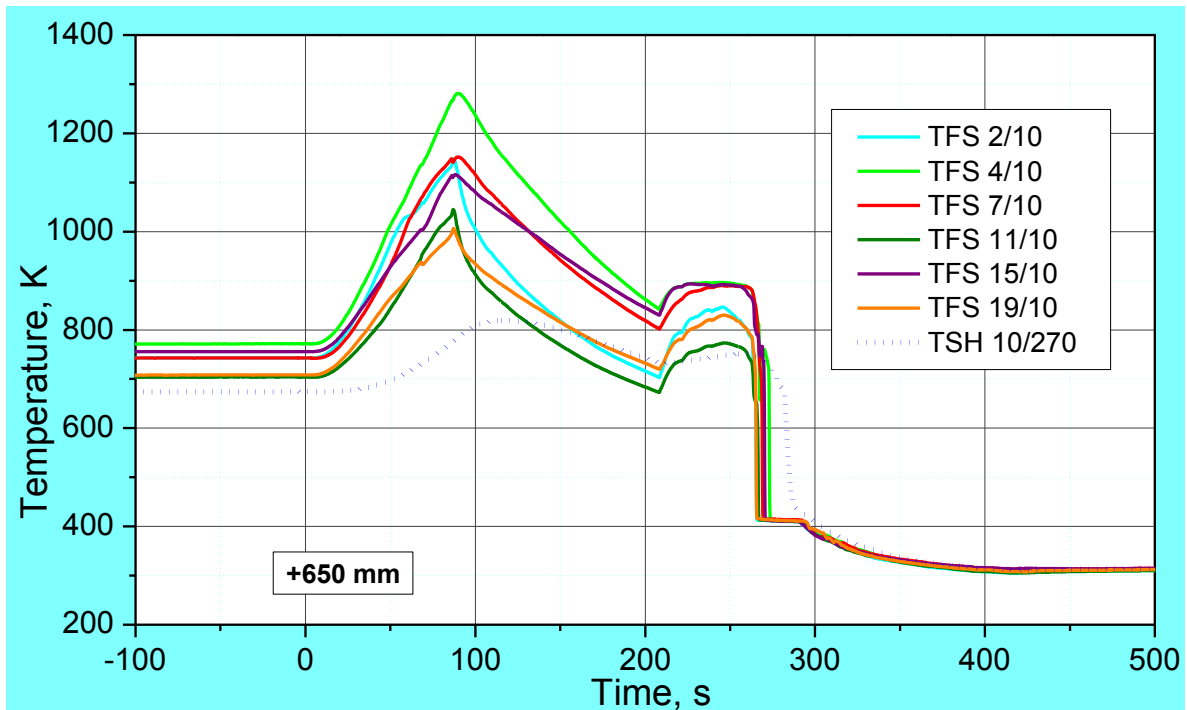


**Figure 31** QUENCH-L1; Temperatures measured by rod cladding (TFS) and shroud (TSH 10/270) thermocouples at 650 mm elevation.

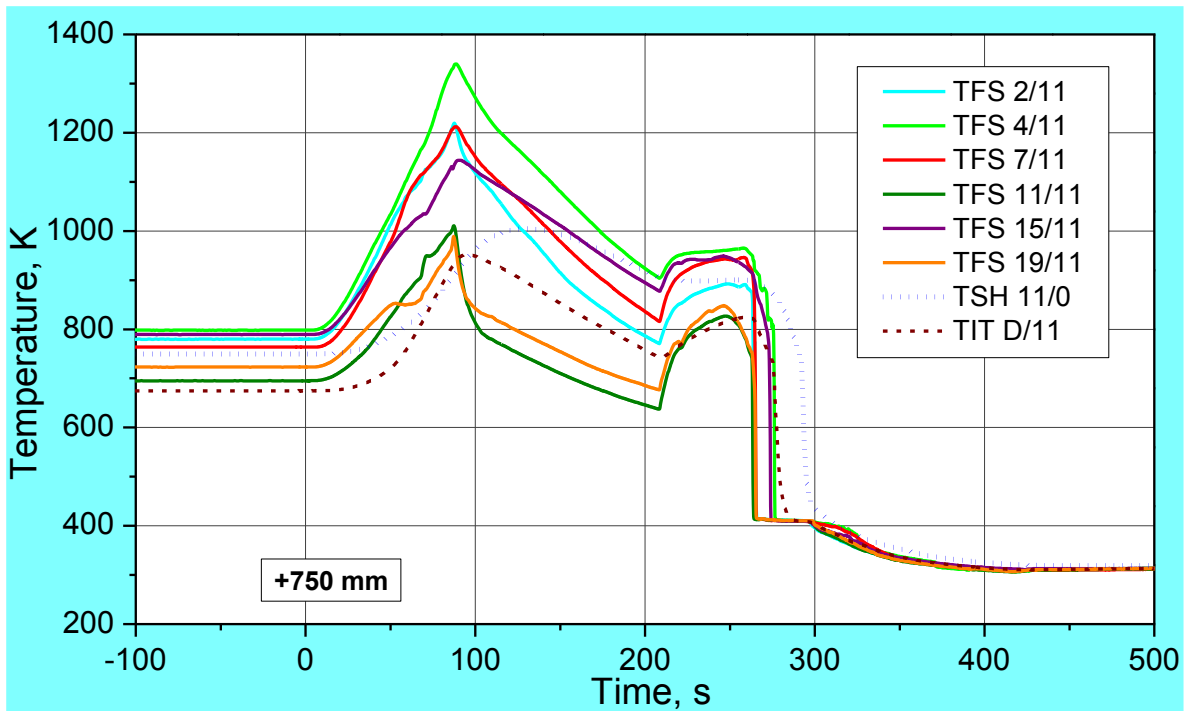


**Figure 32** QUENCH-L1; Temperatures measured by rod cladding (TFS) and shroud (TSH 11/0), and corner rod internal (TIT D/11) thermocouples at 750 mm elevation.

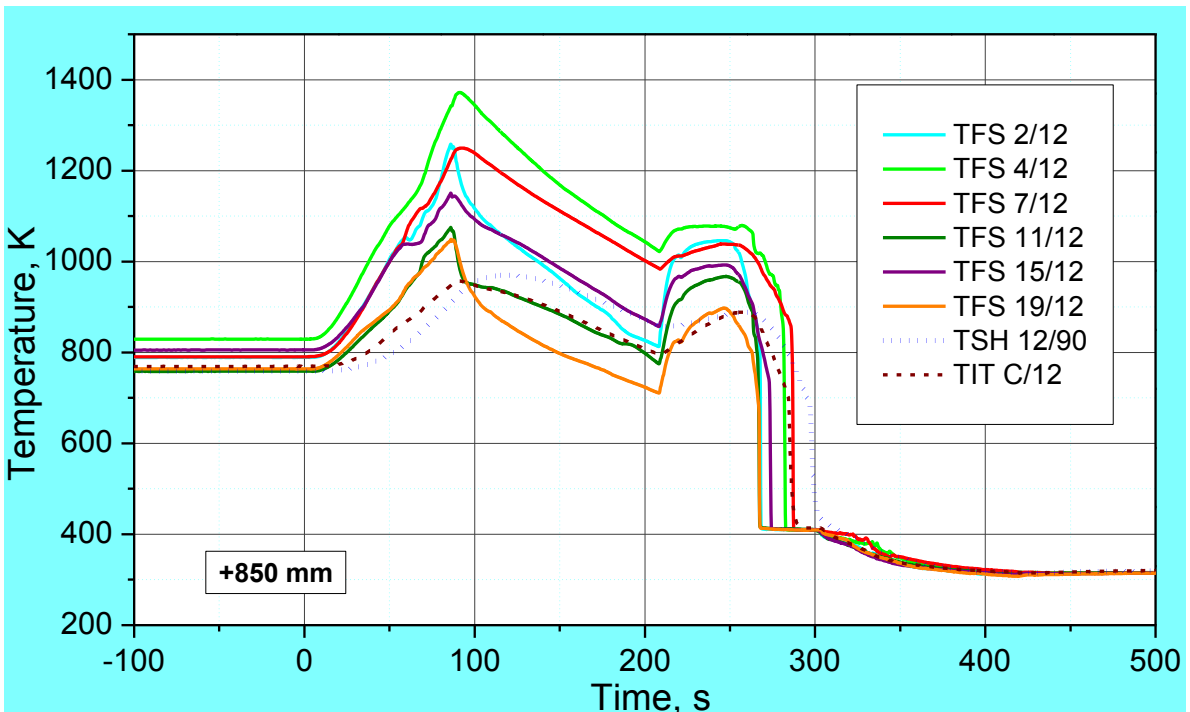


**Figure 33** QUENCH-L1; Temperatures measured by rod cladding (TFS) and shroud (TSH 12/90), and corner rod internal (TIT C/12) thermocouples at 850 mm elevation.

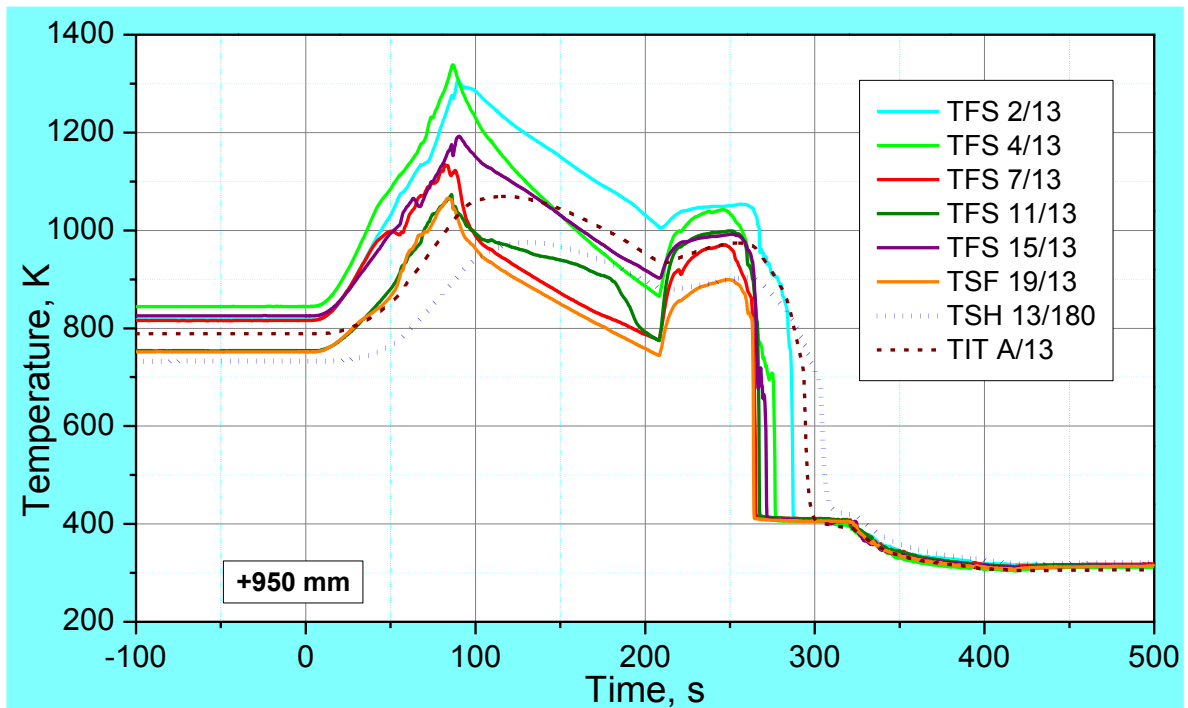


**Figure 34** QUENCH-L1; Temperatures measured by rod cladding (TFS) and shroud (TSH 13/90), and corner rod internal (TIT A/13) thermocouples at 950 mm elevation.

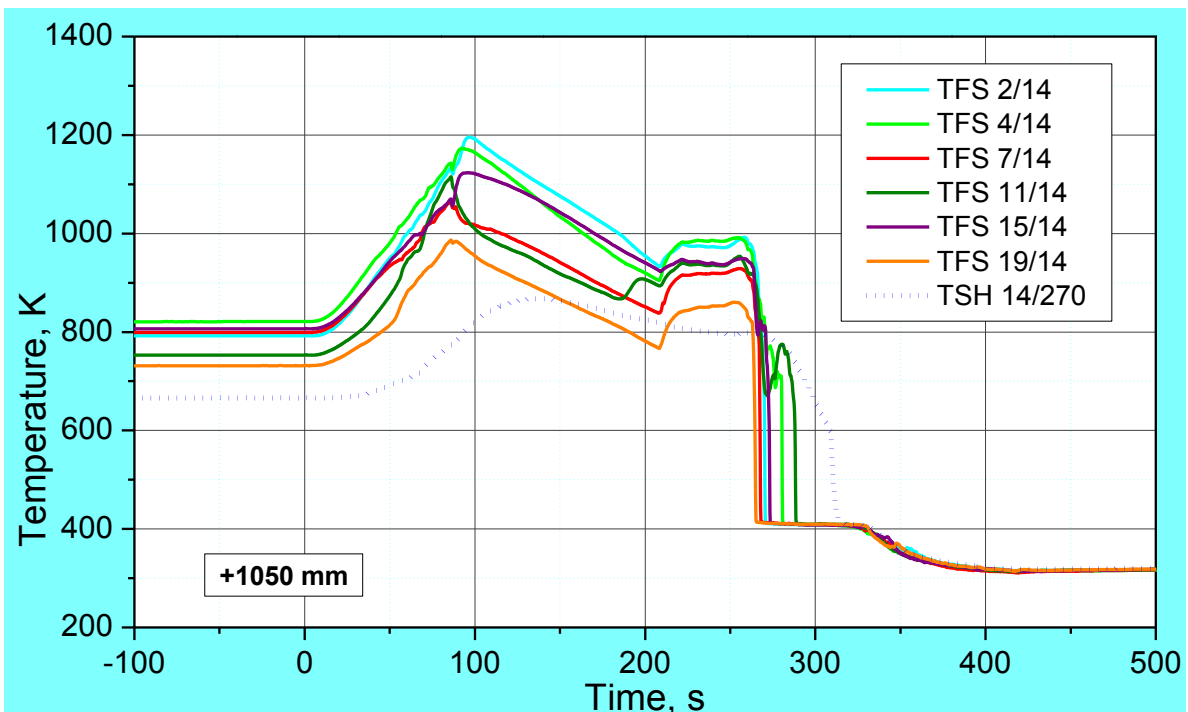


**Figure 35** QUENCH-L1; Temperatures measured by rod cladding (TFS) and shroud (TSH 14/270) thermocouples at 1050 mm elevation.

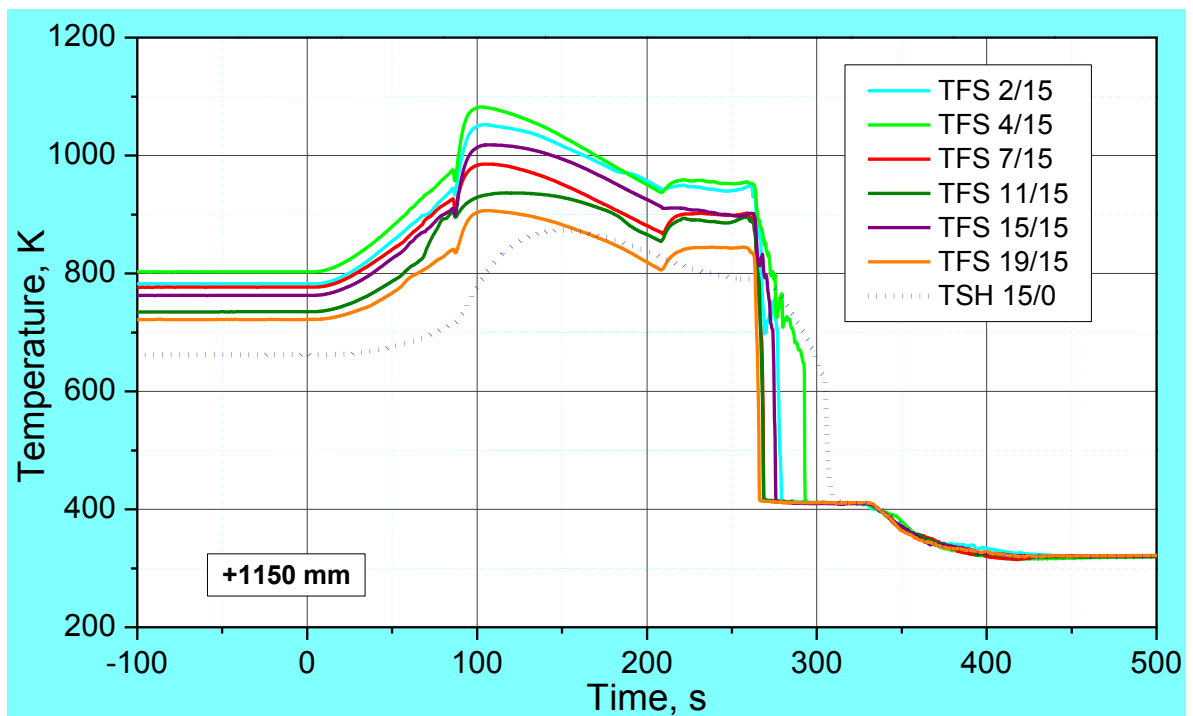


**Figure 36** QUENCH-L1; Temperatures measured by rod cladding (TFS) and shroud (TSH 15/0) thermocouples at 1150 mm elevation.

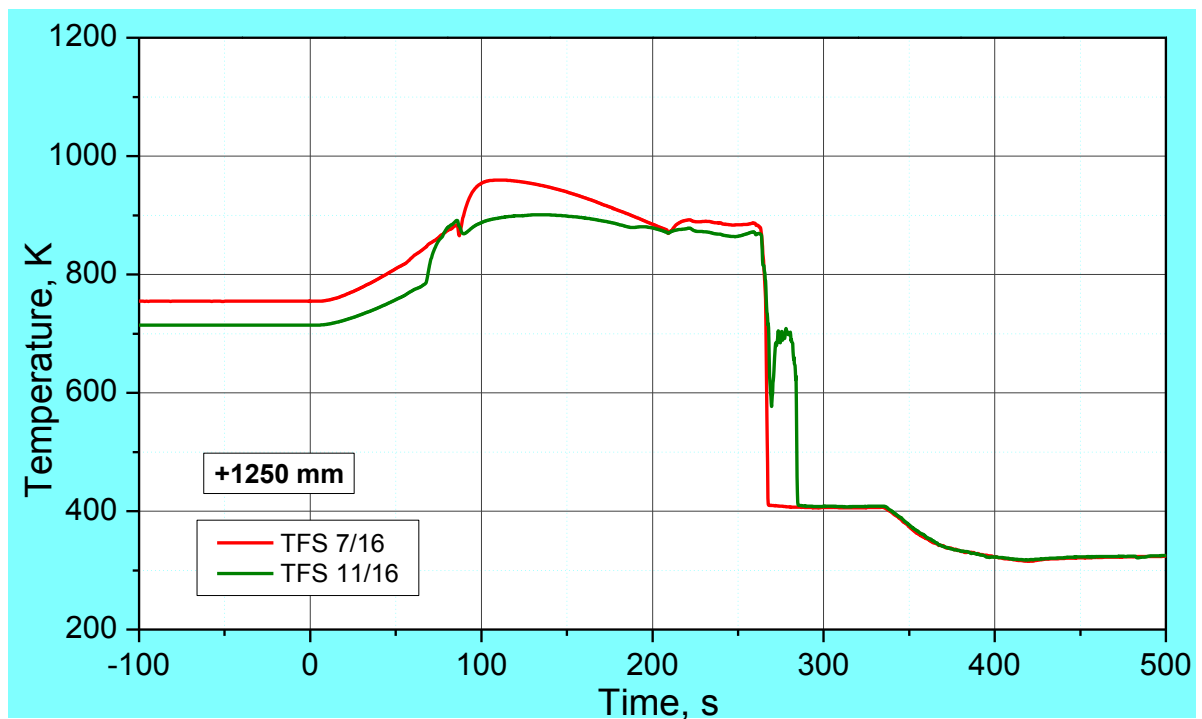


**Figure 37** QUENCH-L1; Temperatures measured by rod cladding (TFS) thermocouples at 1250 mm elevation.

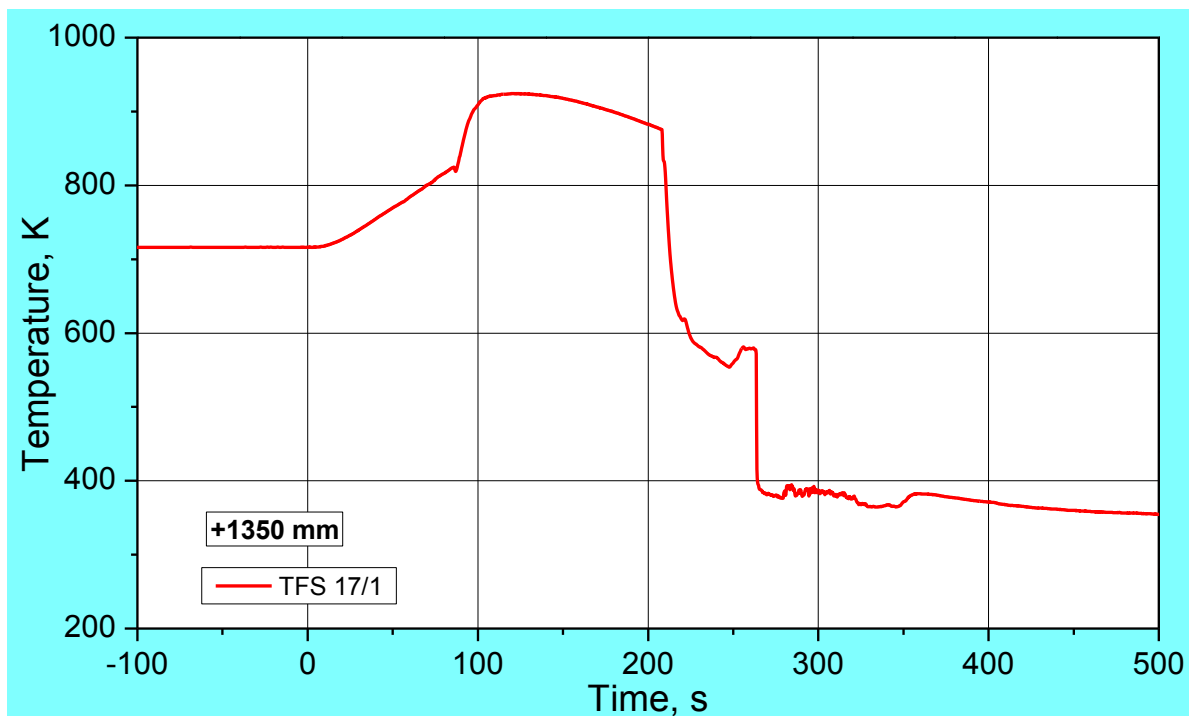


**Figure 38** QUENCH-L1; Temperatures measured by rod cladding (TFS 7/17) thermocouple at 1350 mm elevation.

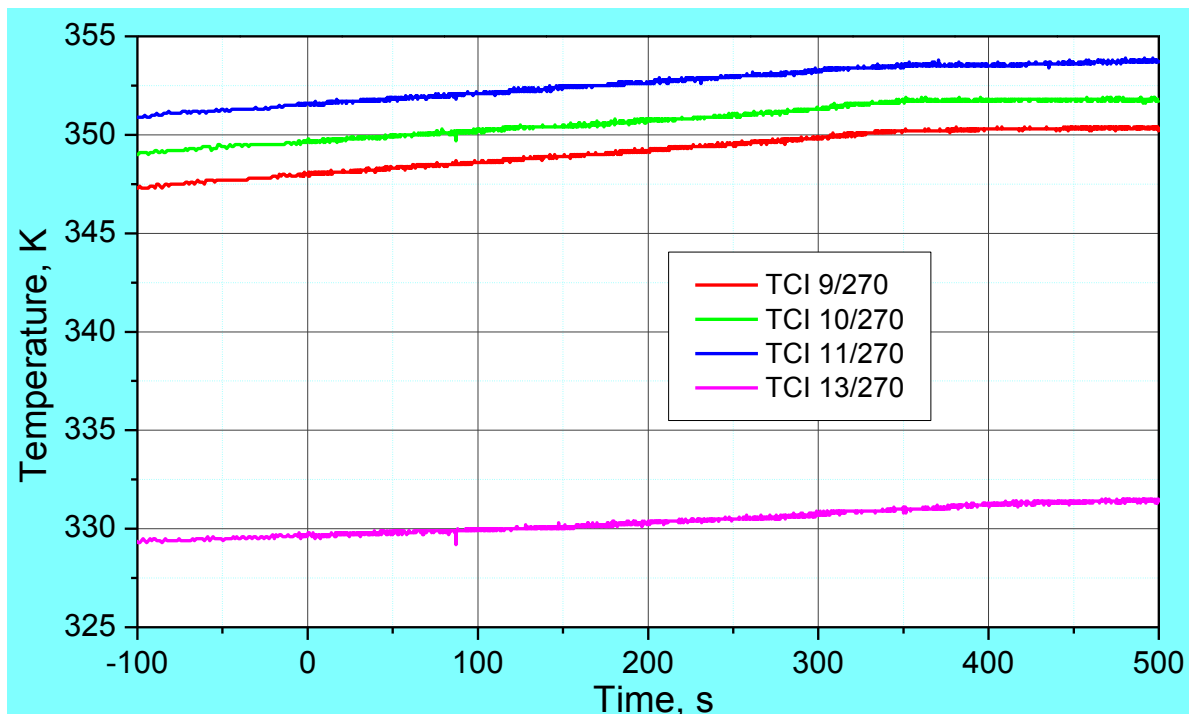


**Figure 39** QUENCH-L1; Overview of the TCI (inner cooling jacket).

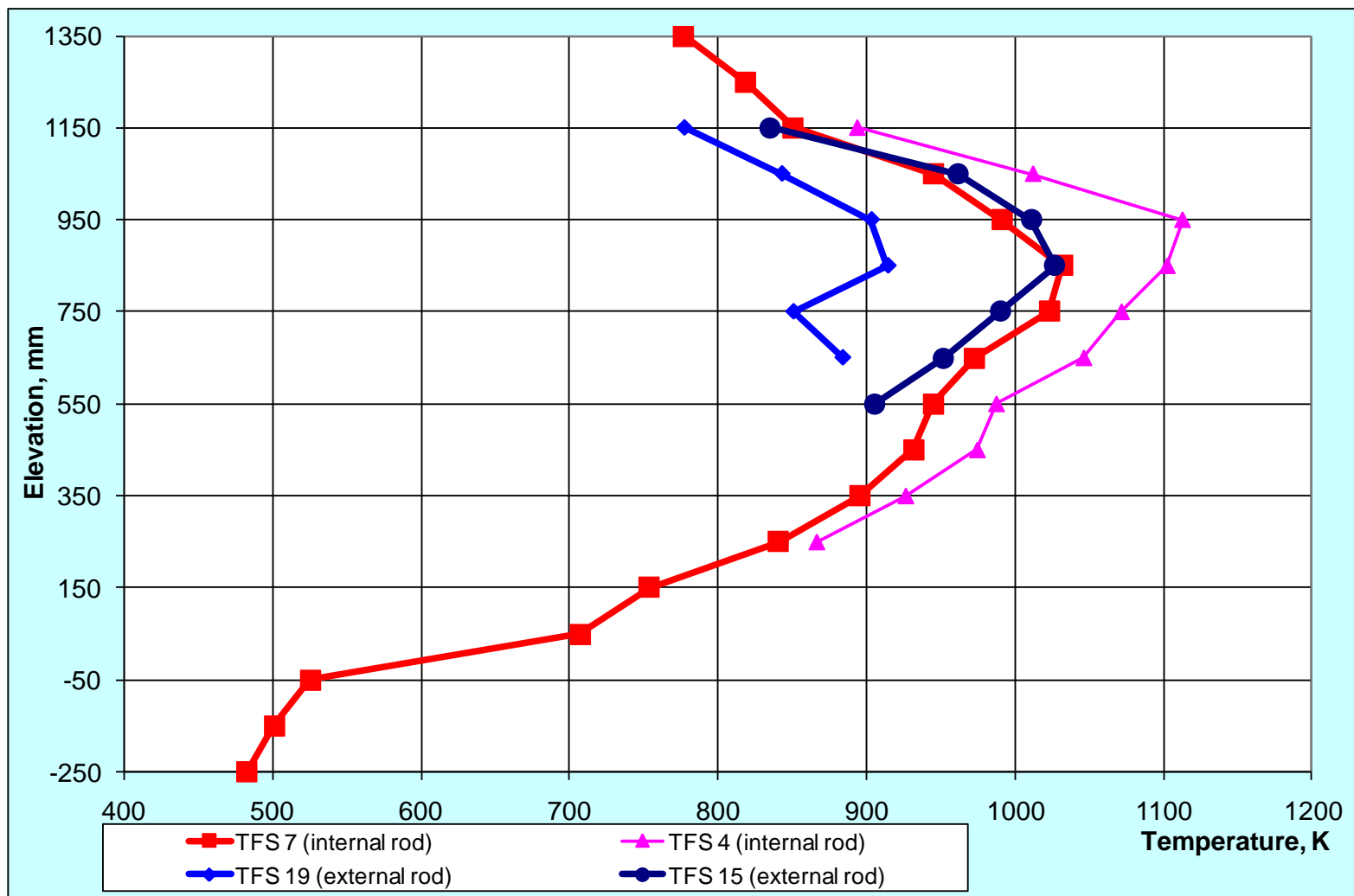


**Figure 40** QUENCH-L1; Axial and radial temperature distribution on time of the first burst case for selected rods.

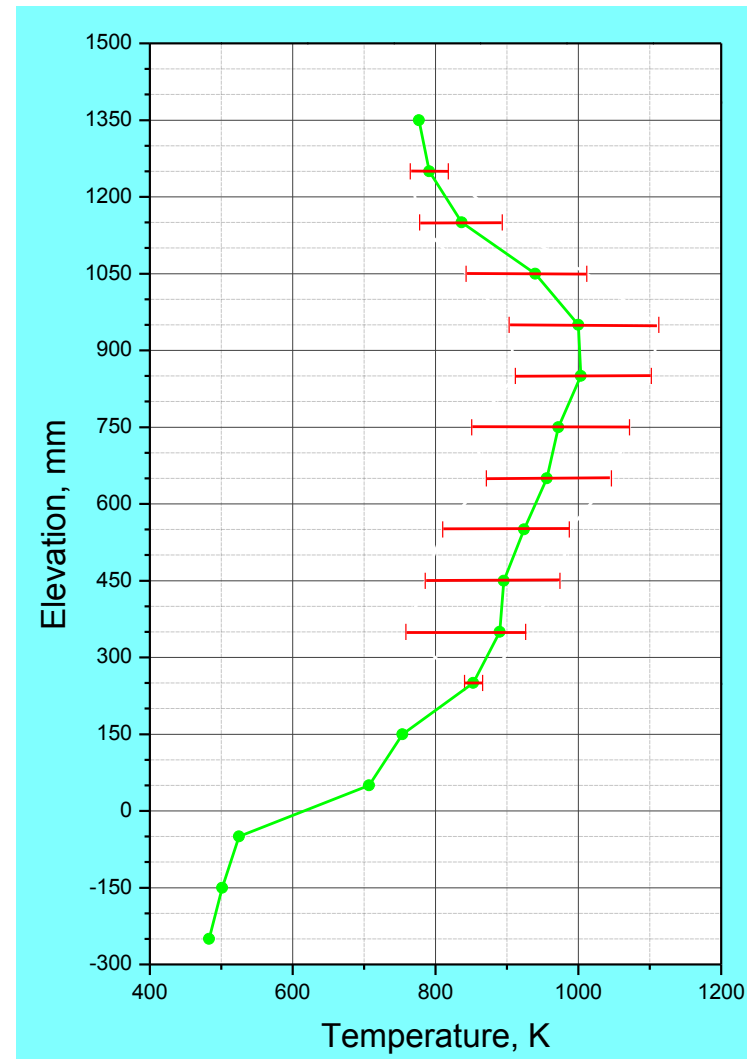
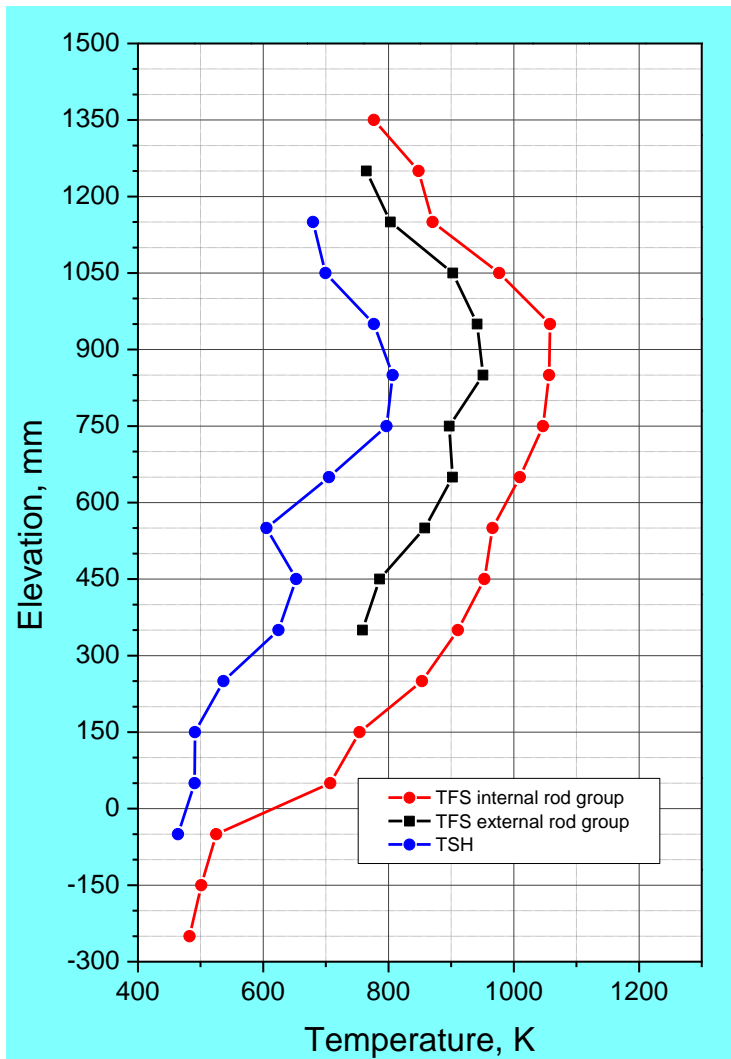


**Figure 41** QUENCH-L1; Axial temperature profile TFS internal and external rod group together with TSH, left, and axial temperature profile of all TFS, right, at 55.2 s (first cladding burst).



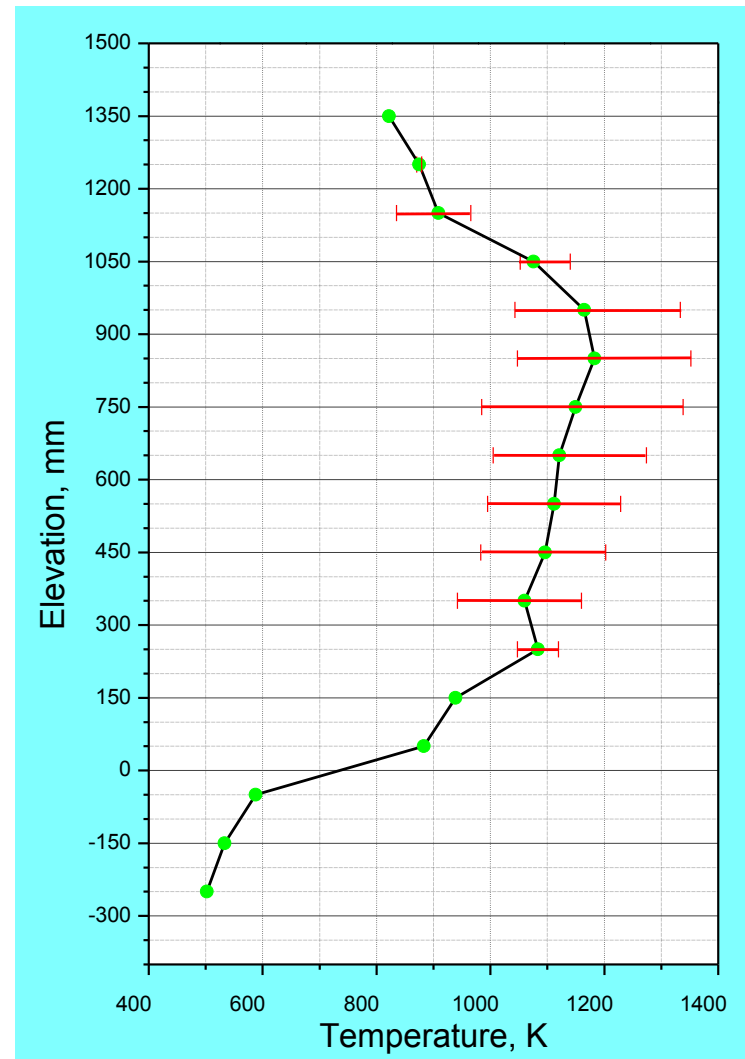
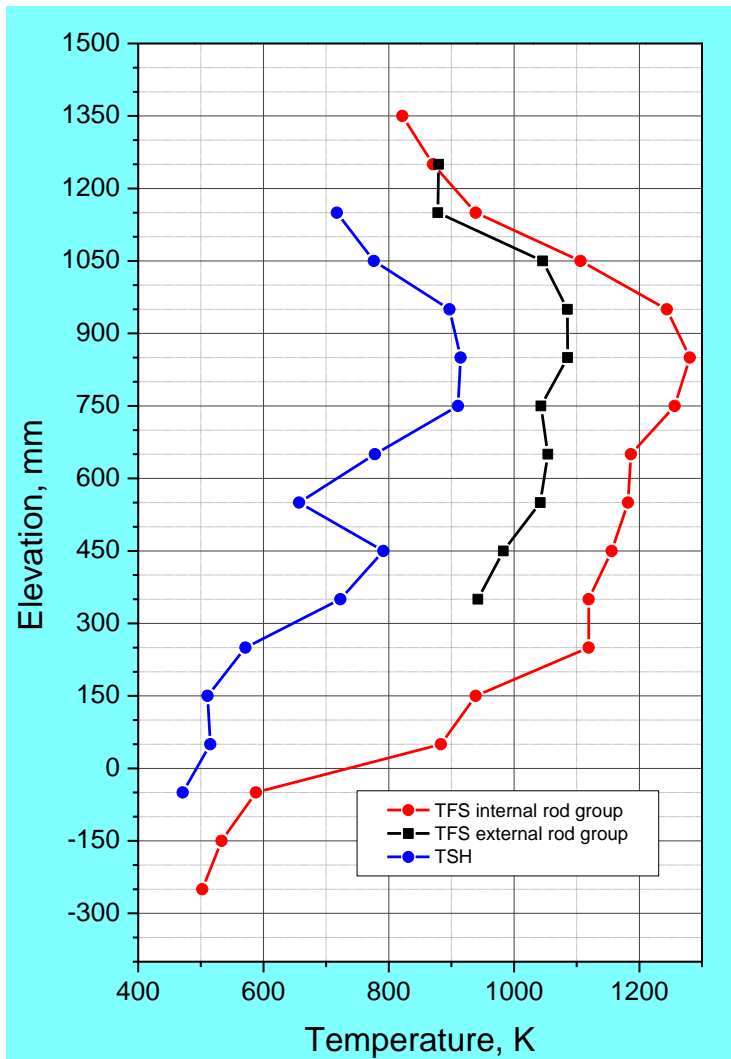


**Figure 42** QUENCH-L1; Axial temperature profile TFS internal and external rod group together with TSH, left, and axial temperature profile of all TFS, right, at 87.6 (last cladding burst).

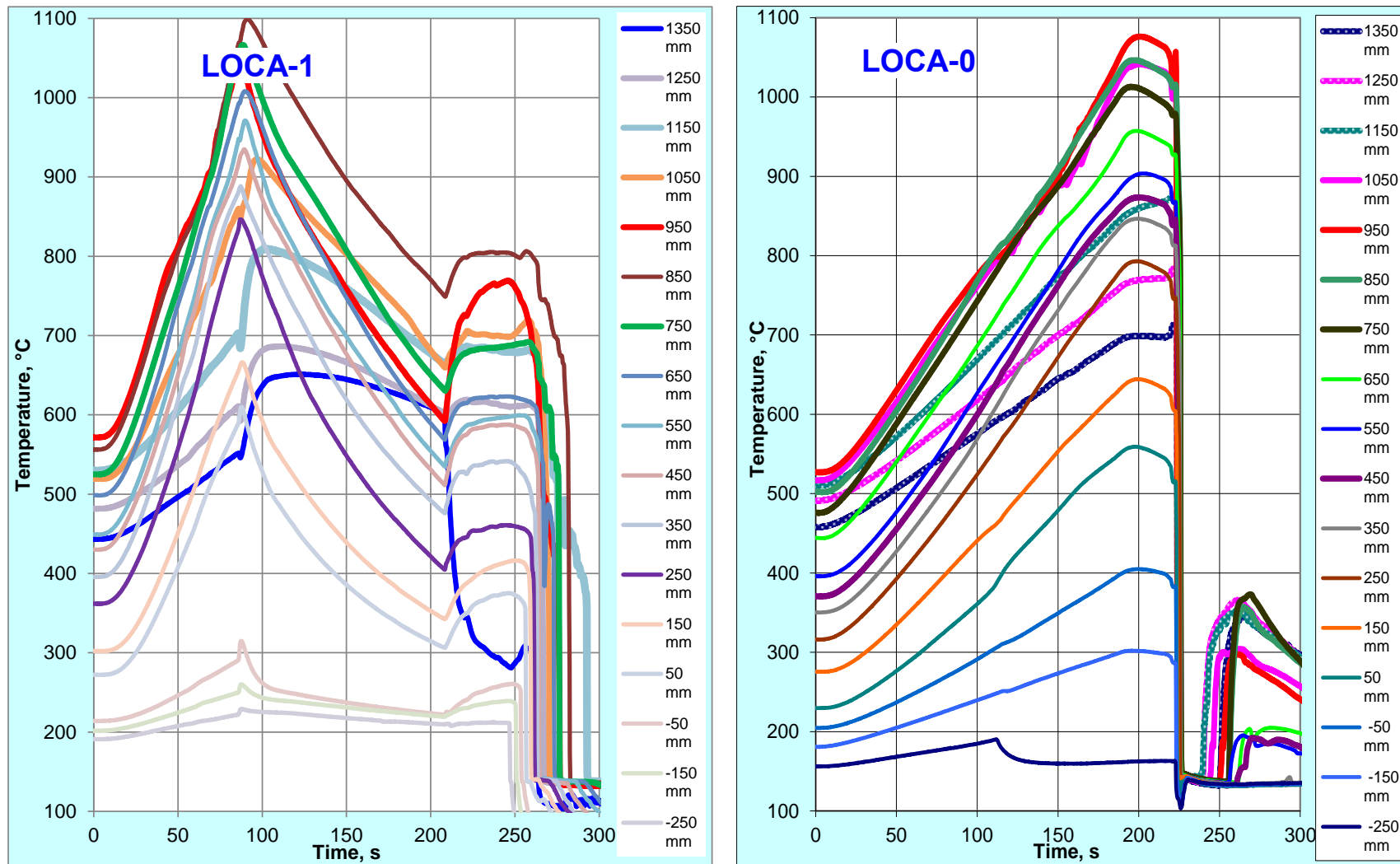


**Figure 43** Comparison of maximal cladding temperatures at different elevations for QUENCH-L0 and -L1.

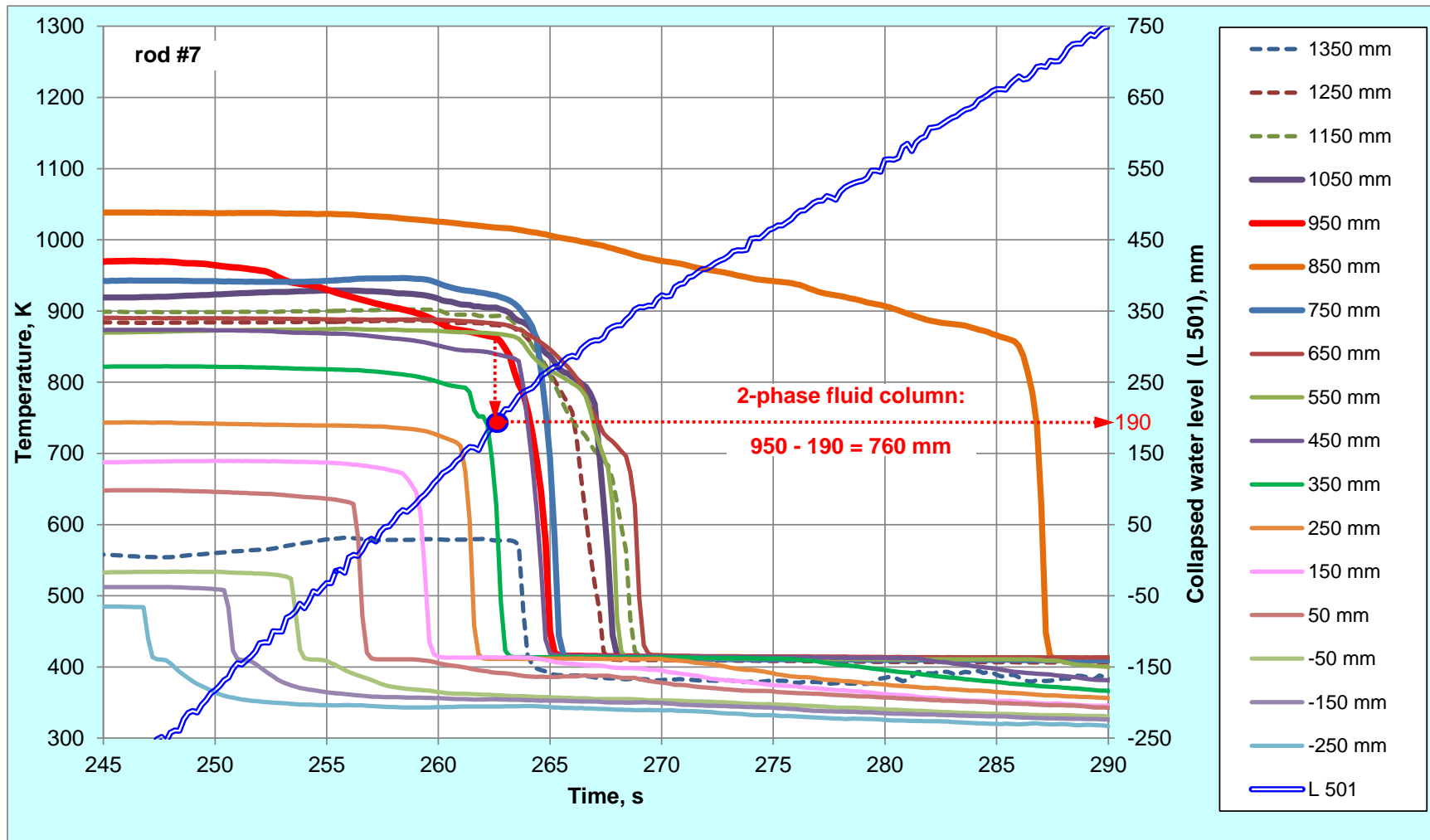
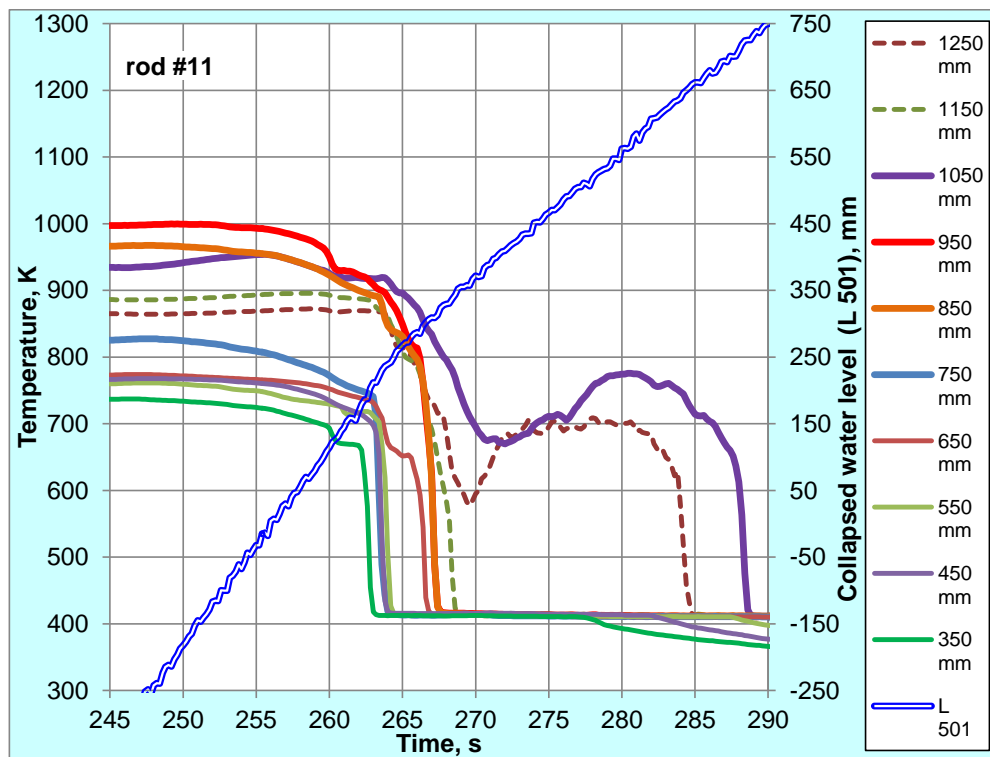
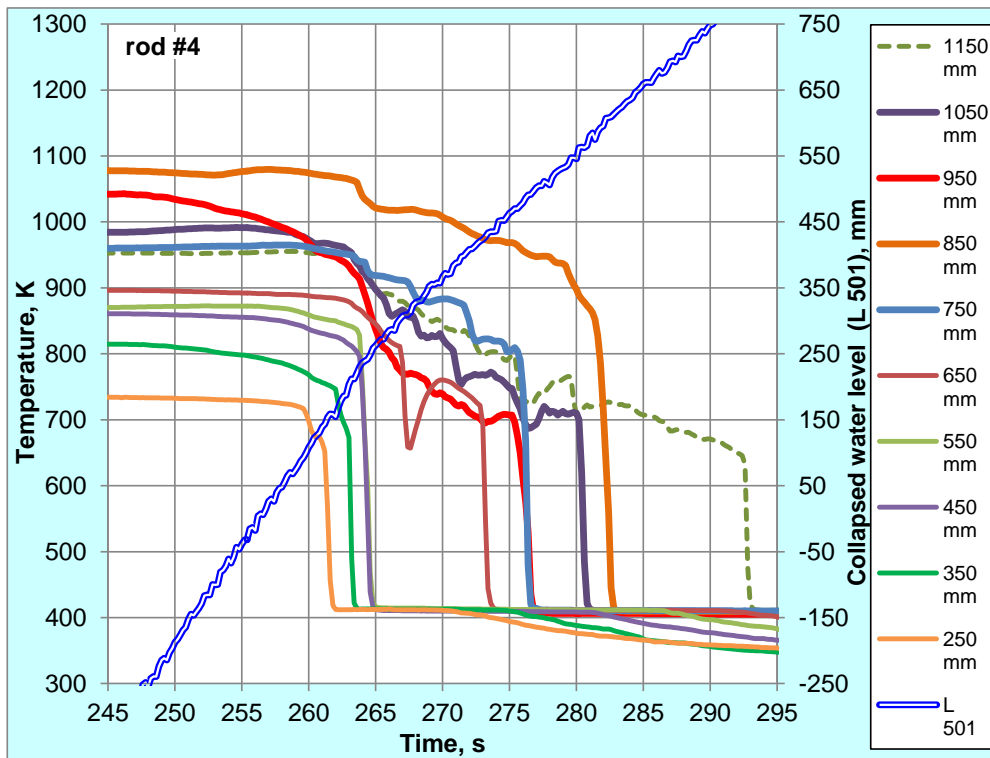


Figure 44 QUENCH-L1; Sequence of thermocouple wetting of rod #7 by 2-phase fluid formed above collapsed water front.



**Figure 45** QUENCH-L1; Sequence of thermocouple wetting of rods #4 and #11 by 2-phase fluid formed above collapsed water front.

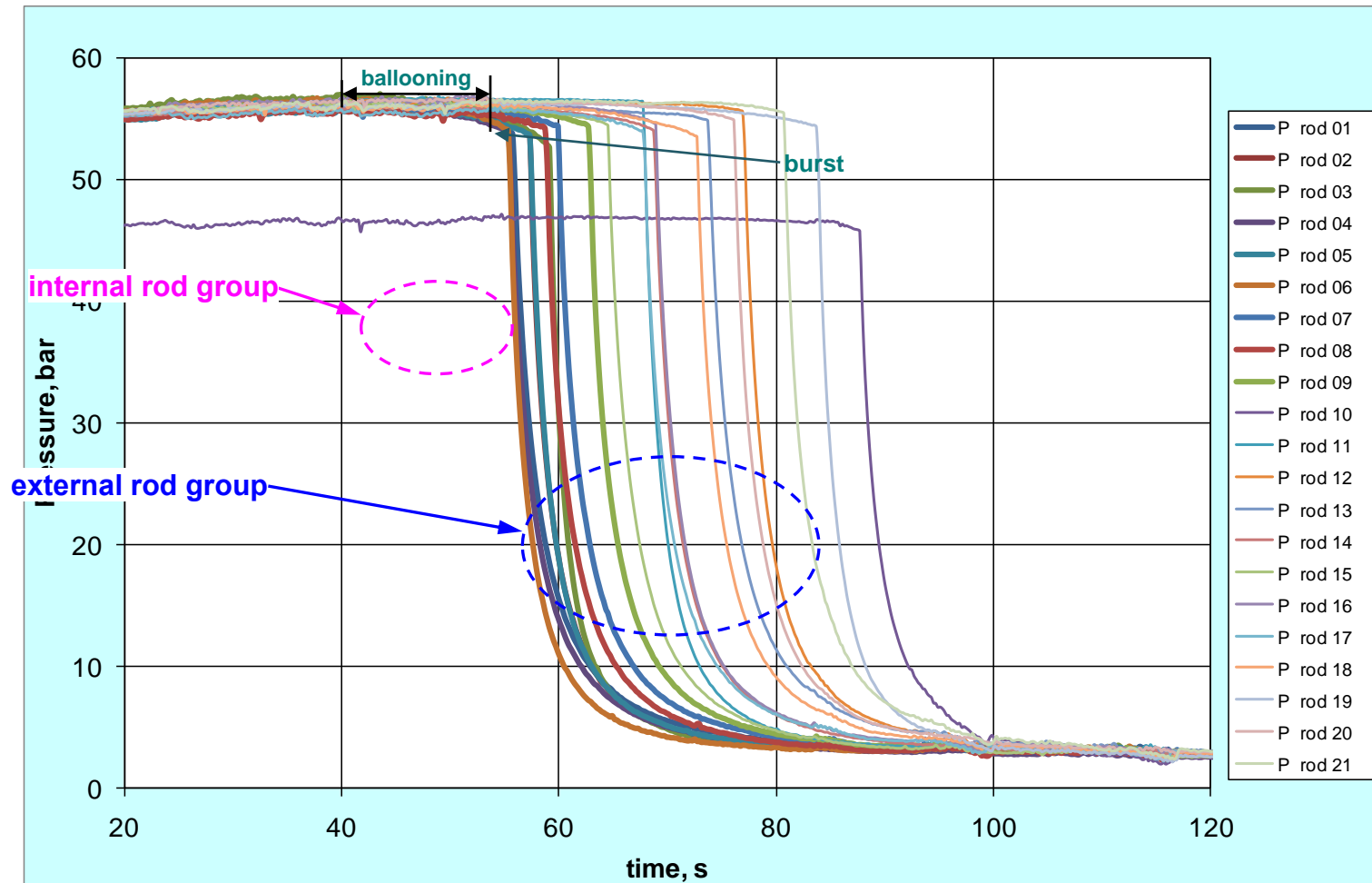


Figure 46 QUENCH-L1; Pressure changing during heating phase; ballooning and burst.

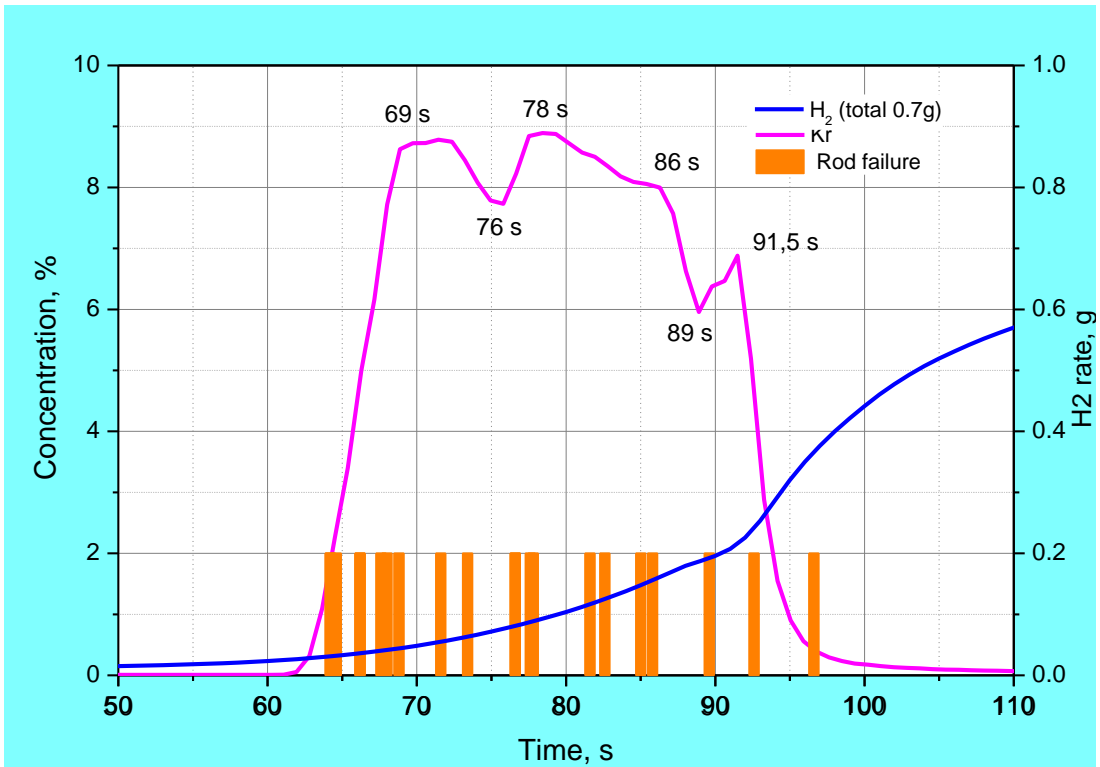


Figure 47 a QUENCH-L1; Mass spectrometer measurements: integral hydrogen release and krypton as burst indicator.

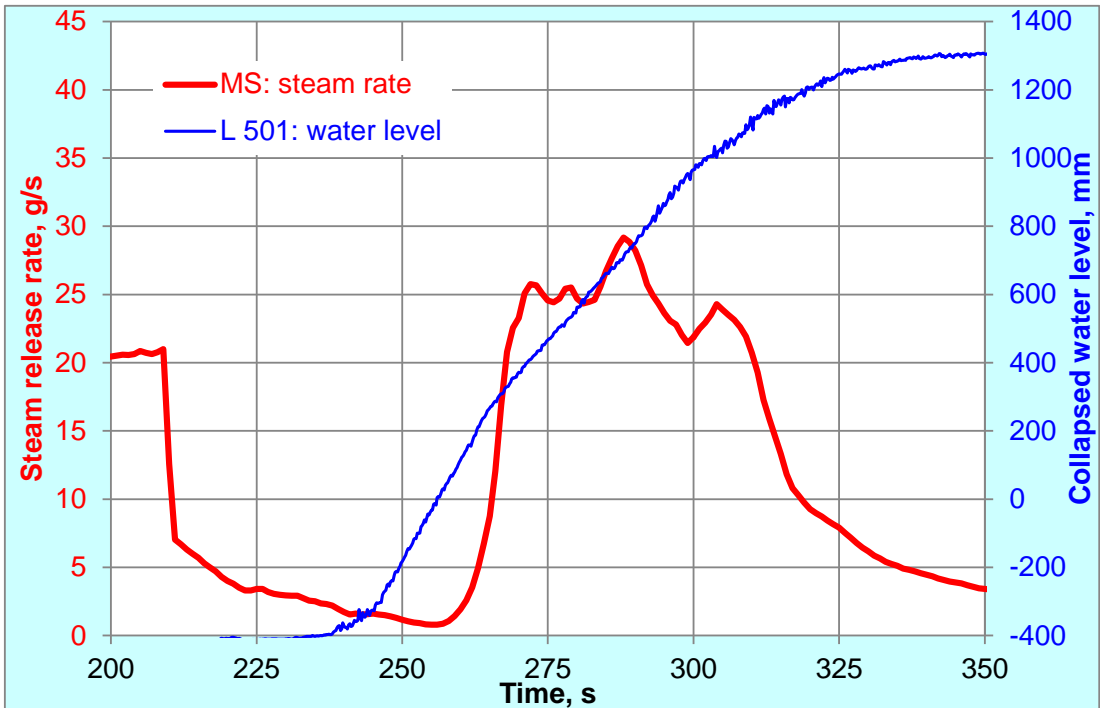


Figure 47 b QUENCH-L1; Mass spectrometer measurements: steam release during reflood.



0°



90°



180°



270°

**Figure 48** QUENCH-L1; Post-test bundle view between GS3 and GS4: buckled rods.



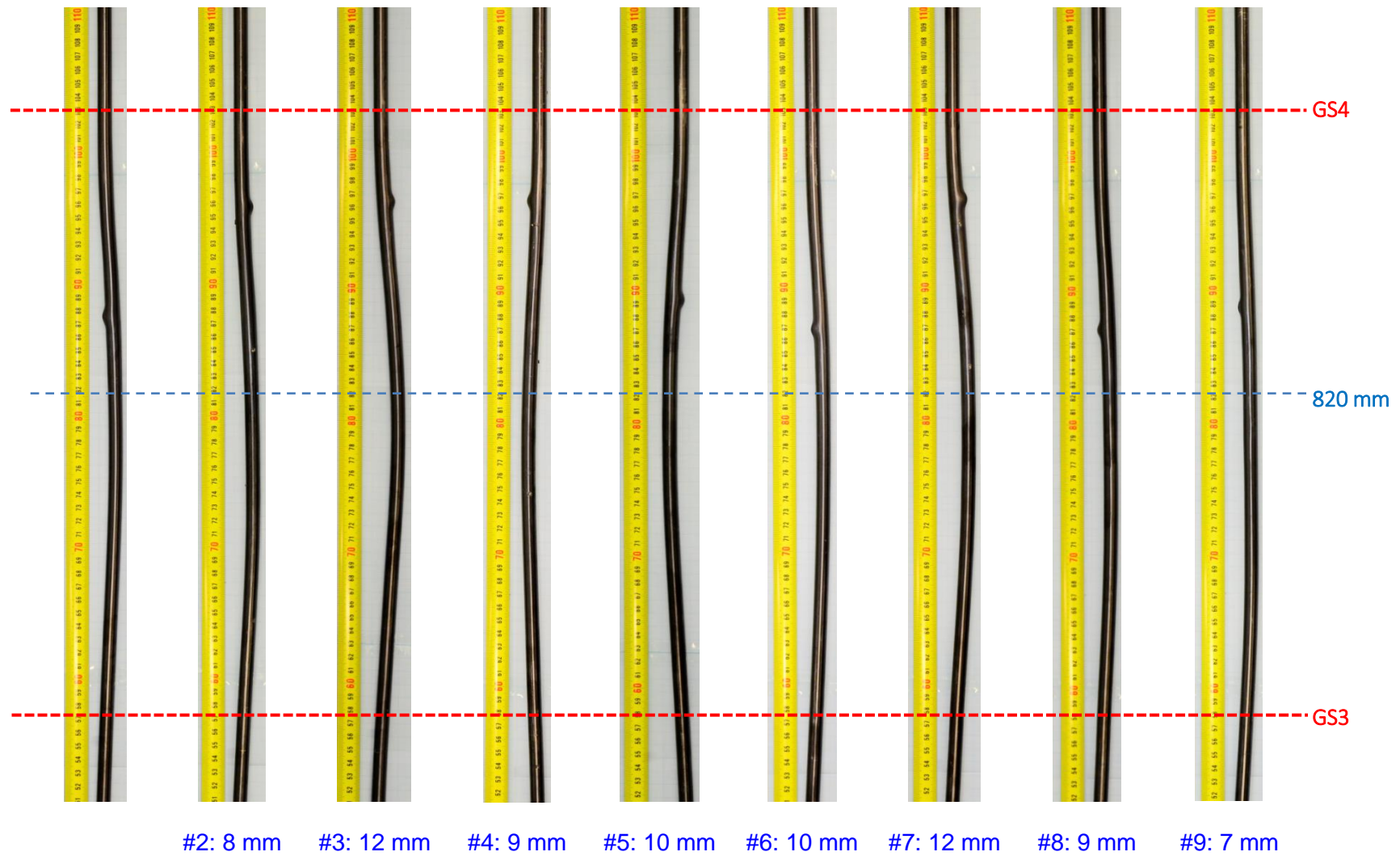


**Figure 49** QUENCH-L1; Bending of central rods with indication of maximal bending for each rod.



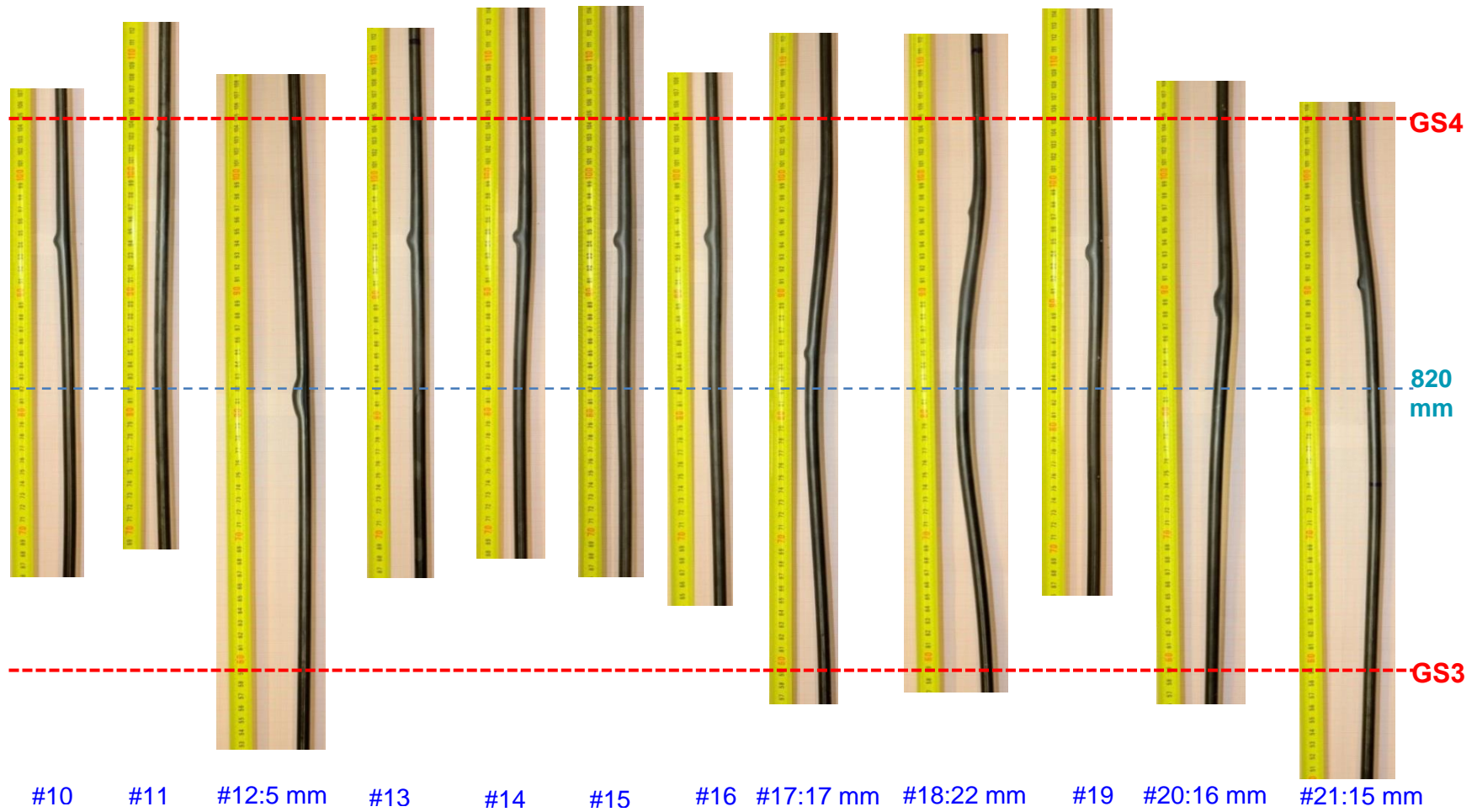


**Figure 50** QUENCH-L1; Bending of periphery rods with indication of maximal bending values.

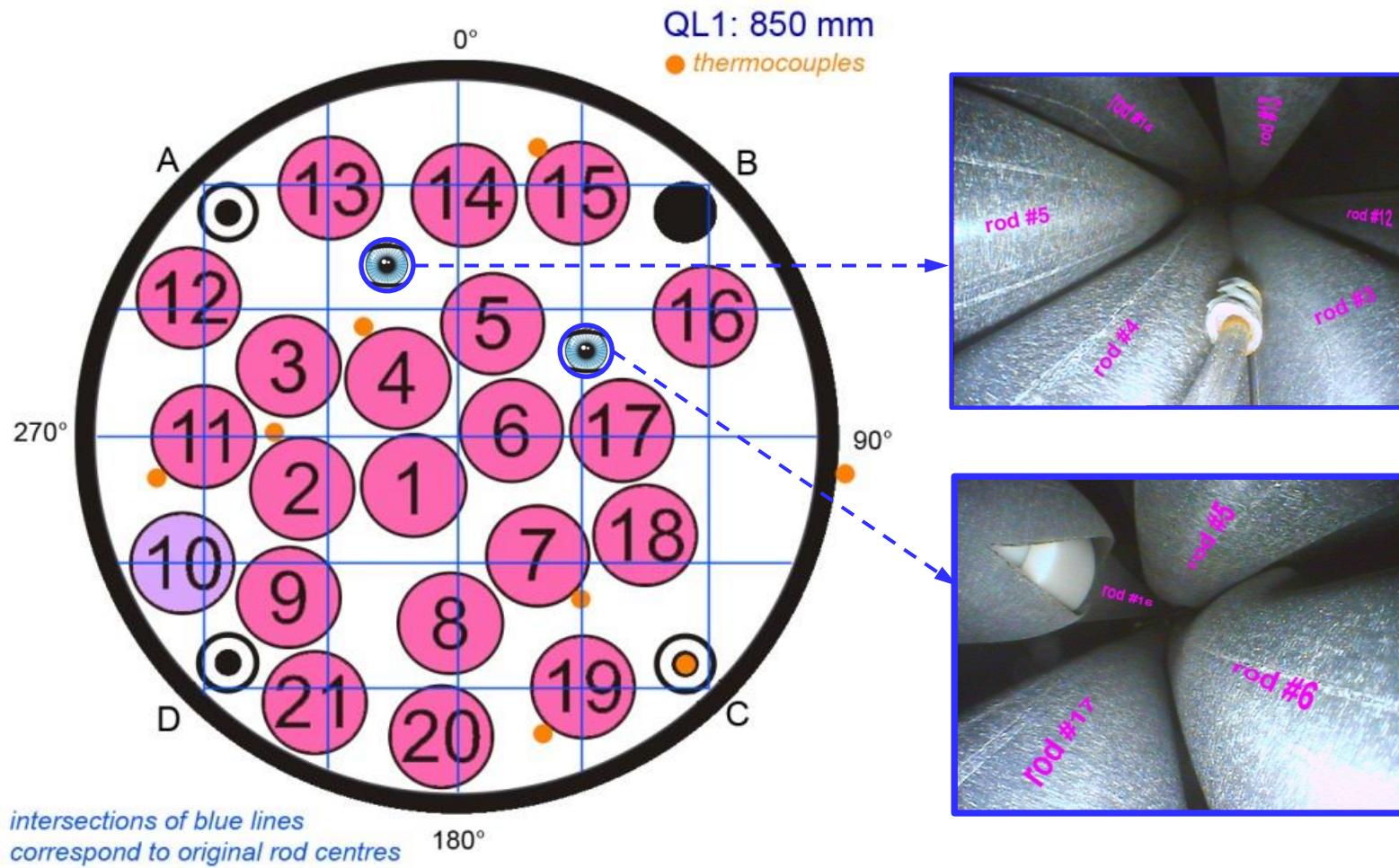


**Figure 51** QUENCH-L1; Estimation of rod positions near to middle elevation between two spacer grids (on the basis of videoscope observations).

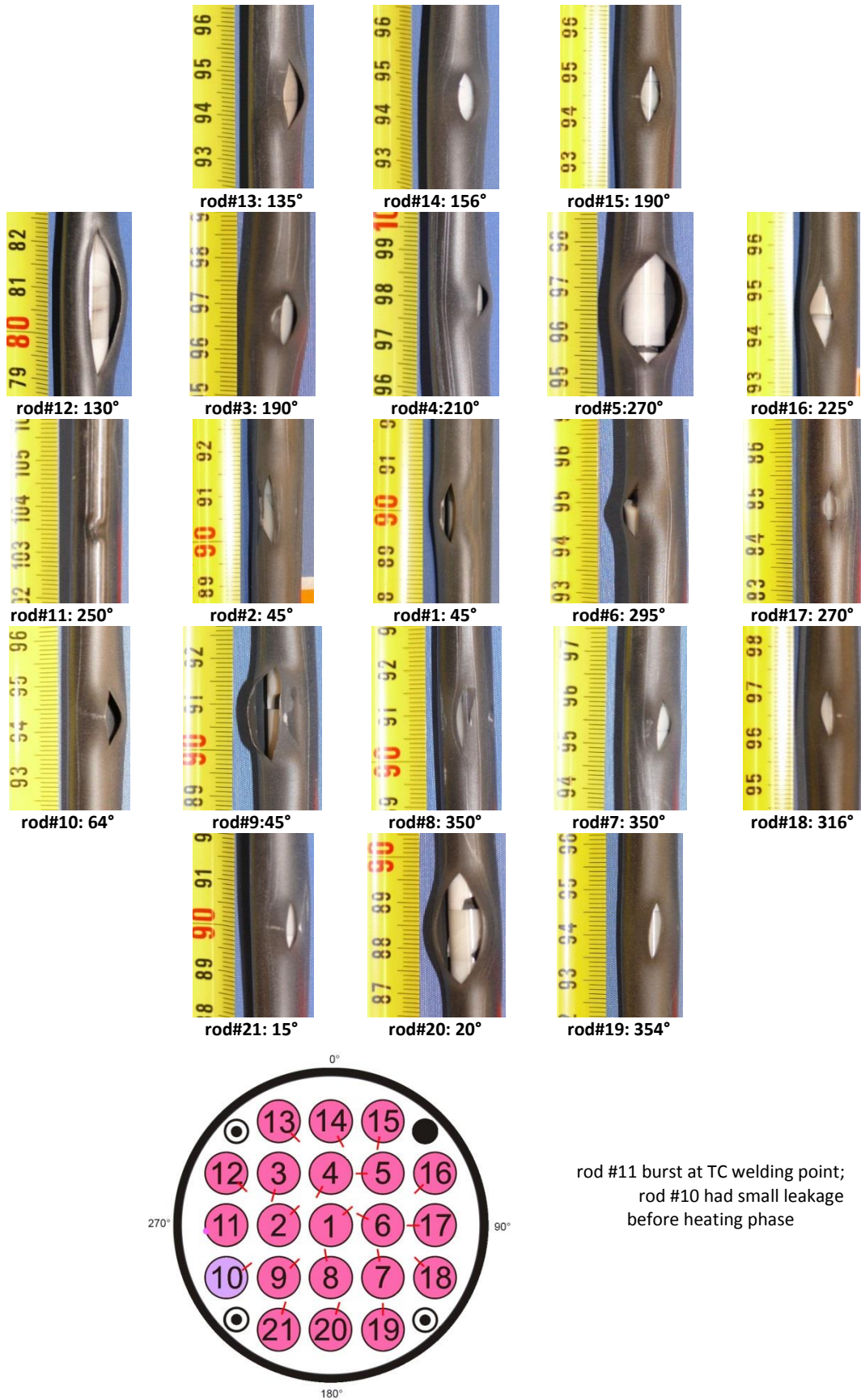
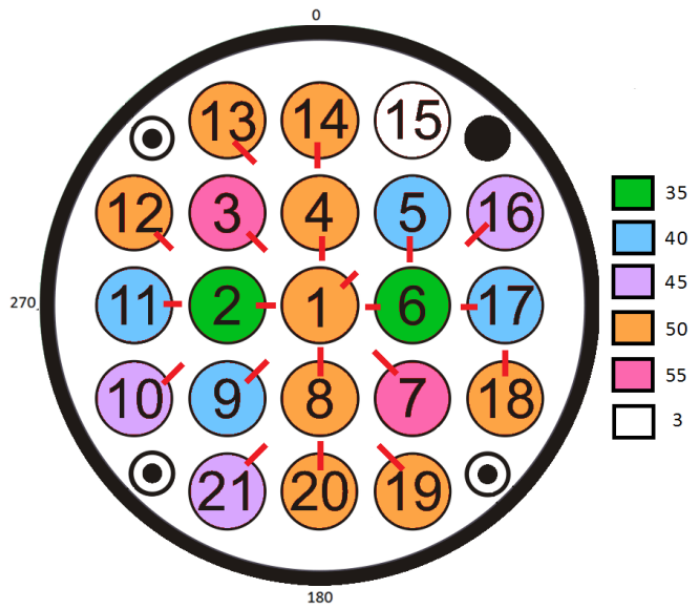
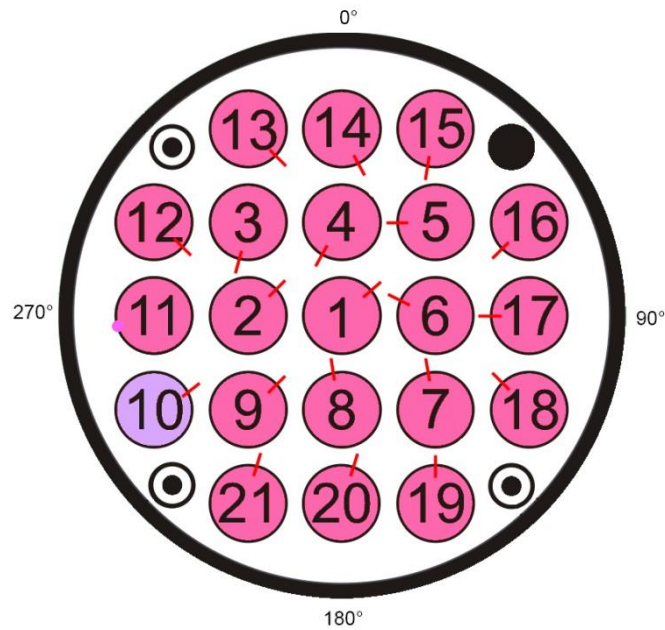


**Figure 52** QUENCH-L1; Axial and circumferential burst positions.





QUENCH-L0; Colours show values of different rod pressurisation in bar



QUENCH-L1; Pressure of rod #10 was about 46 bar before burst, for all other rods about 55 bar.

**Figure 53** QUENCH-L0 and -L1; Comparison of circumferential positions of bursts.

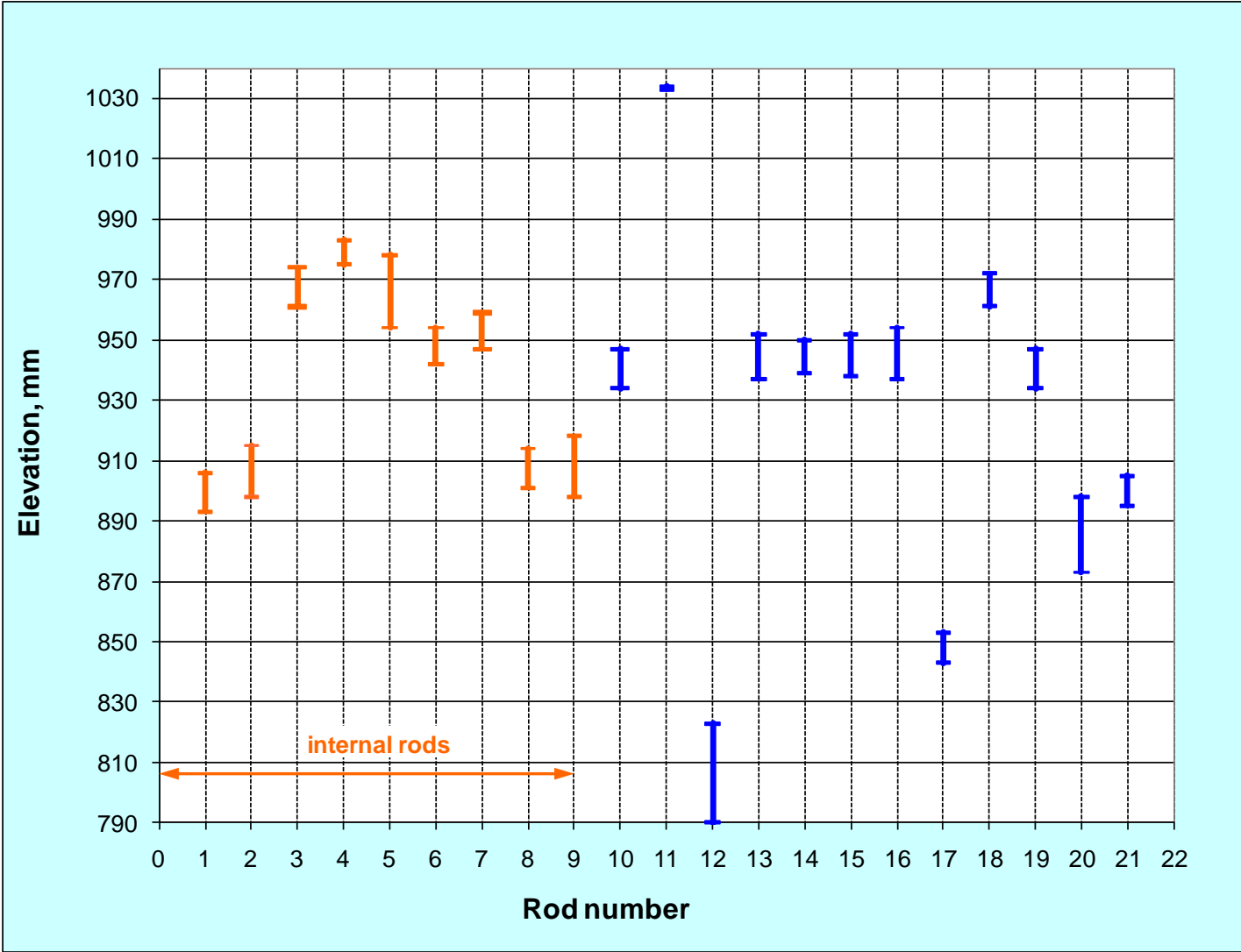
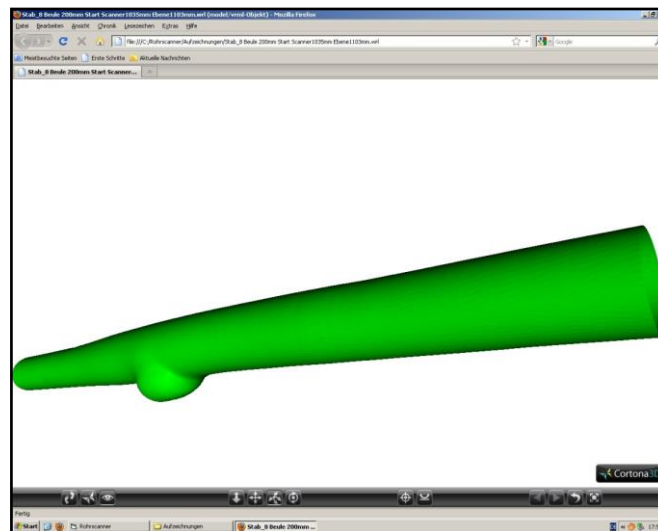


Figure 54 QUENCH-L1; Axial burst positions.



scanner facility



reconstructed scanned surface of rod #8:  
angle step 1°; axial step 0.5 mm; scanned length 200 mm

Figure 55 QUENCH-L1; Tube scanner laser profilometry.

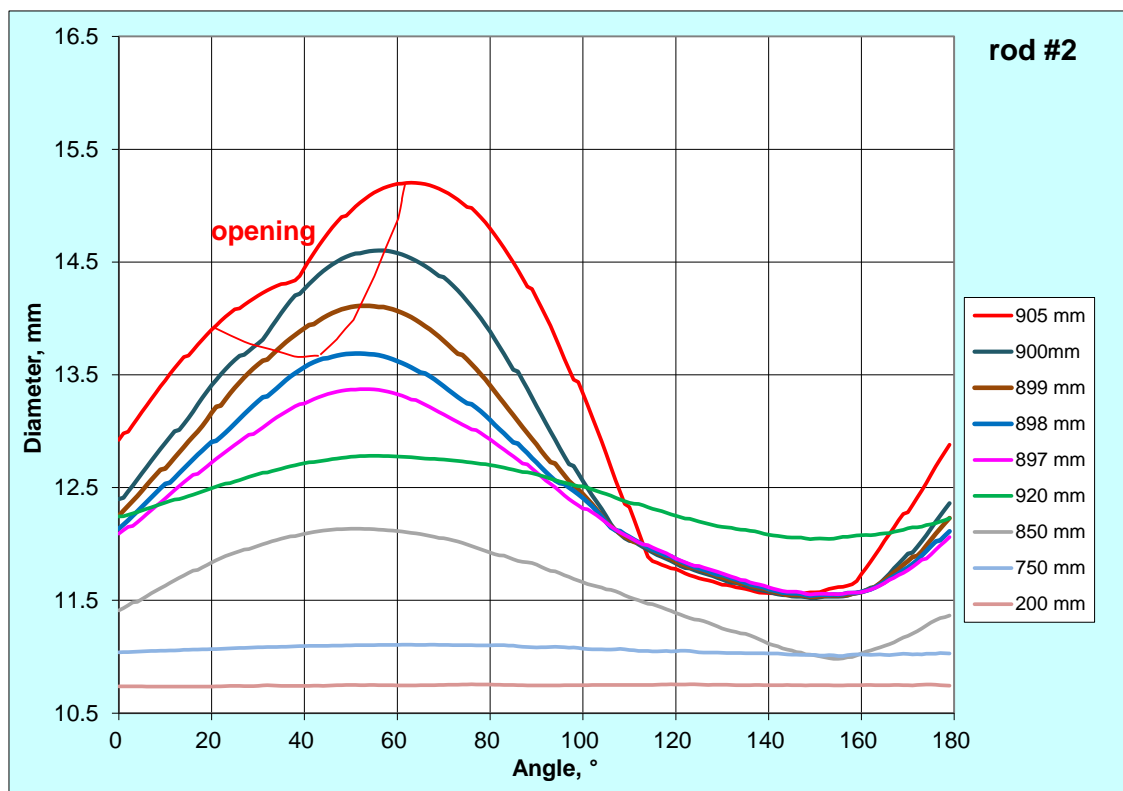
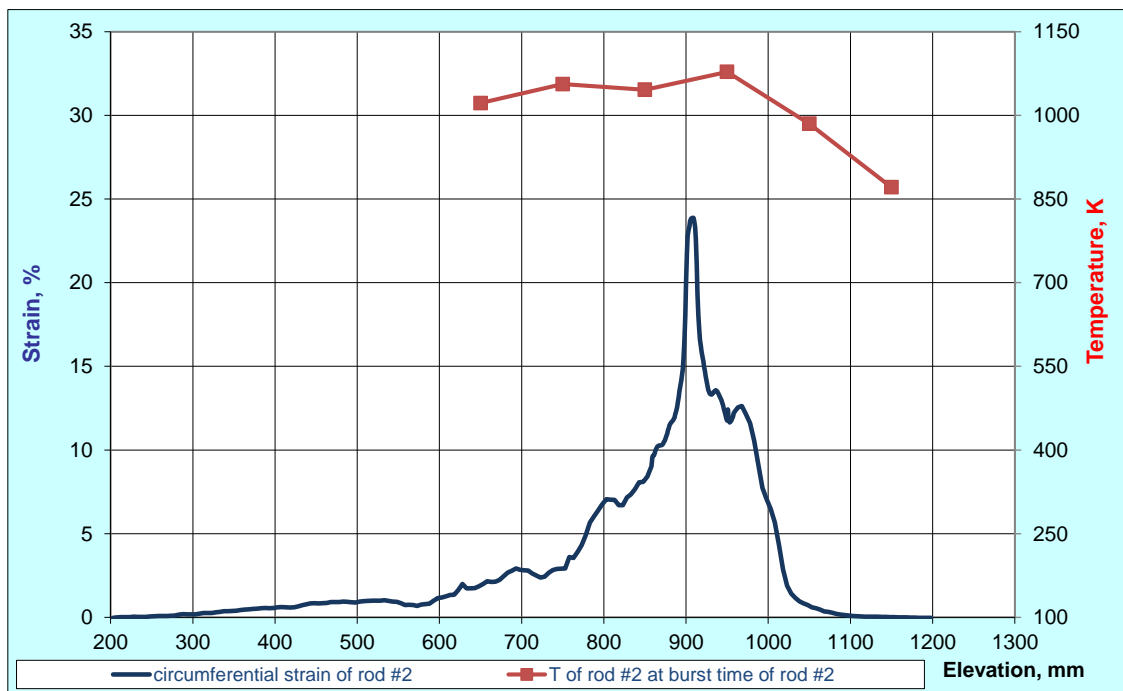


**Figure 56** QUENCH-L1, Rod #2; longitudinal circumferential strain changing (top); azimuthal diameter changing downwards from burst (bottom).

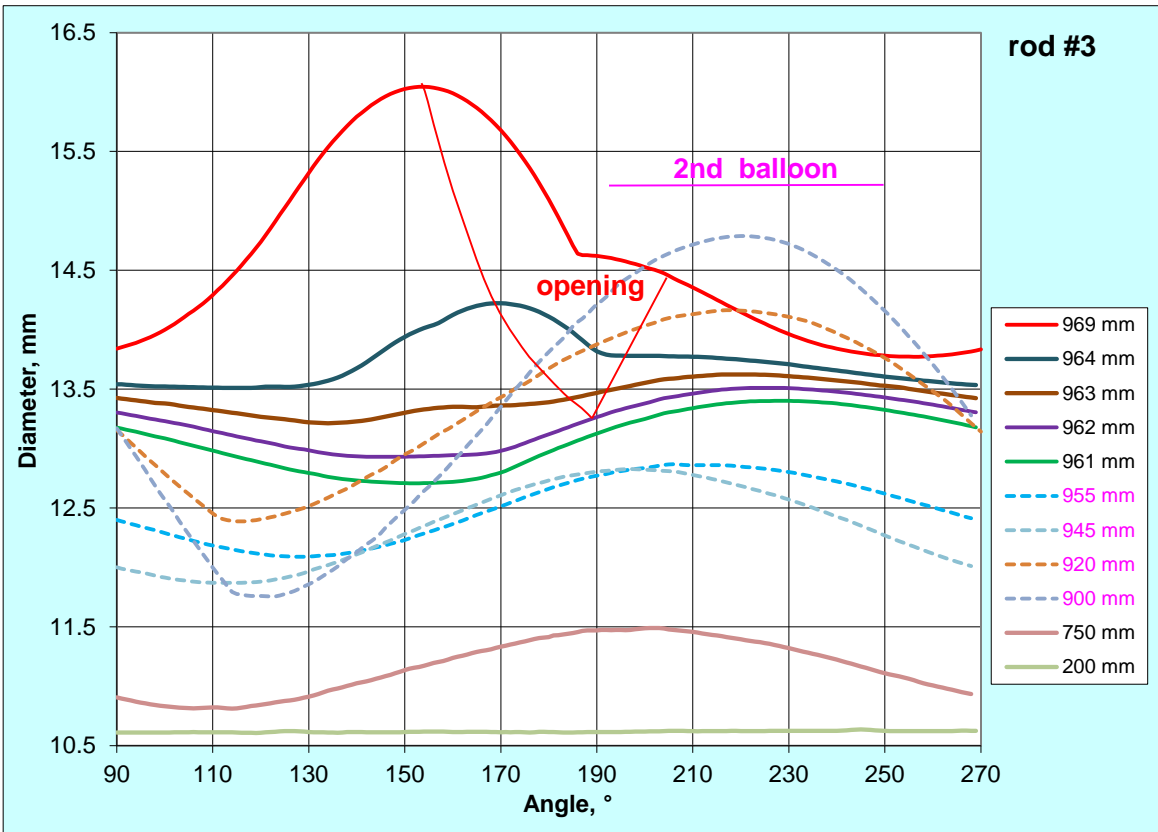
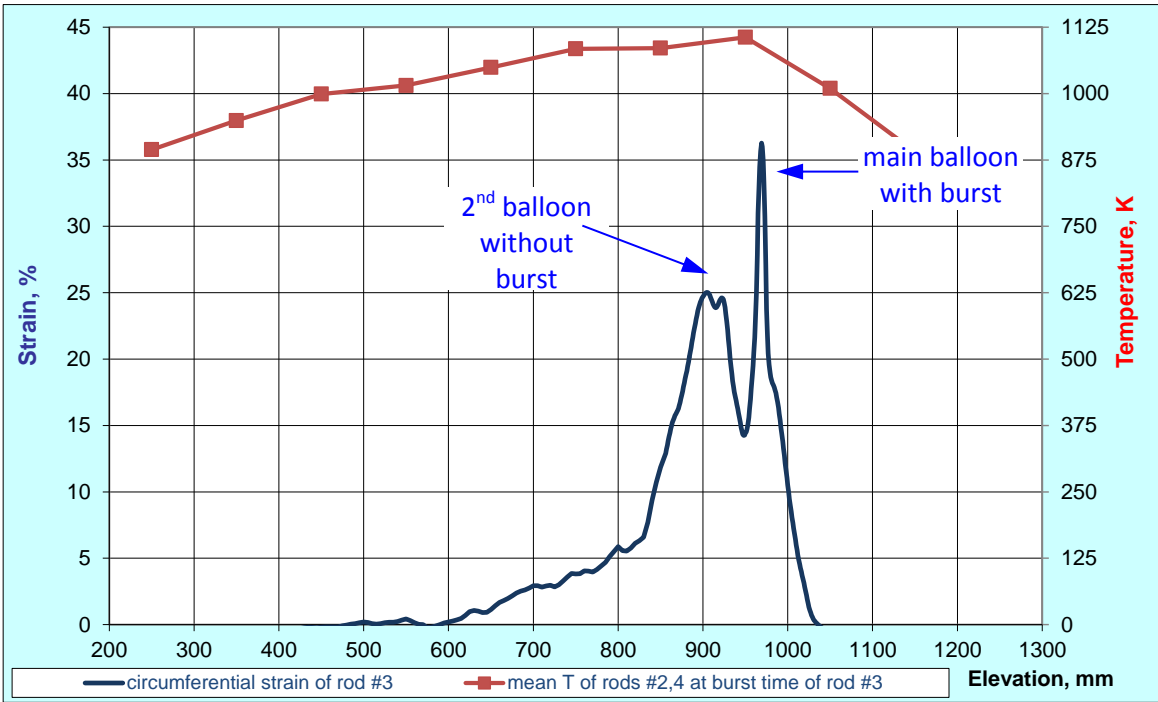


**Figure 57** QUENCH-L1, Rod #3; longitudinal circumferential strain changing (top); azimuthal diameter changing downwards from burst (bottom).



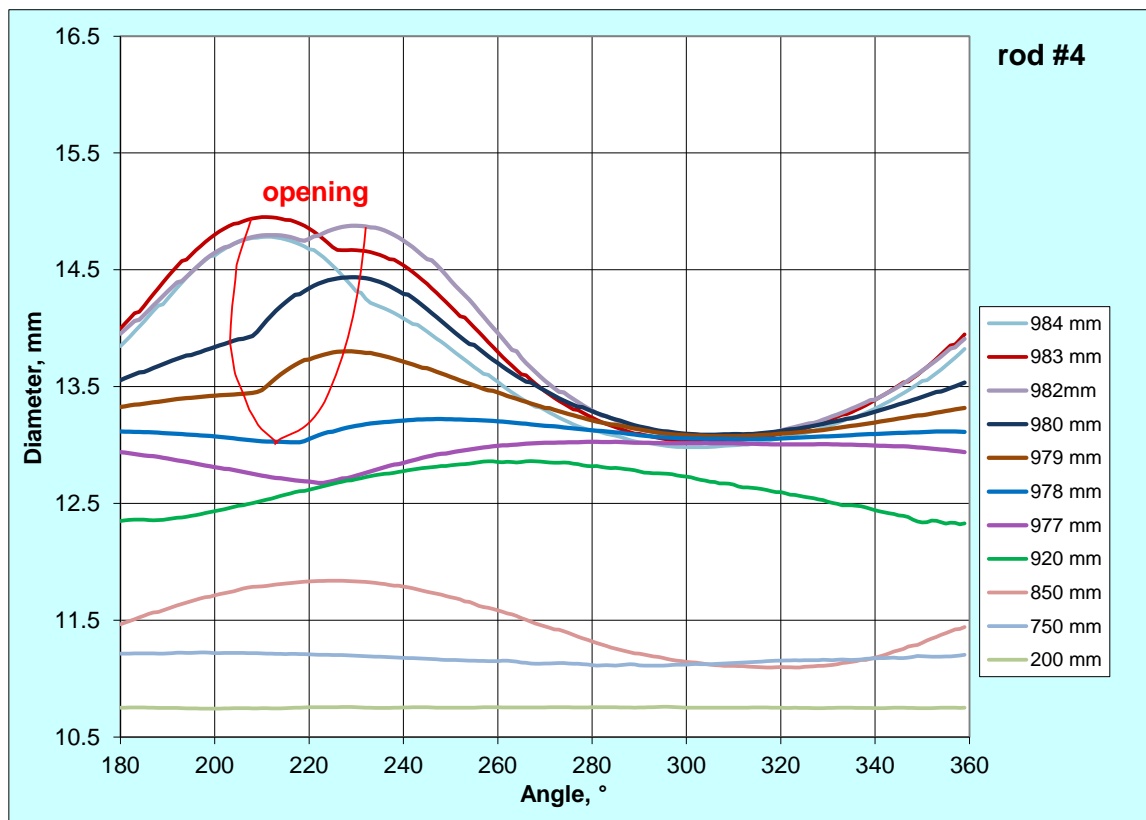
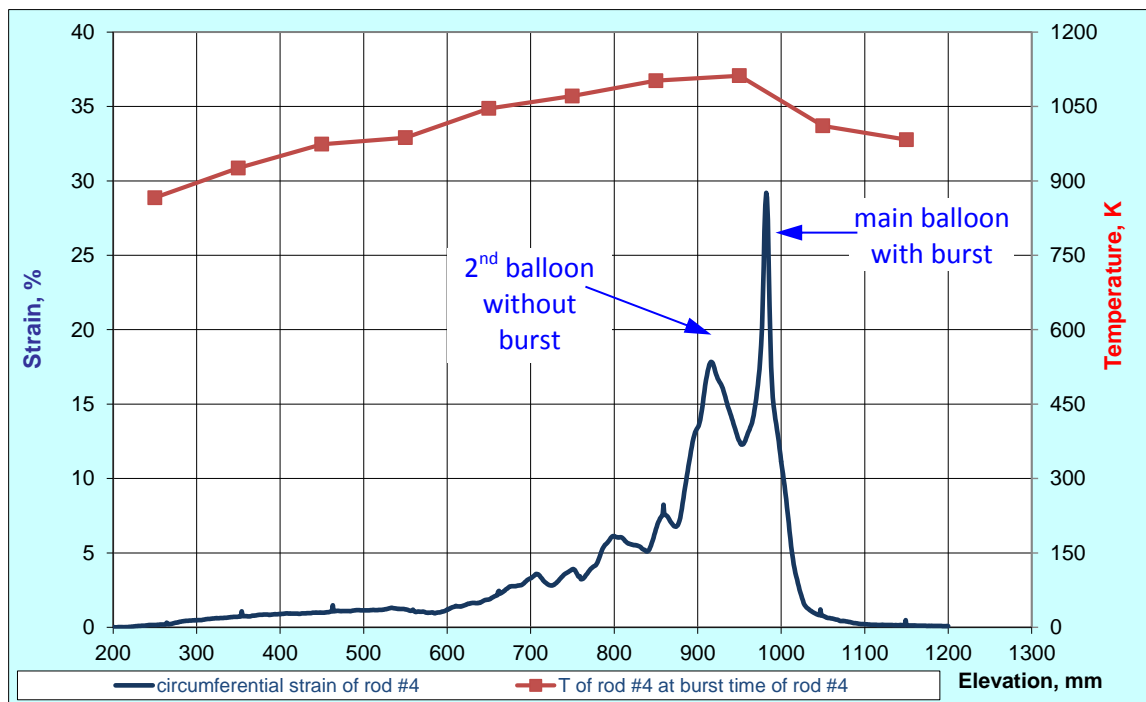


**Figure 58** QUENCH-L1, Rod #4; longitudinal circumferential strain changing (top); azimuthal diameter changing downwards from burst (bottom).

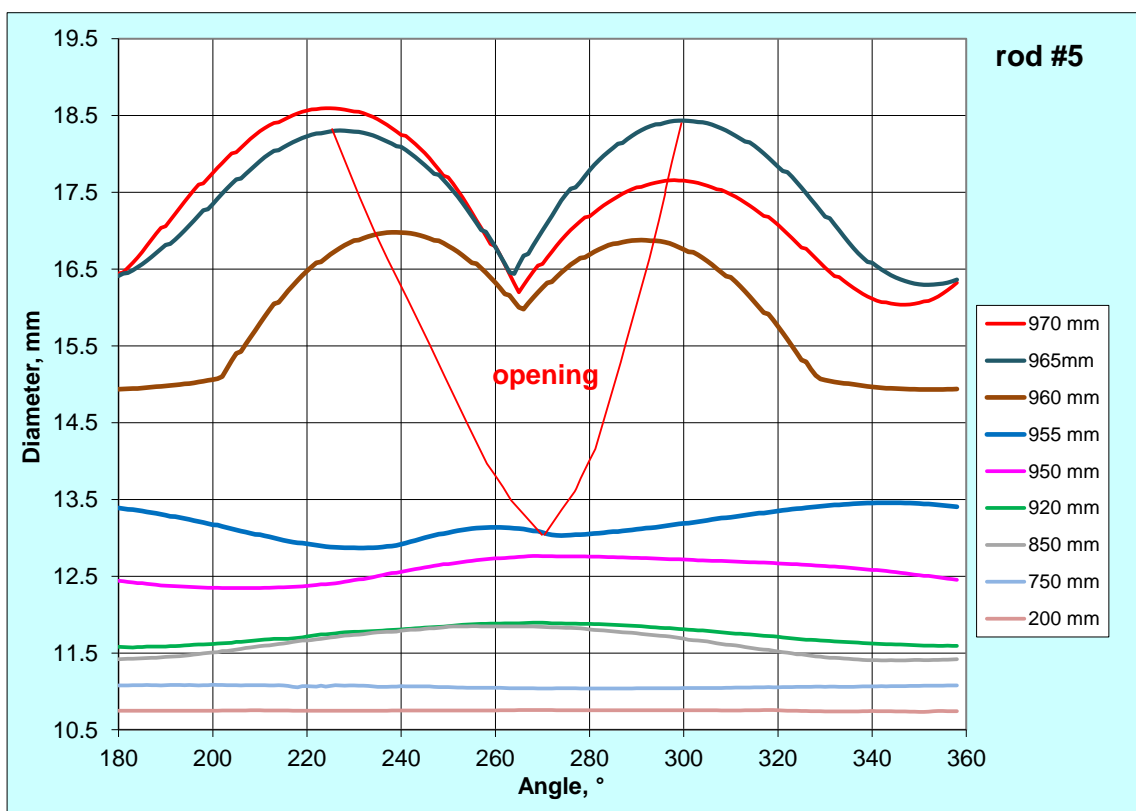
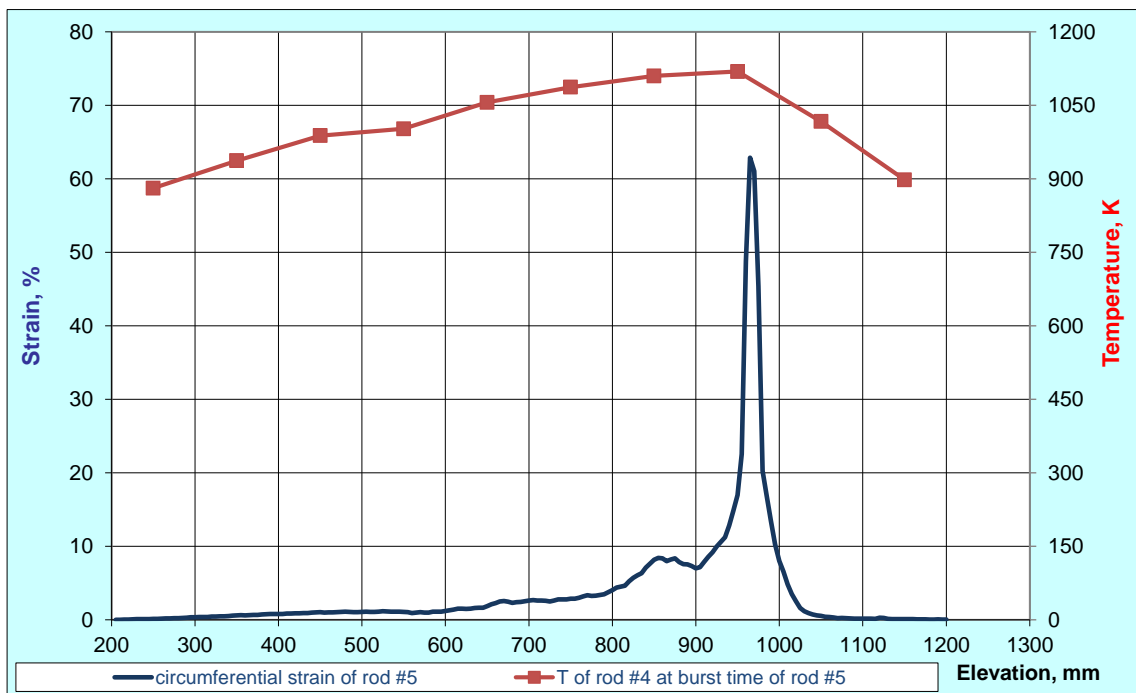


**Figure 59** QUENCH-L1, Rod #5; longitudinal circumferential strain changing (top); azimuthal diameter changing downwards from burst (bottom).

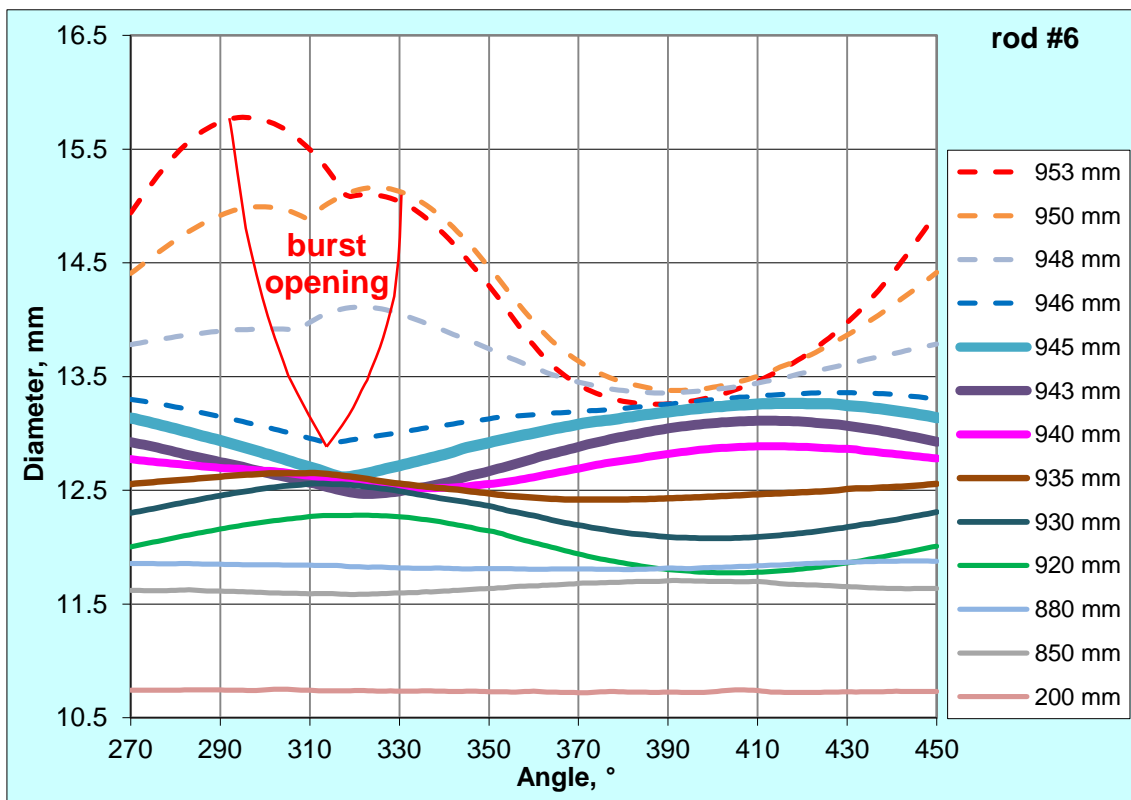
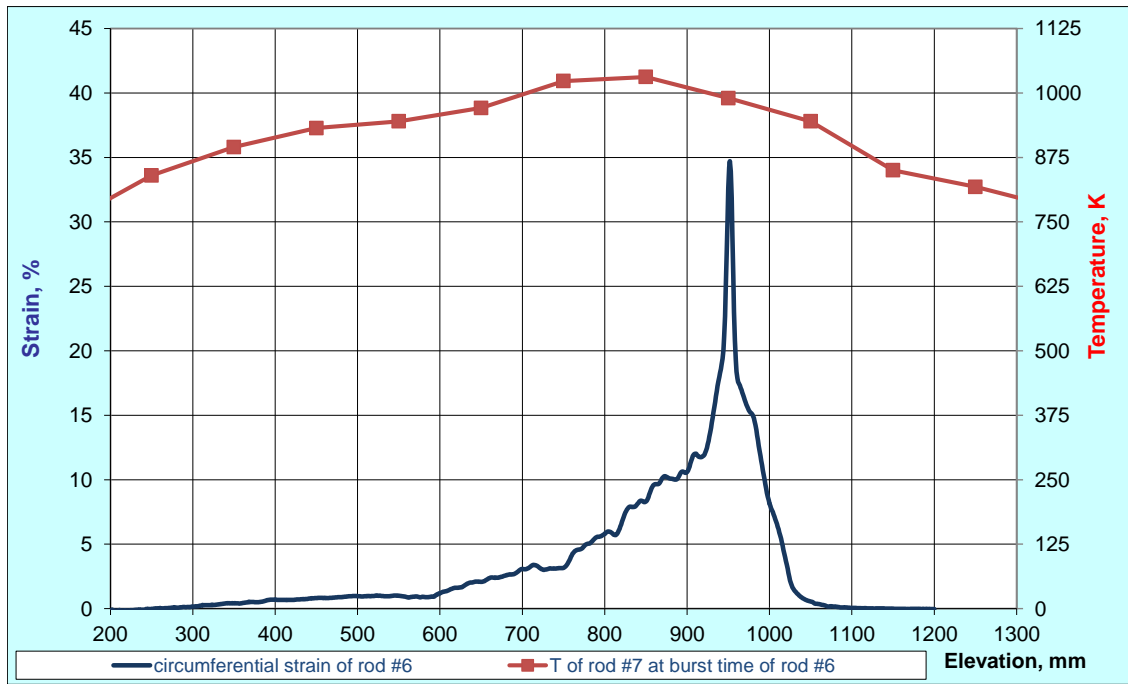


**Figure 60** QUENCH-L1, Rod #6; longitudinal circumferential strain changing (top); azimuthal diameter changing downwards from burst (bottom).

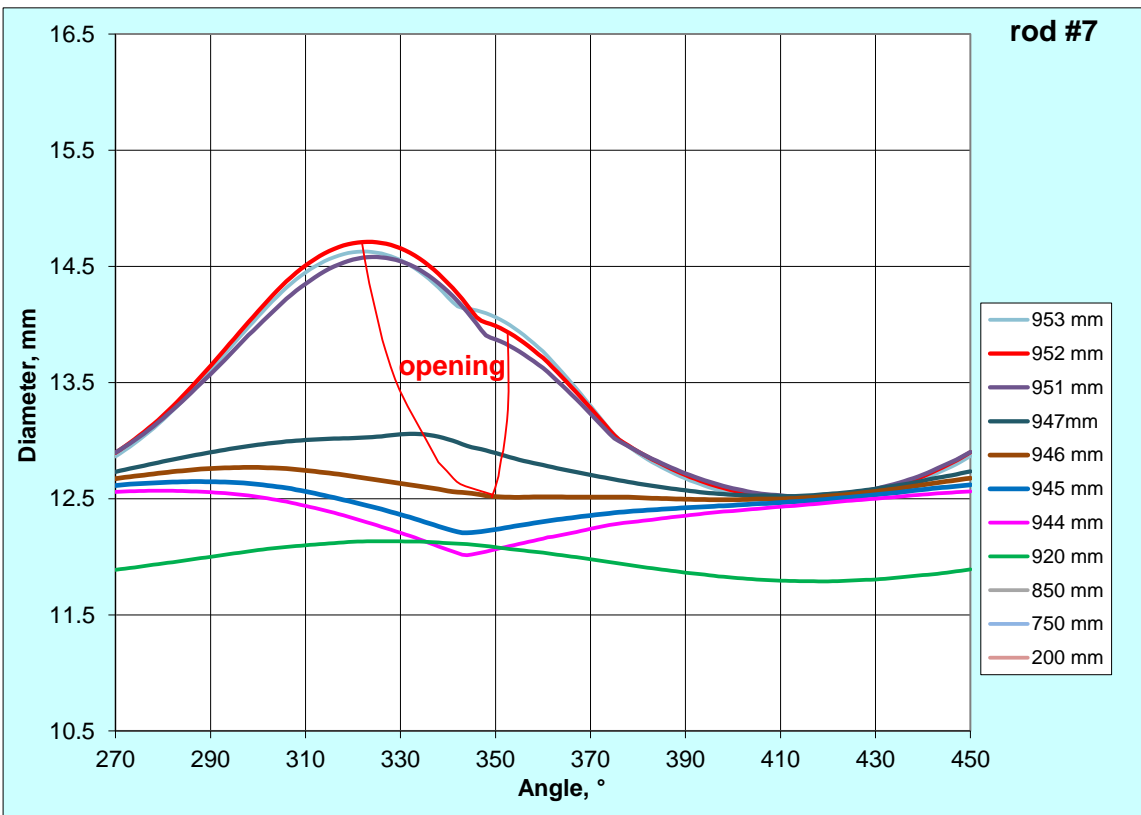
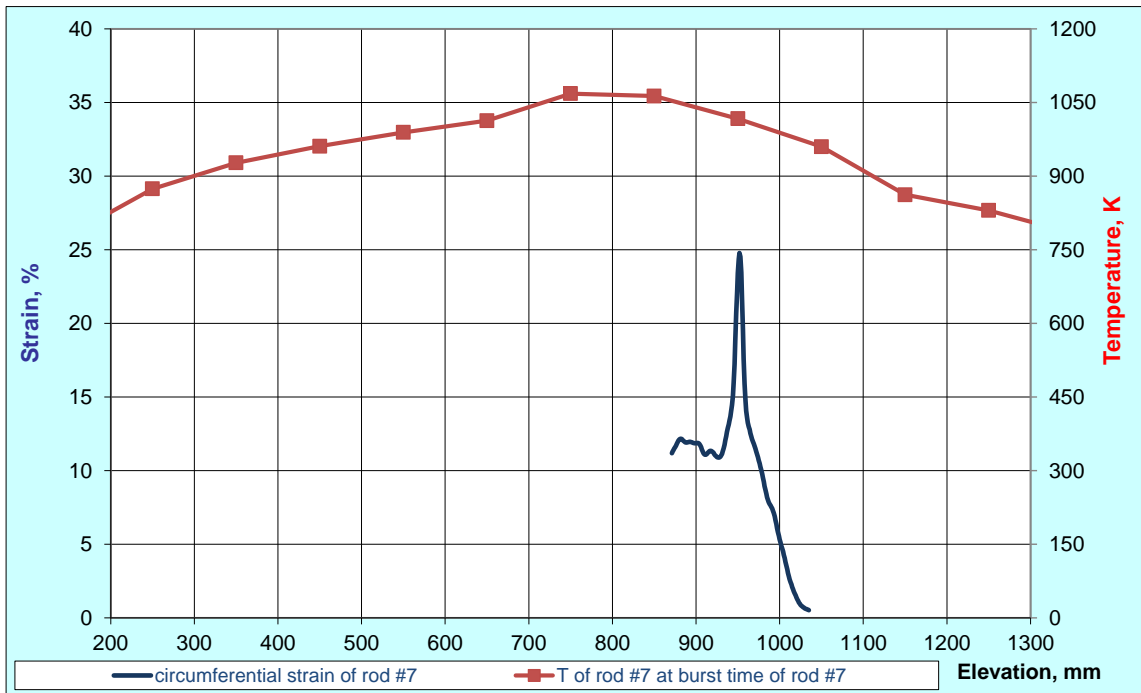


**Figure 61** QUENCH-L1, Rod #7; longitudinal circumferential strain changing (top); azimuthal diameter changing downwards from burst (bottom).

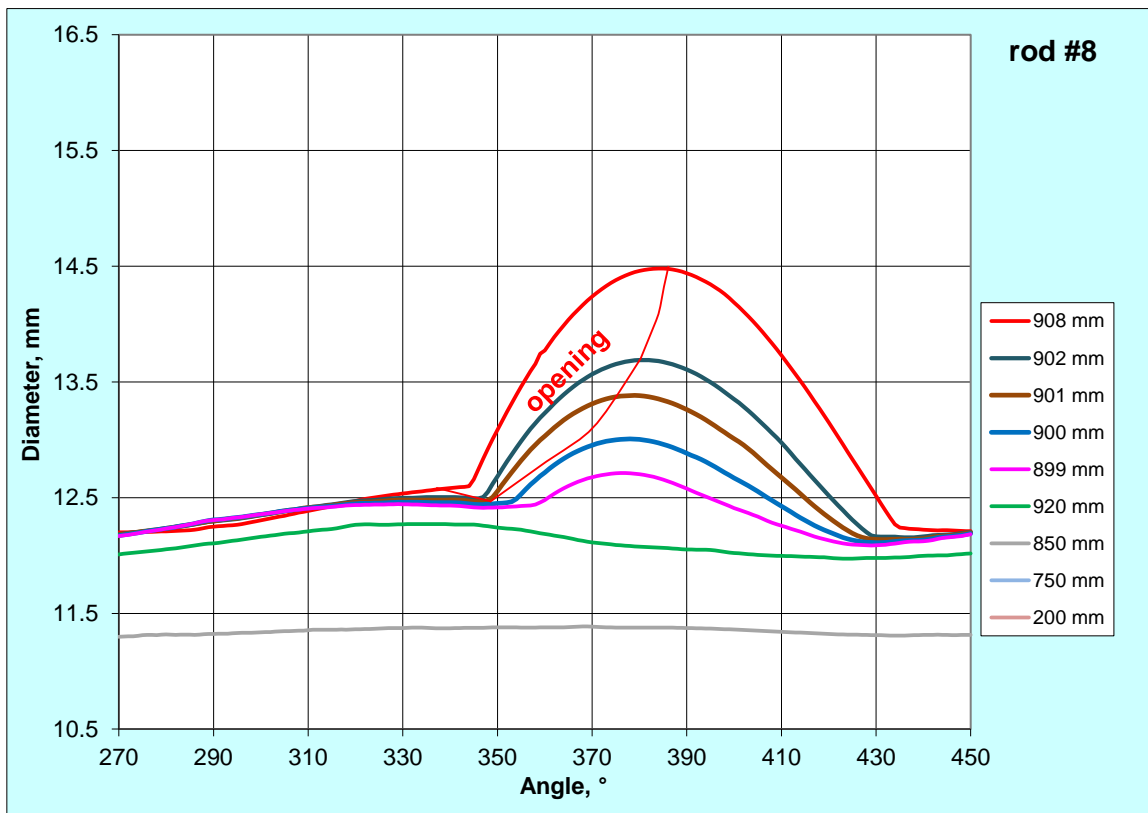
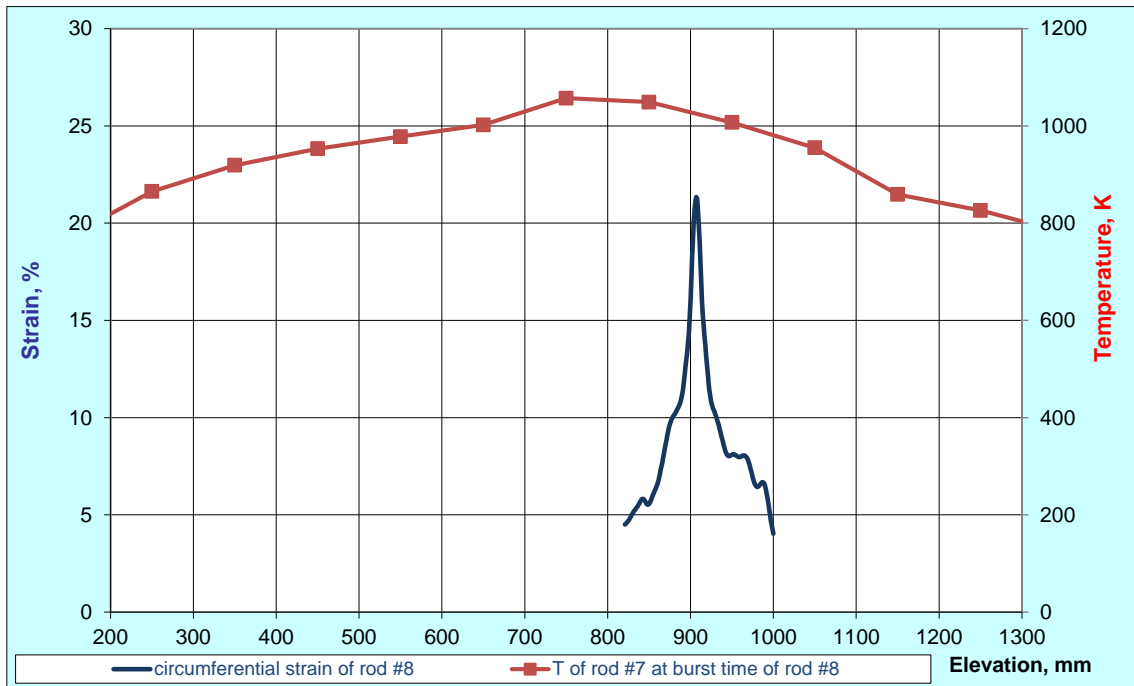


**Figure 62** QUENCH-L1, Rod #8; longitudinal circumferential strain changing (top); azimuthal diameter changing downwards from burst (bottom).

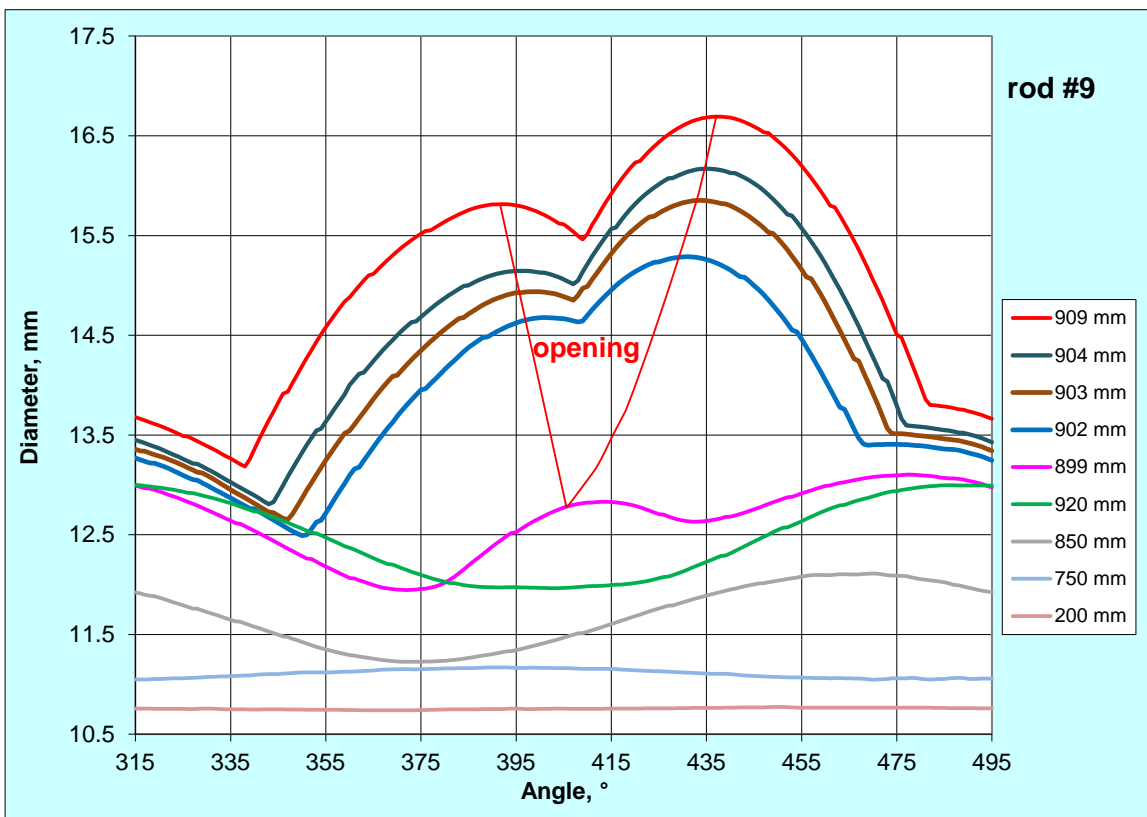
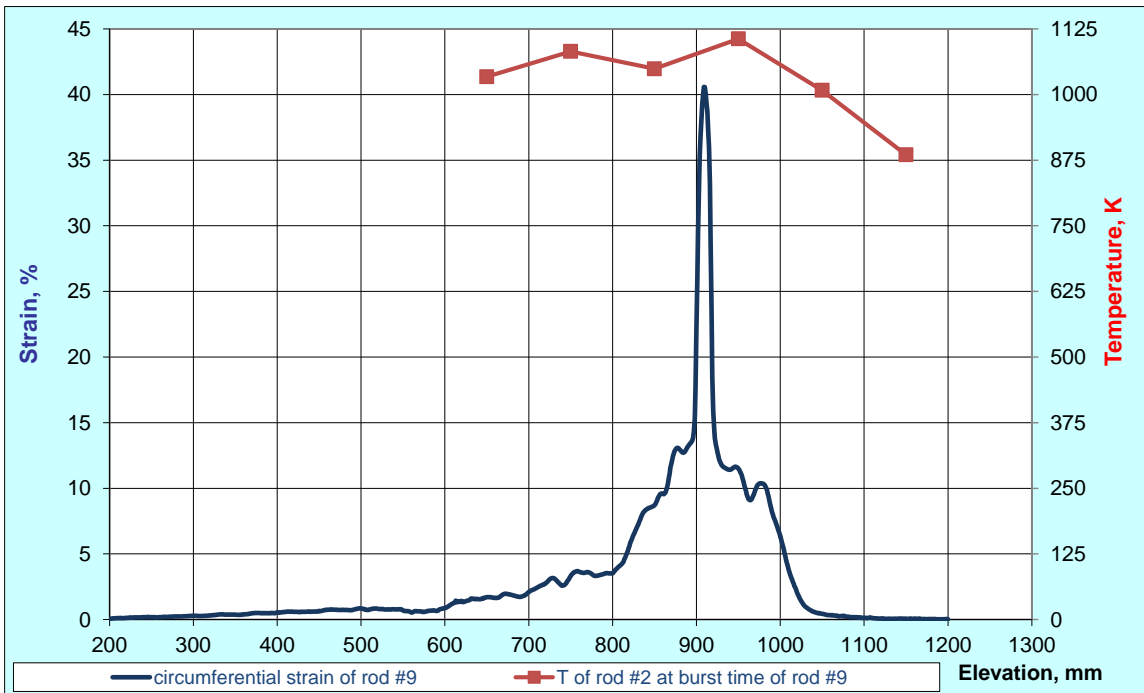


**Figure 63** QUENCH-L1, Rod #9; longitudinal circumferential strain changing (top); azimuthal diameter changing downwards from burst (bottom).

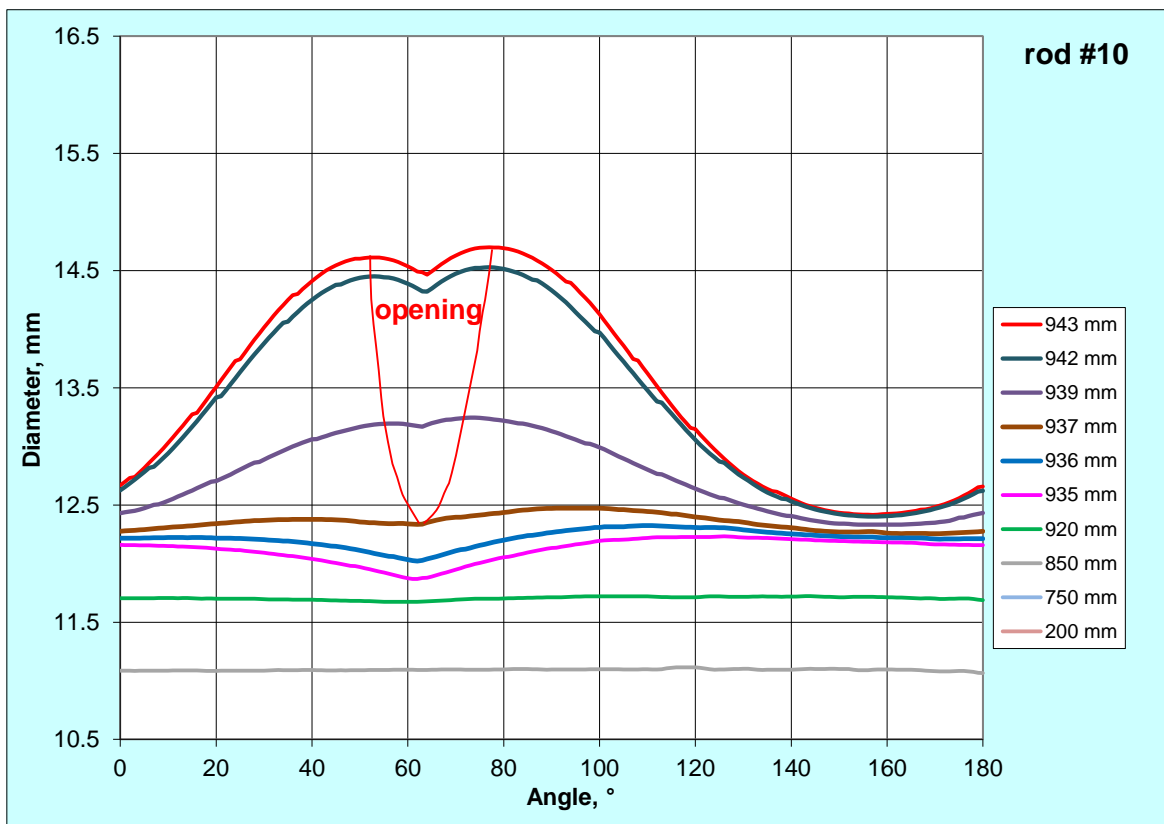
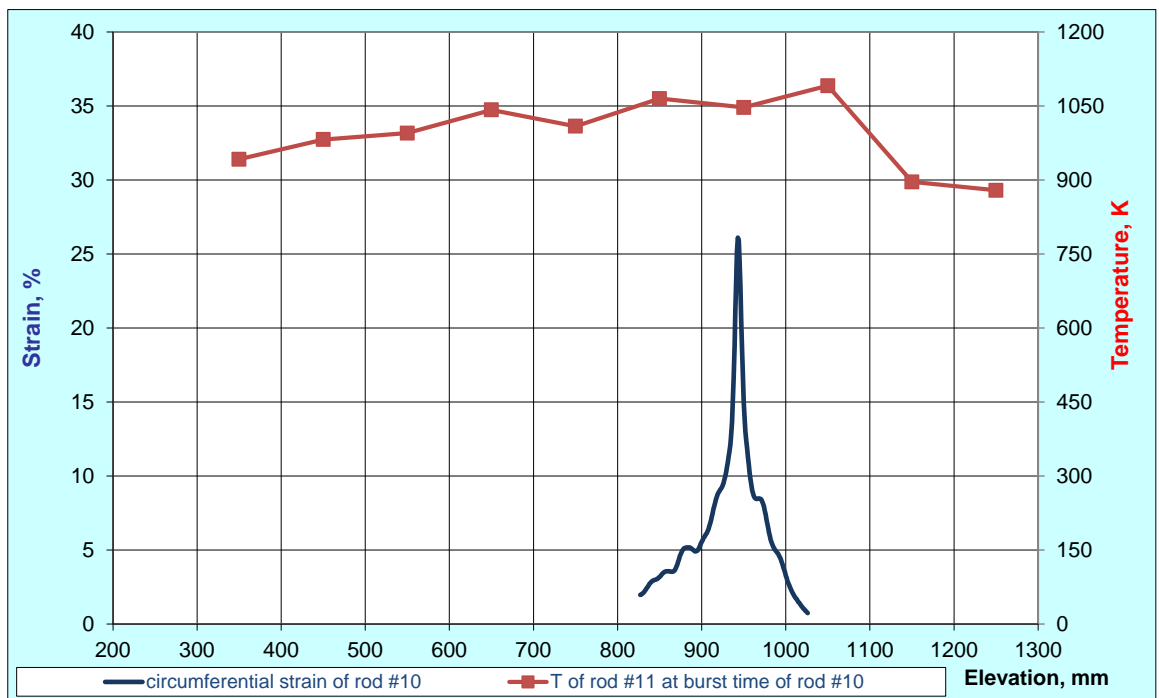


**Figure 64** QUENCH-L1, Rod #10; longitudinal circumferential strain changing (top); azimuthal diameter changing downwards from burst (bottom).

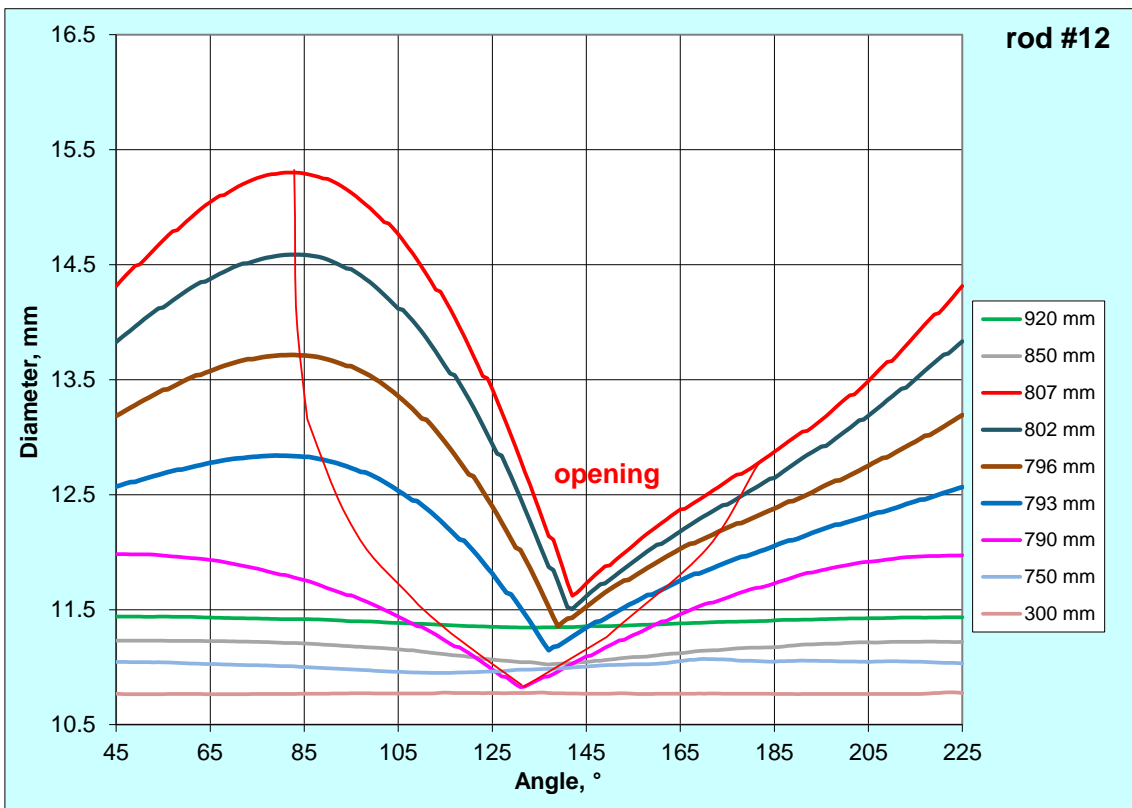
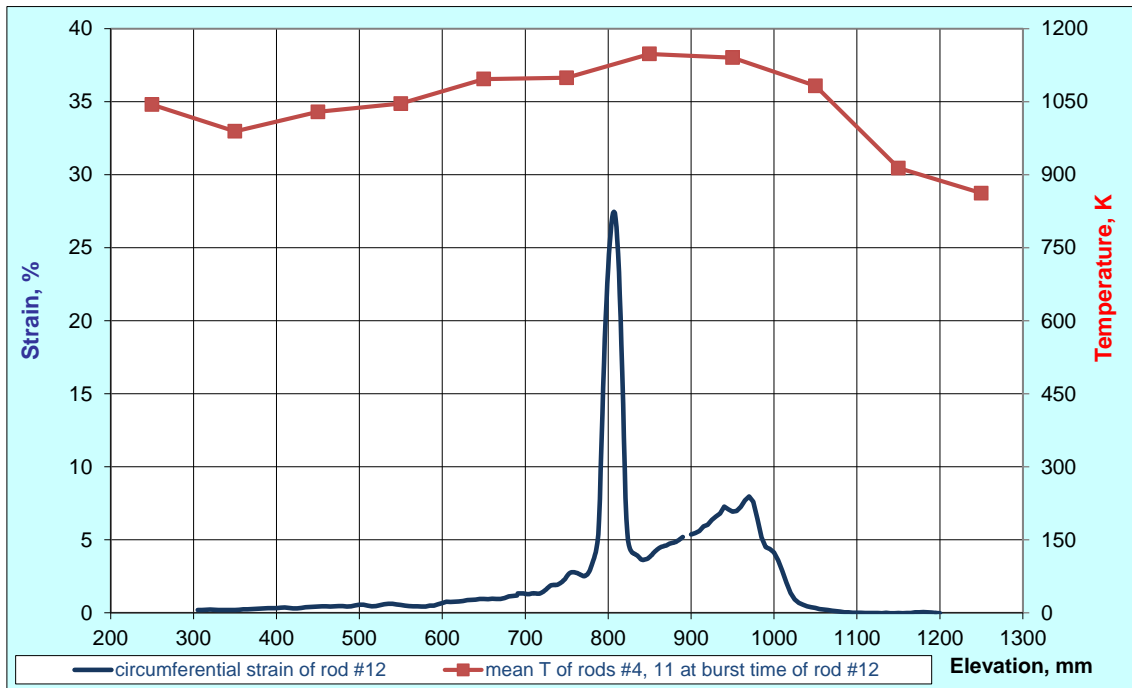


**Figure 65** QUENCH-L1, Rod #12; longitudinal circumferential strain changing (top); azimuthal diameter changing downwards from burst (bottom).



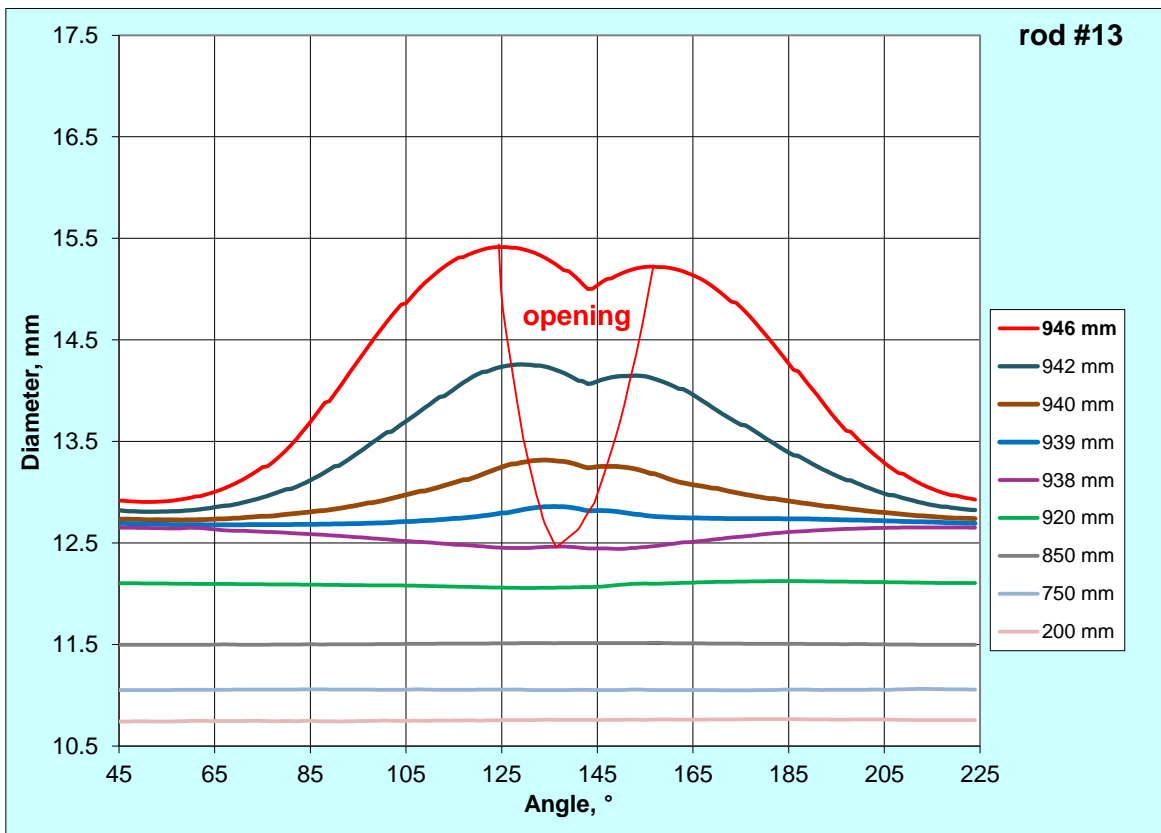
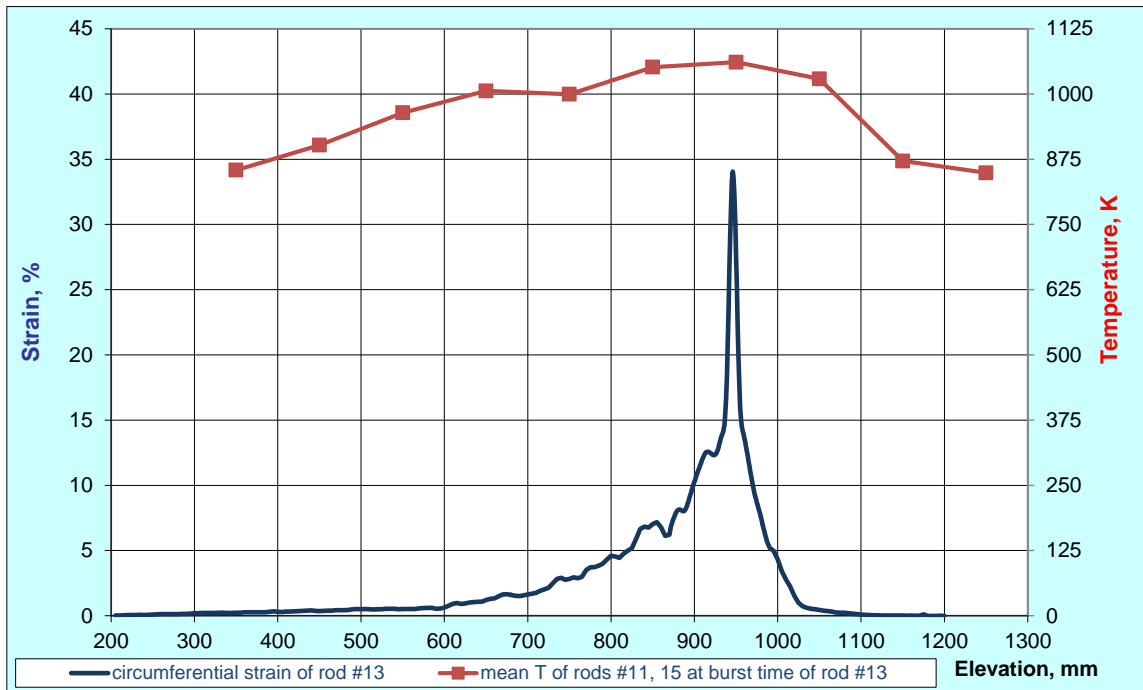
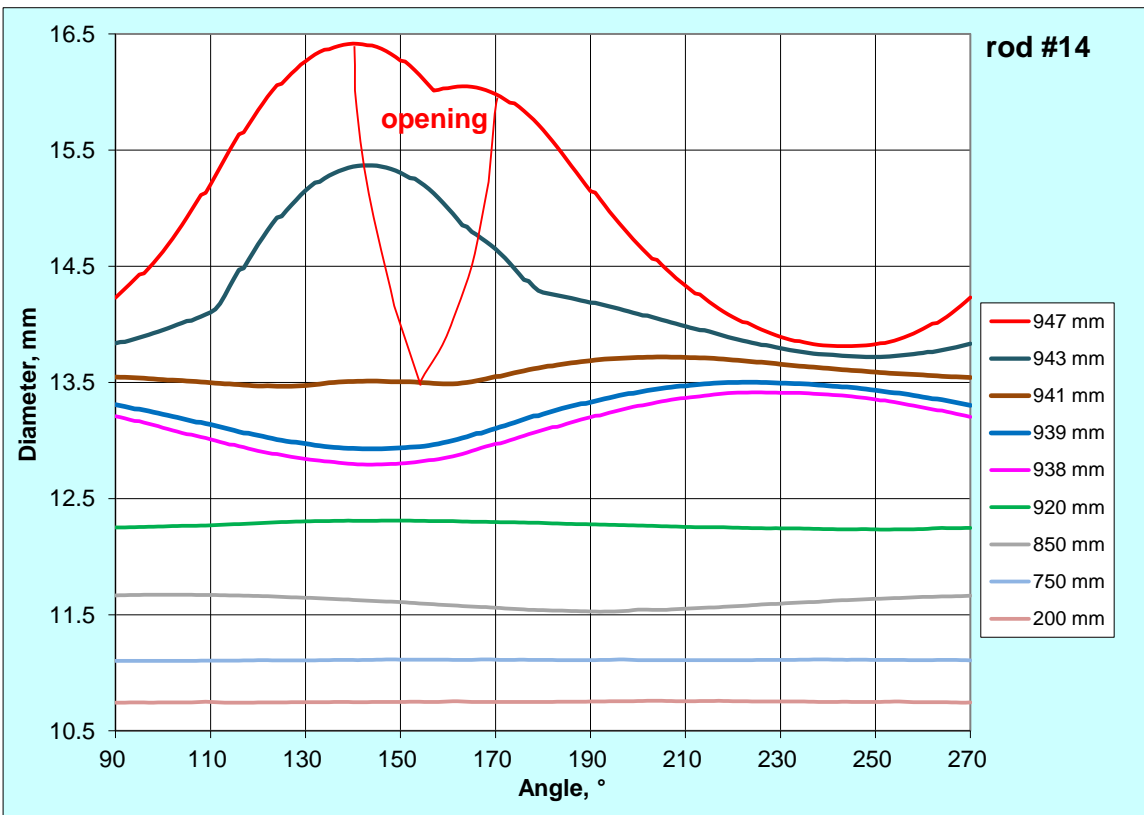
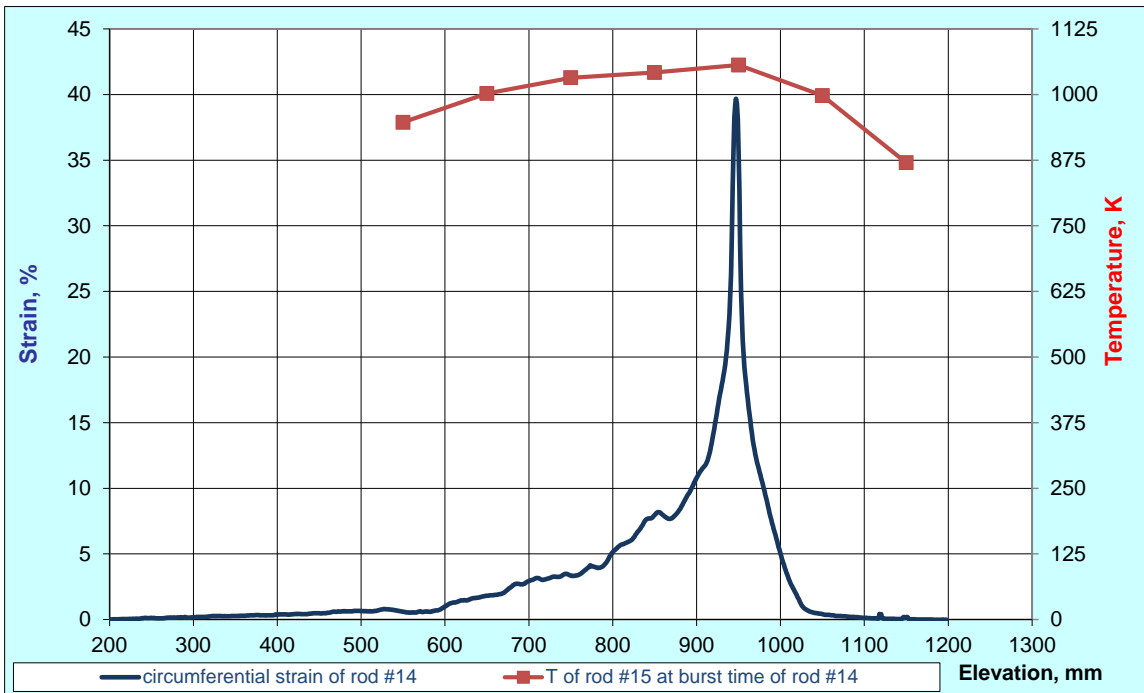
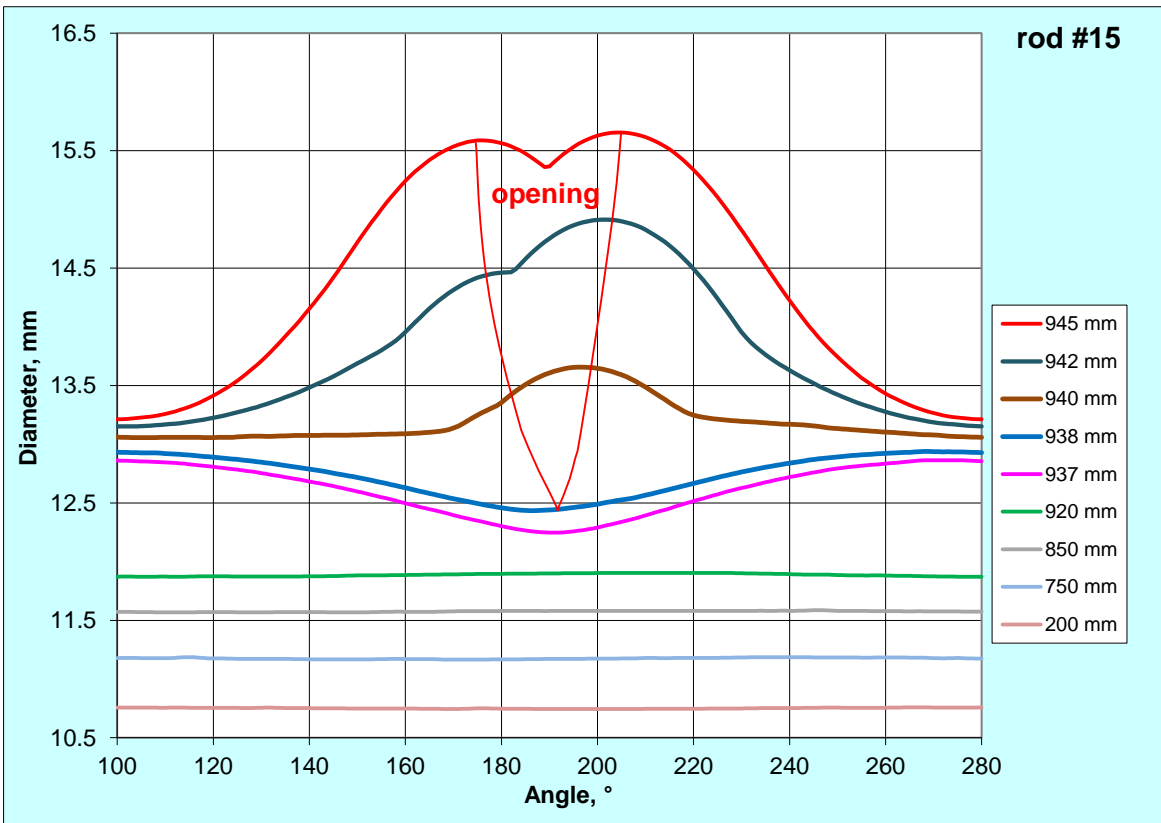
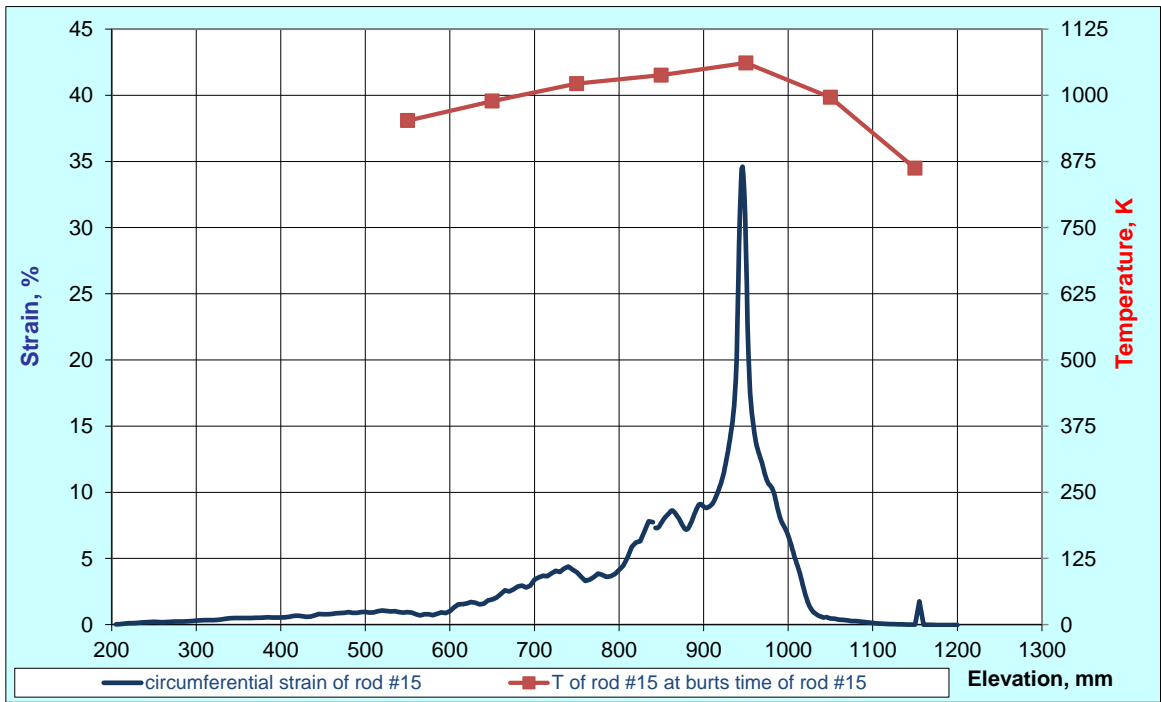


Figure 66 QUENCH-L1, Rod #13; longitudinal circumferential strain changing (top); azimuthal diameter changing downwards from burst (bottom).



**Figure 67** QUENCH-L1, Rod #14; longitudinal circumferential strain changing (top); azimuthal diameter changing downwards from burst (bottom).



**Figure 68** QUENCH-L1, Rod #15; longitudinal circumferential strain changing (top); azimuthal diameter changing downwards from burst (bottom).

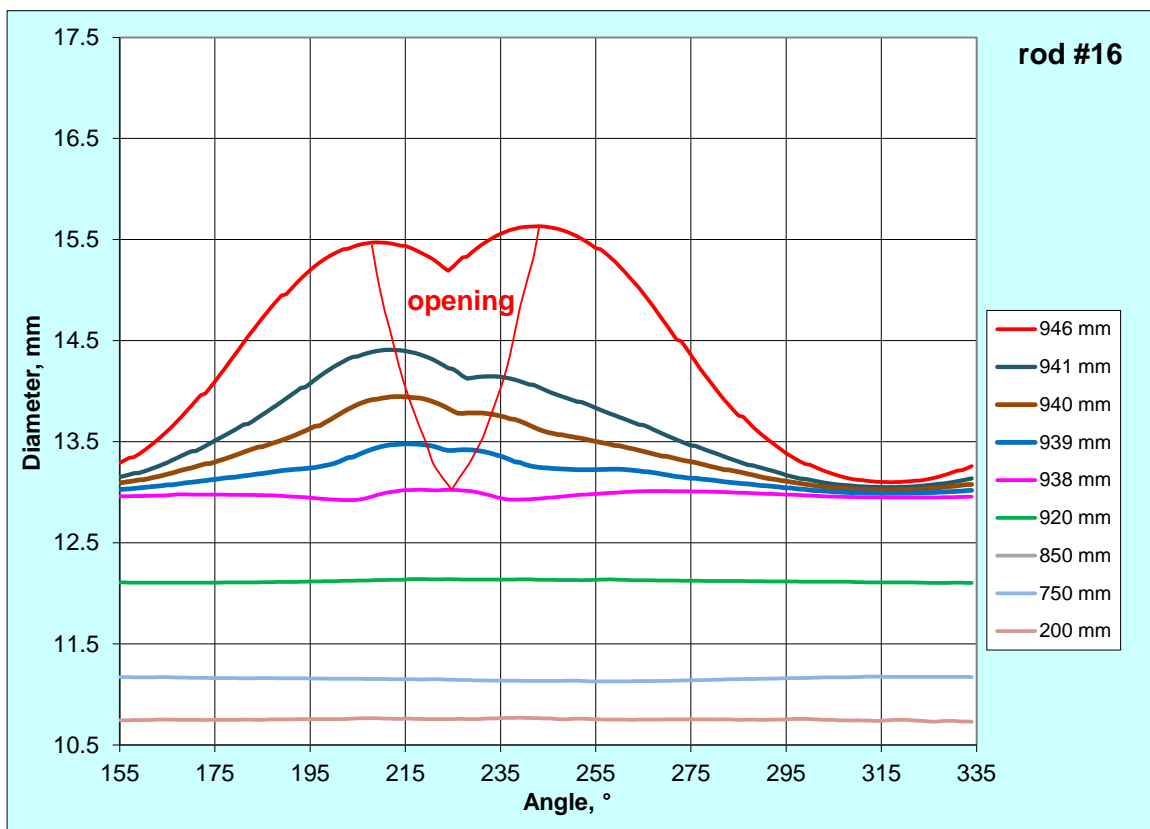
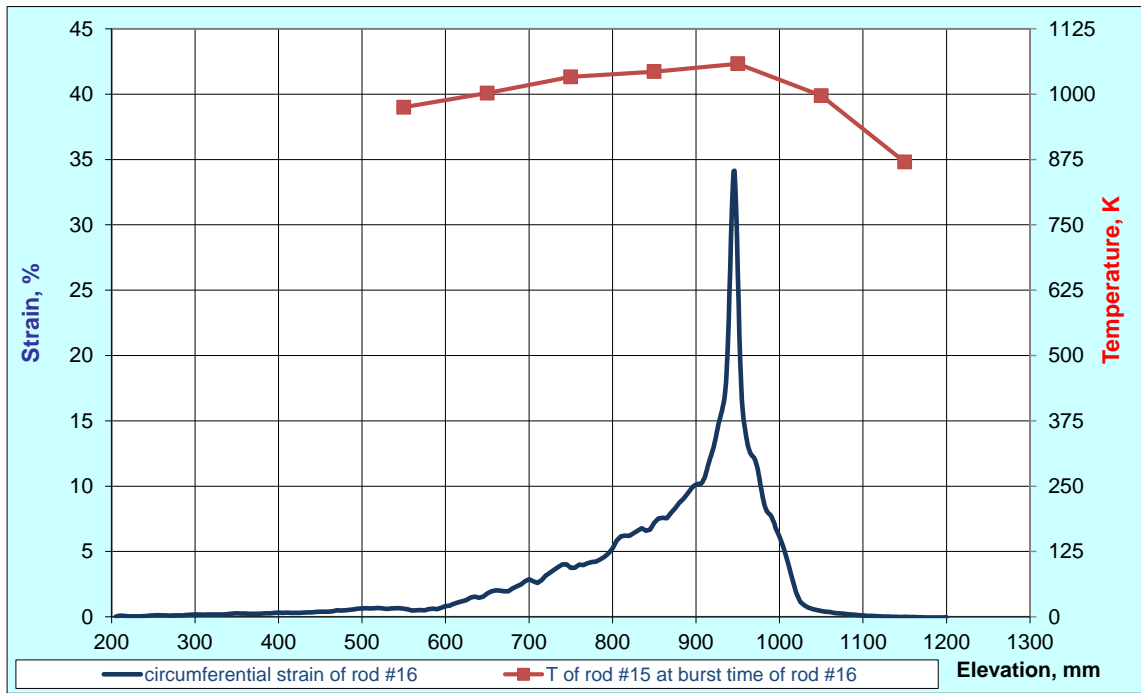


**Figure 69** QUENCH-L2, Rod #16; longitudinal circumferential strain changing (top); azimuthal diameter changing downwards from burst (bottom).

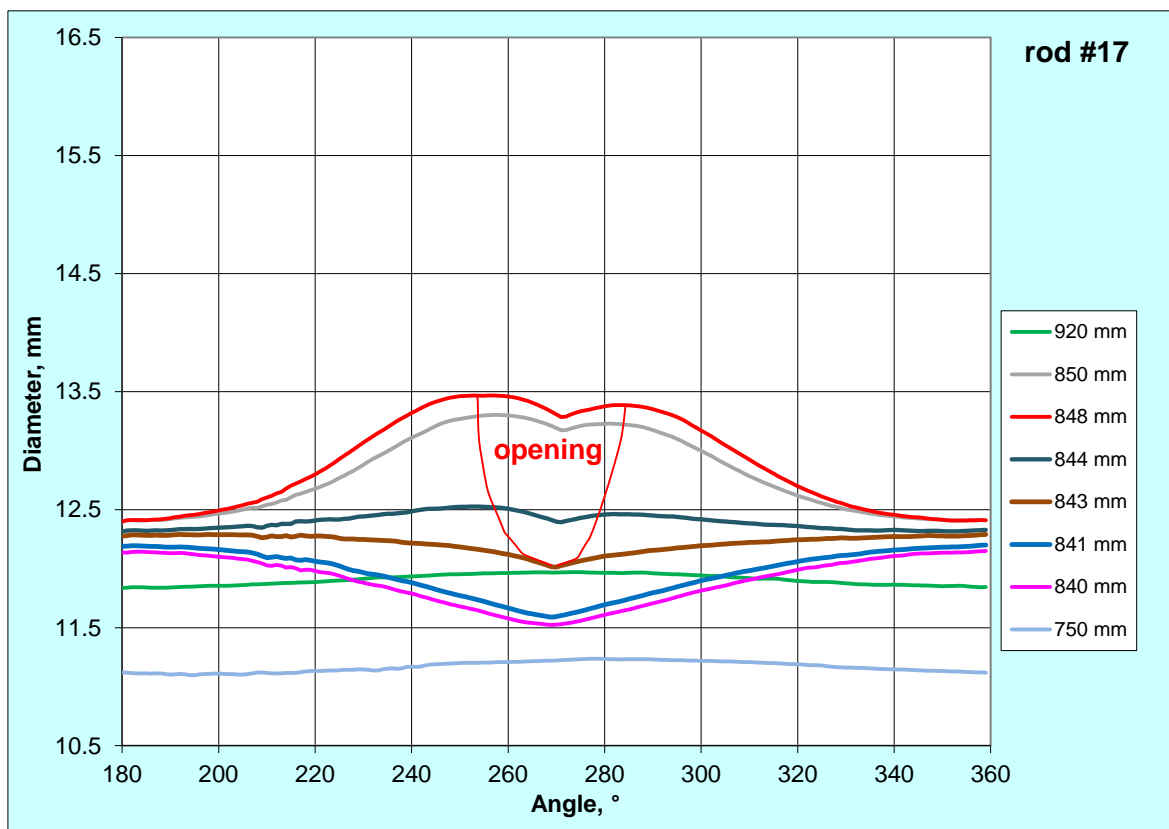
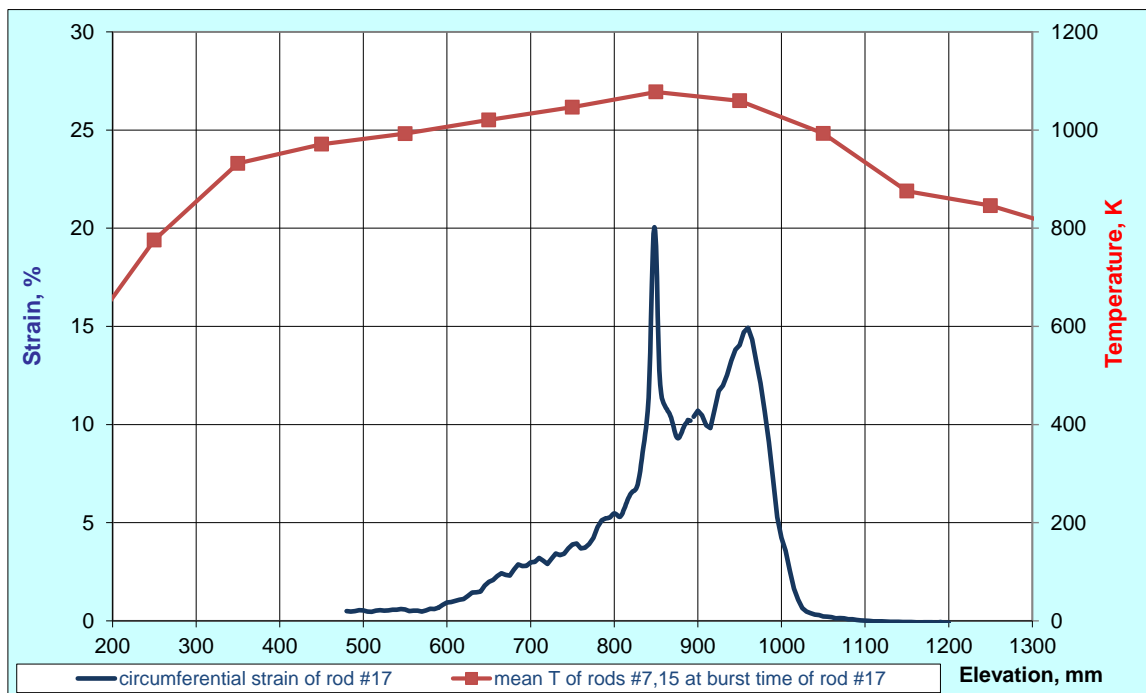


**Figure 70** QUENCH-L1, Rod #17; longitudinal circumferential strain changing (top); azimuthal diameter changing downwards from burst (bottom).

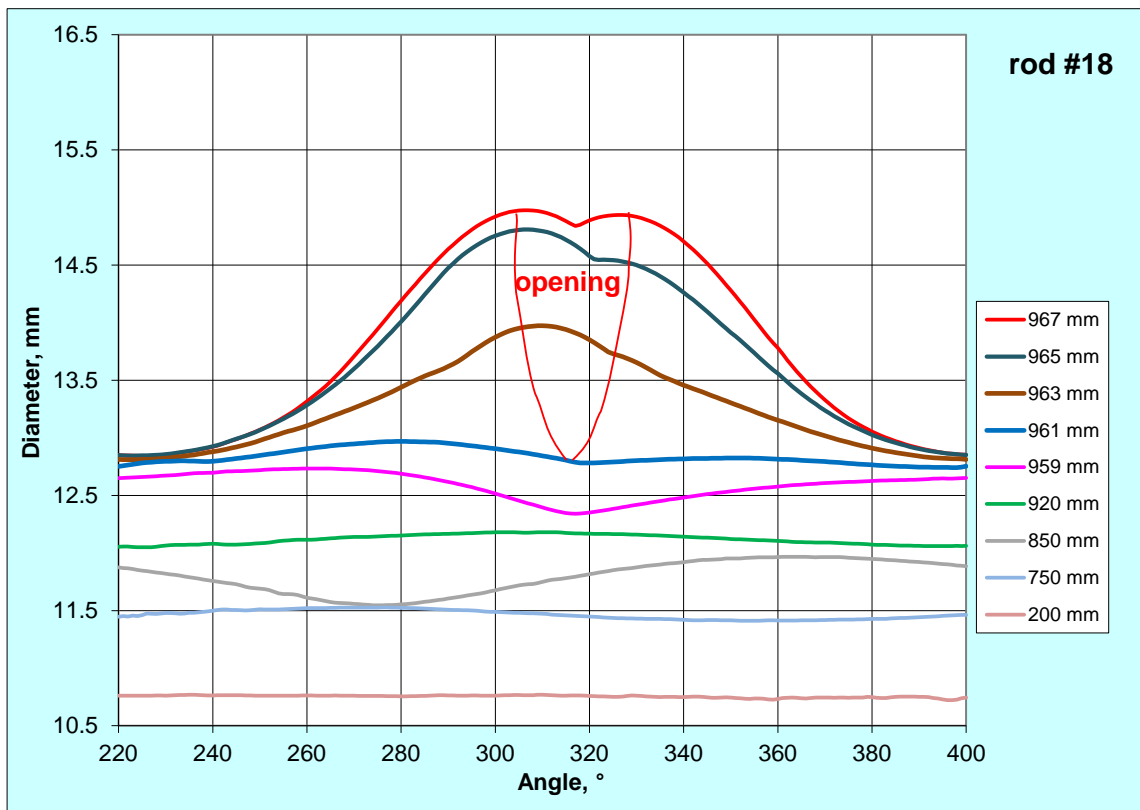
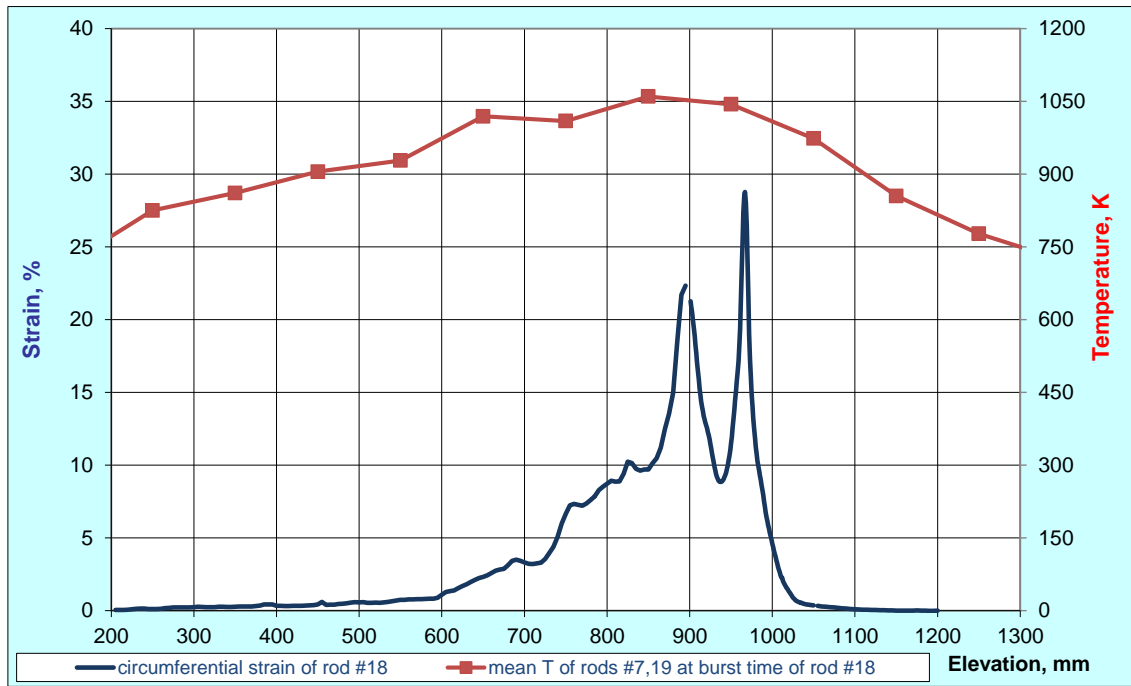


**Figure 71** QUENCH-L1, Rod #18; longitudinal circumferential strain changing (top); azimuthal diameter changing downwards from burst (bottom).

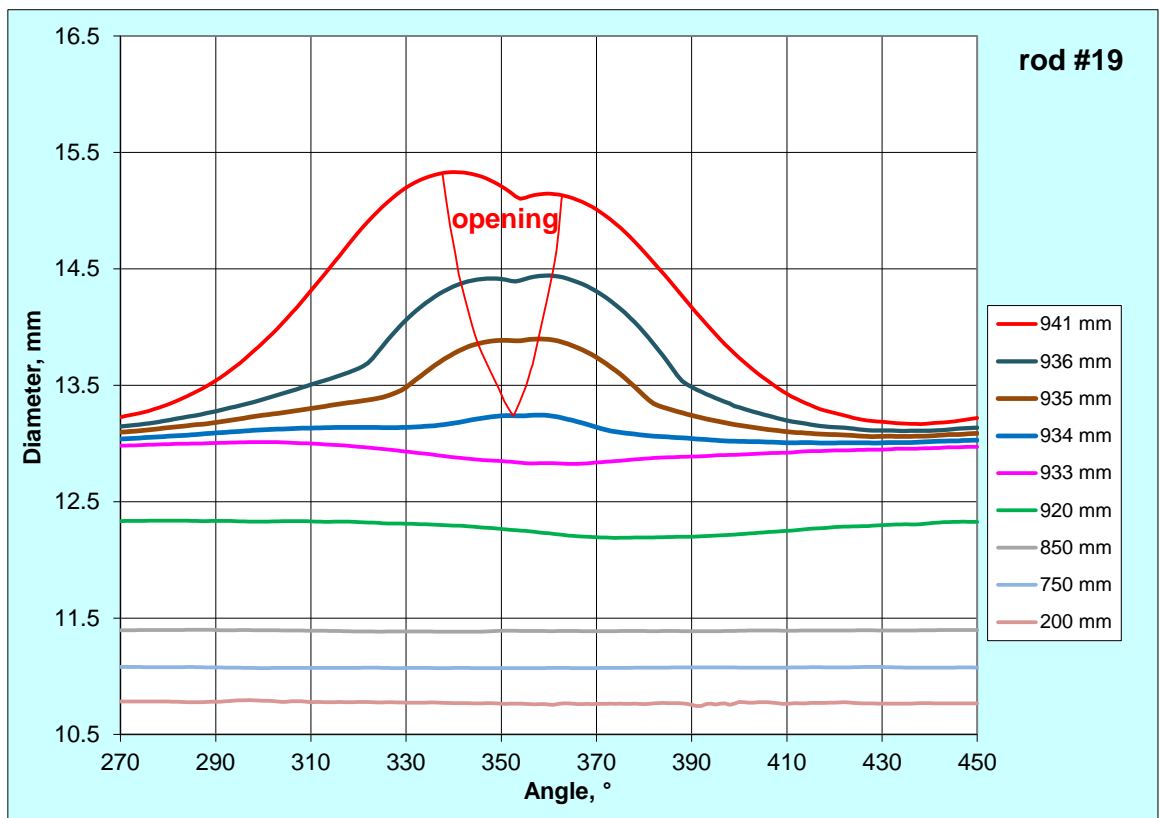
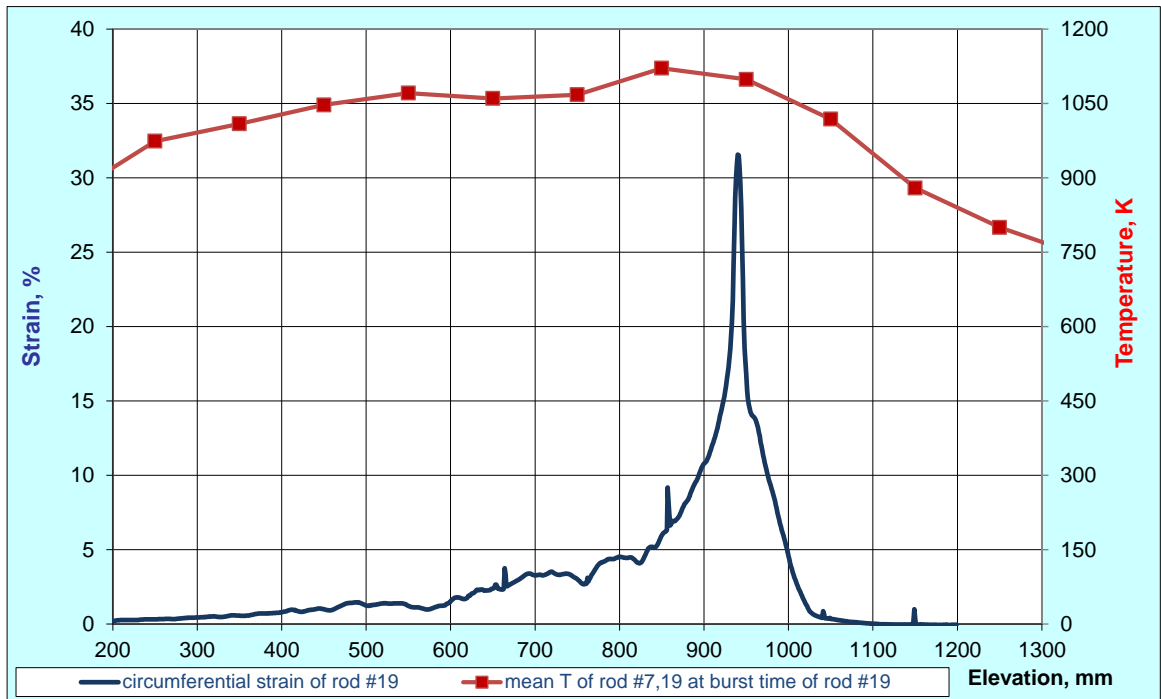


**Figure 72** QUENCH-L1, Rod #19; longitudinal circumferential strain changing (top); azimuthal diameter changing downwards from burst (bottom).

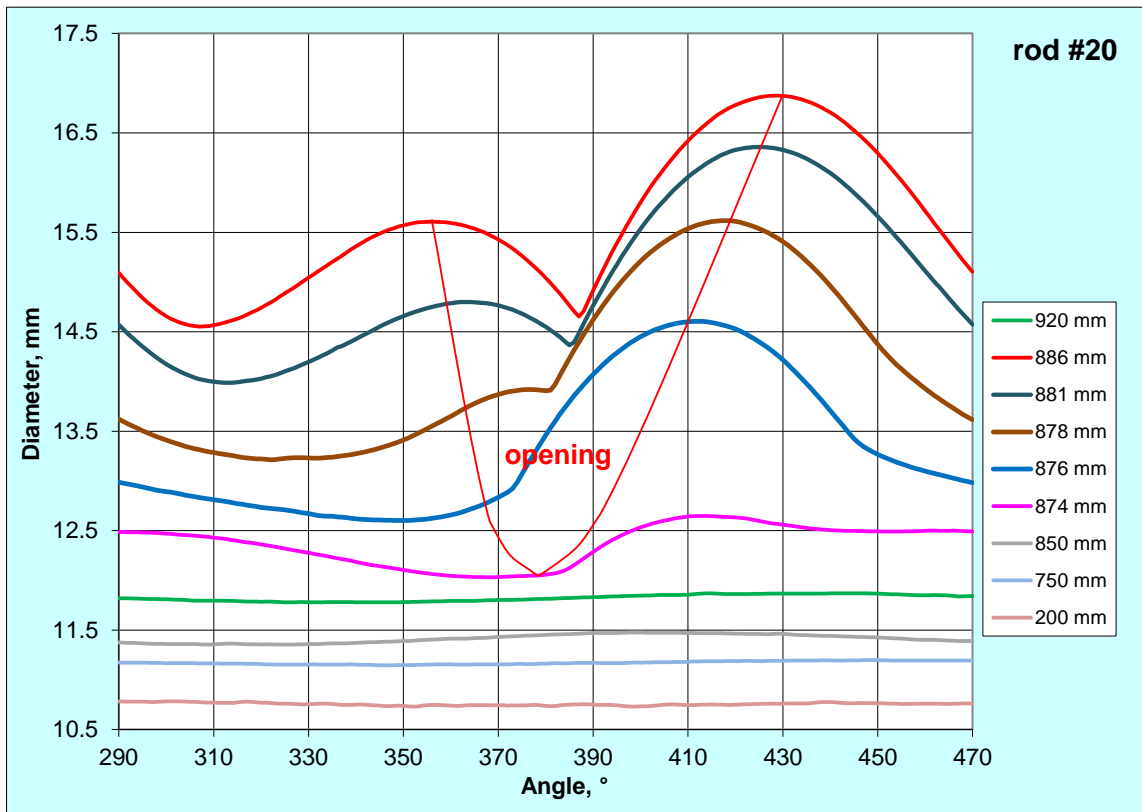
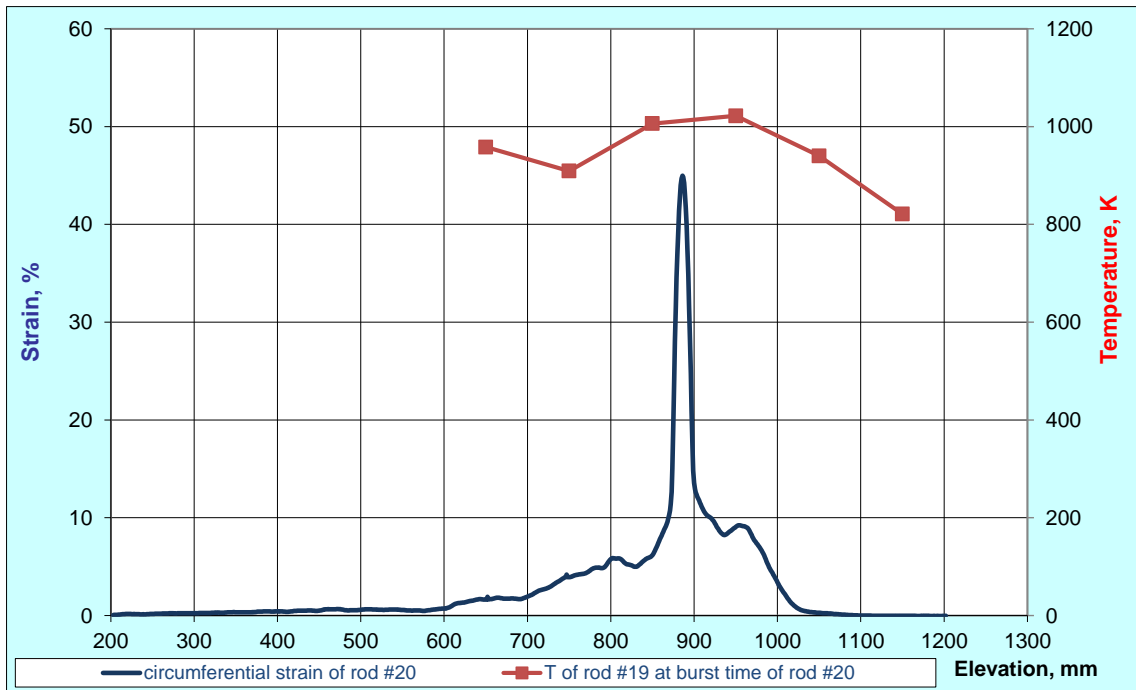


**Figure 73** QUENCH-L1, Rod #20; longitudinal circumferential strain changing (top); azimuthal diameter changing downwards from burst (bottom).



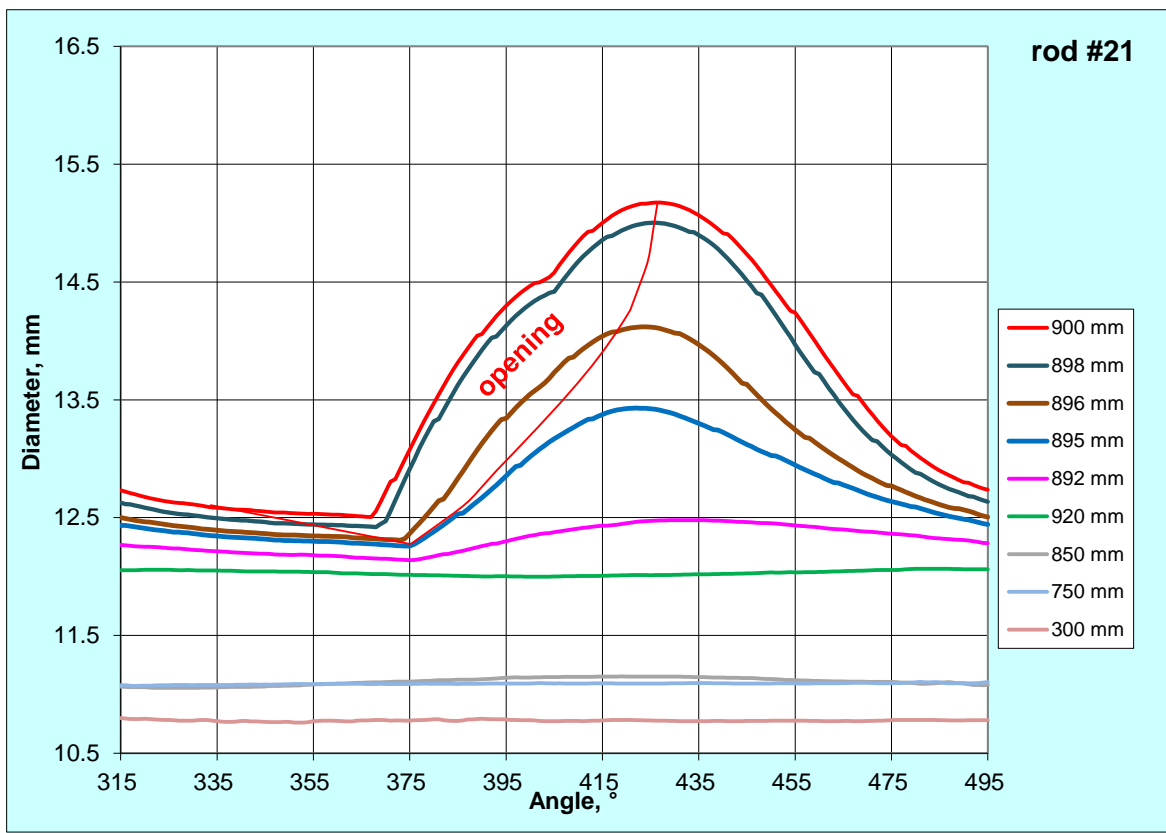
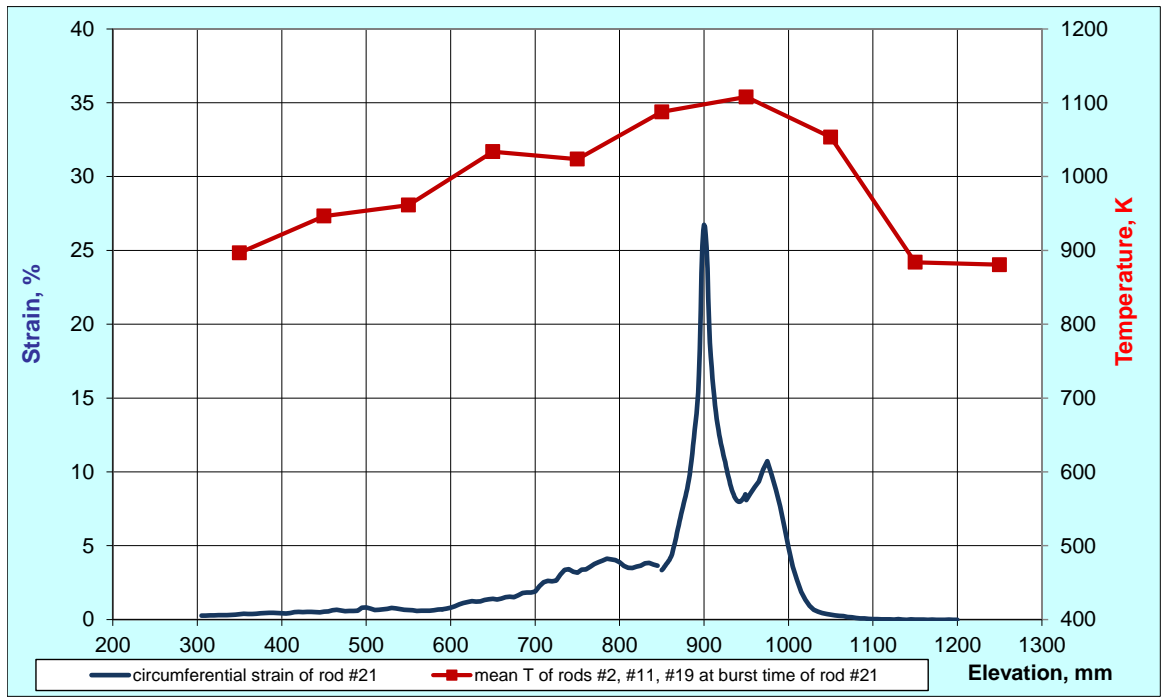
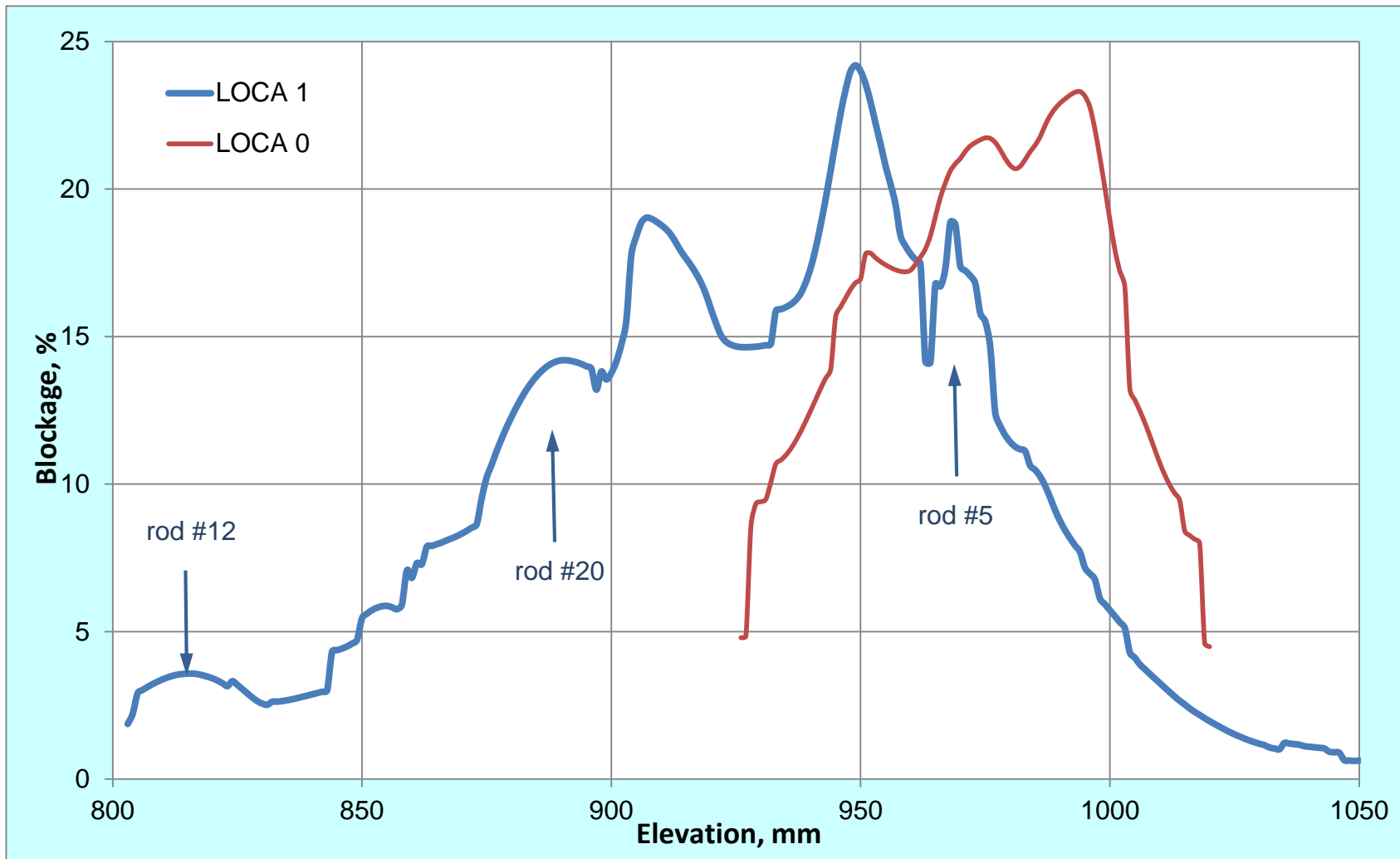
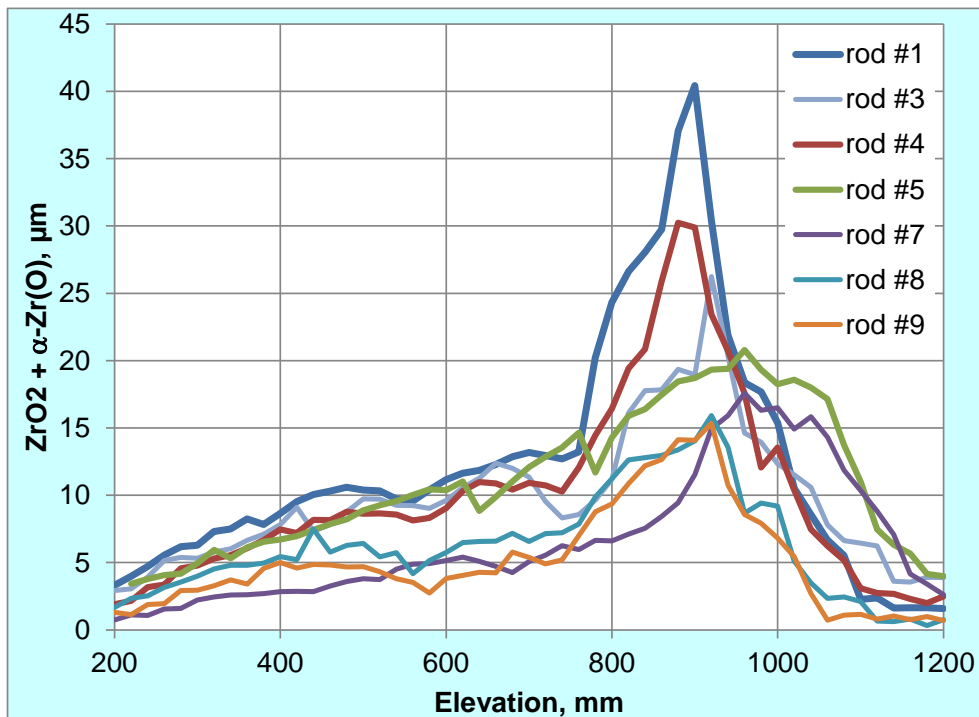


Figure 74 QUENCH-L1, Rod #21; longitudinal circumferential strain changing (top); azimuthal diameter changing downwards from burst (bottom).



**Figure 75** Blockage of coolant channel for QUENCH-L0 and -L1 bundles.



**Figure 76** QUENCH-L1; Results of eddy-current measurements of axial layer thickness distribution for inner rods.

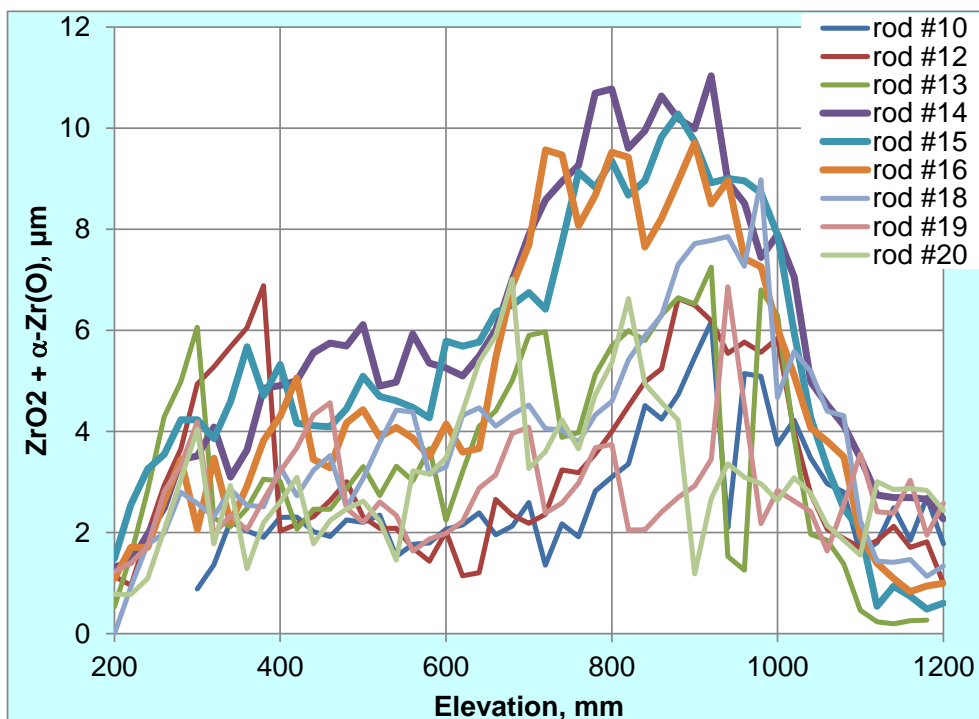


**Figure 77** QUENCH-L1; Results of eddy-current measurements of axial layer thickness distribution for outer rods.

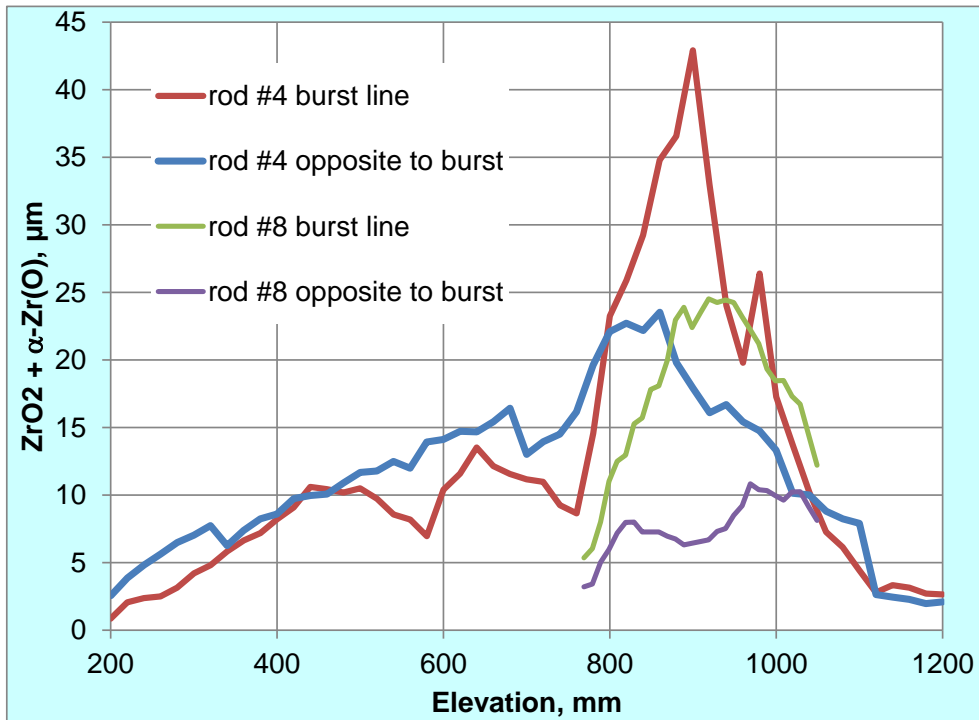


**Figure 78** QUENCH-L1; Results of eddy-current measurements of axial layer thickness distribution for two opposite sides of rods #4 and #8.

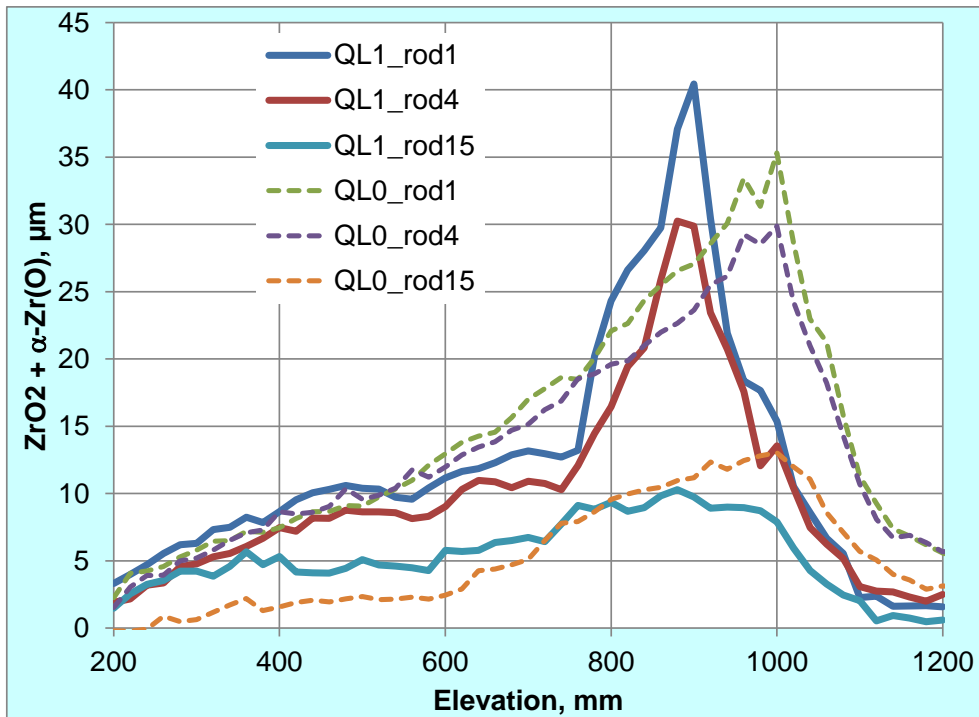
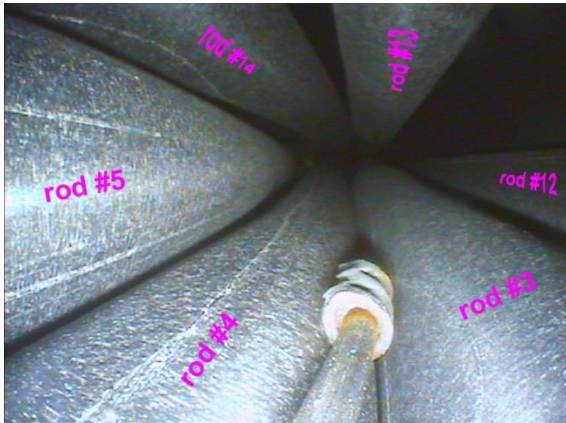


**Figure 79** Comparison of eddy-current measurements of axial layer thickness distribution for bundles QUENCH-L1 and QUENCH-L0.



at corn. rod A, elevation 850 mm:  
TC TFS 4/12, bending of rods #3, #4, #5  
from the outer rods to centre rod



at corn. rod A, elevation 950 mm:  
TC TFS 4/13



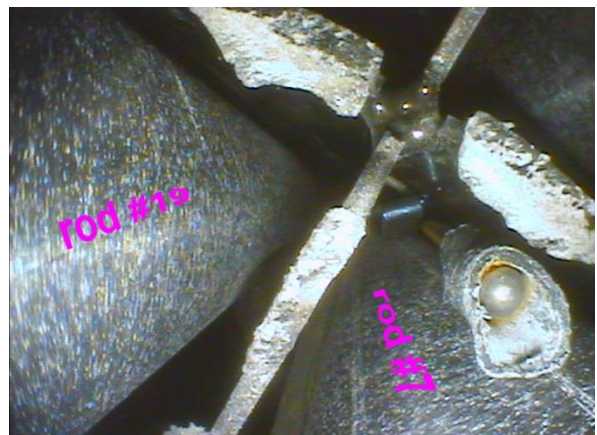
at corn. rod B, elevation 950 mm: bending of  
rod #17



at corn. rod B, elevation 950 mm:  
fragmented pellets blocked the burst  
opening of rod #16



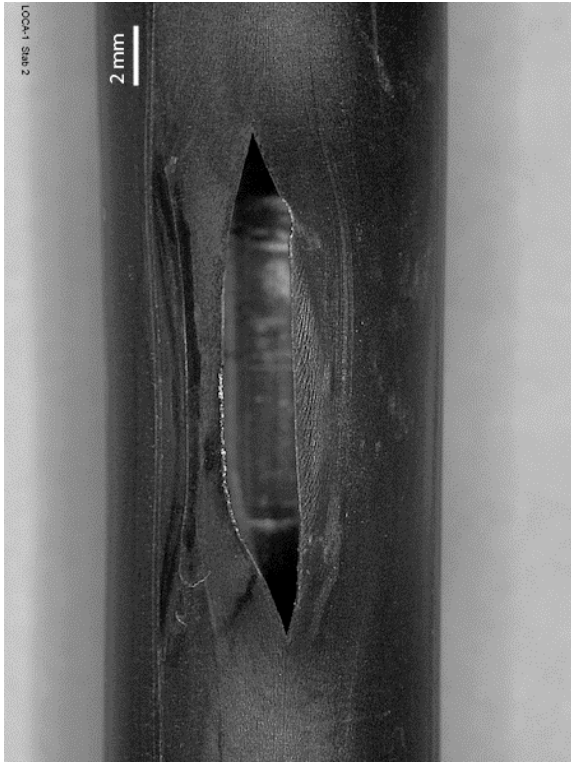
at corn. rod C, elevation 950 mm:  
TC TFS 7/13, bending of rod #18



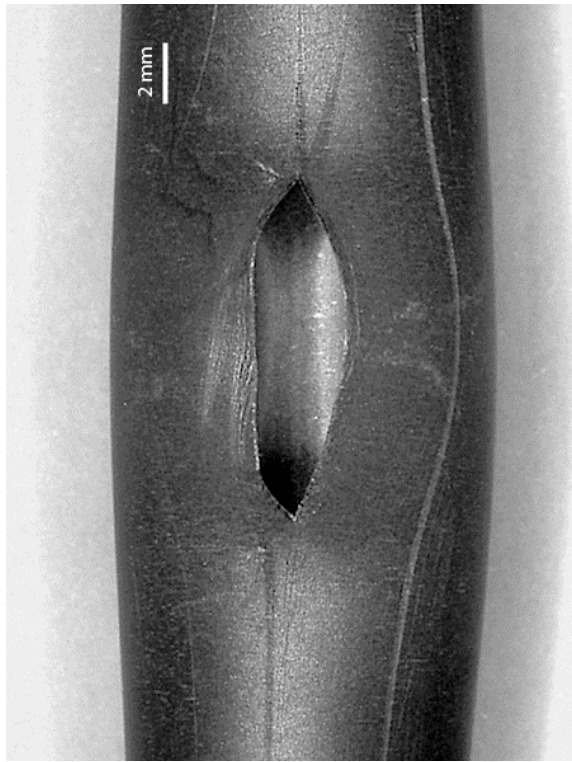
at corn. rod C, elevation 1050 mm:  
TC TFS 7/14, partially oxidised grid spacer

**Figure 80** QUENCH-L1; Post-test bundle investigation by videoscope at positions of three withdrawn corner rods.

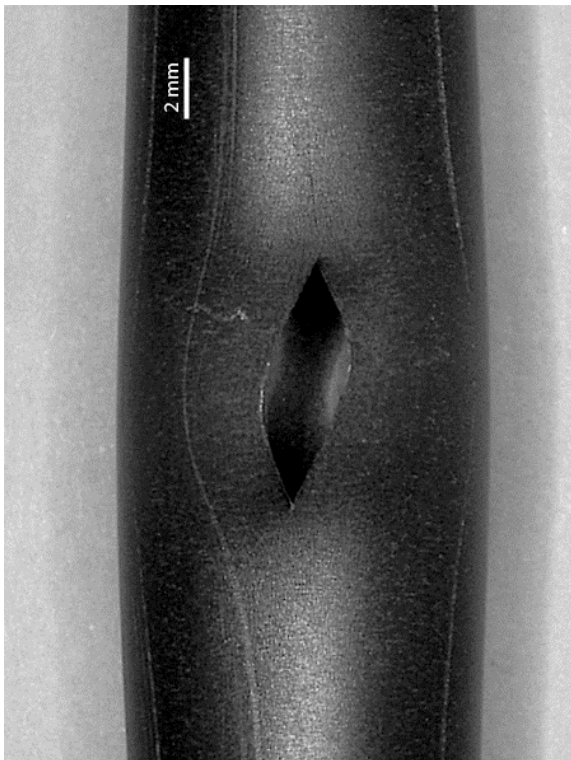




Rod #2 at 45°,  $A_{burst} = 29,5 \text{ mm}^2$



Rod #3 at 190°  $A_{burst} = 25 \text{ mm}^2$

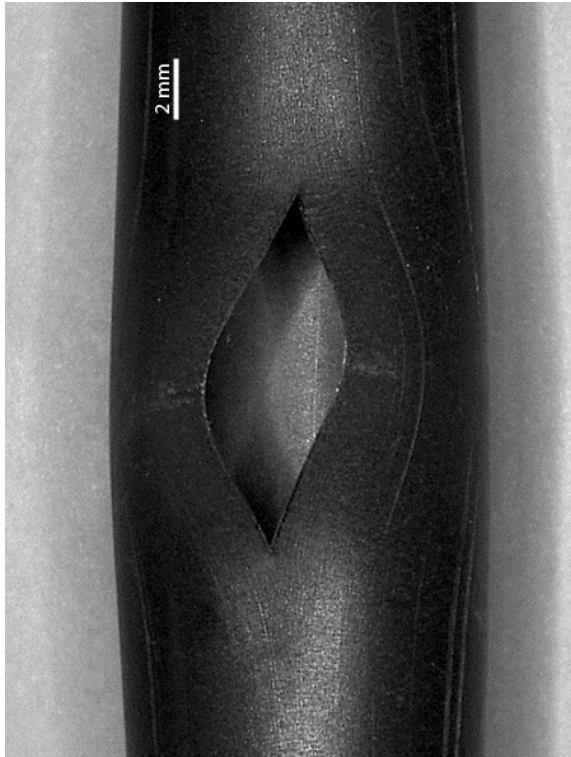


Rod #4 at 210°,  $A_{burst} = 13,5 \text{ mm}^2$

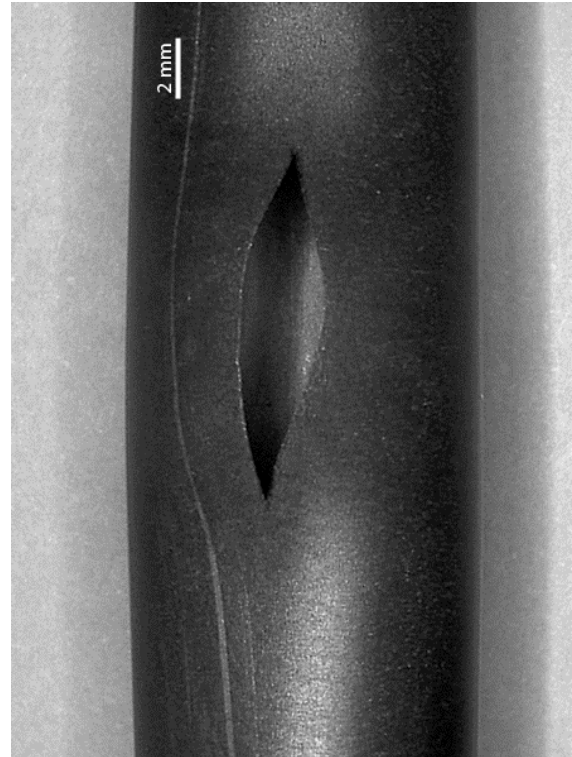


Rod #5 at 270°,  $A_{burst} = 198 \text{ mm}^2$

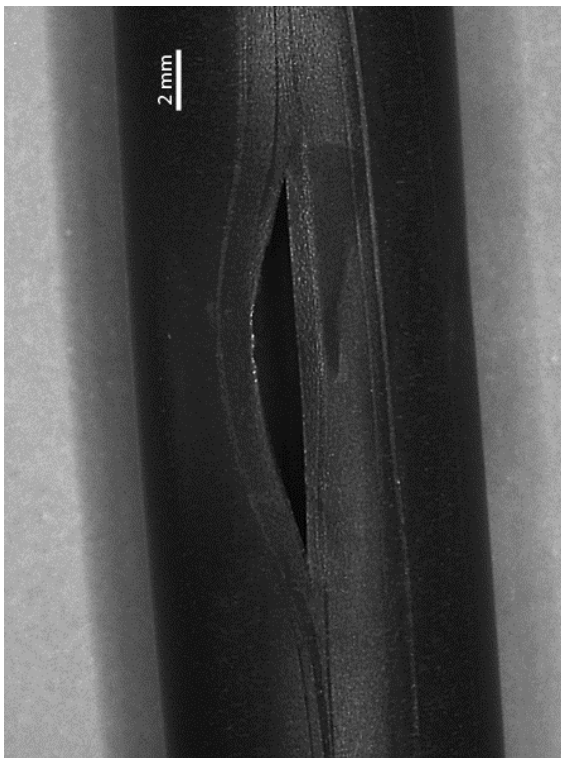
**Figure 81** QUENCH-L1; Overview of burst structures of rods #2 - #5.



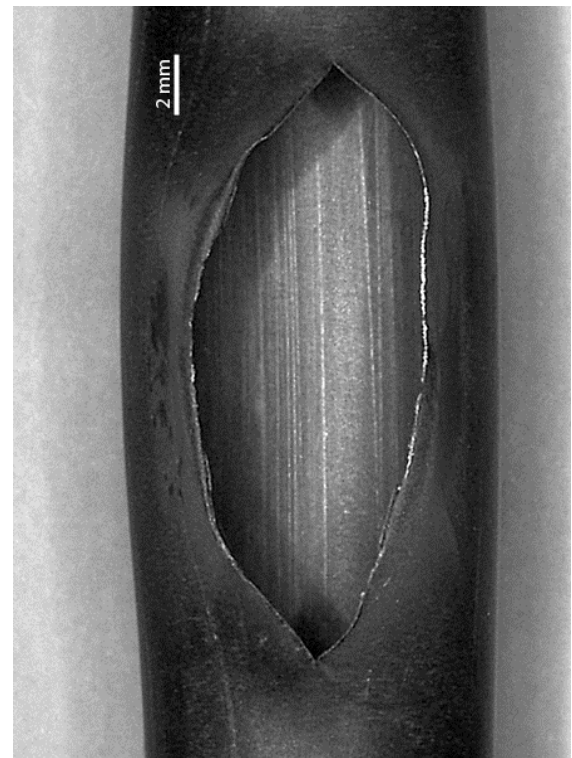
Rod #6 at 280°,  $A_{burst} = 30 \text{ mm}^2$



Rod #7 at 20°  $A_{burst} = 19,5 \text{ mm}^2$

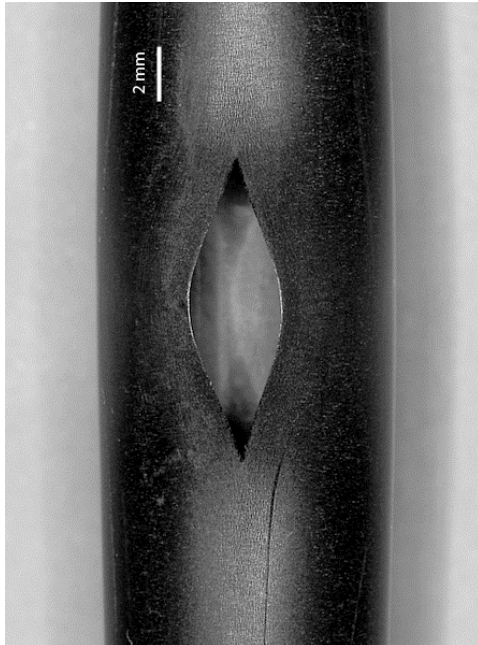


Rod #8 at 0°,  $A_{burst} = 11 \text{ mm}^2$

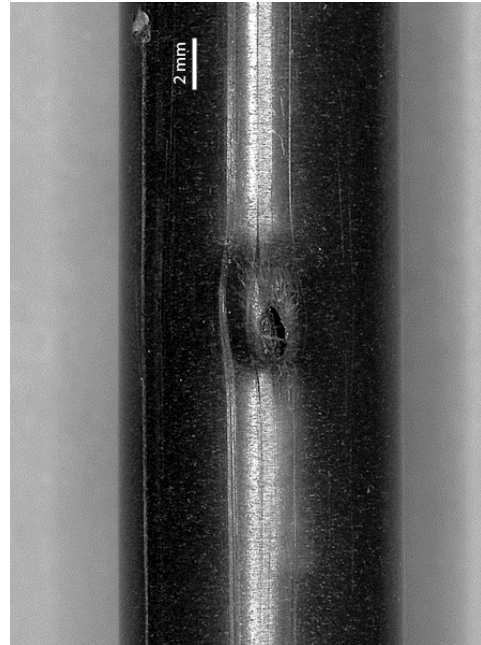


Rod #9 at 45°,  $A_{burst} = 110 \text{ mm}^2$

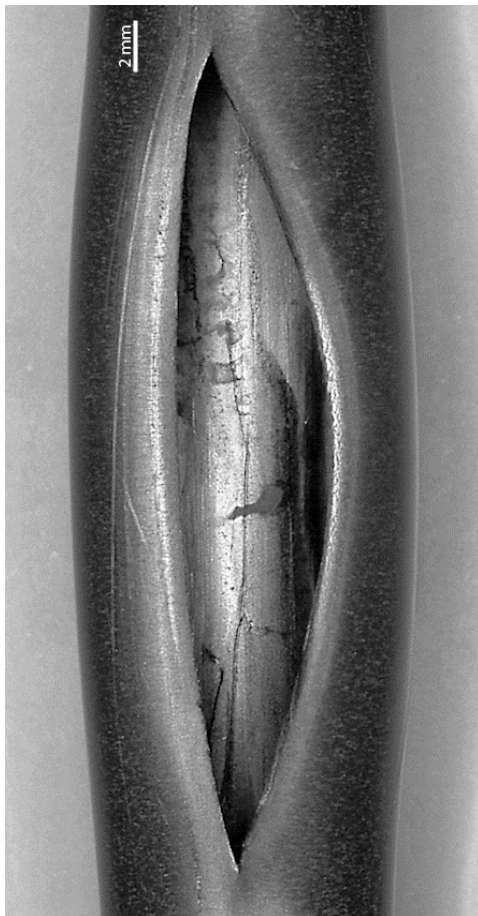
**Figure 82** QUENCH-L1; Overview of burst structures of rods #6 - #9.



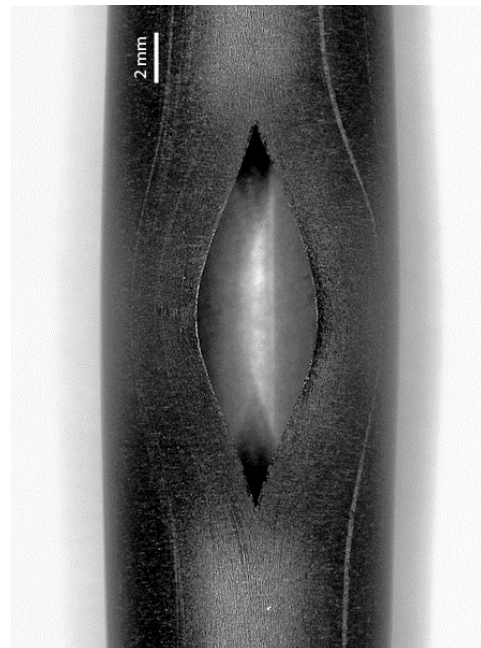
Rod #10 at 80°,  $A_{burst} = 24 \text{ mm}^2$



Rod #11 at 250°  $A_{burst} = 0,4 \text{ mm}^2$



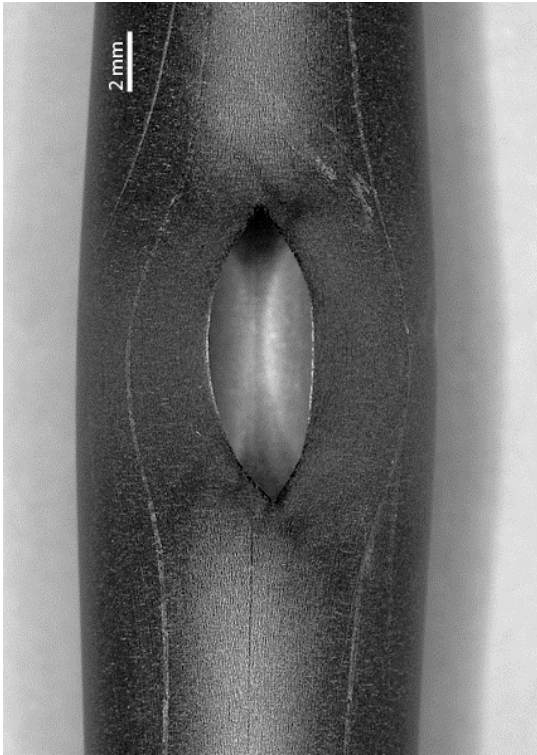
Rod #12 at 130°,  $A_{burst} = 126 \text{ mm}^2$



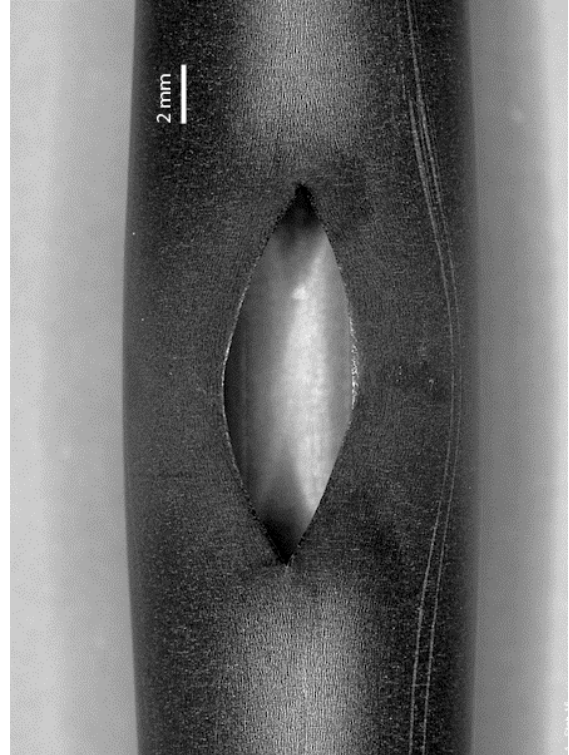
Rod #13 at 135°,  $A_{burst} = 40 \text{ mm}^2$

**Figure 83** QUENCH-L1; Overview of burst structures of rods #10 - #13.

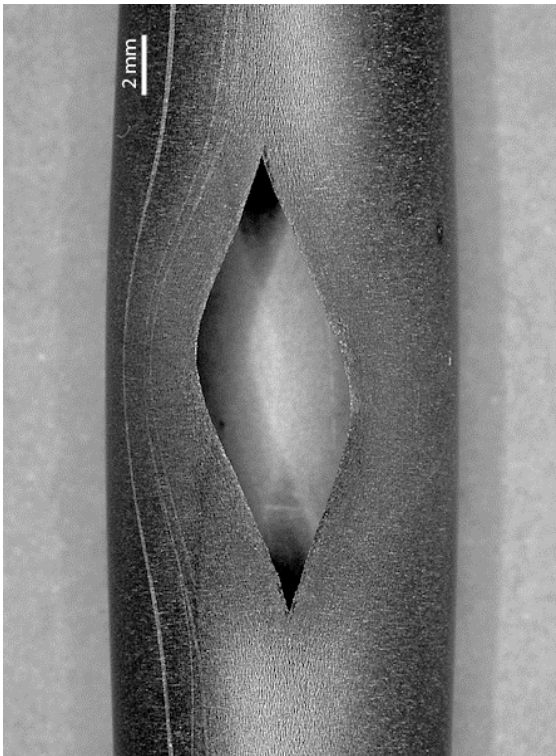




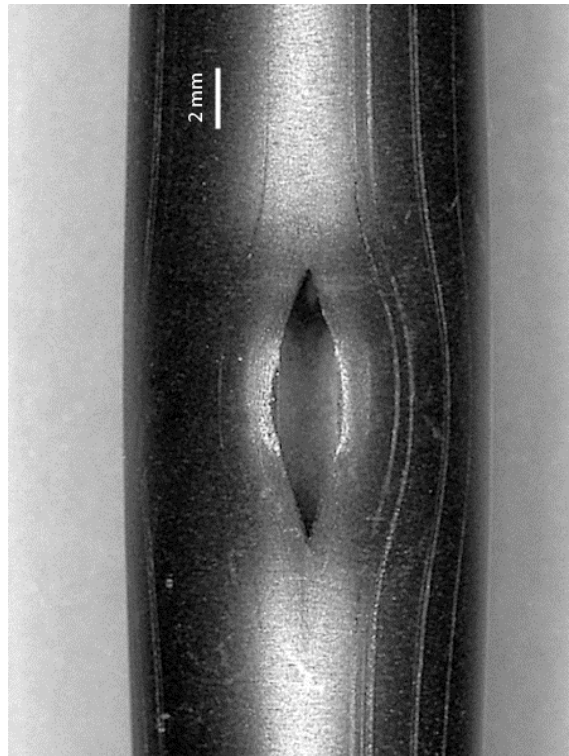
Rod #14 at 150°,  $A_{burst} = 24 \text{ mm}^2$



Rod #15 at 190°,  $A_{burst} = 35 \text{ mm}^2$



Rod #16 at 225°,  $A_{burst} = 42 \text{ mm}^2$

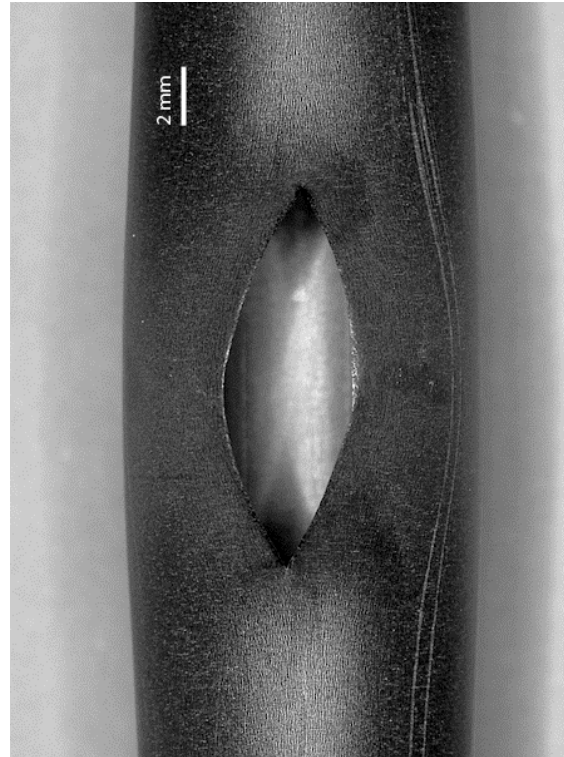


Rod #17 at 270°,  $A_{burst} = 18 \text{ mm}^2$

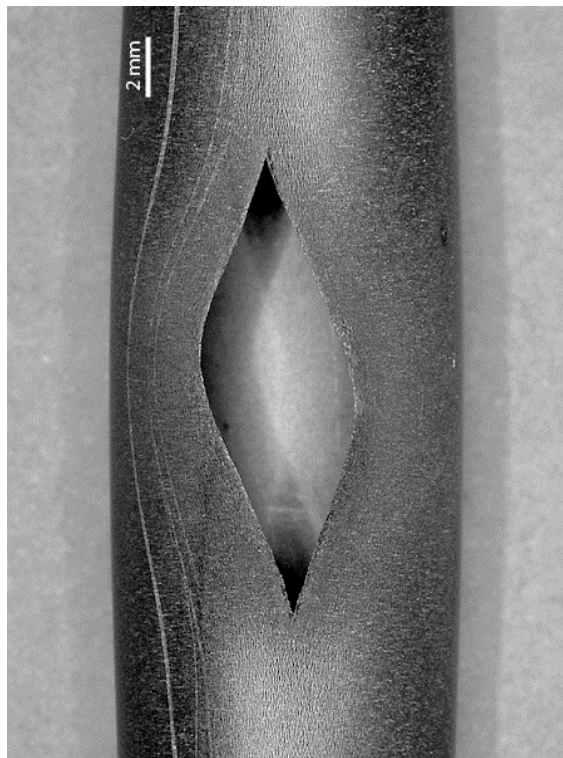
**Figure 84** QUENCH-L1; Overview of burst structures of rods #14 - #17.



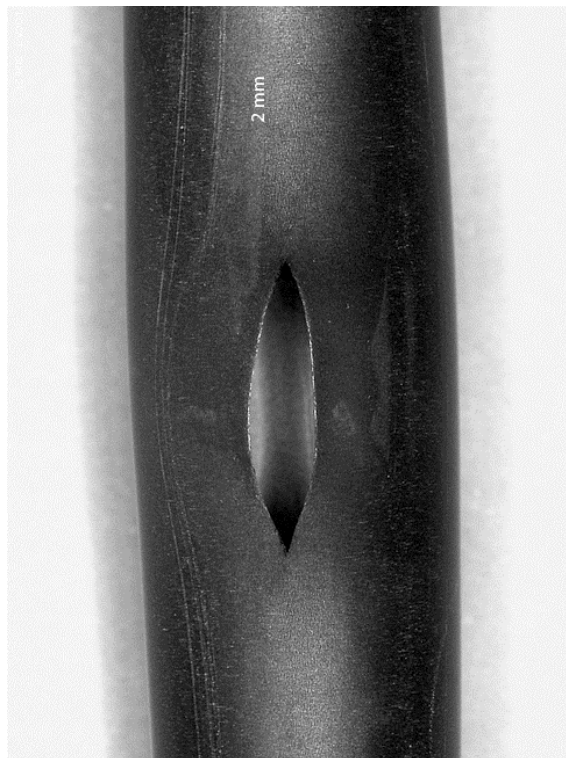
Rod #18 at 45°,  $A_{burst} = 17 \text{ mm}^2$



Rod # 19 at 0°,  $A_{burst} = 22 \text{ mm}^2$



Rod #20 at 20°  $A_{burst} = 92 \text{ mm}^2$

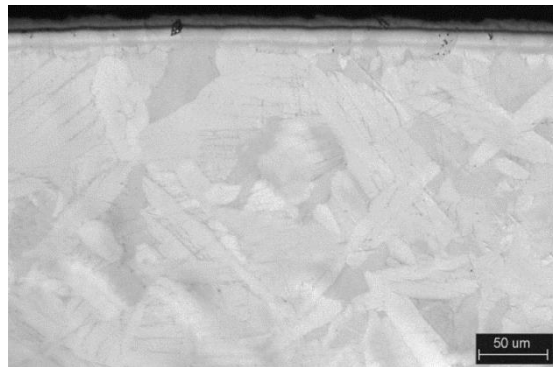


Rod #21 at ,45°,  $A_{burst} = 17 \text{ mm}^2$

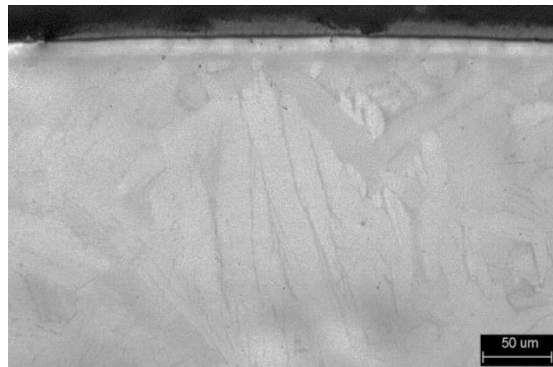
**Figure 85** QUENCH-L1; Overview of burst structures of rods #18 - #21.



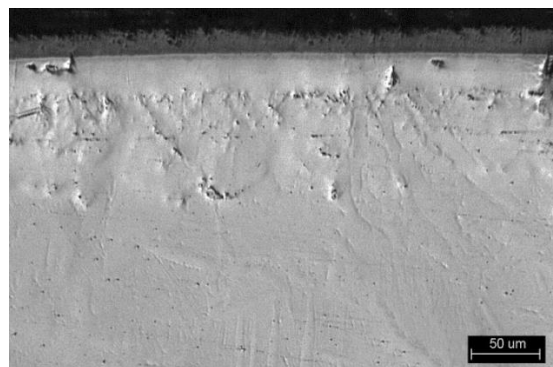
1010 mm, 225°; ZrO<sub>2</sub>: 8 μm; α-Zr(O): 8 μm



990 mm, 225°; ZrO<sub>2</sub>: 10 μm; α-Zr(O): 12 μm



940 mm, 225°; ZrO<sub>2</sub>: 14 μm; α-Zr(O): 12 μm



900 mm, 225°; ZrO<sub>2</sub>: 19 μm; α-Zr(O): 28 μm

**Figure 86** QUENCH-L1; Structure of cladding layers for rod #1 at cladding side opposite to burst opening.

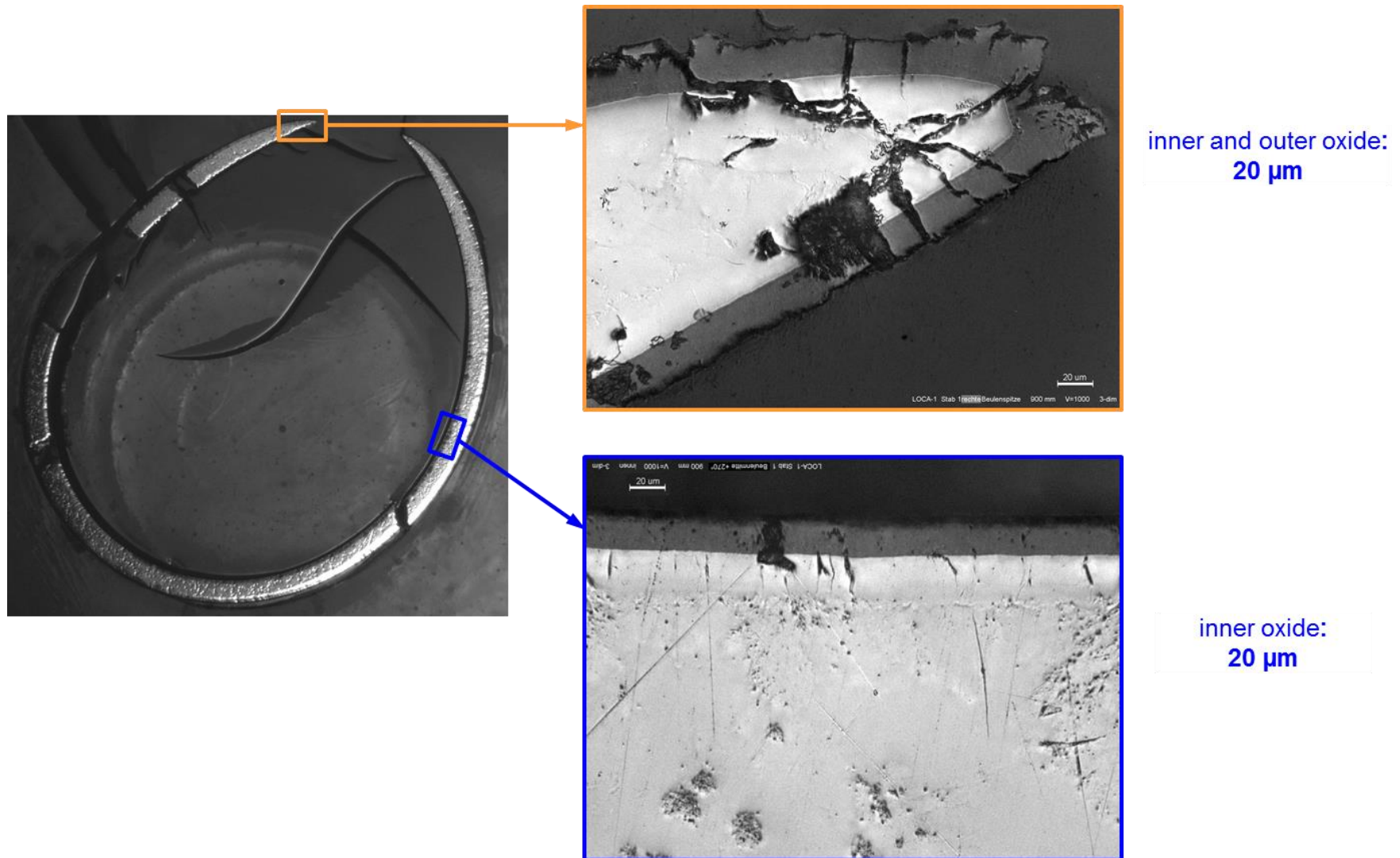
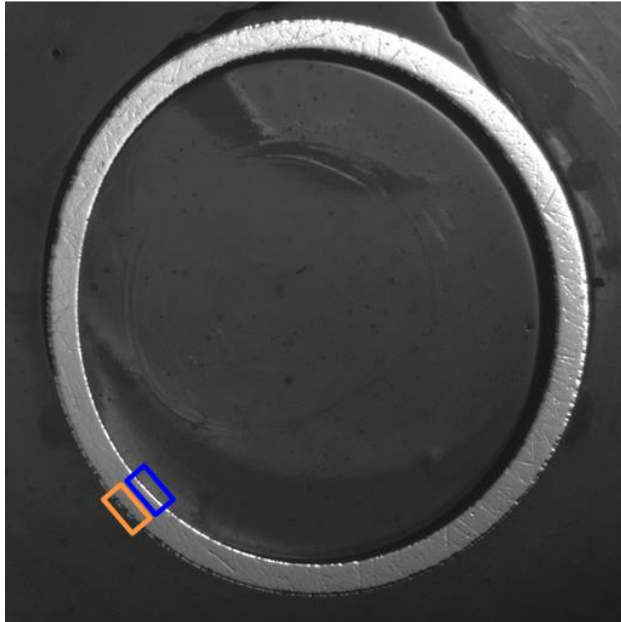
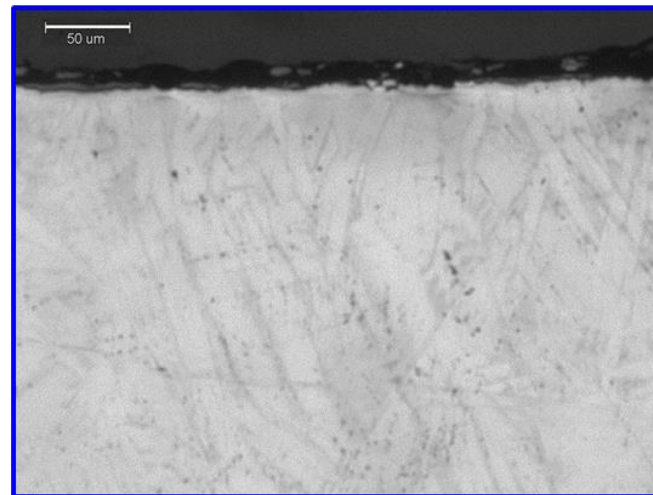


**Figure 87** QUENCH-L1; Outer and inner cladding oxidation at elevation 900 mm for rod #1.





outer oxide:  
12 μm



inner oxide:  
4 μm

**Figure 88** QUENCH-L1; Outer and inner cladding oxidation at elevation 920 mm for rod #1.

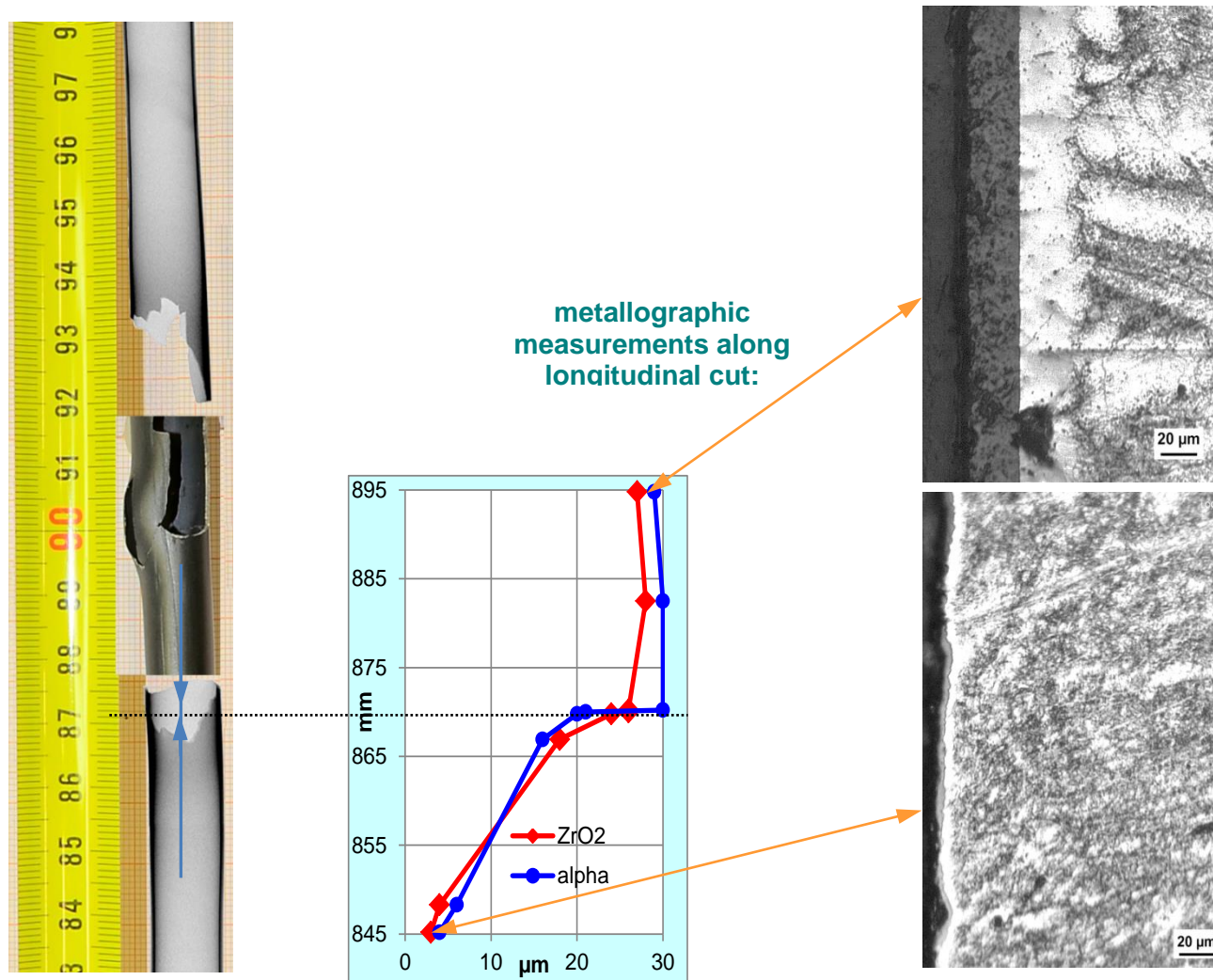


**Figure 89** QUENCH-L1; Axial distribution of inner oxidation in region of hydrogen band below burst opening for rod #1 at azimuth 315°.

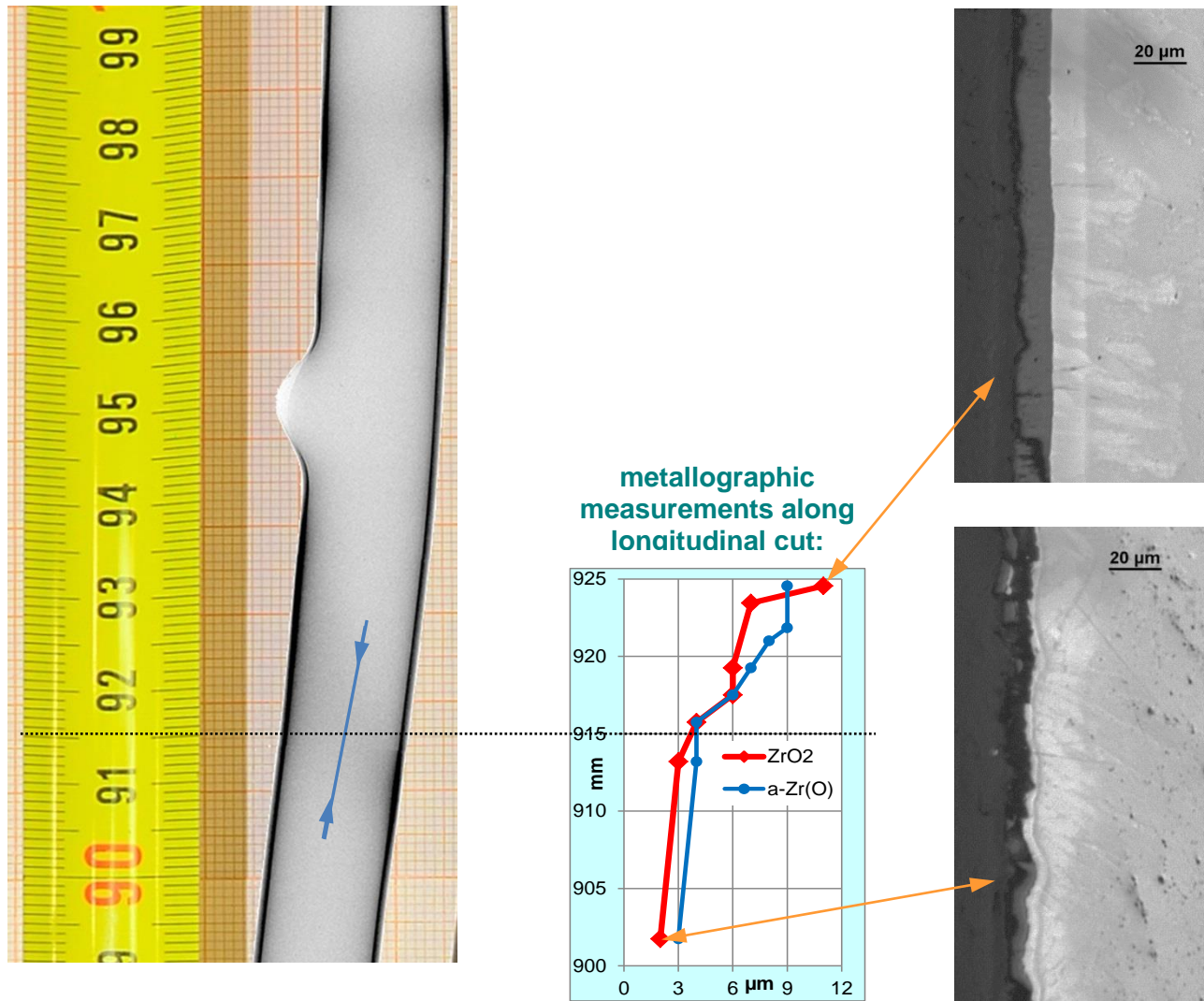


**Figure 90** QUENCH-L1; Axial distribution of inner oxidation in region of secondary hydrogenation for rod #6 at azimuth 25°.

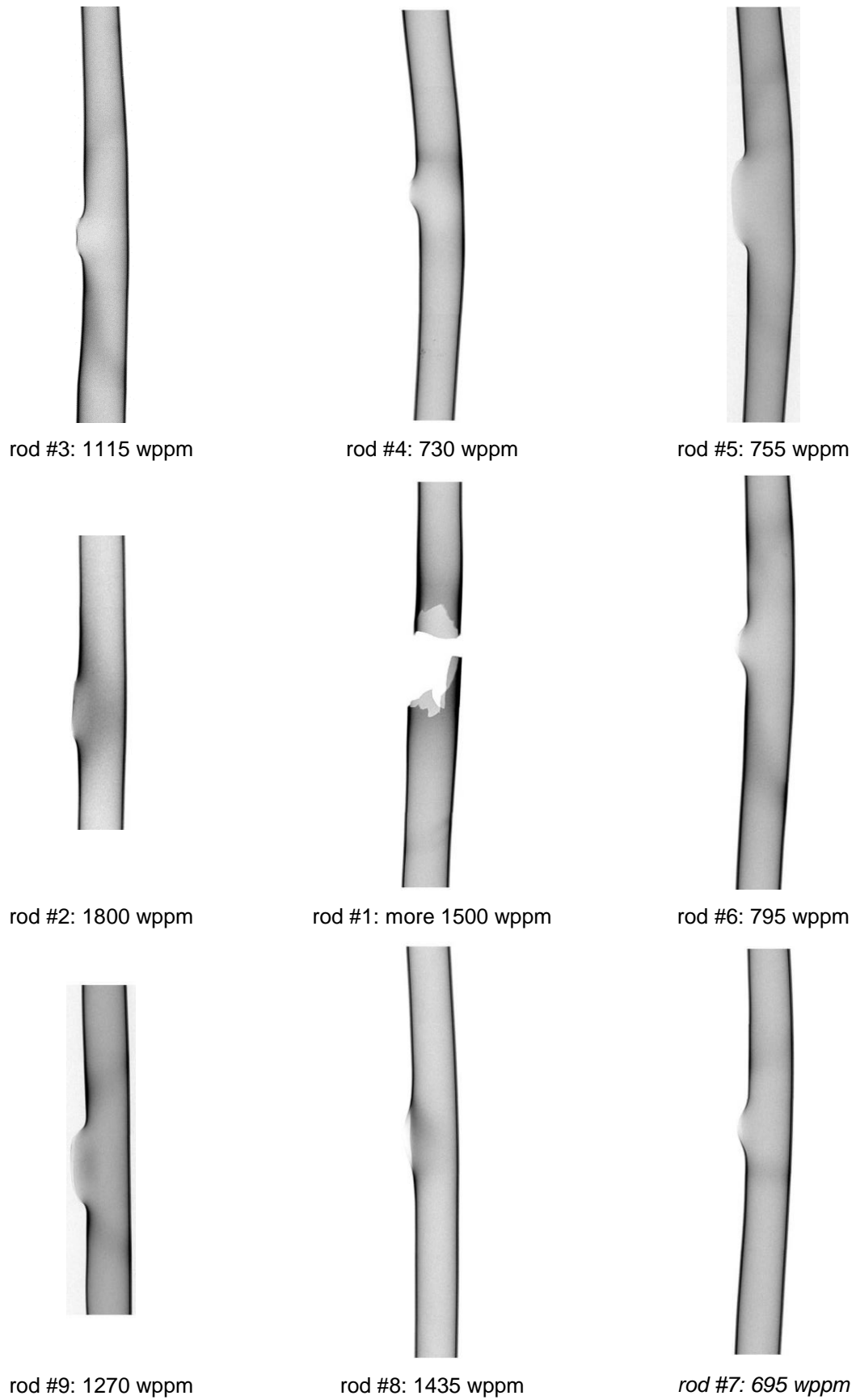


**Figure 91** QUENCH-L1; Hydrogen bands on neutron radiographs of inner rods and maximum hydrogen content.



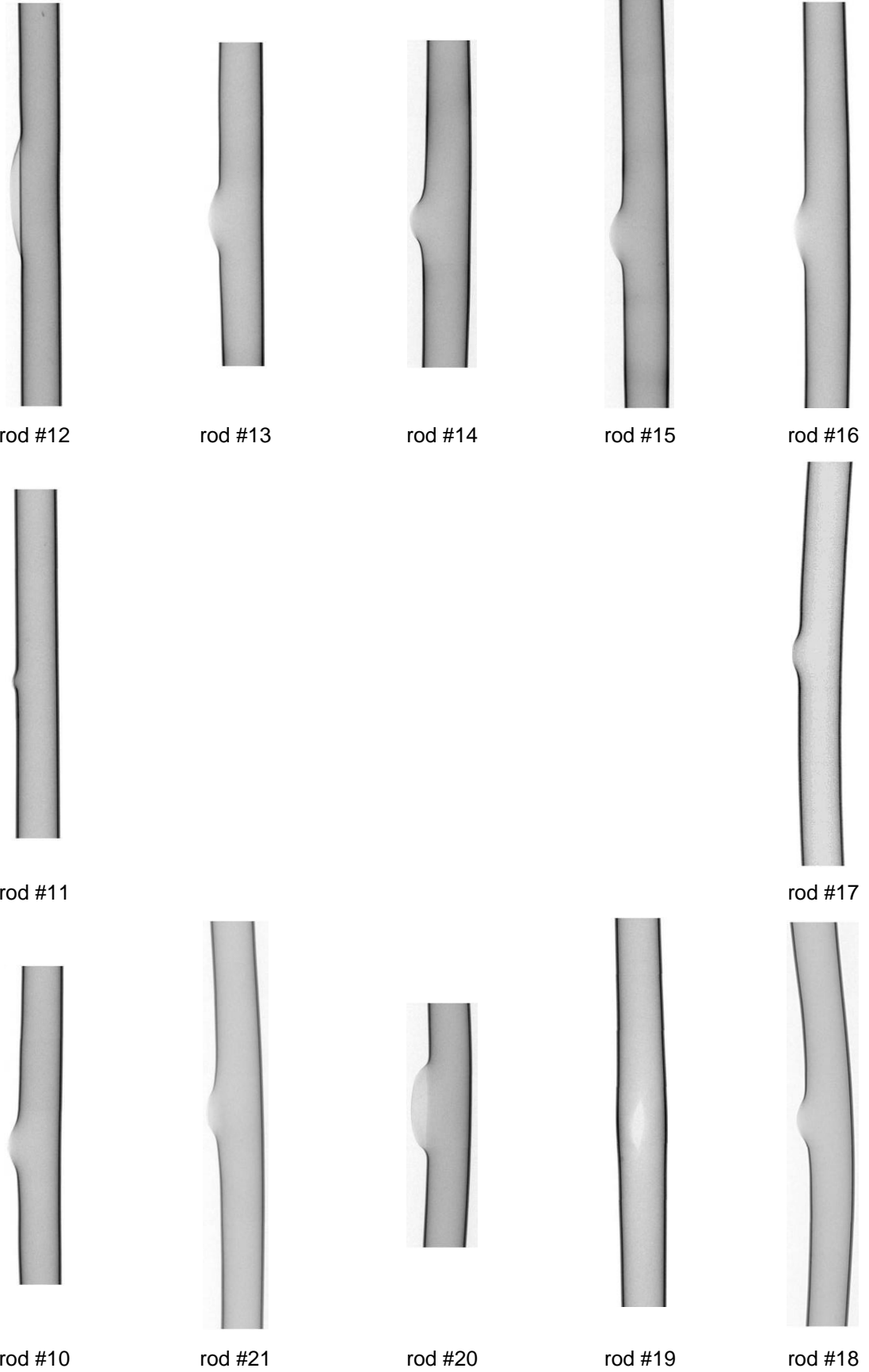


**Figure 92** QUENCH-L1; Absence of hydrogen bands on neutron radiographs of outer rods.

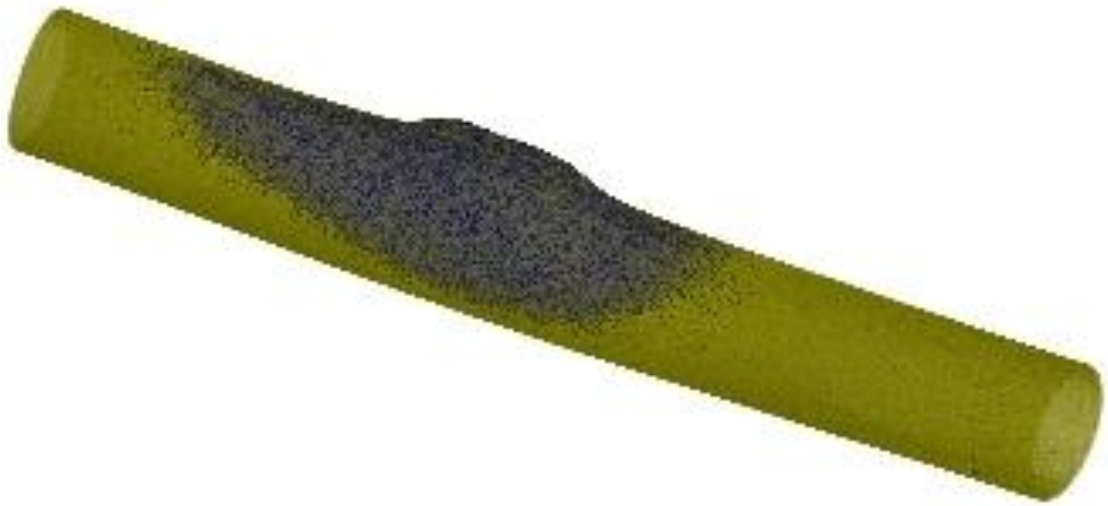


**Figure 93** QUENCH-L1; Tomography projection of the reconstructed hydrogen distribution in rod #2.

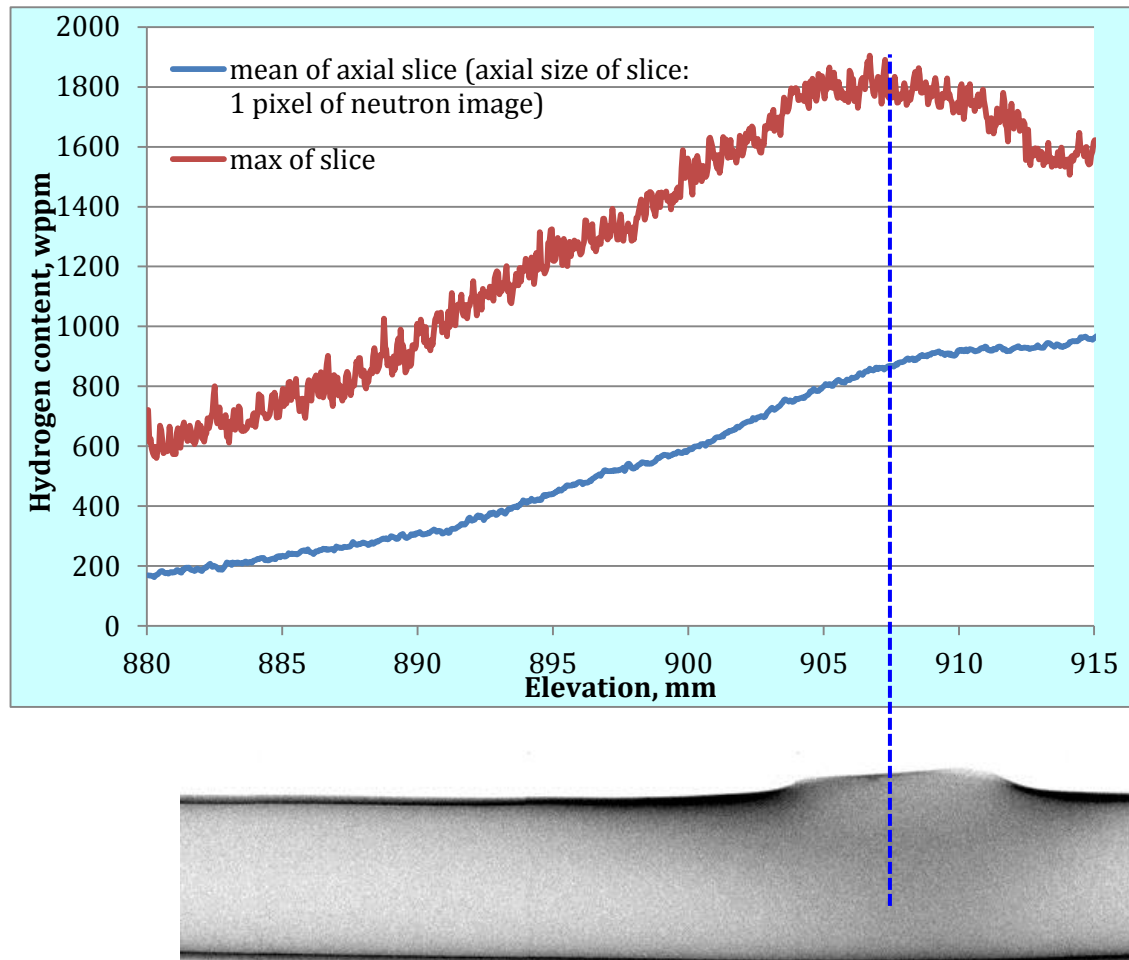


**Figure 94** QUENCH-L1; correspondance between reconstruction of tomography image and plots of mean and maximal hydrogen concentration in rod #2.

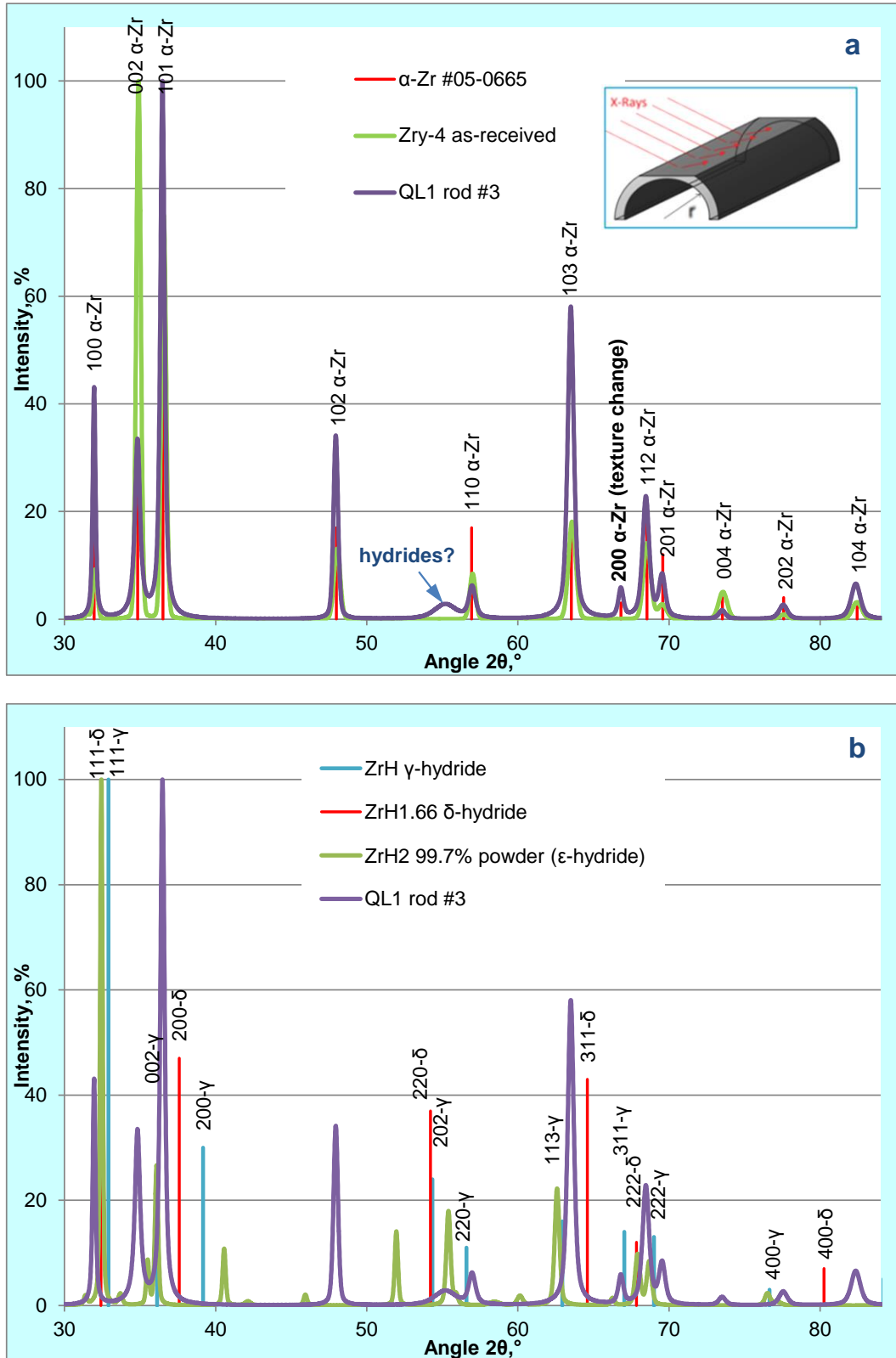


**Figure 95** QUENCH-L1; Results of XRD analyses for hydrogen bands of rod #3 (max hydrogen content 1115 wppm). Comparison with as received cladding (a) and with hydrides (b).

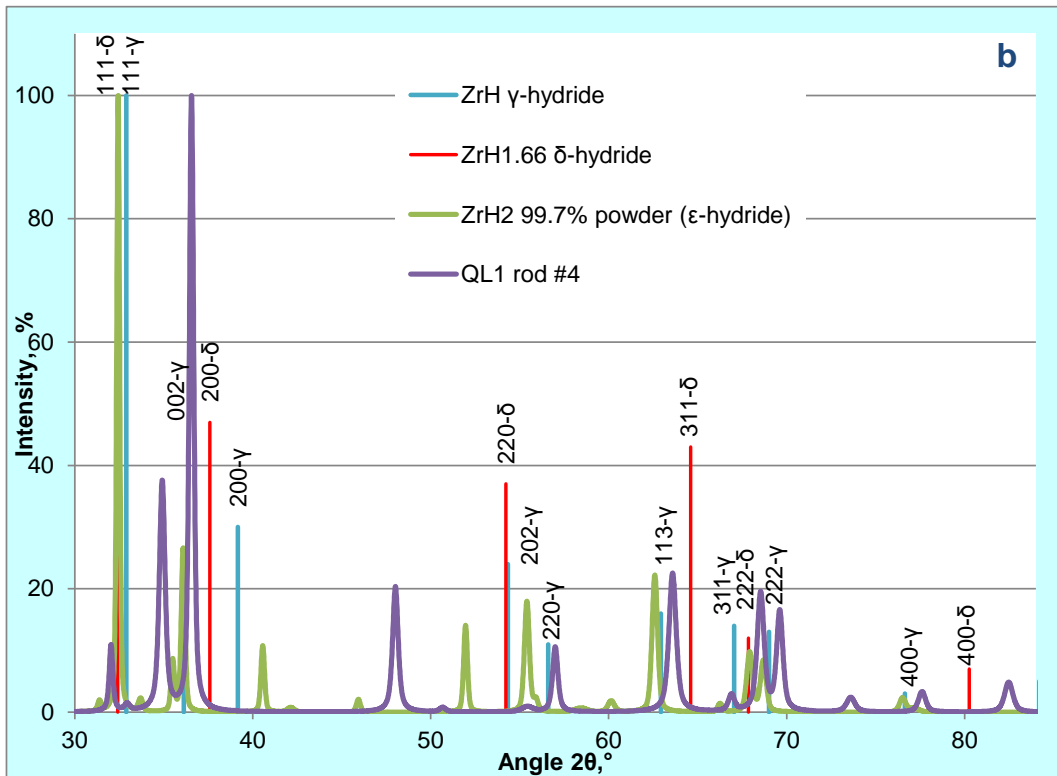
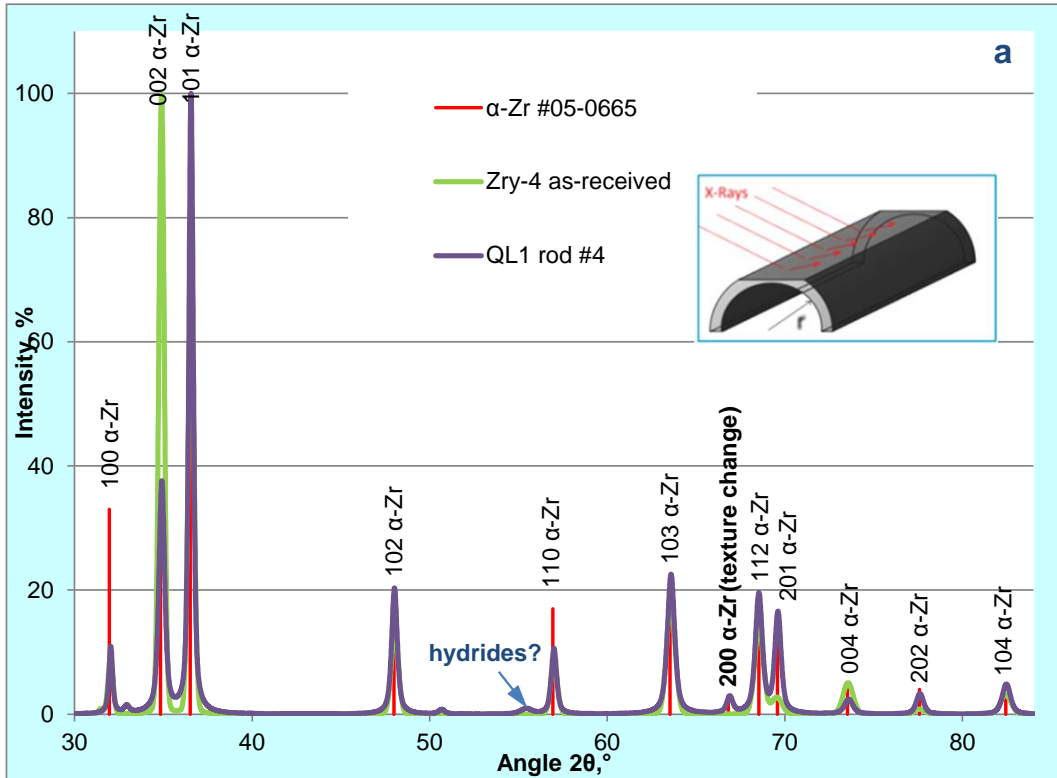


**Figure 96** QUENCH-L1; Results of XRD analyses for hydrogen bands of rod #4 (max hydrogen content 730 wppm). Comparison with as received cladding (a) and with hydrides (b).

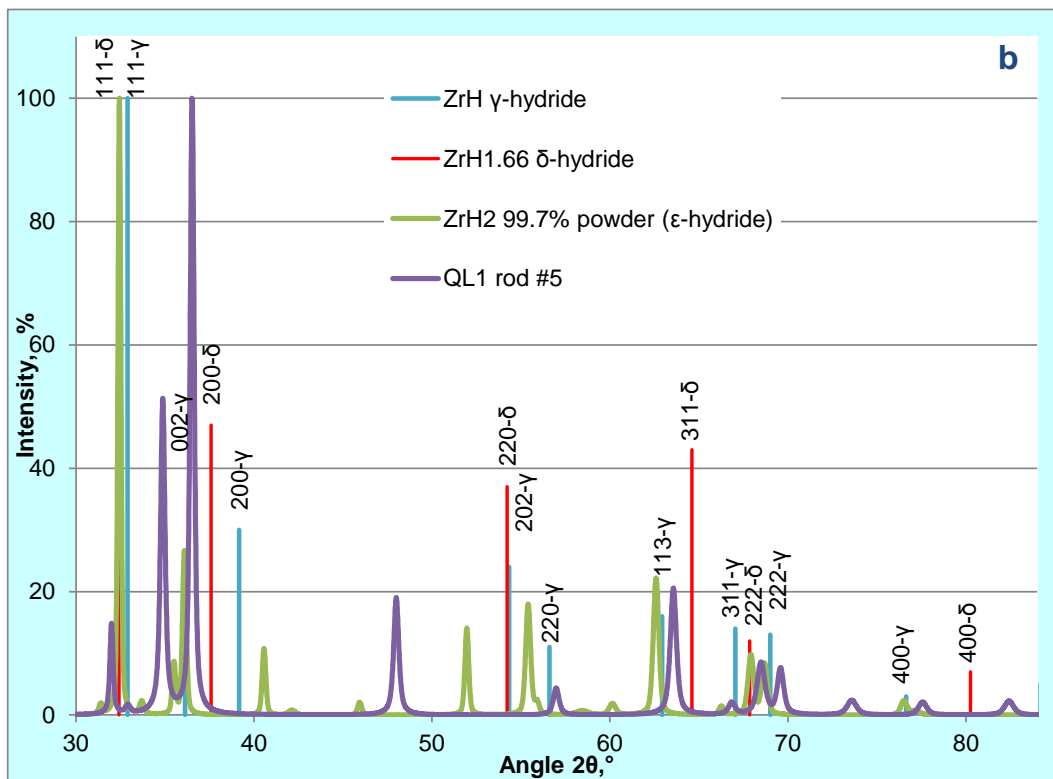
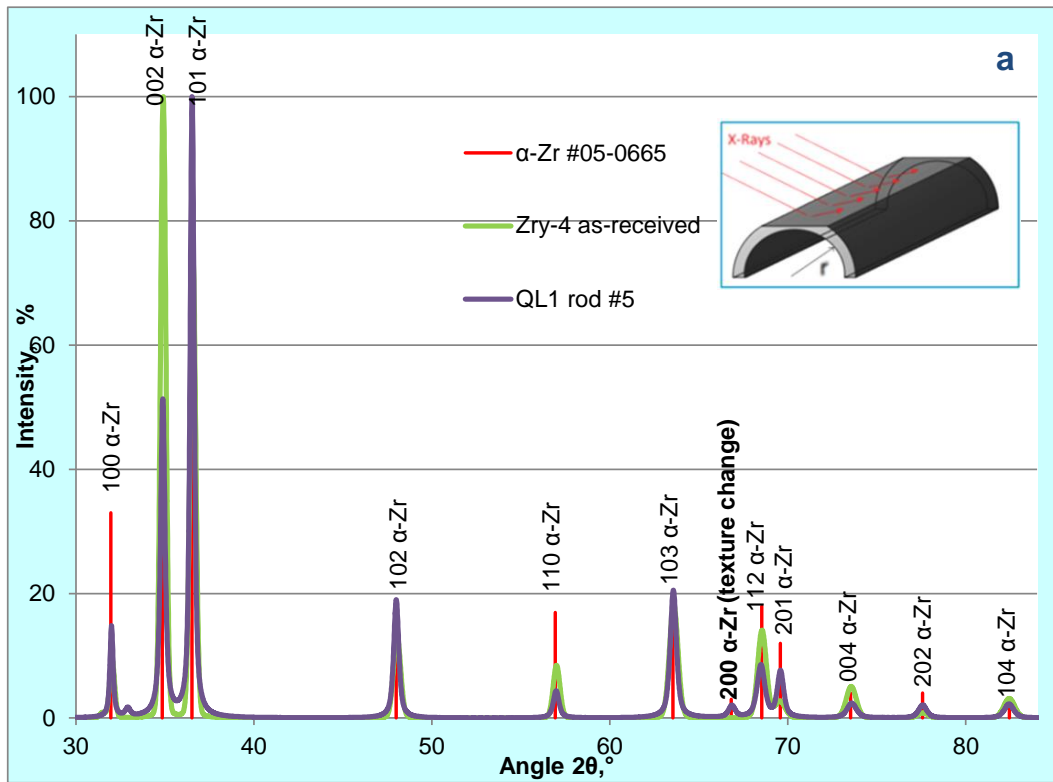


**Figure 97** QUENCH-L1; Results of XRD analyses for hydrogen bands of rod #5 (max hydrogen content 755 wppm). Comparison with as received cladding (a) and with hydrides (b).

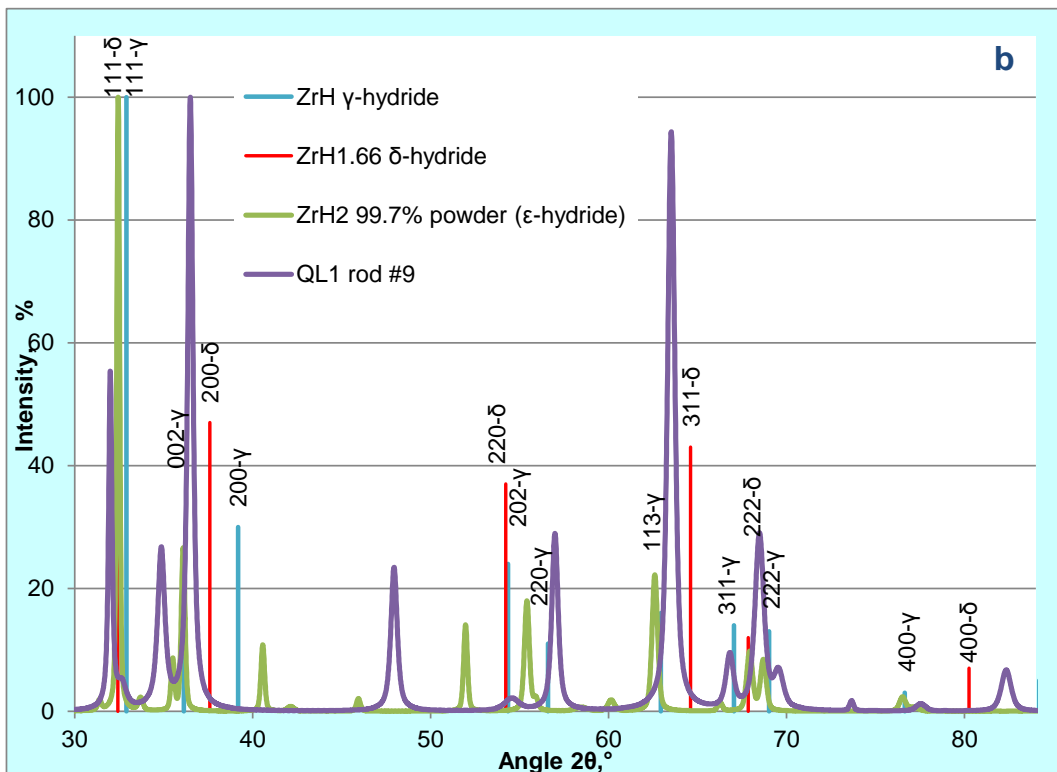
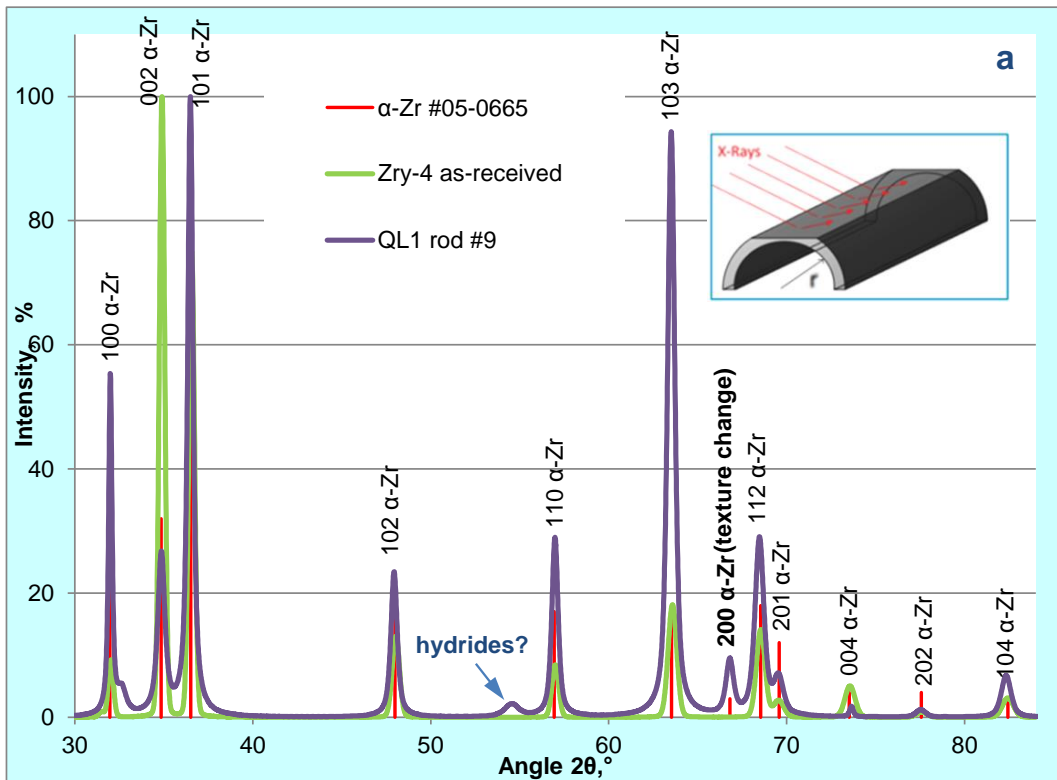


**Figure 98** Fig QUENCH-L1; Results of XRD analyses for hydrogen bands of rod #9 (max hydrogen content 1270 wppm). Comparison with as received cladding (a) and with hydrides (b)

QL0: 3

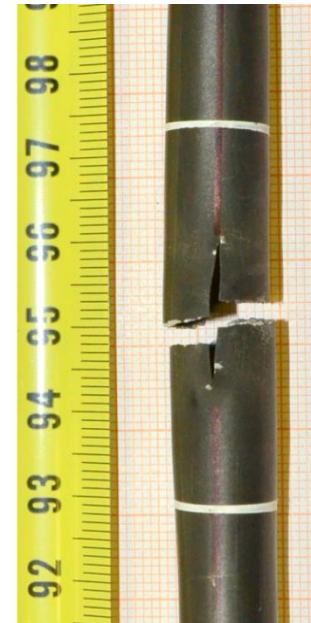
QL1: only stress concentration



hydrogen embrittlement (inner rods with  $C_H \sim 2000$ wppm)      stress concentration (outer rods with  $C_H \sim 1000$ wppm)      necking (outer rods)



rod #4



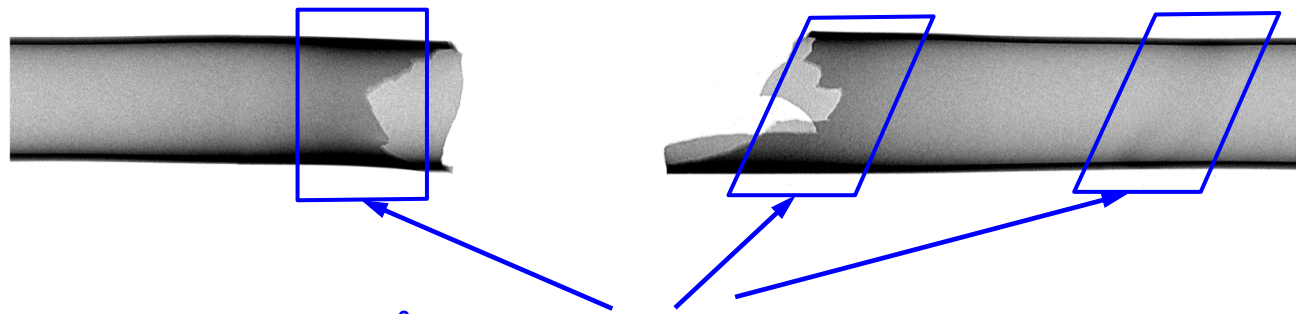
rod #6



rod #9

Figure 99 QUENCH-L0 and QUENCH-L1; Fracture modes, occurred in tensile tests.





<sup>0</sup>n -radiography: hydrogenated bands

(secondary hydrogenation during oxidation of the inner cladding surface through the burst opening)

max hydrogen concentration  
in hydrogenated bands (according to  
estimation derived for QUENCH-L0):

$$C_H(t) \approx 2 \cdot 10^3 \cdot \frac{k_{H_2} \bar{p}_{H_2}}{\rho_{Zry} LRT} t \approx 1500 \text{ wppm}$$

for T=1173 K and t=150s,  
p=6000Pa

Figure 100 QUENCH-L1; Central rod #1: brittle rupture during handling.

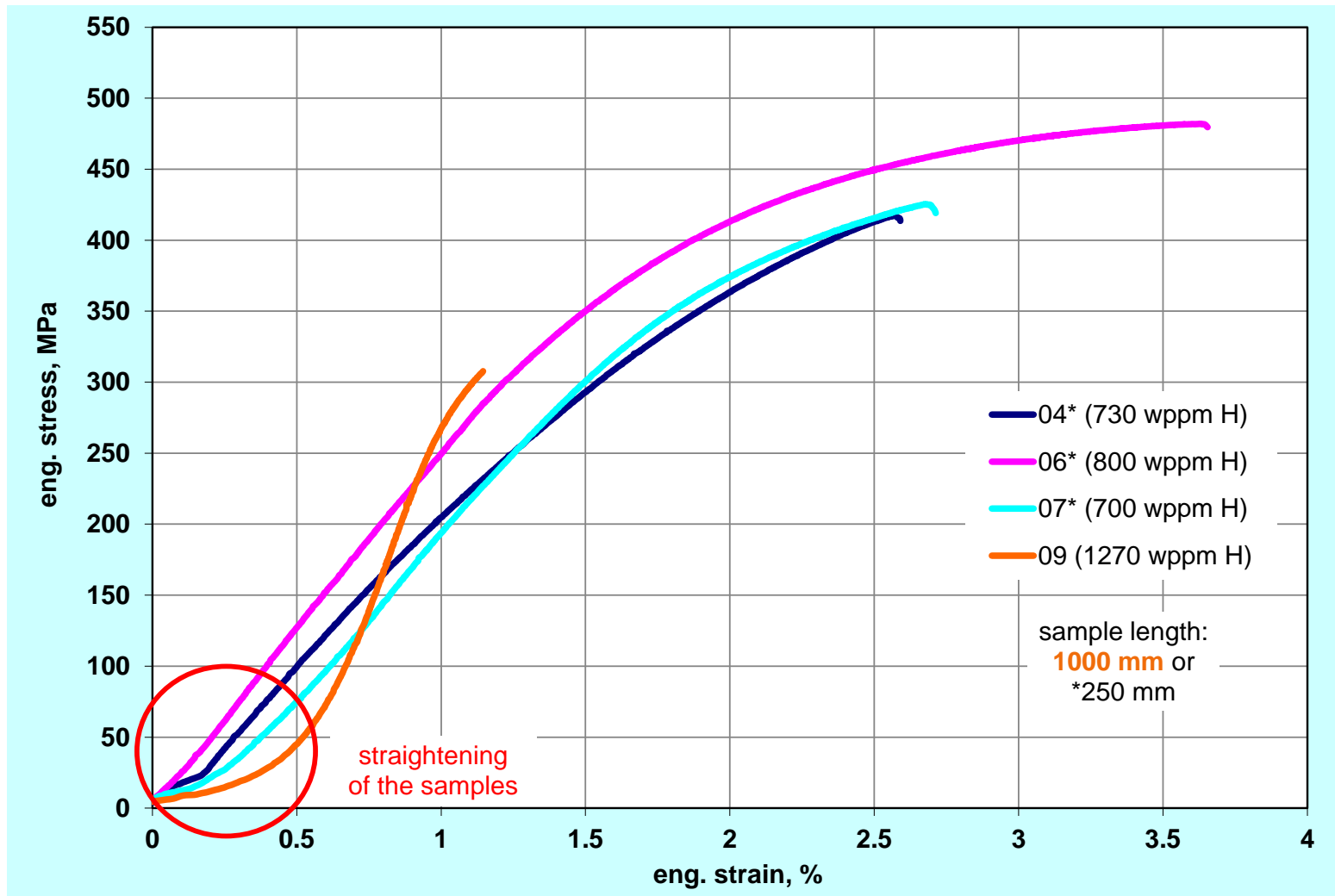


Figure 101 QUENCH-L1; Results of tensile tests for inner rods.

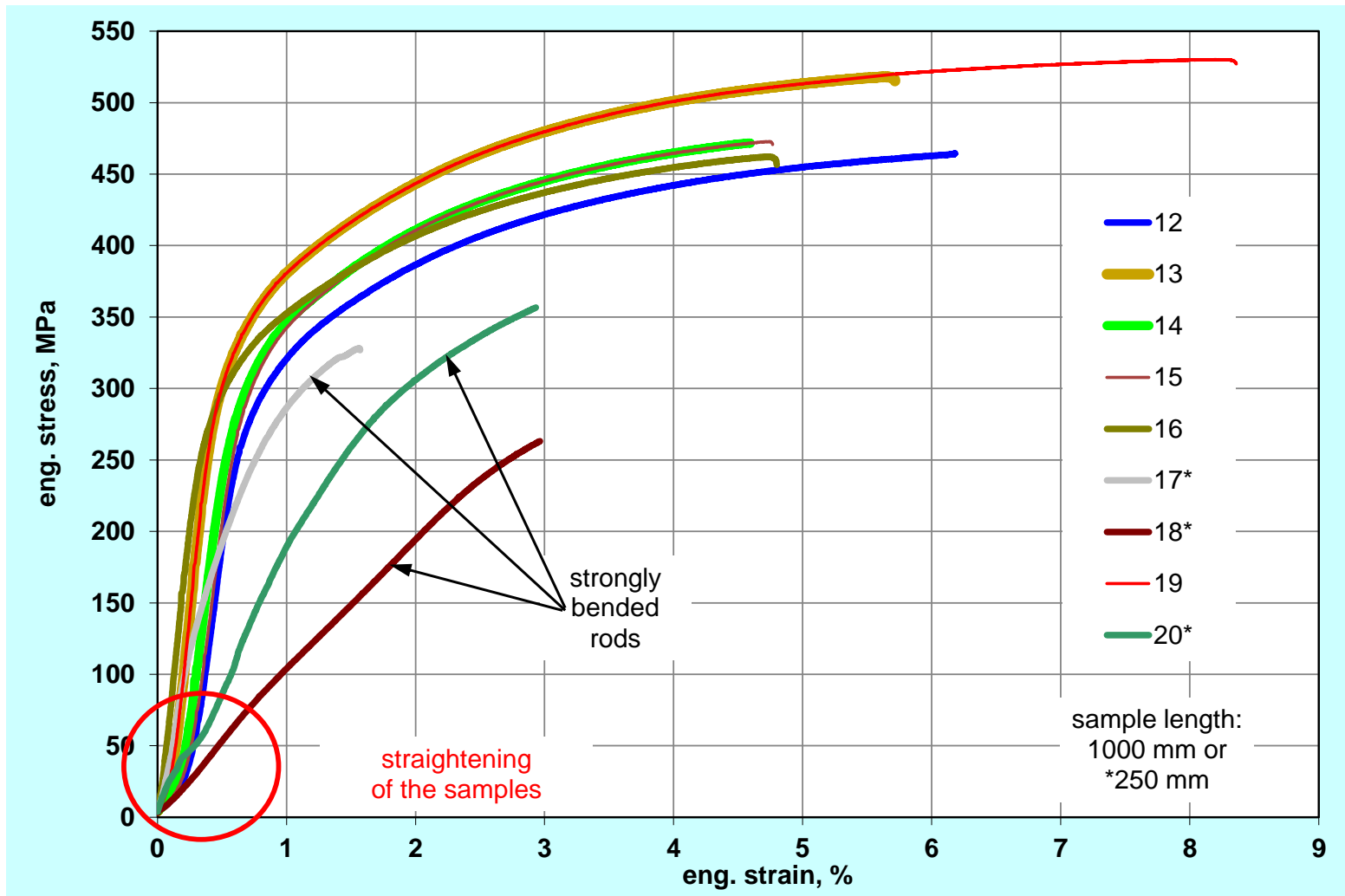
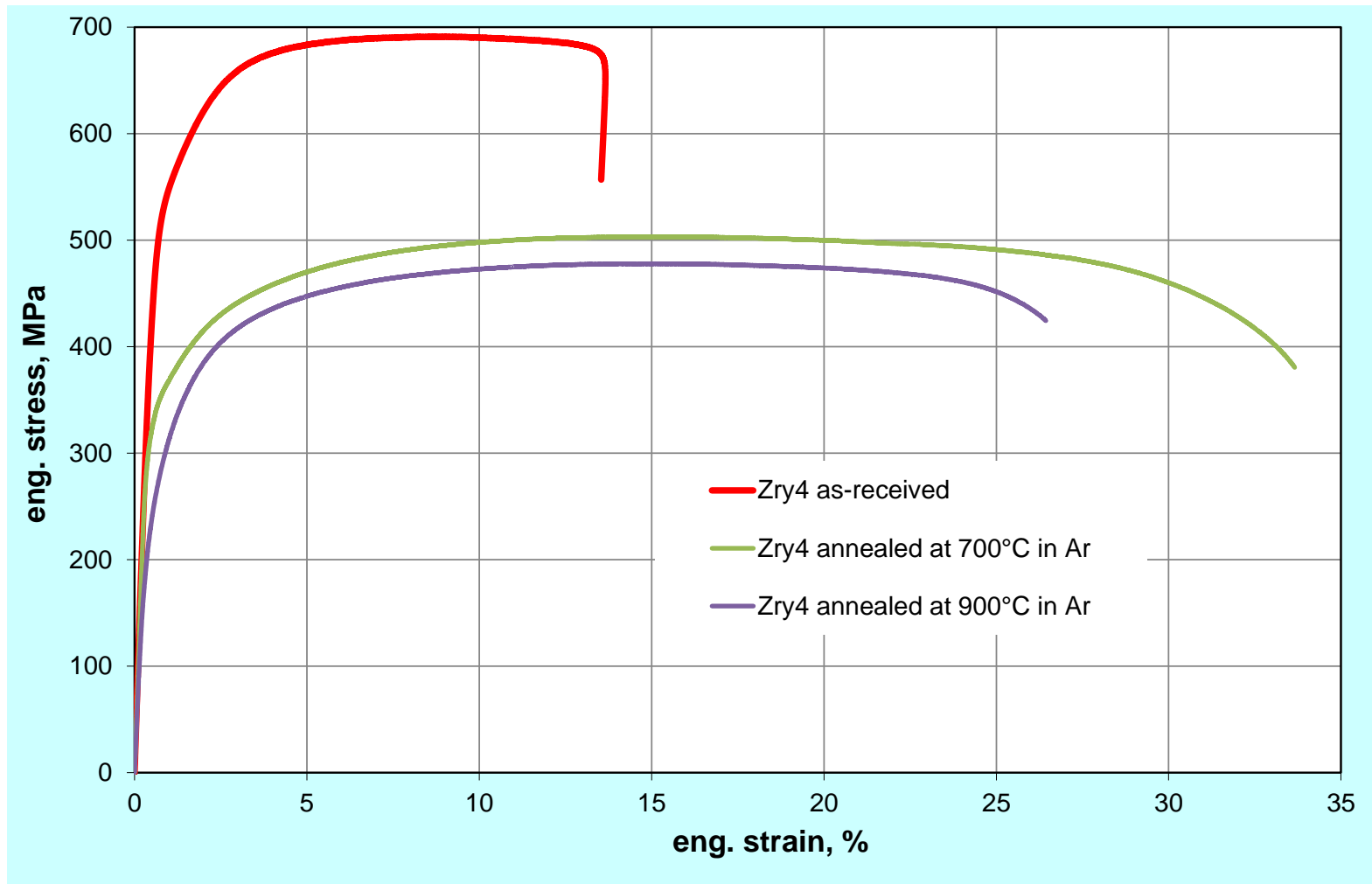


Figure 102 QUENCH-L1; Results of tensile tests for outer rods.



**Figure 103** Results of tensile tests on as-received and annealed Zircaloy-4 claddings, failure by necking.

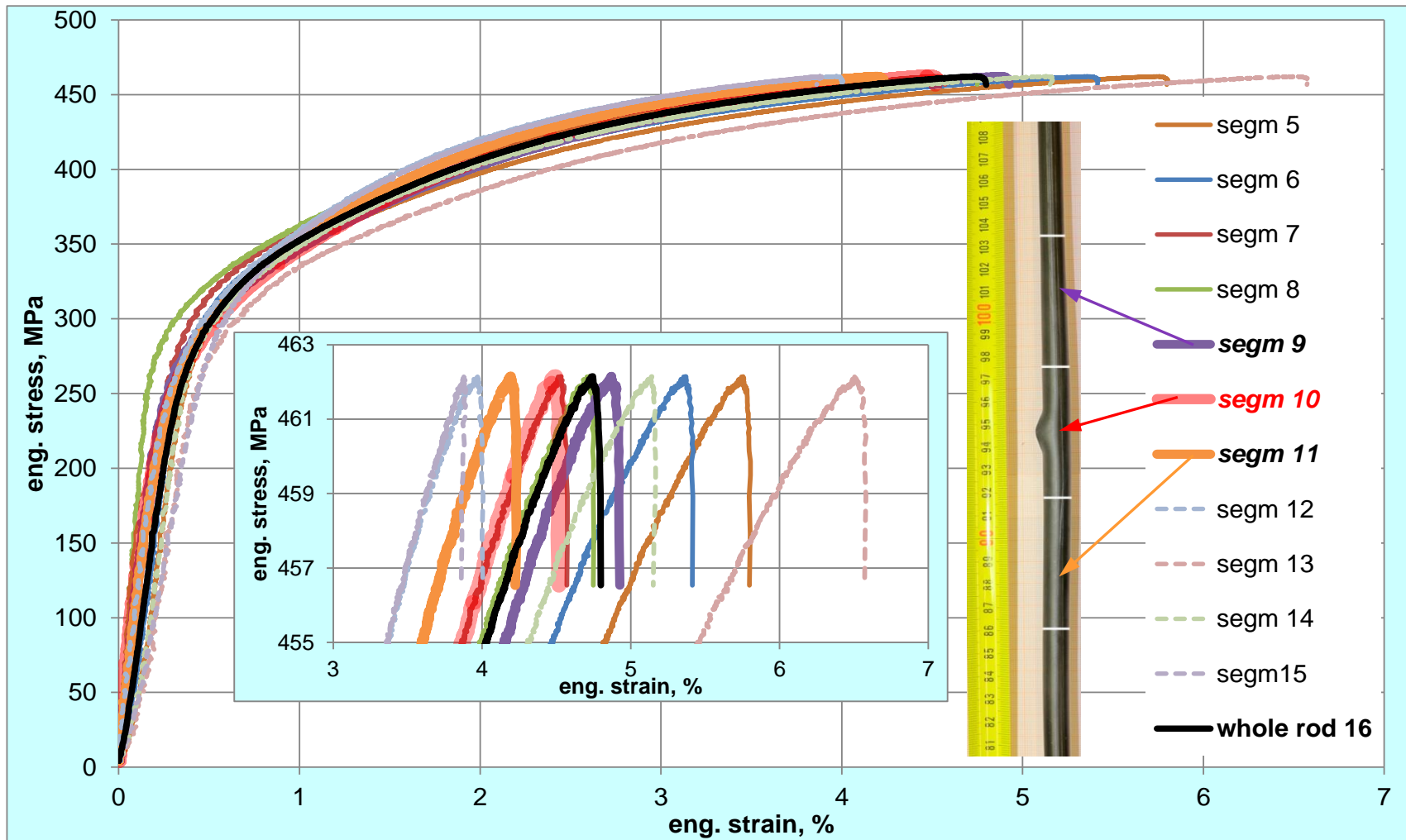



Figure 104 QUENCH-L1; Optical recognition of segment strains during tensile test with rod #16. Failure due to pre-crack inside burst



The QUENCH-LOCA project on out-of-pile bundle tests under conditions of a loss-of-coolant reactor accident is integral part of the Nuclear Safety Program at the Karlsruhe Institute for Technology. The overall objective of this bundle test series is the investigation of ballooning, burst and secondary hydrogen uptake of the fuel cladding tubes under representative design basis accident conditions.

The first test QUENCH-L1 was performed with 21 Zircaloy-4 cladding tubes not preoxidised on 22.07.2010 as commissioning test and terminated with reflood immediately after the transient phase. The QUENCH-L1 test was performed on 02.02.2012 as reference test, using a similar bundle compared to the QUENCH-L0 test but including a cool-down phase between transient and reflood. The total length of each fuel rod simulator, electrically heated by central tungsten heater, is 2.5 m. Each rod was separately pressurized with krypton with initial pressure of 55 bar. The duration of transient with increase of the peak cladding temperature from 800 to 1373 K was 87 s. The decreased yield strength and increased ductility of the heated cladding resulted in a progressive ballooning and consequent burst of all of the pressurized rods. The first burst occurred on 55 s after transient initiation. All pressurized rods failed within the next 32 s. The experiment continued by cooling phase with power decrease to 3.5 kW to simulate decay heat and increase of steam rate from 2 to 20 g/s. The cooling phase was followed by 100 g/s water injection at 207 s. Post-test investigations showed strain values between 25 and 50% at hottest cladding positions with oxidation degree corresponding to 2% ECR. Maximal blockage of cooling channel is 24%. No hydrogen bands around the burst openings were observed by means of neutron radiography for outer rods. Hydrogen content inside hydrogen bands of inner rods varied between 695 and 1690 wppm. Similar to QUENCH-L0, the oxide layer thickness on the inner cladding surface was measured up to 25  $\mu\text{m}$  at burst elevations and less 2  $\mu\text{m}$  at hydrogenated bands. All claddings (excluding central rod #1) were fractured due to stress concentration at the burst position – similar to rods of the QUENCH-L0 bundle with hydrogen concentration <1500 wppm.